Nizar Abcha · Efim Pelinovsky
Innocent Mutabazi *Editors*

Nonlinear Waves and Pattern Dynamics

Springer

Nonlinear Waves and Pattern Dynamics

Nizar Abcha · Efim Pelinovsky
Innocent Mutabazi
Editors

Nonlinear Waves and Pattern Dynamics

Springer

Editors
Nizar Abcha
Normandie Université, UNICAEN, UNIROUEN, CNRS, UMR 6143, M2C
Caen
France

Innocent Mutabazi
Normandie Université, Unihavre, CNRS, UMR 6294, LOMC
Le Havre
France

Efim Pelinovsky
Department of Nonlinear Geophysical Processes
Institute of Applied Physics of the Russian Academy of Sciences
Nizhny Novgorod
Russia

ISBN 978-3-319-78192-1 ISBN 978-3-319-78193-8 (eBook)
https://doi.org/10.1007/978-3-319-78193-8

Library of Congress Control Number: 2018935871

© Springer International Publishing AG, part of Springer Nature 2018
This work is subject to copyright. All rights are reserved by the Publisher, whether the whole or part of the material is concerned, specifically the rights of translation, reprinting, reuse of illustrations, recitation, broadcasting, reproduction on microfilms or in any other physical way, and transmission or information storage and retrieval, electronic adaptation, computer software, or by similar or dissimilar methodology now known or hereafter developed.
The use of general descriptive names, registered names, trademarks, service marks, etc. in this publication does not imply, even in the absence of a specific statement, that such names are exempt from the relevant protective laws and regulations and therefore free for general use.
The publisher, the authors and the editors are safe to assume that the advice and information in this book are believed to be true and accurate at the date of publication. Neither the publisher nor the authors or the editors give a warranty, express or implied, with respect to the material contained herein or for any errors or omissions that may have been made. The publisher remains neutral with regard to jurisdictional claims in published maps and institutional affiliations.

Printed on acid-free paper

This Springer imprint is published by the registered company Springer International Publishing AG part of Springer Nature
The registered company address is: Gewerbestrasse 11, 6330 Cham, Switzerland

Preface

Alexander Borisovich Ezersky graduated from the Gorky State University (Russia) in 1976 and integrated the Nonlinear Wave Department of the Institute of Applied Physics (IAP) of the Russian Academy of Sciences (RAS) where he prepared the doctoral thesis (Ph.D.) under the supervision of Prof. Mikhail Rabinovich. His scientific spectrum covered different areas of physics such parametric waves, acoustics, electronics, and hydrodynamics. Since 2000 to 2006, he had occupied position as a regular invited professor in Le Havre where he performed a long-term experiment of soliton excitation in wave channel and the effect of solitons in sediment transport. He had a CNRS visiting position at the University of Rouen where he collaborated on the stability of the wake behind a heated cylinder.

A. Ezersky worked at the Institute of Applied Physics (Russia) until September 2007 before he moved to the University of Caen Normandie in France as a Professor of Mechanics with a research position in the Laboratory of Continental and Coastal Morphodynamics where he reactivated research topic on the experimental hydrodynamics and its applications to sediment transportation.

His colleagues from Le Havre and Caen have had long-term cooperation on different problems of pattern formations in Taylor–Couette systems and water waves. He brought a deep physical insight from his wide spectrum of knowledge of nonlinear problems from electronic systems, parametric waves, pattern formation, and marine hydrodynamics.

He has published more than a hundred of scientific papers and he coauthored with M. Rabinovich and P. Weidman the book *The Dynamics of Patterns*, published in 2000 by World Scientific. He has advised several doctoral students and has acted as referee of many doctoral thesis and habilitations, especially in France.

Alexander had a very respectful attitude to his students and collaborators, creating a secure environment for fruitful scientific exchanges. His Russian colleagues have expressed their experience and souvenirs while they were working at the Institute of Applied Physics in Nizhny Novgorod, Russia.

We all have lost a great scientist and also a friend who left us very early. Our thoughts go to his family in Caen (Natasha, Artem, Katia).

The present book gathers chapters from his colleagues from Russia, especially those from Nizhny Novgorod Institute of Applied Physics of the Russian Academy of Science and from France, with whom he has been collaborating on experimental and theoretical developments.

The book is subdivided into two parts. Part I contains eight chapters related to nonlinear water waves and Part II addresses in five chapters, patterns dynamics in nonequilibrium media. The contributions of Alexander B. Ezersky were valuable from both the experimental and the theoretical points of view.

We thank all the authors for their contributions and the Springer Editor for having kindly accepted the edition of this book in memory of our colleague and friend, Prof. Alexander Borisovich Ezersky.

Alexander Ezersky (28.11.1953–21.07.2016)

Caen, France
Le Havre, France
Nizhny Novgorod, Russia
February 2018

Nizar Abcha
Innocent Mutabazi
Efim Pelinovsky

Alexander Ezersky, An Exceptional Scientist: Colleagues' Testimony

Alexander (Sasha) Ezersky was our close colleague and friend. We had a privilege to work with him at the Institute of Applied Physics of the Russian Academy of Sciences (IAP RAS) in Nizhny Novgorod for a long time. In this preface to the book dedicated to his memory, we share our brief memories of Sasha as we knew him and will remember him.

Alexander Ezersky at the conference "Nonlinear Wave Processes," August 2005

M. Rabinovich: Sasha Ezersky began his research career at my laboratory at IAP RAS after graduating from the Radiophysics Department of the Gorky State University in 1976. But we had got acquainted with him earlier when he was a graduate student. He immediately became involved in the life of our team and gained the authority of a thoughtful experimenter. He worked on the impact of sound on a vortex wake behind a streamlined cylinder, investigation of the dynamics of defects in Faraday ripples, and the origin of two-dimensional turbulence in soap films. His very first article was published in one of the leading physical journals—*Journal of Experimental and Theoretical Physics* [1].

Sasha had a rare gift to combine theory and experiment. He preferred key experiments, and the adjective *elegant* was often suitable for his research. I recall with great pleasure our joint work with Sasha and Patrick Weidman on the book devoted to pattern formation [2]. Sasha was my student, my friend, and colleague. I really treasure this friendship and I am sure that his name will remain in science.

Sasha was a very thoughtful person both in work and in communication with people. He always defended his point of view, gently but persistently. Apart from the specific research interests, he was fascinated by the history of science and always referenced the pioneering works. He introduced me to the extremely interesting Faraday's Diary.

Board of the Department of Hydrophysics and Acoustics at IAP (December, 1978). Front row: Head of the Department Vladimir Talanov (center), Heads of Laboratories Lev Ostrovsky (left) and Mikhail Rabinovich (right). Upper row: Department activists Yury Stepanyants (left) and Alexander Ezersky (right)

L. Ostrovsky: Our scientific encounters with Sasha Ezersky started in the early 1980s resulted in our joint publication with him and Yury Stepanyants. We investigated negative energy waves (NEW) in hydrodynamics in which dissipation can cause instability. Sasha was actively involved in an important physical problem: a fluid layer moving over a stationary viscous layer [3]. In this case, "losses" due to radiation and viscosity, which normally produce wave attenuation, lead to exponential growth for NEWs. This expands the range of classical instability of tangential discontinuity known for ideal fluids. In that work, he demonstrated that he was also a very good theoretician.

Our collaboration with Sasha included another important problem: generation of a mean flow by a weakly nonlinear wave [3]. We showed that, along with the well-known Stokes-type drift (mean current within the wave amplitude limits), a depth-distributed countercurrent appears in a two-layer fluid. Also we worked with Sasha on the interaction between acoustic waves and hydrodynamic vortices. This problem stemmed from fundamental issues such as "superradiation" from rotating objects first addressed by Y. B. Zel'dovch in the early 1970s. Sasha performed a fine theoretical and experimental work in this area.

It was always easy and pleasant to communicate with Sasha, be it about science or other topics; that was not only my impression. I often observed him discussing, with calm emotion characteristic of him, various topics with people from my laboratory. Everyone I knew liked him.

Y. Stepanyants: Our collaboration with Sasha started as soon as he joined our Department at IAP RAS in 1976. Our first joint paper [1] was devoted to the sudden onset of a chaotic regime of oscillations in a set of coupled oscillators under the action of an external harmonic excitation. Then, we published jointly two other papers on water waves in currents [3] where NEWs play an important role.

Sasha's distinctive feature was his deep insight into the studied problems, which greatly enhanced our understanding of complex physical phenomena not only in the field of his direct interests. Our mutual friend and colleague Anatoly Mansfeld from IAP RAS asked me if Sasha could help him resolve a difficulty in his work not directly related to Sasha. I passed this request to Sasha, and he was happy to consult Anatoly on that issue. It was just 3 months before his death in July 2016.

Sasha was a very practical person in everyday life. For instance, he easily replaced a car accumulator for our mutual friend in France, helped me to erect a brick wall in my house, or quickly learned how to operate a benzene saw (we used to earn on the side together during summer vacation in taiga). Work with him was especially pleasant thanks to his cheerful character and sense of humor.

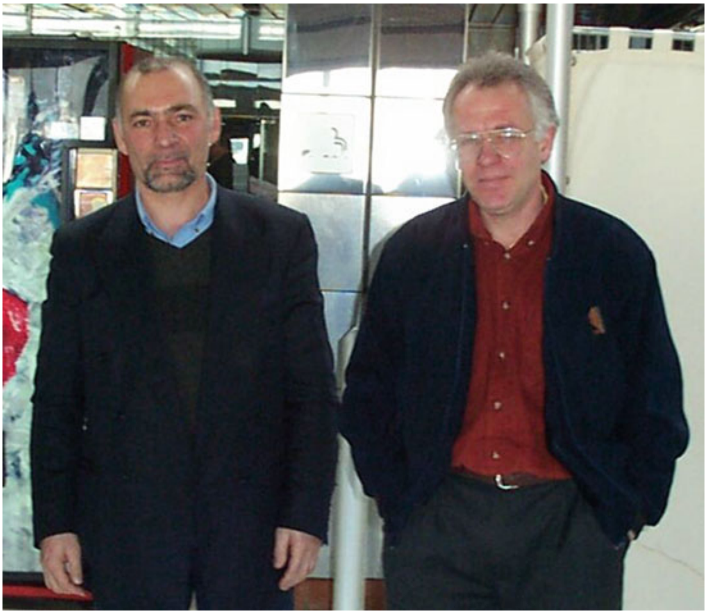

Meeting at Charles de Gaulle airport, Paris, December, 2001. Yury Stepanyants (left) and Alexander Ezersky (right)

After the collapse of the Soviet Union, we were fated to live and work in different countries, but we continued to keep in contact and sometimes met at conferences. In December 2001, we met by chance at the Charles de Gaulle airport in Paris and then took a flight to Moscow together. In December 2014, I visited Sasha in Caen (France) where he lived with his family. We spent a lovely evening together with his wife Natalia and our mutual colleague Germain Rousseaux discussing scientific, political, and many other issues. Sasha's interests at that time were focused basically on laboratory experiments on water waves in nonuniform basins. Later, Germain and I demonstrated a possibility to model a Bose–Einstein condensation in a relatively simple laboratory setup with water waves; the paper dedicated to the memory of Sasha Ezersky is included in this book.

In August 2015, we learned that Sasha had been diagnosed with a malicious form of cancer. For some period, it seemed that he overcame the disease.

He resumed working and discussing scientific problems. Alas, that improvement did not last long… Sasha will always be warmly remembered by many people who knew him and especially those who had the chance to share with him scientific activities.

Lev Ostrovsky
University of Colorado, Boulder, USA

Mikhail Rabinovich
BioCircuits Institute, University of California
San Diego, La Jolla, CA, USA

Yury Stepanyants
School of Agricultural, Computational
and Environmental Sciences
Faculty of Health, Engineering and Sciences
University of Southern Queensland
Toowoomba, QLD, Australia

References

1. A.B. Ezersky, M.I. Rabinovich, Yu. A. Stepanyants and M.F. Shapiro, Stochastic oscillations of a parametrically excited nonlinear chain. *Sov. Phys. JETP* **49**(3), 500–504 (1979).
2. A.B. Ezersky, L.A. Ostrovsky and Yu. A. Stepanyants, Wave-induced flows and their contribution to the energy of wave motions in a fluid. *Izv. Acad. Sci. USSR, Atmospheric and Oceanic Physics* **17**(11), 890–895(1981).
3. M.I. Rabinovich, A.B. Ezersky and P.D. Weidman, *The Dynamics of Patterns*, World Scientific Pub. Co Inc. (2001).

Contents

Part I Nonlinear Water Waves and Applications

Part II Patterns in Nonequilibrium Media

Contributors

Nizar Abcha Normandie Université, UNICAEN, UNIROUEN, CNRS, UMR 6143, M2C, 14000 Caen, France

Vladimir Chernov Institute of Applied Physics, Russian Academy of Sciences of the Nizhny Novgorod, Nizhny Novgorod, Russia

Wuttersack Chokchai CNRS, M2C, Normandie Université, UNICAEN, UNIROUEN, Caen, France

Olivier Crumeyrolle Normandie Université, Unihavre, CNRS, UMR 6294, LOMC, 76600 Le Havre, France

Ira Didenkulova Nizhny Novgorod State Technical University n.a. R.E. Alekseev, Nizhny Novgorod, Russia; Department of Marine Systems, Tallinn University of Technology, Tallinn, Estonia

O. A. Druzhinin Institute of Applied Physics, Russian Academy of Sciences, Nizhny Novgorod, Russia

Angel Durán Departamento de Matemática Aplicada, E.T.S.I. Telecomunicación, Universidad de Valladolid, Valladolid, Spain

Denys Dutykh Université Savoie Mont Blanc, LAMA, UMR 5127 CNRS, Le Bourget-du-Lac Cedex, France; Université Grenoble Alpes, Université Savoie Mont Blanc, CNRS, LAMA, Chambéry, France

Alexander Ezersky CNRS, M2C, Normandie Université, UNICAEN, UNIROUEN, Caen, France

Armelle Jarno Normandie Université, Unilehavre, CNRS, UMR 6294, LOMC, Le Havre Cedex, France

Fayçal Kelai Normandie Université, Unihavre, CNRS, UMR 6294, LOMC, 76600 Le Havre, France

Christian Kharif CNRS, Centrale Marseille, IRPHE, Aix-Marseille Université, Marseille, France

Noureddine Latrache FRE CNRS 3744 IRDL, Université de Brest, Brest, France

Patrice Le Gal Aix-Marseille Université, CNRS, Centrale Marseille, IRPHE, Technopôle de Château Gombert, Marseille Cedex 13, France

Jean-Claude Lecordier Laboratoire de Thermodynamique CNRS UMR 6614—CORIA, Université de Rouen Site Universitaire du Madrillet, Saint Etienne du Rouvray, France

François Marin Normandie Université, Unilehavre, CNRS, UMR 6294, LOMC, Le Havre Cedex, France

Dimitrios Mitsotakis School of Mathematics and Statistics, Victoria University of Wellington, Wellington, New Zealand

Dominique Mouaze CNRS, M2C, Normandie Université, UNICAEN, UNIROUEN, Caen, France

Innocent Mutabazi Normandie Université, Unihavre, CNRS, UMR 6294, LOMC, 76600 Le Havre, France

G. V. Osipov Department of Control Theory, Nizhny Novgorod State University, Nizhny Novgorod, Russia

Pierre Paranthoën Laboratoire de Thermodynamique CNRS UMR 6614—CORIA, Université de Rouen Site Universitaire du Madrillet, Saint Etienne du Rouvray, France

Efim Pelinovsky Nizhny Novgorod State Technical University n.a. R.E. Alekseev, Nizhny Novgorod, Russia; National Research University—Higher School of Economics, Nizhny Novgorod, Russia; Institute of Applied Physics, Nizhny Novgorod, Russia

A. Pikovsky Institute for Physics and Astronomy, University of Potsdam, Potsdam-Golm, Germany

Mikhail Rabinovich BioCircuits Institute, University of California, San Diego, La Jolla, USA

Germain Rousseaux CNRS, Institut Pprime, UPR 3346, Université de Poitiers—ISAE ENSMA, Futuroscope Cedex, France

D. A. Sergeev Institute of Applied Physics, Russian Academy of Sciences, Nizhny Novgorod, Russia

Alexey Slunyaev Institute of Applied Physics, Russian Academy of Sciences, Nizhny Novgorod, Russia

L. A. Smirnov Institute of Applied Physics, Nizhny Novgorod, Russia

Yury Stepanyants Faculty of Health, Engineering and Sciences, School of Agricultural, Computational and Environmental Sciences, University of Southern Queensland, Toowoomba, QLD, Australia

Julien Touboul CNRS / INSU, IRD, MIO, Université de Toulon, Aix-Marseille Université, La Garde, France

Yu I. Troitskaya Institute of Applied Physics, Russian Academy of Sciences, Nizhny Novgorod, Russia

W.-T. Tsai Taiwan National University, Taipei, Taiwan

M. Vdovin Institute of Applied Physics, Russian Academy of Sciences, Nizhny Novgorod, Russia

Gautier Verhille Aix-Marseille Université, CNRS, Centrale Marseille, IRPHE, Technopôle de Château Gombert, Marseille Cedex 13, France

Patrick Weidman Department of Mechanical Engineering, University of Colorado, Boulder, USA

Part I
Nonlinear Water Waves and Applications

Peregrine's System Revisited

Angel Durán, Denys Dutykh and Dimitrios Mitsotakis

Abstract In 1967, D. H. PEREGRINE proposed a BOUSSINESQ-type model for long waves in shallow waters of varying depth Peregrine (J Fluid Mech 27:815–827, 1967, [70]). This prominent paper turned a new leaf in coastal hydrodynamics along with contributions by Serre (La Houille Blanche 8:374–388, 1953, [72]) and Green and Naghdi (J Fluid Mech 78:237–246, 1976, [47]) and many others since then. Several modern BOUSSINESQ-type systems stem from these pioneering works. In the present work, we revise the long wave model traditionally referred to as the PEREGRINE system. Namely, we propose a modification of the governing equations, which is asymptotically similar to the initial model for weakly nonlinear waves, while preserving an additional symmetry of the complete water wave problem. This modification procedure is called the *invariantization*. We show that the improved system has well-conditioned dispersive terms in the swash zone, hence allowing for efficient and stable run-up computations.

A. Durán
Departamento de Matemática Aplicada, E.T.S.I. Telecomunicación, Universidad
de Valladolid, Campus Miguel Delibes, Paseo de Belen 15, 47011 Valladolid, Spain
e-mail: angel@mac.uva.es

D. Dutykh (✉)
Université Savoie Mont Blanc, LAMA, UMR 5127 CNRS, Campus Scientifique,
73376 Le Bourget-du-Lac Cedex, France
e-mail: Denys.Dutykh@univ-smb.fr

D. Dutykh
Université Grenoble Alpes, Université Savoie Mont Blanc, CNRS, LAMA,
73000 Chambéry, France

D. Mitsotakis
School of Mathematics and Statistics, Victoria University of Wellington, PO Box 600,
Wellington 6140, New Zealand
e-mail: dimitrios.mitsotakis@vuw.ac.nz

N. Abcha et al. (eds.), *Nonlinear Waves and Pattern Dynamics*,
https://doi.org/10.1007/978-3-319-78193-8_1

1 Introduction

Nowadays, BOUSSINESQ-type equations have become the models of choice in the near-shore hydrodynamics. Proposed for the first time in 1871 by Boussinesq [15], these equations have been substantially improved in works by Serre [72], Peregrine [70], Green and Naghdi [47] and many others.[1] Nowadays, it is almost impossible to list all the bibliography on this subject. Since several decennaries researchers have essentially focused their effort on extending the validity of these models from shallow waters to intermediate depths [60, 61, 63] under the increasing demand of the coastal engineering community. We refer to [20] for a recent *reasoned* review of this topic. The derivation of these equations on flat geometries was reviewed in [55] and the spherical case was covered in [54].

The true success of BOUSSINESQ-type equations has to deal with the description of the wave breaking phenomenon. Classical nonlinear shallow water equations (NSWE) predict waves to break too early. Thus, the validity region of NSWE is limited only to the inner surf zone. The success story of BOUSSINESQ systems begins when they were shown to model fairly well breaking waves (see [90]). However, the research on robust and efficient numerical methods lags behind the current state of the art in the modelling [8, 11, 41]. Main problems arise from the numerical treatment of the shoreline and the stability of the resulting method. Most of the computational algorithms run into numerical troubles when a sufficiently big amplitude wave reaches the run-up region. These problems are obviously due to the uncontrolled numerical instabilities coming from the dispersive terms discretization (see [8]). These difficulties were reported presumably for the first time in [62] (this emphasis is ours):

> However, to make this technique [slot technique] operational in connection with Boussinesq type models a couple of problems call for special attention. […] Firstly *the Boussinesq terms are switched off* at the still water shoreline, where their relative importance is extremely small anyway. Hence in this region the equations simplify to the nonlinear shallow water equations.

This extremely pragmatic point of view is still shared nowadays by a number of researchers. However, in our opinion, it is the model which has to decide naturally whether the dispersion is important or not. Ideally, the treatment of dry areas today should be as simple and natural as the treatment of shock waves in shock-capturing schemes [81]. In this study, we present a fully dispersive numerical simulation of a wave run-up on a complex beach where dispersive terms are present in the entire domain.

The main idea of this study is to revise the original PEREGRINE system [70]. Some properties of the complete water wave problem have been lost as a price to pay for the model simplification. Namely, as for many other models derived by asymptotic methods, we loose the invariance under vertical translations. If no special care is taken, we inevitably loose this property, since the asymptotic expansion is performed

---

[1] The steady version of the celebrated SERRE–GREEN–NAGHDI equations can be traced back up to Lord RAYLEIGH [59].

in a very particular frame of reference (around the mean water level $z = 0$). However, the full water wave problem possesses this symmetry (cf. [10]).

The model we propose in this study is asymptotically similar to the original system since we add only higher order contributions which are formally negligible while greatly improving structural properties of the model. Consequently, the linear dispersion relation of the original system is conserved as well. The great improvement consists in dispersive terms which are better conditioned from the numerical point of view and they fit better our physical intuition about their relative importance when we approach the shoreline. A similar attempt of improving dispersive terms by adding nonlinear contributions was also undertaken recently in [1, 9]. The procedure presented in this study is sometimes referred to in the literature as the invariantization process. Conservative versions of some NWOGU-type systems have been proposed in [7, 44].

The present study is organized as follows. In Sect. 2, we present some rationale on the PEREGRINE system and its invariantization, with particular emphasis on the numerical generation of solitary wave solutions of the modified system, which are studied in Sect. 3. Some elements on the numerical discretization by the finite volume method are given in Sect. 4. Then, some numerical results are shown in Sect. 5 while applications to waves generated due to landslides are presented in Sect. 6. Finally, the main conclusions and perspectives of this study are outlined in Sect. 7.

2 Mathematical Modelling

Consider a CARTESIAN coordinate system in two space dimensions $(x,\ z)$ to simplify the notation. The $z-$axis is taken vertically upwards and the $x-$axis is horizontal and coincides traditionally with the still water level. The fluid domain is bounded below by the bottom $z = -h(x)$ and above by the free surface $z = \eta(x,\ t)$. Below we will also need the total water depth $H(x,\ t) \overset{\text{def}}{:=} h(x) + \eta(x,\ t)$. The sketch of the fluid domain is given in Fig. 1. The flow is supposed to be incompressible and the fluid is inviscid. An additional simplifying assumption of the flow irrotationality is traditionally made as well.

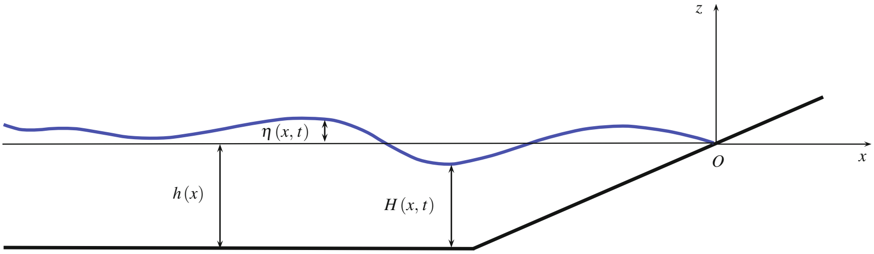

Fig. 1 Sketch of the fluid domain with a sloping beach

Remark 1 We would like to underline the fact that in the presence of a free surface the vorticity does not remain zero even if it is so initially. A singularity at the free surface (e.g. the wave breaking) may lead to vortex sheets creation. However, the water wave theory is not supposed to hold when a wave breaking event occurs.

Under the previously described physical assumptions, Peregrine [70] derived the following system of equations which is valid in the Boussinesq long wave regime:

$$\eta_t + \big((h + \eta)\, u\big)_x = 0\,, \tag{1}$$

$$u_t + u\, u_x + g\, \eta_x - \frac{h}{2}\,(h\, u)_{xxt} + \frac{h^2}{6}\, u_{xxt} = 0\,, \tag{2}$$

where $u\,(x,\ t)$ is the depth-averaged fluid velocity, g is the gravity acceleration and under-scripts ($u_x \overset{\text{def}}{:=} \frac{\partial u}{\partial x}$, $\eta_t \overset{\text{def}}{:=} \frac{\partial \eta}{\partial t}$) denote partial derivatives.

2.1 Symmetry Analysis

In this section, we assume the bottom to be flat, i.e. $h = d = \text{const} > 0$. Otherwise, bathymetry variations will destroy a part of symmetries of the governing Eqs. (1), (2). The infinitesimal generators of symmetries transformations for the classical PEREGRINE system are given here:

$$\mathscr{X}_1 = \frac{\partial}{\partial t}\,,$$
$$\mathscr{X}_2 = \frac{\partial}{\partial x}\,,$$
$$\mathscr{X}_3 = u\,\frac{\partial}{\partial u} + 2\,(\eta + d)\,\frac{\partial}{\partial \eta} - t\,\frac{\partial}{\partial t}\,.$$

It is not difficult to see that the generator $\mathscr{X}_1$ corresponds to time translations:

$$\tilde{t} = t + \varepsilon_1\,, \qquad \tilde{x} = x\,, \qquad \tilde{\eta} = \eta\,, \qquad \tilde{u} = u\,.$$

Similarly, the generator $\mathscr{X}_2$ gives translations in space:

$$\tilde{t} = t\,, \qquad \tilde{x} = x + \varepsilon_2\,, \qquad \tilde{\eta} = \eta\,, \qquad \tilde{u} = u\,.$$

Finally, the generator $\mathscr{X}_3$ is nothing else but a scaling transformation:

$$\tilde{t} = \mathrm{e}^{-\varepsilon_3}\, t\,, \qquad \tilde{x} = x\,, \qquad \tilde{\eta} = \mathrm{e}^{2\,\varepsilon_3}\,(d + \eta) - d\,, \qquad \tilde{u} = \mathrm{e}^{\varepsilon_3}\, u\,.$$

There are no other symmetry transformations of the classical PEREGRINE system. If this system possessed a LAGRANGIAN structure, we could employ NOETHER theorem to convert symmetries to conservation laws [67]. For instance, space translations $\mathscr{X}_2$ correspond to the momentum conservation. The time translations $\mathscr{X}_1$ would yield the energy conservation equation, if we only could apply the NOETHER theorem. This is one of the reasons why it is widely believed that the classical PEREGRINE system has no energy functional. However, using some other complementary methods [13, 22] we were able to compute an additional conservation law, which can be associated to the energy:

$$\Bigl(\tfrac{1}{2}\,u^2 + g\,(d\,+\,\eta)\,\ln(d\,+\,\eta)\,-\,g\,\eta\,-\,\frac{d^2}{6}\,u\,u_{xx}\Bigr)_t + \\ \Bigl[\tfrac{1}{3}\,u^3\,+\,g\,u\,(d\,+\,\eta)\,\ln(d\,+\,\eta)\,+\,\frac{d^2}{6}\,u_x\,u_t\,-\,\frac{d^2}{6}\,u\,u_{tx}\Bigr]_x\,=\,0\,.$$

The last conservation law can be used, for example, to check the accuracy of numerical schemes over even bottoms for the sake of validation. In some situations, additional conservation laws might be used in theoretical investigations as well.

2.2 Dimensionless Equations

Some of our developments below will be more transparent if we work in dimensionless variables. The classical long wave scaling is the following:

$$x'\,\stackrel{\text{def}}{:=}\,\frac{x}{\ell}\,,\quad z'\,\stackrel{\text{def}}{:=}\,\frac{z}{h_0}\,,\quad t'\,\stackrel{\text{def}}{:=}\,\frac{g}{h_0}\,t\,,\quad \eta'\,\stackrel{\text{def}}{:=}\,\frac{\eta}{a}\,,\quad u'\,\stackrel{\text{def}}{:=}\,\frac{u}{\sqrt{g\,h_0}}\,,$$

where h_0, a, ℓ are the characteristic water depth, wave amplitude and wavelength, respectively. The following dimensionless numbers are defined from them:

$$\varepsilon\,\stackrel{\text{def}}{:=}\,\frac{a}{h_0}\,,\quad \mu^2\,\stackrel{\text{def}}{:=}\,\Bigl(\frac{h_0}{\ell}\Bigr)^2\,,\quad \mathrm{S}\,\stackrel{\text{def}}{:=}\,\frac{\varepsilon}{\mu^2}\,.$$

Parameters ε and μ^2 measure the wave nonlinearity and dispersion, while the so-called STOKES–URSELL number S measures the relative importance of these effects. In the BOUSSINESQ regime, the STOKES–URSELL number is supposed to be of the order of one, i.e. $\mathrm{S}\,\sim\,1$. The importance of this parameter is discussed by, e.g. URSELL [82]. The PEREGRINE system (1), (2) in scaled variables at the order $\mathscr{O}\,(\varepsilon\,+\,\mu^2)$ reads (primes are dropped below for the sake of convenience):

$$\eta_t\,+\,\bigl((h\,+\,\varepsilon\,\eta)\,u\bigr)_x\,=\,0\,,$$

$$u_t + \varepsilon u u_x + \eta_x - \mu^2 \Bigl(\frac{h}{2}(hu)_{xxt} - \frac{h^2}{6} u_{xxt}\Bigr) = \mathscr{O}(\varepsilon^2 + \varepsilon \mu^2 + \mu^4),$$

where on the right-hand side of the last equation we put the order of neglected terms. Since the STOKES–URSELL number S $\sim$ 1, we have asymptotic similarity relations in the BOUSSINESQ regime:

$$\varepsilon^2 \sim \varepsilon \mu^2 \sim \mu^4 .$$

2.3 Vertical Translations

In this section, we examine an important property of the water wave problem—invariance under vertical translations (subgroup G_5 in Theorem 4.2, Benjamin and Olver [10]). This transformation is described by the following simple change of variables:

$$z \leftarrow z + d, \quad \eta \leftarrow \eta - d, \quad h \leftarrow h + d, \quad u \leftarrow u, \tag{3}$$

where d is some constant. Here again, it is straightforward to check that the mass conservation Eq. (1) remains invariant under transformation (3), while Eq. (2) produces many additional dispersive terms proportional to the constant translation d:

$$u_t + u u_x + g \eta_x - \frac{h}{2}(hu)_{xxt} + \frac{h^2}{6} u_{xxt} - \frac{hd}{6} u_{xxt} - \frac{d^2}{3} u_{xxt} - \frac{d}{2}(hu)_{xxt} = 0 .$$

The reason for this discrepancy is that the coefficient $h^n(x)$ $(n = 1, 2)$ in front of the dispersive terms is not invariant under the vertical shift. The right variable to use is the total water depth $H(x, t) = h(x) + \eta(x, t)$ which is independent of the chosen coordinate reference frame. Here again, the discrepancy is a result of the asymptotic expansion around the still water level. Consequently, the derived model is valid only for this particular choice of the coordinate axis Ox. To make system (1), (2) frame independent, we shall add higher order nonlinear terms which are asymptotically negligible but have important implications in structural properties of the resulting model.

In dimensionless variables, the total water depth is expressed as $H(x, t) = h(x) + \varepsilon \eta(x, t)$. As a corollary, we obtain two asymptotic relations which will be used below:

$$h = H + \mathscr{O}(\varepsilon), \qquad h_x = H_x + \mathscr{O}(\varepsilon), \qquad H_t = \mathscr{O}(\varepsilon).$$

Mathematically, it means that the bathymetry function should be completed by an $\mathscr{O}(\varepsilon)$ term to become invariant under vertical translations. While performing this invariantization, we will also recast our model in conservative variables (H, Q), where $Q \overset{\text{def}}{:=} H\,u$ is the horizontal momentum. This modification will allow us to employ those numerical methods developed in the literature for the discretization of nonlinear shallow water equations (NSWE) [27, 35, 40, 91].

The mass conservation Eq. (1) in the new variables trivially reads:

$$H_t + Q_x = 0\,, \tag{4}$$

while the momentum conservation Eq. (2) will require more computations. First of all, we multiply Eq. (4) by u, Eq. (2) by H and add them to have

$$(Hu)_t + \bigl(\varepsilon H u^2 + \frac{1}{2\varepsilon} H^2\bigr)_x - \mu^2\Bigl(\frac{H\,h}{2}(h\,u)_{xxt} - \underbrace{\frac{H\,h^2}{6}\,u_{xxt}\Bigr)}_{(**)} = \frac{1}{\varepsilon} H\,h_x\,. \tag{5}$$

In the perspective of writing governing equations in the conservative form, the term (**) has to be transformed using this relation:

$$u_{xx} \equiv \Bigl(\frac{h\,u}{h}\Bigr)_{xx} = (h\,u)\Bigl(2\,\frac{h_x^2}{h^3} - \frac{h_{xx}}{h^2}\Bigr) - 2\,\frac{h_x}{h^2}\,(h\,u)_x + \frac{1}{h}\,(h\,u)_{xx}\,.$$

Consequently, after simple computations, Eq. (5) takes the form:

$$\begin{aligned}(H\,u)_t + \bigl(\varepsilon H\,u^2 + \frac{1}{2\,\varepsilon} H^2\bigr)_x - \mu^2\Bigl(\frac{H\,h}{3}\,(h\,u)_{xxt} + \frac{H}{3}\,(h\,u)(h\,u)_{xxx}\\ + \frac{H\,h_x}{3}\,(h\,u)_{xt} - \frac{1}{3}\,\bigl(\frac{H}{h}\,h_x^2 - \frac{1}{2}\,H\,h_{xx}\bigr)\,(h\,u)_t\Bigr) = \frac{1}{\varepsilon}\,H\,h_x\,.\end{aligned}$$

The last equation is ready for the invariantization process. For illustrative purposes, we show these computations only for the first dispersive term:

$$\mu^2\,\frac{H\,h}{3}\,(h\,u)_{xxt} = \frac{\mu^2}{3}\,H^2\,(H\,u)_{xxt} + \mathscr{O}(\varepsilon\,\mu^2) = \frac{\mu^2}{3}\,H^2\,Q_{xxt} + \mathscr{O}(\varepsilon\,\mu^2)\,.$$

Thus, we add again only higher order terms which have no impact on linear dispersive characteristics of the initial system. By proceeding in an analogous manner with all other dispersive terms and turning back to dimensional variables we obtain the following momentum conservation equation:

$$\begin{aligned}\Bigl(1 + \frac{1}{3}\,H_x^2 - \frac{1}{6}\,H\,H_{xx}\Bigr)\,Q_t - \frac{1}{3}\,H^2\,Q_{xxt} - \frac{1}{3}\,H\,H_x\,Q_{xt}\\ + \Bigl(\frac{Q^2}{H} + \frac{g}{2}\,H^2\Bigr)_x = g\,H\,h_x\,.\end{aligned} \tag{6}$$

The system (4), (6) (that will be called the modified PEREGRINE system or, in a shorthand notation, the m-PEREGRINE system) actually has more advantages than being simply invariant under two additional transformations. The added value of this invariantization process goes far beyond the initial symmetry consideration. Namely, in this way, we extend the system validity to the run-up process and improve the numerical conditioning of dispersive terms. For the first time, Eqs. (4), (6) were used and validated for wave run-up problems in [37].

In natural environments, dispersive effects become gradually less and less important when a wave travels shoreward to become negligible in the shoreline vicinity. This is the reason why NSWE can be successfully used to describe to some extent the run-up process. This physical observation can be translated into the mathematical language by the condition that dispersive terms go to zero when the total water depth vanishes. If this condition is not fulfilled, numerical instabilities may appear as reported by BELLOTTI and BROCCHINI [9]:

> In our attempt to use these equations from intermediate waters up to the shoreline (see Bellotti and Brocchini [8]) we run into numerical troubles when reaching the run-up region, i.e. $x > 0$. These problems were essentially related to numerical instabilities due to the uncontrolled growth of the dispersive contributions (i.e. $\mathscr{O}(\mu^2)$-terms).

The reason for the extended numerical stability of the proposed model is twofold. First of all, in the numerical algorithm, we have to invert at some point an elliptic operator written over the time derivative in Eq. (6):

$$\Big(1 + \frac{1}{3}\,H_x^2 - \frac{1}{6}\,H\,H_{xx}\Big)\,q - \frac{1}{3}\,H^2\,q_{xx} - \frac{1}{3}\,H\,H_x\,q_x = W,$$

where W is a known function arising from the advective terms discretization. It turns out that the resulting linear system is better conditioned if the model is written in terms of the total water depth. The second stability advantage comes from the fact that almost all dispersive terms naturally vanish as we approach the shoreline.

Remark 2 It is noted that the same invariantization technique can be used also for the case of moving bottom bathymetry and for higher dimensions, cf. Sect. 6.

2.3.1 Symmetry Analysis

The symmetries of the m-PEREGRINE system (over flat bottom) can be computed using the standard methods as we did for the classical counterpart in Sect. 2.1. The dimension of the symmetry group turns out to be the same as above. The infinitesimal generators are given below:

$$\begin{aligned}
\mathscr{X}_1 &= \frac{\partial}{\partial t}\,, \\
\mathscr{X}_2 &= \frac{\partial}{\partial x}\,, \\
\mathscr{X}_3 &= t\,\frac{\partial}{\partial t} + 2x\,\frac{\partial}{\partial x} + 2H\,\frac{\partial}{\partial H} + 3Q\,\frac{\partial}{\partial Q}\,.
\end{aligned}$$

The generated symmetry transformations are essentially the same. Generator $\mathscr{X}_1$ yields time translations:

$$\tilde{t} = t + \varepsilon_1\,, \qquad \tilde{x} = x\,, \qquad \tilde{H} = H\,, \qquad \tilde{Q} = Q\,,$$

while $\mathscr{X}_2$ gives translations in space:

$$\tilde{t} = t\,, \qquad \tilde{x} = x + \varepsilon_2\,, \qquad \tilde{H} = H\,, \qquad \tilde{Q} = Q\,.$$

Finally, $\mathscr{X}_3$ is a scaling transformation[2]:

$$\tilde{t} = \mathrm{e}^{\varepsilon_3}\,t\,, \qquad \tilde{x} = \mathrm{e}^{2\,\varepsilon_3}\,x\,, \qquad \tilde{H} = \mathrm{e}^{2\,\varepsilon_3}\,H\,, \qquad \tilde{Q} = \mathrm{e}^{3\,\varepsilon_3}\,Q\,.$$

2.3.2 Pressure Distribution

For some practical applications, we need to estimate the pressure field inside the fluid and more particularly at the bottom. For example, the operational NOAA Tsunami Warning System heavily relies on a network of DART buoys detecting tsunami waves by measuring the pressure at the ocean bottom [12, 79]. In this section, we propose a way to reconstruct the pressure field in the whole water column.

In the original work of [70], one can find the following correct asymptotic expansion for the pressure field:

$$p = -z + \varepsilon\,\eta + \mu^2\bigl(z\,(h\,u)_{x\,t} + \tfrac{1}{2}\,z^2\,u_{x\,t}\bigr) + \mathscr{O}(\varepsilon^2 + \varepsilon\,\mu^2 + \mu^4)\,. \tag{7}$$

The first two terms on the right-hand side correspond to the usual hydrostatic pressure while the last two terms are purely non-hydrostatic contributions brought by dispersive effects.

However, the original expression (7) for the pressure given by the asymptotic expansion method has one important drawback. Namely, it satisfies the free surface dynamic boundary condition $p|_{z\,=\,\varepsilon\,\eta} = 0$ only to the leading order. Consequently, the first improvement we propose is to add some specific higher order terms to recover this property at all orders we retain in the equation:

---

[2] Notice, please, that this scaling is different from $\mathscr{X}_3$ given in Sect. 2.1.

$$p \approx -z + \varepsilon\eta + \mu^2\big((z - \varepsilon\eta)(hu)_{xt} + \tfrac{1}{2}\mu^2(z - \varepsilon\eta)^2 u_{xt}\big).$$

Now, we will make a transformation consistent with the modified PEREGRINE system (4), (6) which consists in replacing h by its asymptotically equivalent *and* invariant by vertical translations counterpart H in the third term[3] of the last formula:

$$p \approx -z + \varepsilon\eta + \mu^2\big((z - \varepsilon\eta)(H u)_{xt} + \tfrac{1}{2}\mu^2(z - \varepsilon\eta)^2 u_{xt}\big).$$

Finally, if we turn back to the dimensional and conservative variables, the final expression for the pressure will take this form:

$$\frac{p}{\rho} = g(\eta - z) + (z - \eta)Q_{xt} + \frac{1}{2}(z - \eta)^2\Big(\frac{Q}{H}\Big)_{xt}.$$

where ρ is the constant fluid density. It is straightforward now to compute the pressure value at the bottom by evaluating the last expression at $z = -h$:

$$\frac{p}{\rho}\bigg|_{z=-h} = gH + HQ_{xt} + \frac{1}{2}H^2\Big(\frac{Q}{H}\Big)_{xt}.$$

The latter can be directly used, for example, to compute synthetic pressure records which can be compared with real observations in deep ocean [79].

2.4 Galilean Invariance

In the same line of ideas, there is a question of the GALILEAN invariance of various BOUSSINESQ-type equations. In this section, we check whether the PEREGRINE system (1), (2) remains invariant under the GALILEAN transformation. This issue was already addressed in the context of some other systems by Christov [23].

The procedure is classical. First of all, we assume throughout this section the bottom to be flat $h = \text{const}$. We choose another frame of reference which moves uniformly rightwards with constant celerity c. Analytically, it is expressed by the following change of variables:

$$x \leftarrow x - ct, \quad t \leftarrow t, \quad \eta(x,t) \leftarrow \eta(x - ct, t), \quad u(x,t) \leftarrow u(x - ct, t) + c. \tag{8}$$

After some simple computations, one can easily check that the mass conservation Eq. (1) remains invariant under the GALILEAN boost (8), while Eq. (2) has an extra term (*):

---

[3] The asymptotic argument holds here since this term is $\mathscr{O}(\mu^2)$.

$$u_t + u u_x + g \eta_x - \frac{h}{2}(h u)_{xxt} + \frac{h^2}{6} u_{xxt} + \underbrace{\frac{c h^2}{3} u_{xxx}}_{(*)} = 0 .$$

Consequently, the PEREGRINE system in its original form does not possess the very basic GALILEAN invariance property while the complete water wave problem does (subgroups $G_{7,8}$ in three dimensions, see Theorem 4.2, BENJAMIN and Olver [10]). Some consequences of this shortcoming are discussed in [23].

In order to recover the broken symmetry, we propose to modify Eq. (2) in the following way:

$$u_t + u u_x + g \eta_x - \frac{h}{2}(h u)_{xxt} + \frac{h^2}{6} u_{xxt} - \frac{h}{3} u (h u)_{xxx} = 0 . \qquad (9)$$

If we perform the same computations as above, we will see that the modified model (1), (9) remains invariant under the GALILEAN boost (8). In order to understand better this modification, we have to switch to dimensionless variables:

$$u_t + \varepsilon u u_x + \eta_x - \mu^2\Big(\frac{h}{2}(h u)_{xxt} - \frac{h^2}{6} u_{xxt}\Big) - \varepsilon \mu^2 \frac{h}{3} u (h u)_{xxx} = 0 .$$

Now, it is clear that we add a higher order $\mathcal{O}(\varepsilon \mu^2)$ nonlinear dispersive term which normally has to be omitted according to the philosophy of asymptotic methods. However, we prefer to retain it to recover an important physical property of the model—the GALILEAN invariance.

Remark 3 Since the term $\frac{h}{3} u (h u)_{xxx}$ is a nonlinear dispersive term, it has no effect on linear dispersion characteristics of the original model. The same remark applies to developments presented below as well.

Consequently, we are able to add a higher order dispersive term to Eq. (2) which makes the system GALILEAN invariant. The invariantization process in variables (η, u) is straightforward. However, if we rewrite the modified system in terms of the conservative variables (H, Q) we loose again the GALILEAN invariance property. One of the reasons is that transformation (8) is more complex in these variables. For example, the following chain rules apply:

$$Q_t \rightarrow Q_t - c Q_x + c (H_t - c H_x) , \qquad Q_x \rightarrow Q_x + c H_x .$$

The invariantization of the modified PEREGRINE system (4), (6) under the GALILEAN symmetry remains an open question. The discussion of the GALILEAN invariance of a few other nonlinear dispersive wave systems can be found in [31].

3 Solitary Waves

Dispersive wave equations possess an important class of solutions—the solitary waves (SW) which result from a balance between nonlinear and dispersive effects [21, 30, 53, 71]. The comprehension of these solutions allows to assess some properties of the dispersive system under consideration. We note that analytical SW solutions are not known even for the classical PEREGRINE system [70]. We have not been able to construct closed-form solutions to the m-PEREGRINE system either. Consequently, we will apply numerical methods which allow to approximate them accurately [89].

A travelling wave solution has the following form:

$$H(x,\,t)\;\equiv\;H(X)\,,\qquad Q(x,\,t)\;\equiv\;Q(X)\,,\qquad X\;\overset{\text{def}}{:=}\;x\,-\,c_s\,t\,,$$

where c_s is the wave propagation speed in an inertial frame of reference. After substituting this *ansatz* into the governing Eqs. (4), (6), we obtain the following system of two coupled ordinary differential equations (ODEs):

$$-\,c_s\,H'\,+\,Q'\;=\;0\,, \tag{10}$$

$$-c_s\Bigl(1\,+\,\frac{1}{3}\,(H')^2\,-\,\frac{1}{6}\,H\,H''\Bigr)\,Q'\,+\,\frac{c_s}{3}\,H^2\,Q''' \\ +\,\frac{c_s}{3}\,H\,H'\,Q''\,+\,\Bigl(\frac{Q^2}{H}\,+\,\frac{g}{2}\,H^2\Bigr)'\;=\;0\,, \tag{11}$$

where functions $H(X)$ and $Q(X)$ are assumed to be sufficiently smooth, even and decaying to zero along with all their derivatives as $|X|\;\to\;\infty$. Throughout this section, we will consider the wave propagation over a flat bottom, i.e. $h\;\equiv\;\text{const.}$

The former Eq. (10) can be used to eliminate the variable $Q(X)$ from the latter equation. It will be more convenient also to work with the free surface elevation $\eta(X)$:

$$L_0\,\eta\;=\;(gh\,-\,c_s^2)\,\eta'\,+\,\frac{c_s^2\,h^2}{3}\,\eta'''\,+\,\Bigl(\frac{c_s^2\,\eta^2}{h\,+\,\eta}\Bigr)'\,+\,\frac{g}{2}\,(\eta^2)'\,-\,\frac{c_s^2}{3}\,(\eta')^3 \\ +\,\frac{c_s^2}{3}\,(2\,h\,\eta\,+\,\eta^2)\,\eta'''\,+\,\frac{c_s^2}{2}\,(h\,+\,\eta)\eta'\eta''\;=\;0\,. \tag{12}$$

Once the free surface elevation $\eta(X)$ is determined, the velocity can be found from the mass conservation (10):

$$u(X)\;=\;\frac{c_s\,\eta(X)}{h\,+\,\eta(X)}\,,\qquad Q(X)\;=\;c_s\,\eta(X)\,. \tag{13}$$

Solitary wave profiles $(\eta(X),\, u(X))$ can be obtained numerically by approximating solutions to the differential Equation (12) and then using (13) to compute the velocity profile.

Several strategies to this end exist in the literature (see [89] and references therein). The one considered here consists of two steps. First, the NEWTON method is applied to (12): from an initial iteration $\eta^{[0]}(X)$ and if the approximation $\eta^{[\nu]}(X)$, $\nu = 0, 1, \ldots$ to the profile $\eta(X)$ at the νth iteration is known, then $\eta^{[\nu+1]}(X)$ is obtained by solving the equation

$$L^{[\nu]}\Delta\eta^{[\nu]} = -L_0\,\eta^{[\nu]}, \tag{14}$$

where $\Delta\eta^{[\nu]} \overset{\text{def}}{:=} \eta^{[\nu+1]} - \eta^{[\nu]}$, L_0 is given by (12) and $L^{[\nu]}$ is the linearized operator of Eq. (12) evaluated at $\eta^{[\nu]}(X)$.

The second step of our numerical procedure is the discretization of (14), which will be inspired by several works of J. BOYD (for more details see [16–19]). For $N \geq 1$ and large $L > 0$, the system (14) is discretized on the interval $\bigl(-L,\, L\bigr)$ by the collocation points

$$x_k = -L + (2k+1)\,h, \qquad h = \frac{L}{N}, \qquad k = 0, \ldots, N-1. \tag{15}$$

For $\nu = 0, 1, \ldots$, the approximation $\eta_h^{[\nu]}$ to the νth iteration $\eta^{[\nu]}$ is sought in the space $\mathbb{S}_h$, based on (15), of trigonometric interpolation polynomials of the form

$$Z_h(x) = \sum_{j=0}^{N-1} Z_j \cos\Bigl(\frac{\pi}{2L}\, j\,(x+L)\Bigr).$$

The discrete version of (14) is then as follows. If $\eta^{[\nu]} \in \mathbb{S}_h$ is known, we search for the incremental term $\Delta\eta_h^{[\nu]} \overset{\text{def}}{:=} \eta_h^{[\nu+1]} - \eta_h^{[\nu]}$ in $\mathbb{S}_h$, i.e.

$$\Delta\eta^{[\nu]}(x) = \sum_{j=0}^{N-1} \alpha_j^{[\nu]} \cos\Bigl(\frac{\pi}{2L}\, j\,(x+L)\Bigr),$$

and evaluate (14) at the collocation points (15). This leads to a linear system for the coefficients $\alpha^{[\nu]} = (\alpha_0^{[\nu]}, \ldots, \alpha_{N-1}^{[\nu]})^\top$ of the form

$$L_h^{[\nu]}\,\alpha^{[\nu]} = f^{[\nu]}, \tag{16}$$

where the matrix $L_h^{[\nu]} = \bigl(L_{ij}^{[\nu]}\bigr)_{i,j=0}^{N-1}$ and the vector $f^{[\nu]} = (f_0^{[\nu]}, \ldots, f_{N-1}^{[\nu]})^\top$ are computed as

$$L_{ij}^{[\nu]} = L^{[\nu]} \cos\Bigl(\frac{\pi}{2L}\, j\,(x+L)\Bigr)\Big|_{x=x_i}, \qquad f_k^{[\nu]} = -L_0\,\eta^{[\nu]}\Big|_{X=x_k},$$

for $i,\ k\ =\ 0,\ \ldots,\ N\ -\ 1$. We note that the construction of coefficients $f^{[\nu]}$ in (16) requires the computation of derivatives of $\eta_h^{[\nu]}$ up to the third order at the points (15). Finally, in order to pass to the next iteration $\eta_h^{[\nu+1]}$. Equation (16) has to be solved. The ill-conditioning of the resulting system is treated using the pseudo-inverse technique combined with the iterative refinement (see [18, 28, 46, 52] for more details). This method solves Eq. (16) in the least squares sense and the solution has a minimum norm.

The overall iterative process is controlled, in a standard way, by two parameters: (*i*) a maximum number of iterations and (*ii*) a tolerance governing the relative error between two consecutive iterations or the residual error:

$$\varepsilon_1\,[\nu]\ =\ \frac{\|\,\eta^{[\nu]}\ -\ \eta^{[\nu\,-\,1]}\,\|}{\|\,\eta^{[\nu]}\,\|}\,,\qquad \varepsilon_2\,[\nu]\ =\ \|\,L_0\,\eta^{[\nu]}\,\|\,, \tag{17}$$

measured in some norm $\|\cdot\|$ (in the experiments reported below, both the EUCLIDEAN and the maximum norms (l_∞) were implemented). Thus, the iteration stops when the maximum number of iterations is attained or when any of the errors (17) is below a prescribed tolerance.

3.1 Numerical Results

The described above numerical procedure will be tested and used now to compute several travelling wave solutions to the m-PEREGRINE Equations (4), (6). For the sake of convenience, we will solve equations in the dimensionless form which is readily obtained by setting dimensional constants $g\ =\ 1$ and $d\ =\ 1$. The tolerance parameter in the control of the iterations is chosen to be equal to 10^{-13}. The exact solution to the classical SERRE equations [25, 32, 72] is chosen as the initial approximation at the first iteration.

The behaviour of the relative error $\varepsilon_1\,[\nu]$ and absolute error $\varepsilon_2\,[\nu]$ during the iterations is shown in Fig. 2 for two values of the propagation velocity $c_s\ =\ 1.05$ and 1.1. In both cases, the iterations are stopped since the first error drops below the prescribed tolerance. The errors in Fig. 2 are measured in the maximum (l_∞) norm. The results in the EUCLIDEAN (l_2) norm are completely similar. We can see that a relatively small number of iterations is needed to achieve the convergence. However, higher values of the propagation speed c_s lead to higher nonlinearities. Consequently, more iterations are needed until the convergence is attained. The dependence of the number of iterations on the speed value c_s is illustrated in Fig. 3. The metamorphosis of these profiles as we change gradually the propagation speed c_s is shown in Fig. 4.

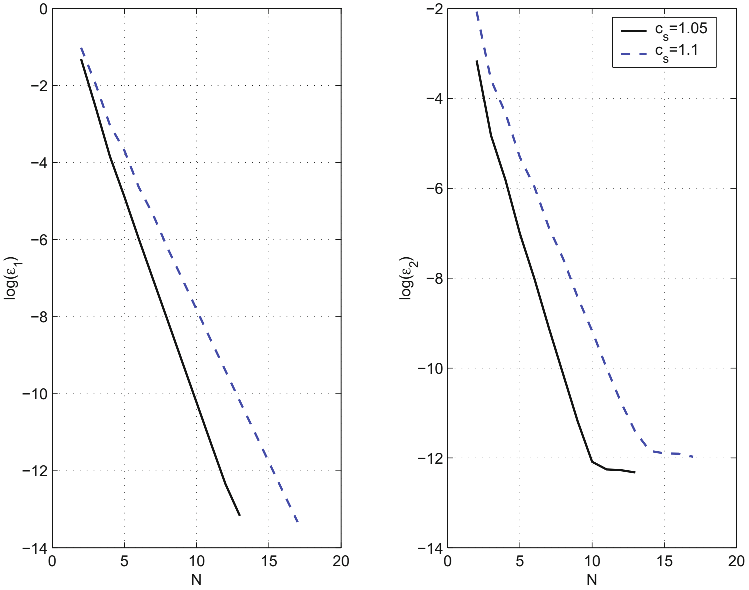

Fig. 2 Decimal logarithm of the relative errors defined in (17). Relative difference between two iterations $\varepsilon_1 \, [\nu]$ is shown in the left image, while the residual of the equation is depicted on the right. The convergence is illustrated for two values of the propagation velocities $c_s = 1.05$ (black solid line) and 1.1 (blue dashed line)

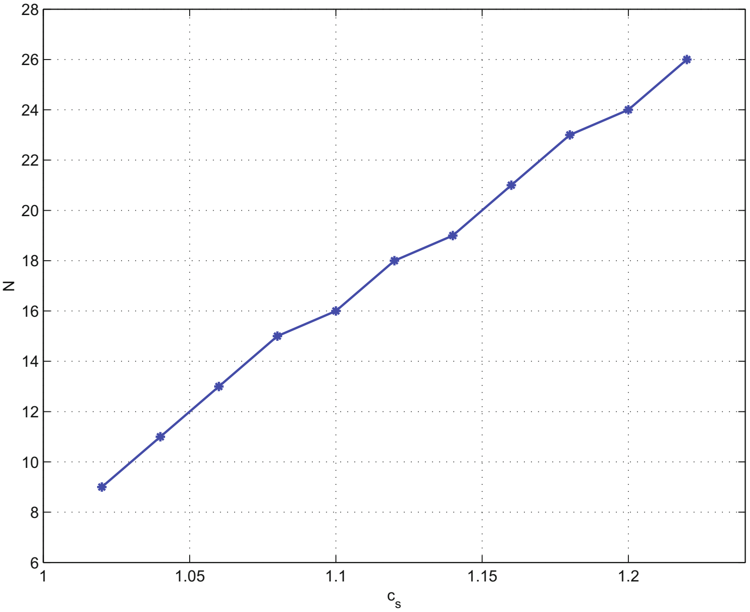

Fig. 3 Dependence of the number of iterations needed to achieve the convergence on the solitary wave propagation speed c_s

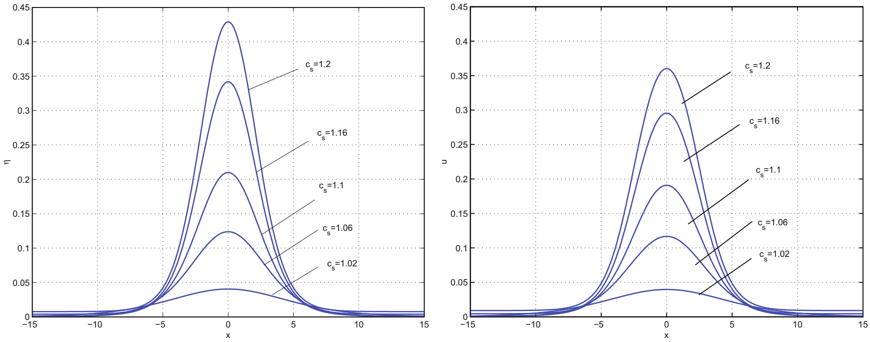

(a) $\eta-$profile (b) $u-$profile

Fig. 4 Solitary wave profiles for various values of the propagation speed c_s are superposed on the same image to show the evolution of the shape while changing this parameter. On the left image, we show the free surface profile, while the right image depicts the horizontal velocity variable. The lowest curve corresponds to the smallest values of $c_s = 1.02$ and the highest solution is obtained for $c_s = 1.2$

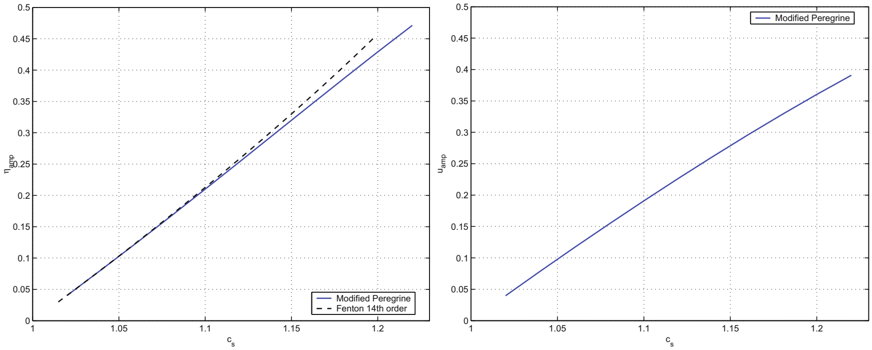

(a) Free surface (b) Horizontal velocity

Fig. 5 Speed–amplitude relation for the m-PEREGRINE system. On the left image, we show the free surface elevation amplitude and compare it to the 14th-order FENTON's solution. On the right image, we show the horizontal velocity amplitude as a function of the propagation speed c_s

For illustrative purposes, we provide several computed amplitudes (free surface elevation and horizontal velocity) of the solitary waves for various values of the propagation speed c_s. This speed–amplitude relation is represented graphically in Fig. 5. We make also a comparison with the 14th-order FENTON's solution for the full water wave problem (for more details see [42, 58]). One can notice a good agreement with the m-PEREGRINE system proposed in the previous Section.

4 Numerical Discretization

In this section, we present briefly the rationale on numerical methods we use to discretize the system (4), (6) we derived above: Below, we follow the great lines of our previous work [37].

4.1 Finite Volume Scheme

We begin our presentation by a discretization of the hyperbolic part of equations (which are simply the classical nonlinear shallow water equations) and then, in the second time, we discuss the treatment of dispersive terms. The modified PEREGRINE system (4), (6) can be formally put under this quasi-linear form:

$$\mathbb{D}\,(v_t) \;+\; [\,f\,(v)\,]_x \;=\; s\,(v)\,, \tag{18}$$

where $v, f\,(v)$ are the conservative variables and the advective flux function, respectively:

$$v \;=\; \begin{pmatrix} H \\ Q \end{pmatrix}, \quad f\,(v) \;=\; \begin{pmatrix} Q \\ \dfrac{Q^2}{H} \;+\; \dfrac{g}{2}\,H^2 \end{pmatrix}.$$

The source term $s\,(v)$ contains the topography effects and $\mathbb{D}\,(v_t)$ is the dispersion:

$$s\,(v) \;=\; \begin{pmatrix} 0 \\ g\,H\,h_x \end{pmatrix}, \quad \mathbb{D}\,(v_t) \;=\; \begin{pmatrix} H_t \\ \Bigl(1 \;+\; \frac{1}{3}\,H_x^2 \;-\; \frac{1}{6}\,H\,H_{xx}\Bigr)\,Q_t \;-\; \frac{1}{3}\,H^2\,Q_{xxt} \;-\; \frac{1}{3}\,H\,H_x\,Q_{xt} \end{pmatrix}.$$

Since the time derivative of the horizontal momentum Q is defined implicitly, we will have to invert a linear elliptic operator with non-constant coefficients.

The JACOBIAN of the advective flux $f\,(v)$ can be easily computed:

$$\mathbb{A}\,(v) \;=\; \frac{\partial f\,(v)}{\partial v} \;=\; \begin{pmatrix} 0 & 1 \\ g\,H - \Bigl(\dfrac{Q}{H}\Bigr)^2 & \dfrac{2\,Q}{H} \end{pmatrix}.$$

The JACOBIAN $\mathbb{A}\,(v)$ has two distinctive eigenvalues:

$$\lambda^{\pm} \;=\; \frac{Q}{H} \;\pm\; c_s \;\equiv\; u \;\pm\; c_s\,, \qquad c_s \;\overset{\text{def}}{:=}\; \sqrt{g\,H}\,.$$

The corresponding right and left eigenvectors are provided here:

$$R \;=\; \begin{pmatrix} 1 & 1 \\ \lambda^+ & \lambda^- \end{pmatrix}, \qquad L \;=\; R^{-1} \;=\; -\frac{1}{2\,c_s}\begin{pmatrix} \lambda^- & -1 \\ -\lambda^+ & 1 \end{pmatrix}.$$

Let us fix a partition of $\mathbb{R}$ into cells (or finite volumes) $\mathscr{C}_i = \left[x_{i-\frac{1}{2}}, x_{i+\frac{1}{2}}\right]$ with cell centres $x_i = \frac{1}{2}(x_{i-\frac{1}{2}} + x_{i+\frac{1}{2}})$, $i \in \mathbb{Z}$. Let Δx_i denotes the length of the cell $\mathscr{C}_i$. Without any loss of generality we assume the partition to be uniform, i.e. $\Delta x_i \equiv \Delta x, \forall i \in \mathbb{Z}$. We would like to approximate the solution $v(x, t)$ by discrete values. In order to do so, we introduce the cell average of v on the cell $\mathscr{C}_i$, i.e.

$$\bar{v}_i(t) \overset{\text{def}}{:=} \bigl(\bar{H}_i(t), \bar{Q}_i(t)\bigr) = \frac{1}{\Delta x}\int_{\mathscr{C}_i} v(x, t)\,\mathrm{d}x\,.$$

A simple integration of (18) over the cell $\mathscr{C}_i$ leads the following exact relation:

$$\mathbb{D}(\bar{v}_t)_i + \frac{1}{\Delta x}\Bigl(f(v(x_{i+\frac{1}{2}}, t)) - f(v(x_{i-\frac{1}{2}}, t))\Bigr) = \frac{1}{\Delta x}\int_{\mathscr{C}_i} s(v)\,\mathrm{d}x\,.$$

Since the discrete solution is discontinuous at cell interfaces $x_{i+\frac{1}{2}}$, $i \in \mathbb{Z}$, the heart of the matter in the finite volume method is to replace the flux through cell faces by the so-called numerical flux function:

$$f(v(x_{i\pm\frac{1}{2}}, t)) \approx \mathscr{F}_{i\pm\frac{1}{2}}(\bar{v}^L_{i\pm\frac{1}{2}}, \bar{v}^R_{i\pm\frac{1}{2}})\,,$$

where $\bar{v}^{L,R}_{i\pm\frac{1}{2}}$ are reconstructions of conservative variables $\bar{v}$ from left and right sides of each cell interface. The reconstruction procedure employed in the present study will be described below. Consequently, the semi-discrete scheme takes the form:

$$\mathbb{D}(\bar{v}_t)_i + \frac{1}{\Delta x}\bigl(\mathscr{F}_{i+\frac{1}{2}} - \mathscr{F}_{i-\frac{1}{2}}\bigr) = \S_i\,, \tag{19}$$

where $\S_i \approx \frac{1}{\Delta x}\int_{\mathscr{C}_i} s(v)\,\mathrm{d}x$ is an approximation of the topographic term on the right-hand side of (6). In the present study we employ the standard hydrostatic reconstruction [2] to obtain a well-balanced scheme. The expression for matrix $\mathbb{D}$ will be detailed below in Sect. 4.3.

In order to discretize the advective flux $f(v)$, we use the FVCF scheme [45]:

$$\mathscr{F}(v, w) = \frac{f(v) + f(w)}{2} - U(v, w)\,\frac{f(w) - f(v)}{2}\,.$$

The first part of the numerical flux is centred, and the second part is the upwinding introduced through the JACOBIAN sign matrix $U(v, w)$ defined as

$$U(v, w) = \operatorname{sign}\bigl(\mathbb{A}(\mu)\bigr)\,, \qquad \operatorname{sign}(\mathbb{A}) = R\cdot\operatorname{diag}(s^+, s^-)\cdot L\,, \qquad s^\pm \overset{\text{def}}{:=} \operatorname{sign}(\lambda^\pm)\,.$$

The average state $\mu = (\mu_1(v, w), \mu_2(v, w))$ between the left $v = (H^L_{i+\frac{1}{2}}, u^L_{i+\frac{1}{2}})$ and the right $w = (H^R_{i+\frac{1}{2}}, u^R_{i+\frac{1}{2}})$ states[4] is defined as the ROE average:

$$\mu_1 = \frac{H^L_{i+\frac{1}{2}} + H^R_{i+\frac{1}{2}}}{2}, \qquad \mu_2 = \frac{\sqrt{H^L_{i+\frac{1}{2}}}\, u^L_{i+\frac{1}{2}} + \sqrt{H^R_{i+\frac{1}{2}}}\, u^R_{i+\frac{1}{2}}}{\sqrt{H^L_{i+\frac{1}{2}}} + \sqrt{H^R_{i+\frac{1}{2}}}}.$$

After some simple algebraic computations, one can find the following expression for the sign matrix $U(v, w)$:

$$U(v, w) = \frac{1}{2c}\begin{pmatrix} s^-(\mu_2 + c) - s^+(\mu_2 - c) & s^+ - s^- \\ (s^+ - s^-)(c^2 - \mu_2^2) & s^+(\mu_2 + c) - s^-(\mu_2 - c) \end{pmatrix},$$

with $c \overset{\text{def}}{:=} \sqrt{g\,\mu_1}$. We reiterate again that the sign matrix U is evaluated at the average state μ of left and right values.

4.2 High-Order Reconstruction

In order to obtain a higher order scheme in space, we need to replace the piecewise constant data by a piecewise polynomial representation. This goal is achieved by various so-called reconstruction procedures such as MUSCL TVD [56, 83, 84], UNO [51], ENO [50], WENO [88] and many others. In our previous study on Boussinesq-type equations [37], the UNO2 scheme showed a good performance with low dissipation in realistic propagation and run-up simulations.

Remark 4 In TVD schemes, the numerical operator is required (by definition) not to increase the total variation of the numerical solution at each time-step. It follows that the value of an isolated maximum may only decrease in time which is not a good property for the simulation of coherent structures such as solitary waves. The non-oscillatory UNO2 scheme, employed in our study, is only required to diminish the *number* of local extrema in the numerical solution. Unlike TVD schemes, UNO schemes are not constrained to damp the values of each local extremum at every time-step.

The main idea of the UNO2 scheme is to construct a non-oscillatory piecewise-parabolic interpolant $Q(x)$ to a piecewise smooth function $v(x)$ (see [51] for more details). On each segment containing the face $x_{i+\frac{1}{2}} \in [x_i, x_{i+1}]$, the function $Q(x) = q_{i+\frac{1}{2}}(x)$ is locally a quadratic polynomial and wherever $v(x)$ is smooth we have

---

[4] We do not take here the conservative variables (H, Q) since the reconstruction procedure is more accurate and robust in physical variables (H, u).

$$Q(x) - v(x) = \mathscr{O}(\Delta x^3), \qquad \frac{\mathrm{d}Q}{\mathrm{d}x}(x \pm 0) - \frac{\mathrm{d}v}{\mathrm{d}x} = \mathscr{O}(\Delta x^2).$$

Also $Q(x)$ should be non-oscillatory in the sense that the number of its local extrema does not exceed that of $v(x)$. Since $q_{i+\frac{1}{2}}(x_i) = \bar{v}_i$ and $q_{i+\frac{1}{2}}(x_{i+1}) = \bar{v}_{i+1}$, it can be written in the form:

$$q_{i+\frac{1}{2}}(x) = \bar{v}_i + d_{i+\frac{1}{2}} v \cdot \frac{x - x_i}{\Delta x} + \tfrac{1}{2} D_{i+\frac{1}{2}} v \cdot \frac{(x - x_i)(x - x_{i+1})}{\Delta x^2},$$

where $d_{i+\frac{1}{2}} v \overset{\text{def}}{:=} \bar{v}_{i+1} - \bar{v}_i$ and $D_{i+\frac{1}{2}} v$ is closely related to the second derivative of the interpolant since $D_{i+\frac{1}{2}} v = \Delta x^2 q''_{i+\frac{1}{2}}(x)$. The polynomial $q_{i+\frac{1}{2}}(x)$ is chosen to be one the least oscillatory between two candidates interpolating $v(x)$ at (x_{i-1}, x_i, x_{i+1}) and (x_i, x_{i+1}, x_{i+2}). This requirement leads to the following choice of $D_{i+\frac{1}{2}} v$:

$$D_{i+\frac{1}{2}} v \overset{\text{def}}{:=} \operatorname{minmod}\bigl(D_i v, D_{i+1} v\bigr),$$

with

$$D_i v = \bar{v}_{i+1} - 2\bar{v}_i + \bar{v}_{i-1}, \quad D_{i+1} v = \bar{v}_{i+2} - 2\bar{v}_{i+1} + \bar{v}_i,$$

and minmod (x, y) is the usual min mod function defined as

$$\operatorname{minmod}(x, y) = \frac{1}{2}(\operatorname{sign}(x) + \operatorname{sign}(y)) \cdot \min(|x|, |y|).$$

To achieve the second order $\mathscr{O}(\Delta x^2)$ accuracy, it is sufficient to consider piecewise linear reconstructions in each cell. Let $L(x)$ denote this approximately reconstructed function which can be written in this form:

$$L(x) = \bar{v}_i + s_i \cdot \frac{x - x_i}{\Delta x}, \qquad x \in \left[x_{i-\frac{1}{2}}, x_{i+\frac{1}{2}}\right].$$

To make $L(x)$ a non-oscillatory approximation, we use the parabolic interpolation $Q(x)$ constructed below to estimate the slopes s_i within each cell:

$$s_i = \Delta x \cdot \operatorname{minmod}\Bigl(\frac{\mathrm{d}Q}{\mathrm{d}x}(x_i - 0), \frac{\mathrm{d}Q}{\mathrm{d}x}(x_i + 0)\Bigr).$$

In other words, the solution is reconstructed on the cells while the solution gradient is estimated on the dual mesh as it is often performed in more modern schemes [3, 4]. A brief summary of the UNO2 reconstruction can be also found in [37].

4.3 Dispersive Terms Treatment

In this section, we explain how we treat the dispersive terms of the m-PEREGRINE system (4), (6). Here again, we follow in great lines our previous study [37]. The following second-order $\mathscr{O}(\Delta x^2)$ approximations are used to discretize the dispersive terms arising in matrix $\mathbb{D}\,(v_t)$:

$$\frac{1}{\Delta x}\int\limits_{\mathscr{C}_i}\Bigl[1+\frac{1}{3}\,H_x^2-\frac{1}{6}\,H\,H_{xx}\Bigr]Q_t\,\mathrm{d}x\;\approx\;\left(1+\frac{1}{3}\left(\frac{H_{i+1}-H_{i-1}}{2\,\Delta x}\right)^2-\frac{1}{6}\,H_i\,\frac{H_{i+1}-2\,H_i+H_{i-1}}{\Delta x^2}\right)(Q_t)_i\,,$$

$$\frac{1}{\Delta x}\int\limits_{\mathscr{C}_i}\frac{1}{3}\,H\,H_x\,Q_{xt}\,\mathrm{d}x\;\approx\;\frac{1}{3}\,H_i\,\frac{H_{i+1}-H_{i-1}}{2\,\Delta x}\,\frac{(Q_t)_{i+1}-(Q_t)_{i-1}}{2\,\Delta x}\,,$$

$$\frac{1}{\Delta x}\int\limits_{\mathscr{C}_i}\frac{1}{3}\,H^2\,Q_{xxt}\,\mathrm{d}x\;\approx\;\frac{1}{3}\,H_i^2\,\frac{(Q_t)_{i+1}-2\,(Q_t)_i+(Q_t)_{i-1}}{\Delta x^2}\,.$$

Given the previous discretizations we obtain the following semi-discrete scheme:

$$\frac{\mathrm{d}\bar{H}_i}{\mathrm{d}t}+\frac{1}{\Delta x}\bigl(\mathscr{F}^{(1)}_{i+\frac{1}{2}}-\mathscr{F}^{(1)}_{i-\frac{1}{2}}\bigr)\;=\;0\,, \tag{20}$$

$$\mathbb{L}\,\frac{\mathrm{d}\bar{Q}_i}{\mathrm{d}t}+\frac{1}{\Delta x}\bigl(\mathscr{F}^{(2)}_{i+\frac{1}{2}}-\mathscr{F}^{(2)}_{i-\frac{1}{2}}\bigr)\;=\;\mathrm{S}\,(\bar{v})\,. \tag{21}$$

The matrix $\mathbb{D}$ defined above in Eq. (19) can be expressed in terms of the matrix $\mathbb{L}$:

$$\mathbb{D}\;\stackrel{\text{def}}{:=}\;\begin{pmatrix}\mathbb{I} & 0\\ 0 & \mathbb{L}\end{pmatrix},$$

where $\mathbb{I}$ is the identity matrix.

Consequently, in order to obtain the fully discrete scheme from Eqs. (20), (21) we have to invert a system of linear equations with the tridiagonal matrix $\mathbb{L}$. It can be done efficiently with linear complexity. We note that on dry cells the matrix $\mathbb{L}$ becomes simply the identity matrix since $H_i\;\equiv\;0$ in that regions. We reiterate again that we do not switch off the dispersive terms at some empirically chosen depth. It is the wave propagation physics which governs the magnitude of dispersive terms and thus, will decide whether they are important or not.

4.4 Time-Stepping

We assume that the linear system of equations is already inverted leading to a system of ODEs of the form:

$$\bar{v}_t \;=\; \mathscr{N}\,(\bar{v},\, t)\,, \qquad \bar{v}\,(0) \;=\; \bar{v}_0\,.$$

In order to solve numerically the last system of equations, we apply the Bogacki–Shampine method proposed in [14]. It is a Runge–Kutta scheme of the third order with four stages. It has an embedded second-order method which is used to estimate the local error and thus, to adapt the time-step size. Moreover, the Bogacki–Shampine method enjoys the First Same As Last (FSAL) property so that it needs approximately three function evaluations per step. This method is also implemented in the `ode23` function in `Matlab` [73]. The one step of the Bogacki–Shampine method is given by

$$\begin{aligned}
k_1 \;&=\; \mathscr{N}\,(\bar{v}^{(n)},\, t_n)\,,\\
k_2 \;&=\; \mathscr{N}\,(\bar{v}^{(n)} \;+\; \tfrac{1}{2}\;\Delta t_n\, k_1,\; t_n \;+\; \tfrac{1}{2}\;\Delta t)\,,\\
k_3 \;&=\; \mathscr{N}\,(\bar{v}^{(n)}) \;+\; \tfrac{3}{4}\;\Delta t_n\, k_2,\; t_n \;+\; \tfrac{3}{4}\;\Delta t)\,,\\
\bar{v}^{(n+1)} \;&=\; \bar{v}^{(n)} \;+\; \Delta t_n \left(\tfrac{2}{9}\; k_1 \;+\; \tfrac{1}{3}\; k_2 \;+\; \tfrac{4}{9}\; k_3\right),\\
k_4 \;&=\; \mathscr{N}\,(\bar{v}^{(n+1)},\; t_n + \Delta t_n)\,,\\
\bar{v}_2^{(n+1)} \;&=\; \bar{v}^{(n)} \;+\; \Delta t_n \left(\tfrac{4}{24}\; k_1 \;+\; \tfrac{1}{4}\; k_2 \;+\; \tfrac{1}{3}\; k_3 + \tfrac{1}{8}\; k_4\right).
\end{aligned}$$

Here, $\bar{v}^{(n)} \;\approx\; \bar{v}\,(t_n)$, Δt is the time-step and $\bar{v}_2^{(n+1)}$ is a second-order approximation to the solution $\bar{v}\,(t_{n\,+\,1})$, so the difference between $\bar{v}^{(n+1)}$ and $\bar{v}_2^{(n+1)}$ gives an estimation of the local error. The FSAL property consists in the fact that k_4 is equal to k_1 in the next time-step, thus saving one function evaluation.

If the new time-step $\Delta t_{n\,+\,1}$ is given by $\Delta t_{n\,+\,1} \;=\; \rho_n\, \Delta t_n$, then according to `H211b` digital filter approach [74, 75], the proportionality factor ρ_n is given by

$$\rho_n \;=\; \left(\frac{\delta}{\varepsilon_n}\right)^{\beta_1} \left(\frac{\delta}{\varepsilon_{n\,-\,1}}\right)^{\beta_2}\; \rho_{n\,-\,1}^{-\alpha}\,, \tag{22}$$

where ε_n is a local error estimation at time-step t_n and constants β_1, β_2 and α are defined as

$$\alpha \;=\; \frac{1}{4}\,, \quad \beta_1 \;=\; \frac{1}{4p}\,, \quad \beta_2 \;=\; \frac{1}{4p}\,.$$

The parameter p is the order of the scheme and $p \;=\; 3$ in our case.

Remark 5 The adaptive strategy (22) can be further improved if we regularize the factor ρ_n before computing the next time-step $\Delta t_{n\,+\,1}$:

$$\Delta t_{n+1} = \hat{\rho}_n \, \Delta t_n \,, \qquad \hat{\rho}_n = \omega(\rho_n) \,.$$

The function $\omega(\rho)$ is called *the time-step limiter* and should be smooth, monotonically increasing and should satisfy the following conditions:

$$\omega(0) < 1 \,, \quad \omega(+\infty) > 1 \,, \quad \omega(1) = 1 \,, \omega'(1) = 1 \,.$$

One possible choice was suggested in [75]:

$$\omega(\rho) = 1 + \kappa \arctan\Bigl(\frac{\rho - 1}{\kappa}\Bigr) \,.$$

In our computations, the parameter κ is set to 1.

Several validations of the above presented numerical scheme, including the convergence tests, run-up simulations as well as the comparison with experimental data [76, 90] can be found in our previous numerical study [37]. Here we make a step forward in the application of the proposed numerical model to practical coastal engineering problems.

5 Numerical Results

Using the numerical method described in the preceding section, we can perform some simulations of the wave run-up onto a plane beach. Consider a setup schematically depicted in Fig. 1. The bathymetry defined on a segment $[a, c]$ is composed of two regions: constant depth region $z = -d_0$, for $x \in [a, b]$ and the constant slope region $z = -d_0 + x\tan(\delta)$, $x \in [b, c]$. We will solve numerically a boundary value problem (BVP). Namely, on the right end ($x = c$) we impose the wall boundary condition $u|_{x=c} = 0$, while on the left boundary ($x = a$) we are given by the incident wave height. In the present study, we will consider the run-up of a monochromatic periodic wave entering from the left side (see Fig. 1):

$$H_0(t) = d_0 + A \sin(\omega t) \,.$$

The computational domain is discretized into $N = 500$ equal control volumes. The time-step value is automatically chosen by the time-stepping algorithm. The values of various physical parameters are given in Table 1.

Remark 6 The rigorous imposing of an incident wave boundary condition in the context of various dispersive wave equations is essentially an open question. However, for the m-PEREGRINE system under consideration, we found an operational solution based on the hyperbolic part of these equations. The general method is described in [68]. The numerical flux through the first left face $x = a$ is found by considering incoming characteristics and is given by this formula:

Table 1 Values of various parameters used in convergence tests

Undisturbed water depth, d_0	1
Gravity acceleration, g	1
Incident wave amplitude, A	0.3
Incident wave frequency, ω	0.8
Final simulation time, T	29.0
Left boundary coordinate, a	-8
Transition coordinate between regions, b	0
Right boundary coordinate, c	16
Beach slope, $\tan(\delta)$	0.14

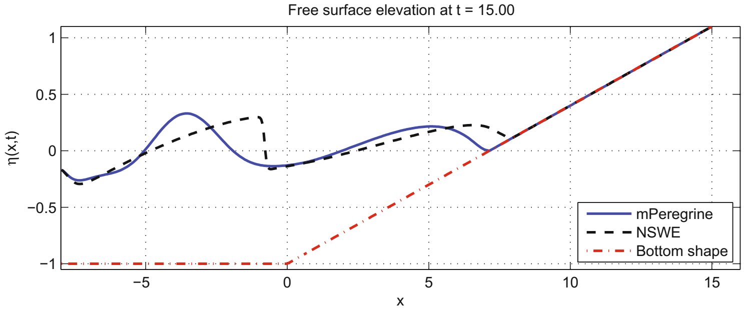

Fig. 6 Free surface snapshot at $t = 15$. The blue solid line corresponds to the m-PEREGRINE system, the black dashed line refers to NSWE and the red dot-dashed line shows the bottom

$$\mathscr{F}\,(x = a,\, t) = \begin{pmatrix} H_0\,(t)\,u_0 \\ H_0\,(t)\,u_0^2 + \frac{g}{2}\,H_0^2\,(t) \end{pmatrix}, \qquad u_0 \overset{\text{def}}{:=} u_1 + \Bigl(1 - \frac{H_1}{H_0}\Bigr)\sqrt{g\,H_1}\,,$$

where $(H_1,\, u_1)$ are the reconstructed physical variables on the left face from the fluid domain. Our numerical tests presented below demonstrate the robustness and efficiency of this approach.

The afore-described situation is simulated with the modified PEREGRINE system (4), (6), but also with classical nonlinear shallow water equations (NSWE) [38, 40, 91]. The comparative results of this simulation are presented in Figs. 6, 7, 8 and 9. We underline that no friction terms are considered in this study. The numerical results we present are based only on mathematical models described above.

During the initial stages, which are not shown in figures for the sake of manuscript compactness, we see the periodic wave entering into the computational domain. The non-dispersive solution is much steeper and first shock waves start to form. Then, the wave continues its propagation towards the shore. During the propagation and run-up processes, the solution to the m-PEREGRINE system is always behind the hyperbolic wave and this is due to dispersive effects which make the wave propagation speed closer to its physical value. The run-up process starts about $t = 15$ and it can be seen

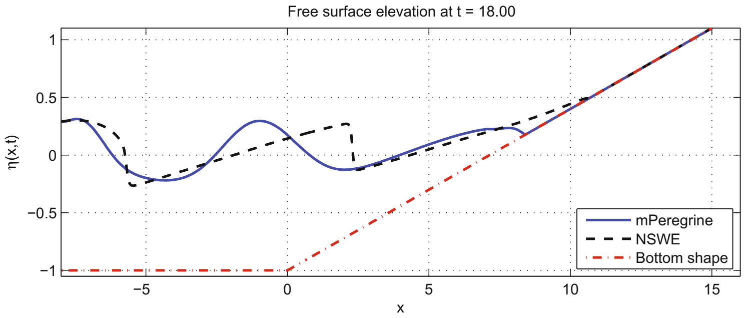

Fig. 7 Free surface snapshot at $t = 18$. The blue solid line corresponds to the m-PEREGRINE system, the black dashed line refers to NSWE and the red dot-dashed line shows the bottom

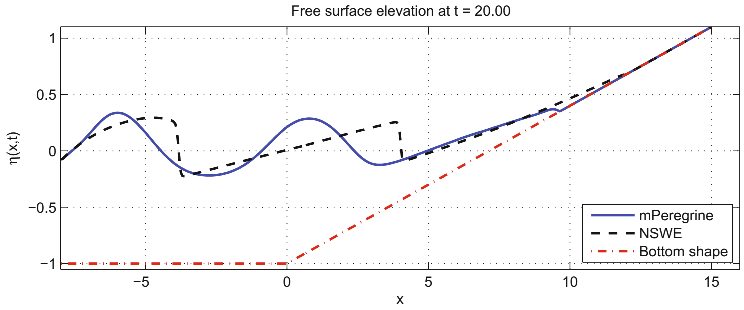

Fig. 8 Free surface snapshot at $t = 20$. The blue solid line corresponds to the m-PEREGRINE system, the black dashed line refers to NSWE and the red dot-dashed line shows the bottom

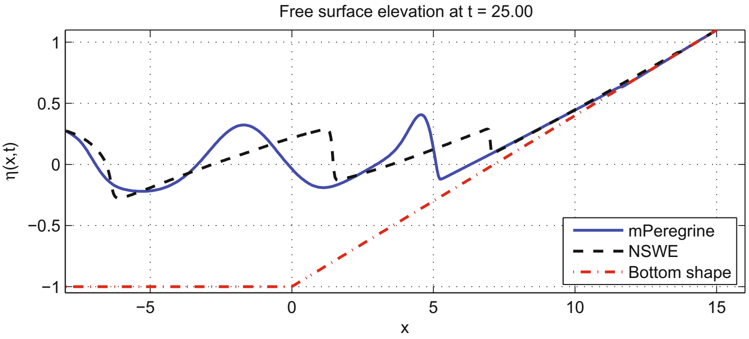

Fig. 9 Free surface snapshot at $t = 25$. The blue solid line corresponds to the m-PEREGRINE system, the black dashed line refers to NSWE and the red dot-dashed line shows the bottom

in Fig. 6. The development of this process is shown in Figs. 7, 8 and 9. Both waves about their maximum run-up height are depicted in Fig. 9. It is interesting to observe a shock-like wave formed by the m-PEREGRINE system near the shore in Fig. 9. It shows that in the shallowest regions the wave dynamics is governed essentially by nonlinear effects. This transition is naturally and automatically captured by our system without adding any ad hoc parameters.

6 Landslide-Generated Waves

Extreme water waves can become an important hazard in coastal areas. Main geophysical mechanisms include underwater earthquakes and landslides. The former genesis mechanism has been intensively investigated since the Tsunami Boxing Day [6, 33, 36, 39, 64–66, 77]. The list of references is far from being exhaustive. In this section, we focus on the latter mechanism—the underwater landslides which can cause some considerable damage in the genesis region. In general, the wavelength of landslide-generated waves is much smaller than the length of transoceanic tsunamis. Consequently, the dispersive effects might be important. This consideration explains why we opt for a dispersive m-PEREGRINE model which is able to simulate the propagation and run-up of weakly nonlinear weakly dispersive water waves on nonuniform beaches.

Most of the landslide models which are currently used in the literature can be conventionally divided into three big categories. The first category contains the simplest models where the landslide shape and its trajectory are known a priori [57, 78, 80]. Another approach consists in assuming that the landslide motion is translational and the sliding mass follows the trajectory of its barycentre. The governing equation of the centre of mass is obtained by projecting all the forces, acting on the slide, onto the horizontal direction of motion [29, 48, 85]. Finally, the third category of models describes the slide-water evolution as a two-layer system, the sliding mass being generally formulated by a SAVAGE–HUTTER type model [43]. Taking into account all the uncertainties which exist in the modelling of the real-world events, we choose in this chapter to study the intermediate level (i.e. the second category) which corresponds better to the precision of the available data in real-world situations. The chosen landslide model will be detailed below in Sect. 6.1.

The original derivation of the PEREGRINE system [70] assumes that the bottom is stationary in time, i.e. $z = -h(x)$. However, in order to simulate the wave generation process by bottom motion, we need to include the time dependence into the bathymetry definition [33, 34]. The bottom dynamics has been included in the PEREGRINE system derivation by Wu [86, 87]:

$$\eta_t + \big((h + \eta)\, u\big)_x = -\, h_t\,,$$

$$u_t + u\,u_x + g\,\eta_x - \frac{h}{2}\,(h\,u)_{x\,x\,t} + \frac{h^2}{6}\,u_{x\,x\,t} = \underbrace{\frac{1}{2}\,h\,h_{x\,t\,t}}_{(*)},$$

where the new term due to the bottom motion is marked with sign (*). By repeating the same invariantization process as above, the system written in conservative variables and with moving bottom can be straightforwardly derived:

$$H_t + Q_x = 0, \tag{23}$$

$$\left(1 + \frac{1}{3}\,H_x^2 - \frac{1}{6}\,H\,H_{x\,x}\right)Q_t - \frac{1}{3}\,H^2\,Q_{x\,x\,t} - \frac{1}{3}\,H\,H_x\,Q_{x\,t} + \left(\frac{Q^2}{H} + \frac{g}{2}\,H^2\right)_x = g\,H\,h_x + \frac{1}{2}\,H^2\,h_{x\,t\,t}\,. \tag{24}$$

The bottom motion enters into the momentum balance Eq. (24) through the source term $\frac{1}{2}\,H\,d_{x\,t\,t}$. The mass conservation Eq. (23) keeps naturally its initial form. We underline that the linear dispersion relation of the m-PEREGRINE system (23), (24) is identical with that the original PEREGRINE model [70] since these models differ only in nonlinear terms and the source terms do not enter into the dispersion relation analysis. The numerical scheme described in Sect. 4 is applied to the moving bottom m-PEREGRINE system (23), (24) without any modification. The new source term is just projected onto cell centres since the function $h\,(x,\,t)$ is prescribed by the bathymetry, the landslide shape and trajectory.

Remark 7 Following the same invariantization, one can derive the two-dimensional modified PEREGRINE system including moving bottom topography:

$$H_t + \nabla\cdot Q = 0 \tag{25}$$

$$Q_t + \nabla\cdot\left(Q\otimes\frac{Q}{H} + \frac{g}{2}\,H^2\,\mathrm{I}\right) - P\,(H,\,Q) = g\,H\,\nabla\,h + \frac{H^2}{2}\nabla h_{tt}\,, \tag{26}$$

where

$$P(H,\,Q) = \frac{H^2}{2}\nabla(\nabla\cdot Q_t) - \frac{H^2}{6}\Delta Q_t - \left(\frac{|\nabla H|^2}{3} - \frac{H\,\Delta H}{6}\right)Q_t + \frac{1}{3}\,H\,\nabla H\cdot\nabla Q_t\,.$$

It is noted that in this case H depends on $(x,\ y,\ t)$ and $Q = H \times (u, v)^T$ with $u\,(x,\ y,\ t)$ and $v\,(x,\ y,\ t)$ being the depth-averaged velocity horizontal components of the fluids velocity in the directions x and y, respectively. This system again contains some high-order correction terms in the source terms that can be simplified without affecting the invariance of vertical translations.

6.1 Landslide Model

In this section, we briefly present a model of an underwater landslide motion. This process has to be addressed carefully since it determines the subsequent formation of water waves. In this study, we will assume the moving mass to be a solid quasi-deformable body with a prescribed shape and known physical properties that preserves its mass and volume. Under these assumptions, it is sufficient to compute the trajectory of the barycentre $x = x_c(t)$ to determine the motion of the whole body. In general, only uniform slopes are considered in the literature in conjunction with this type of landslide models [24, 29, 48, 69, 85]. However, a novel model, taking into account the bottom geometry and curvature effects, has been recently proposed [6]. Hereafter we will follow in great lines this study.

The static bathymetry is prescribed by a sufficiently smooth (at least of the class C^2) and single-valued function $z = -h_0(x)$. The landslide shape is initially prescribed by a localized in space function $z = \zeta_0(x)$. For example, in this study we choose the following shape function:

$$\zeta_0(x) = A\,\operatorname{sech}\bigl(k(x - x_0)\bigr), \tag{27}$$

where the parameter A is the maximum slide height, k is inversely proportional to the slide length and x_0 is the initial position of its barycentre. Obviously, the model description given below is valid for any other reasonable shape.

Since the landslide motion is translational, its shape at time t is given by the function $z = \zeta(x, t) = \zeta_0(x - x_c(t))$. Recall that the landslide centre is located at the point with abscissa $x = x_c(t)$. Then, the impermeable bottom for the water wave problem can be easily determined at any time by simply superposing the static and dynamic components:

$$z = -h(x, t) = -h_0(x) + \zeta(x, t).$$

To simplify the subsequent presentation, we introduce the classical arc-length parametrization, where the parameter $s = s(x)$ is given by the following formula:

$$s = L(x) = \int_{x_0}^{x} \sqrt{1 + (h_0'(\xi))^2}\,\mathrm{d}\xi. \tag{28}$$

The function $L(x)$ is monotonic and can be efficiently inverted to turn back to the original CARTESIAN abscissa $x = L^{-1}(s)$. Within this parametrization, the landslide is initially located at point with the curvilinear coordinate $s = 0$. The local tangential direction is denoted by τ and the normal by n.

The landslide motion is governed by the following differential equation obtained by a straightforward application of NEWTON's second law:

$$m\,\frac{\mathrm{d}^2 s}{\mathrm{d}t^2} = F_\tau(t),$$

where m is the mass and $F_\tau\,(t)$ is the tangential component of the forces acting on the moving submerged body. In order to project the forces onto the axes of local coordinate system, the angle $\theta\,(x)$ between τ and $O\,x$ can be easily determined:

$$\theta\,(x) \;=\; \arctan\bigl(h_0'\,(x)\bigr)\,.$$

Let us denote by ρ_w and ρ_ℓ the densities of the water and sliding material correspondingly. If V is the volume of the slide, then the total mass m is given by

$$m \;\stackrel{\mathrm{def}}{:=}\; (\rho_\ell \;+\; c_w\,\rho_w)\,V\,,$$

where c_w is the added mass coefficient [5]. A portion of the water mass has to be added since it is entrained by the underwater body motion. The volume V can be computed as

$$V \;=\; W\cdot S \;=\; W\int_{\mathbb{R}}\zeta_0\,(x)\,\mathrm{d}\,x\,,$$

where W is the landslide width in the transverse direction. The last integral can be computed exactly for the particular choice (27) of the landslide shape to give

$$V \;=\; \frac{1}{2}\,\ell\,A\,W\,.$$

The total projected force F_τ acting on the landslide can be conventionally represented as a sum of two different kinds of forces denoted by F_g and F_d:

$$F_\tau \;=\; F_g \;+\; F_d\,,$$

where F_g is the joint action of the gravity and buoyancy, while F_d is the total contribution of various dissipative forces (to be specified below). The gravity and buoyancy forces act in opposite directions and their horizontal projection F_g can be easily computed:

$$F_g\,(t) \;=\; (\rho_\ell \;-\; \rho_w)\,W\,g\int_{\mathbb{R}}\zeta\,(x,\;t)\;\sin\bigl(\theta\,(x)\bigr)\,\mathrm{d}\,x\,.$$

Now, let us specify the dissipative forces. The water resistance to the motion force F_r is proportional to the maximal transversal section of the moving body and to the square of its velocity:

$$F_r \;=\; -\frac{1}{2}\,c_d\,\rho_w\,A\,W\,\sigma\,(t)\Bigl(\frac{\mathrm{d}s}{\mathrm{d}t}\Bigr)^2\,,$$

Here, c_d is the resistance coefficient of the water and $\sigma\,(t)\;\stackrel{\mathrm{def}}{:=}\;\operatorname{sign}\bigl(\frac{\mathrm{d}s}{\mathrm{d}t}\bigr)$. The coefficient $\sigma\,(t)$ is needed to dissipate the landslide kinetic energy independently of its direction of motion. The friction force F_f is proportional to the normal force exerted on the body due to the weight:

$$F_f = -c_f\,\sigma(t)\,N(x,\,t)\,.$$

The normal force $N(x,\,t)$ is composed of the normal components of gravity and buoyancy forces but also of the centrifugal force due to the variation of the bottom slope:

$$N(x,\,t) = (\rho_\ell - \rho_w)\,g\,W\int_{\mathbb{R}}\zeta(x,\,t)\cos\bigl(\theta(x)\bigr)\,\mathrm{d}x + \rho_\ell\,W\int_{\mathbb{R}}\zeta(x,\,t)\,\kappa(x)\Bigl(\frac{\mathrm{d}s}{\mathrm{d}t}\Bigr)^2\mathrm{d}x\,,$$

where $\kappa(x)$ is the signed curvature of the bottom which can be computed by the following formula:

$$\kappa(x) = \frac{h_0''(x)}{\bigl(1 + (h_0'(x))^2\bigr)^{\frac{3}{2}}}\,.$$

We note that the last term vanishes for a plane bottom since $\kappa(x) \equiv 0$ in this particular case.

In order to dissipate more energy along the landslide trajectory if it is needed, we complete our model by two supplementary viscous terms:

$$F_d = -c_v\,\frac{\mathrm{d}s}{\mathrm{d}t} - c_b\,\frac{\mathrm{d}s}{\mathrm{d}t}\,\Bigl\{\frac{\mathrm{d}s}{\mathrm{d}t}\Bigr\}\,,$$

where c_v and c_b are some prescribed constants. The first term c_v represents the internal energy loss inside the sliding material. The second term c_b accounts for the dissipation in the boundary layer between the landslide and the solid bottom.

Finally, if we sum up all the contributions of described above forces, we obtain the following second-order differential equation:

$$\begin{aligned}(\gamma + c_w)\,S\,\frac{\mathrm{d}^2 s}{\mathrm{d}t^2} &= (\gamma - 1)\,g\,\Bigl(I_1(t) - c_f\,\sigma(t)\,I_2(t)\Bigr)\\ &\quad - \sigma(t)\Bigl(c_f\,\gamma\,I_3(t) + \frac{1}{2}\,c_d\,A\Bigr)\Bigl(\frac{\mathrm{d}s}{\mathrm{d}t}\Bigr)^2 - c_v\,\frac{\mathrm{d}s}{\mathrm{d}t} - c_b\,\frac{\mathrm{d}s}{\mathrm{d}t}\,\Bigl\{\frac{\mathrm{d}s}{\mathrm{d}t}\Bigr\}\,,\end{aligned} \tag{29}$$

where $\gamma \overset{\text{def}}{:=} \frac{\rho_\ell}{\rho_w} > 1$ is the ratio of densities and integrals $I_{1,\,2,\,3}(t)$ are defined as

$$I_1(t) = \int_{\mathbb{R}} \zeta(x,\, t)\, \sin\bigl(\theta(x)\bigr)\, \mathrm{d}x\,,$$
$$I_2(t) = \int_{\mathbb{R}} \zeta(x,\, t)\, \cos\bigl(\theta(x)\bigr)\, \mathrm{d}x\,,$$
$$I_3(t) = \int_{\mathbb{R}} \zeta(x,\, t)\, \kappa(x)\, \mathrm{d}x\,.$$

Note also that Eq. (29) was simplified by dividing both sides by the width value W. In order to obtain a well-posed initial value problem, Eq. (29) has to be completed by two initial conditions:

$$s(0) \;=\; 0\,, \quad s'(0) \;=\; 0\,.$$

From Eq. (29), it follows that the motion can start only if this condition is fulfilled [6]:

$$I_1(0) \;-\; c_f\, I_2(0) \;=\; \int_{\mathbb{R}} \zeta_0(x)\Bigl[\sin\bigl(\theta(x)\bigr) \;-\; c_f\, \cos\bigl(\theta(x)\bigr)\Bigr]\, \mathrm{d}x \;>\; 0\,.$$

In order to solve numerically Eq. (29), we employ the same BOGACKI–SHAMPINE 3rd order RUNGE–KUTTA scheme that we used to approximate the BOUSSINESQ Equations (23), (24). The integrals $I_{1,\,2,\,3}(t)$ are computed with the trapezoidal rule. Once the landslide trajectory $s \;=\; s(t)$ is found, Eq. (28) is used to find its motion $x \;=\; x(t)$ in the initial CARTESIAN coordinate system.

6.2 Numerical Results

Consider a one-dimensional physical domain $\mathrm{I} \;=\; \bigl[a,\, b\bigr] \;=\; \bigl[-120,\, 120\bigr]$ which is divided into N equal control volumes. This domain is composed of three regions: the left and right curvilinear sloping beaches which surround a generation region of a deformed parabolic shape. Specifically, the static bathymetry function $d_0(x)$ is given by the following expression:

$$d_0(x) \;=\; -\kappa\,\bigl(x^2 \;-\; c^2\bigr) \;+\; A_1\, \mathrm{e}^{-k_1\,(x\,-\,x_1)^2} \;+\; A_2\, \mathrm{e}^{-k_2\,(x\,-\,x_2)^2}\,.$$

Basically, this function represents a parabolic bottom profile deformed by two underwater bumps. We made this nontrivial choice in order to illustrate better the advantages of our landslide model, which was designed to handle general non-flat bathymetries. The values of all physical and numerical parameters are given in Table 2. The bottom profile along with landslide trajectory for these parameters are depicted in Fig. 10. The landslide motion starts from the rest position under the action of the gravity force. We simulate its motion along with the free surface waves

Table 2 Values of various parameters used in the numerical computations

Parameter	Value
Gravity acceleration, g	1.0
Parabolic bottom flatness coefficient, κ	1.5×10^{-3}
Initial shoreline position, c	100.0
Underwater bump amplitude, A_1	2.8
Underwater bump amplitude, A_2	−4.8
Bump characteristic steepness, k_1	0.008
Bump characteristic steepness, k_2	0.003
Bump centre position, x_1	−60.0
Bump centre position, x_2	0.0
Number of control volumes, N	2500
Slide amplitude, A	0.5
Characteristic slide inverse length, k_0	0.16
Initial slide position, x_0	−85.0
Added mass coefficient, c_w	1.0
Water drag coefficient, c_d	1.0
Friction coefficient, c_f	tan 2°
Ratio between water and slide densities, γ	2.0
Boundary layer dissipation coefficient, c_b	0.0035
Internal friction coefficient, c_v	0.0045
Final simulation time, T	150.0

up to time $T = 150.0\ \mathsf{s}$. As it is expected, the landslide remains trapped between two underwater bumps in its final equilibrium position. The speed and acceleration of the slide barycentre during the simulation are represented in Fig. 11. We note the discontinuities in the acceleration record which correspond to the time moments when the velocity changes its sign. We insist that this behaviour is intrinsic to the landslide model in use where the dissipative terms show the discontinuous behaviour at turning points.

One of the important parameters in shallow water flows is the FROUDE number, defined as the ratio between the characteristic fluid velocity to the gravity wave speed. We computed also this parameter along the landslide trajectory:

$$\mathrm{Fr}\,(t) \;\overset{\mathrm{def}}{:=}\; \frac{\left\{x_c'\,(t)\right\}}{\sqrt{g\,d\,\bigl(x_c\,(t),\;t\bigr)}}\,.$$

The result is presented in Fig. 12. We can see that in our case the slide motion remains subcritical as it is the case in most real-world situations [49].

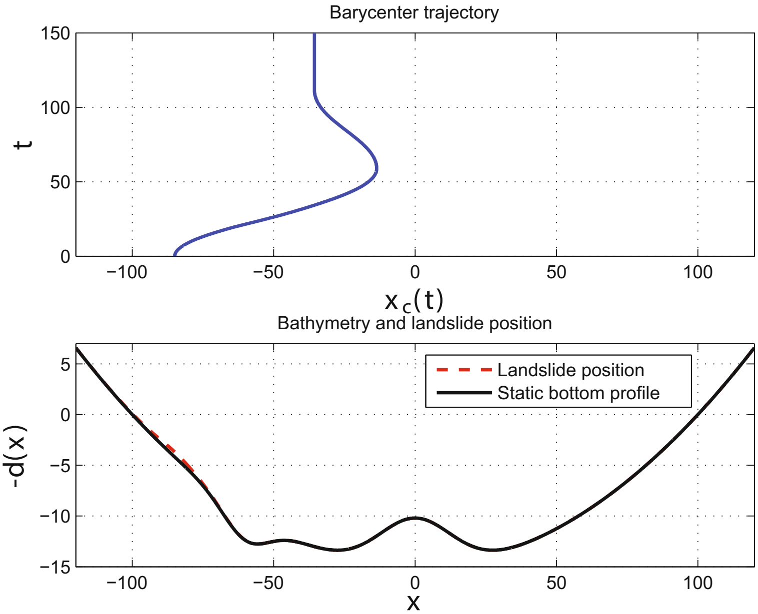

Fig. 10 Bathymetry profile and the landslide trajectory for the parameters given in Table 2. The initial landslide position is shown in the lower image with the red dashed line (- - -)

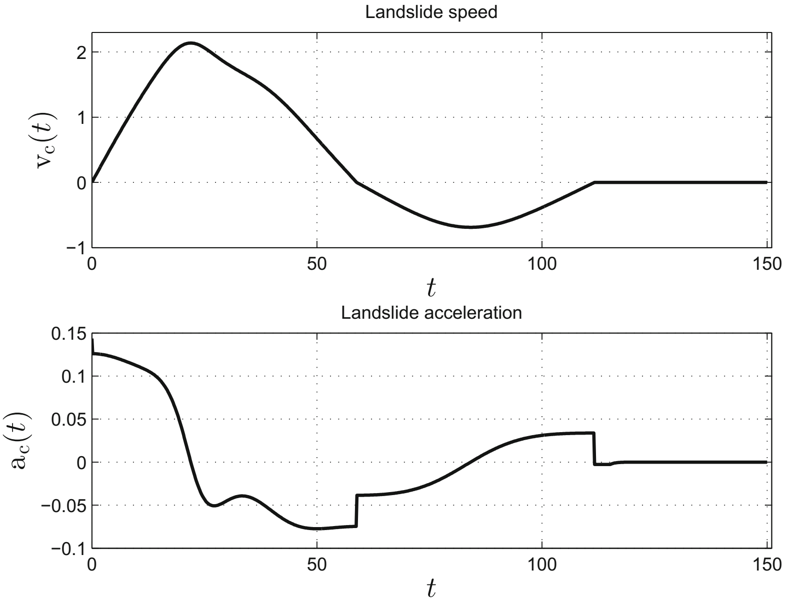

Fig. 11 Landslide speed and acceleration along its trajectory

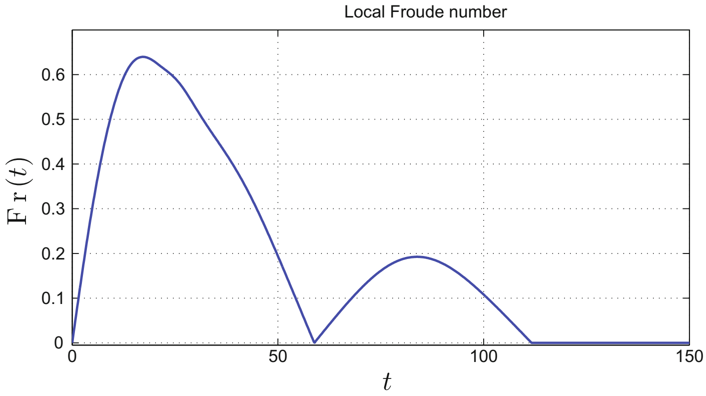

Fig. 12 Local FROUDE number computed along the slide motion

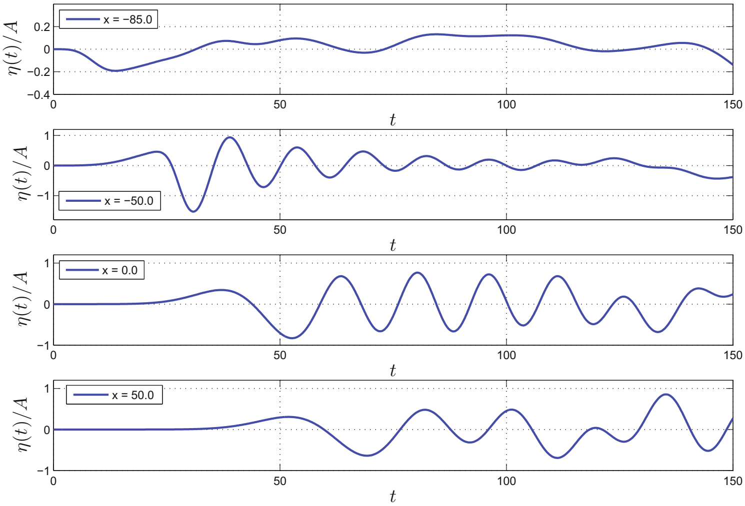

Fig. 13 Synthetic wave gauge records at four different locations. Note the different vertical scales on various images. Wave gauges are located at $x = x_0 = -85.0$, -50.0, 0.0, 50.0 from the top correspondingly. The wave amplitude is relative to the landslide amplitude

In order to measure the free surface elevations due to the underwater landslide, we installed four numerical wave gauges located at $x = x_0$, -50.0, 0.0 and 50.0. The synthetic wave records are presented in Fig. 13. One can see that the biggest quantity of primary interest is the wave run-up onto left and right beaches surrounding the fluid domain. This quantity is estimated numerically using the previously described algorithm. The shoreline motion is represented in Fig. 14. One can see that the landslide scenario under consideration produces much higher run-up values on the beach opposite to the slope where the sliding process takes place. Finally, in order

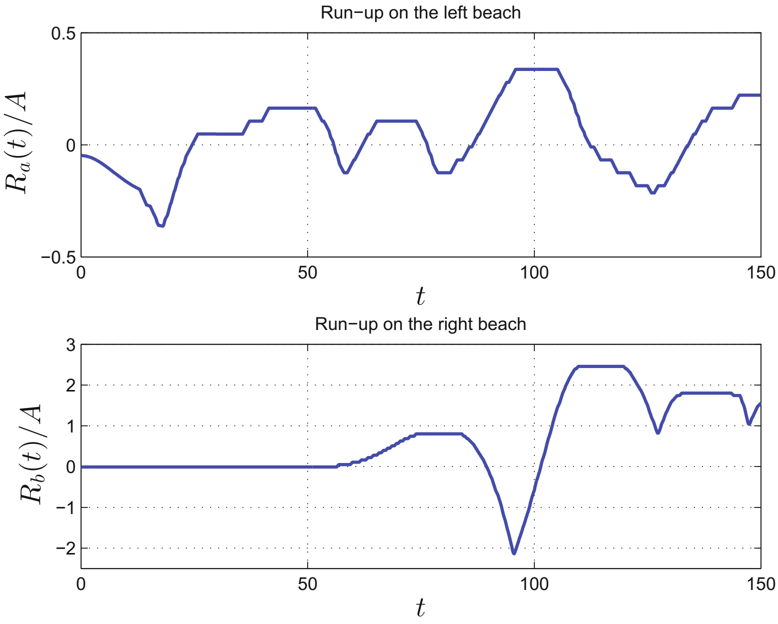

Fig. 14 Wave run-up heights onto left and right non-flat beaches during the simulation

to illustrate the energy transfer process from the landslide motion to the fluid layer, we show the evolution of both energies during the generation process in Fig. 15. We recall that the fluid potential, kinetic and total energies are defined correspondingly as

$$\Pi\,(t) \;\stackrel{\text{def}}{:=}\; \frac{1}{2}\int_{\mathbb{R}} g\,\eta^2\,\mathrm{d}x\,, \quad \mathbb{K}\,(t) \;\stackrel{\text{def}}{:=}\; \frac{1}{2}\int_{\mathbb{R}} (d\;+\;\eta)\,u^2\,\mathrm{d}x\,, \quad \mathbb{E}\,(t) \;\stackrel{\text{def}}{:=}\; \Pi\,(t)\;+\;\mathbb{K}\,(t)\,.$$

The landslide kinetic energy is readily obtained from the differential Equation (29):

$$\mathbb{K}_\ell\,(t) \;\stackrel{\text{def}}{:=}\; \frac{1}{2}\,(\gamma\;+\;c_w)\,S\left(\frac{\mathrm{d}s}{\mathrm{d}t}\right)^2.$$

Our computation shows that only about 10% of the landslide energy is transmitted to the wave. This estimation is in complete accordance with values reported by Harbitz et al. [49].

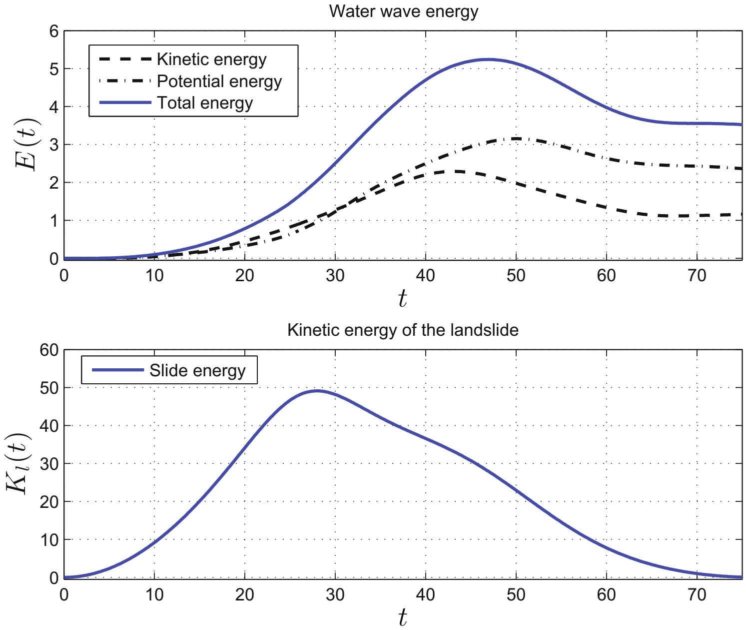

Fig. 15 Fluid and landslide energies evolution during the wave generation process

7 Discussion

Below, we outline the main conclusions and perspectives of our study.

7.1 Conclusions

In the present study, we revisited the celebrated PEREGRINE system for long waves propagation. Namely, our primary goal was to undertake a series of equivalent transformations which do not modify lower order dispersive terms $\mathscr{O}(\mu^2)$, while extending the model stability and validity up to the shoreline. Moreover, the resulting governing equations possess an additional symmetry of the complete water wave problem which were broken as a result of the asymptotic expansion. Hence, our model remains invariant under the vertical translation (subgroup G_5 in Theorem 4.2, Benjamin and Olver [10]). The application of the invariantization process presented in this study can be extended to any other system of BOUSSINESQ type. It can be viewed as a *post treatment* procedure to be applied after the derivation of a particular model. The PEREGRINE system was chosen for illustrative purposes due to its importance and popularity in the water wave community. Of course, this system possesses also several nice properties which explain its wide usage in applications.

The developments made in this study are illustrated with several examples. First of all, we proposed an efficient numerical method to construct travelling wave solutions. Some comparisons with the classical nonlinear shallow water equations (NSWE) were presented for the wave run-up problem onto a plane beach. The effect of dispersive terms is exemplified. In this study, we also presented a model of a landslide motion over general curvilinear bottoms. This model takes into account the effects of bottom curvature, generally neglected in the literature [29, 48, 69, 85]. Despite the inclusion of some new physical effects, the considered slide model is computationally inexpensive and can be potentially used in more operational context. We tested the m-PEREGRINE model on this more realistic case of the wave generation by an underwater landslide. The coupling with the m-PEREGRINE equations was done through the time-dependent bathymetry. Wave run-up records on non-flat beaches were computed. The proposed technique can be directly applied to perform a landslide hazard effects in real-world situations.

7.2 Perspectives

In the present manuscript, we focused on the two-dimensional (2D) physical problem, which became a one-dimensional (1D) mathematical problem thanks to the elimination of explicit dependence on the vertical coordinate (1DH). In future works, we are going to focus on the generalization of the m-PEREGRINE to the 2DH situation with two horizontal directions. There is another question which can be asked even in the 1D case—the energy conservation issue. So far, a successful response to this question has been brought in the variational framework [26].

Acknowledgements D. DUTYKH and A. DURÁN acknowledge the support from project MTM2014-54710-P entitled '*Numerical Analysis of Nonlinear Nonlocal Evolution Problems*' (NANNEP). D. MITSOTAKIS was supported by the MARSDEN FUND administered by the Royal Society of New Zealand.

References

1. M. Antuono, V. Y. Liapidevskii, and M. Brocchini. Dispersive Nonlinear Shallow-Water Equations. *Studies in Applied Mathematics*, 122(1):1–28, 2009.
2. E. Audusse. *Modélisation hyperbolique et analyse numérique pour les écoulements en eaux peu profondes*. PhD thesis, Université Paris VI, 2004.
3. T. J. Barth. Aspects of unstructured grids and finite-volume solvers for the Euler and Navier-Stokes equations. *Lecture series - van Karman Institute for Fluid Dynamics*, 5:1–140, 1994.
4. T. J. Barth and M. Ohlberger. Finite Volume Methods: Foundation and Analysis. In E. Stein, R. de Borst, and T. J. R. Hughes, editors, *Encyclopedia of Computational Mechanics*. John Wiley & Sons, Ltd, Chichester, UK, nov 2004.
5. G. K. Batchelor. *An introduction to fluid dynamics*, volume 61 of *Cambridge mathematical library*. Cambridge University Press, 2000.

6. S. A. Beisel, L. B. Chubarov, D. Dutykh, G. S. Khakimzyanov, and N. Y. Shokina. Simulation of surface waves generated by an underwater landslide in a bounded reservoir. *Russ. J. Numer. Anal. Math. Modelling*, 27(6):539–558, 2012.
7. S. Bellec and M. Colin. On the existence of solitary waves for Boussinesq type equations and Cauchy problem for a new conservative model. *Adv. Differential Equations*, 21(9/10):945–976, 2016.
8. G. Bellotti and M. Brocchini. On the shoreline boundary conditions for Boussinesq-type models. *Int. J. Num. Meth. in Fluids*, 37(4):479–500, 2001.
9. G. Bellotti and M. Brocchini. On using Boussinesq-type equations near the soreline: a note of caution. *Ocean Engineering*, 29:1569–1575, 2002.
10. T. B. Benjamin and P. J. Olver. Hamiltonian structure, symmetries and conservation laws for water waves. *J. Fluid Mech*, 125:137–185, 1982.
11. F. Benkhaldoun and M. Seaïd. New finite-volume relaxation methods for the third-order differential equations. *Commun. Comput. Phys.*, 4:820–837, 2008.
12. E. N. Bernard and V. V. Titov. Improving tsunami forecast skill using deep ocean observations. *Mar. Technol. Soc. J.*, 40(4):23–26, 2007.
13. G. W. Bluman, A. F. Cheviakov, and S. C. Anco. *Applications of Symmetry Methods to Partial Differential Equations*. Springer, New York, 2010.
14. P. Bogacki and L. F. Shampine. A 3(2) pair of Runge-Kutta formulas. *Appl. Math. Lett.*, 2(4):321–325, 1989.
15. J. V. Boussinesq. Théorie de l'intumescence liquide appelée onde solitaire ou de translation se propageant dans un canal rectangulaire. *C.R. Acad. Sci. Paris Sér. A-B*, 72:755–759, 1871.
16. J. P. Boyd. Solitons from sine waves: analytical and numerical methods for non-integrable solitary and cnoidal waves. *Physica D*, 21:227–246, 1986.
17. J. P. Boyd. *Chebyshev and Fourier Spectral Methods*. New York, 2nd edition, 2000.
18. J. P. Boyd. A comparison of numerical algorithms for Fourier extension of the first, second and third kinds. *J. Comput. Phys.*, 178:118–160, 2002.
19. J. P. Boyd. Deleted residuals, the QR-factored Newton iteration, and other methods for formally overdetermined determinate discretizations of nonlinear eigenproblems for solitary, cnoidal, and shock waves. *J. Comput. Phys.*, 179:216–237, 2002.
20. M. Brocchini. A reasoned overview on Boussinesq-type models: the interplay between physics, mathematics and numerics. *Proc. R. Soc. A*, 469(2160):20130496, oct 2013.
21. J. Chambarel, C. Kharif, and J. Touboul. Head-on collision of two solitary waves and residual falling jet formation. *Nonlin. Processes Geophys.*, 16:111–122, 2009.
22. A. F. Cheviakov. Computation of fluxes of conservation laws. *J. Eng. Math.*, 66(1-3):153–173, mar 2010.
23. C. I. Christov. An energy-consistent dispersive shallow-water model. *Wave Motion*, 34:161–174, 2001.
24. L. B. Chubarov, G. S. Khakimzyanov, and N. Y. Shokina. Numerical modelling of surface water waves arising due to movement of underwater landslide on irregular bottom slope. In *Notes on Numerical Fluid Mechanics and Multidisciplinary Design: Computational Science and High Performance Computing IV*, pages 75–91. Springer-Verlag, Berlin, Heidelberg, vol. 115 edition, 2011.
25. D. Clamond and D. Dutykh. Practical use of variational principles for modeling water waves. *Phys. D*, 241(1):25–36, 2012.
26. D. Clamond, D. Dutykh, and D. Mitsotakis. Conservative modified Serre–Green–Naghdi equations with improved dispersion characteristics. *Comm. Nonlin. Sci. Num. Sim.*, 45:245–257, 2017.
27. A. I. Delis, M. Kazolea, and N. A. Kampanis. A robust high-resolution finite volume scheme for the simulation of long waves over complex domains. *Int. J. Numer. Meth. Fluids*, 56:419–452, 2008.
28. J. W. Demmel. *Applied Numerical Linear Algebra*. SIAM, Philadelphia, 1997.
29. M. Di Risio, G. Bellotti, A. Panizzo, and P. De Girolamo. Three-dimensional experiments on landslide generated waves at a sloping coast. *Coastal Engineering*, 56(5-6):659–671, 2009.

30. V. A. Dougalis, A. Durán, M. A. Lopez-Marcos, and D. E. Mitsotakis. A numerical study of the stability of solitary waves of Bona-Smith family of Boussinesq systems. *J. Nonlinear Sci.*, 17:595–607, 2007.
31. A. Duran, D. Dutykh, and D. Mitsotakis. On the Galilean Invariance of Some Nonlinear Dispersive Wave Equations. *Stud. Appl. Math.*, 131(4):359–388, nov 2013.
32. D. Dutykh, D. Clamond, P. Milewski, and D. Mitsotakis. Finite volume and pseudo-spectral schemes for the fully nonlinear 1D Serre equations. *Eur. J. Appl. Math.*, 24(05):761–787, 2013.
33. D. Dutykh and F. Dias. Water waves generated by a moving bottom. In A. Kundu, editor, *Tsunami and Nonlinear waves*, pages 65–96. Springer Verlag (Geo Sc.), 2007.
34. D. Dutykh and F. Dias. Tsunami generation by dynamic displacement of sea bed due to dip-slip faulting. *Mathematics and Computers in Simulation*, 80(4):837–848, 2009.
35. D. Dutykh and F. Dias. Influence of sedimentary layering on tsunami generation. *Computer Methods in Applied Mechanics and Engineering*, 199(21-22):1268–1275, 2010.
36. D. Dutykh and H. Kalisch. Boussinesq modeling of surface waves due to underwater landslides. *Nonlin. Processes Geophys.*, 20(3):267–285, may 2013.
37. D. Dutykh, T. Katsaounis, and D. Mitsotakis. Finite volume schemes for dispersive wave propagation and runup. *J. Comput. Phys.*, 230(8):3035–3061, apr 2011.
38. D. Dutykh and D. Mitsotakis. On the relevance of the dam break problem in the context of nonlinear shallow water equations. *Discrete and Continuous Dynamical Systems - Series B*, 13(4):799–818, 2010.
39. D. Dutykh, D. Mitsotakis, S. A. Beisel, and N. Y. Shokina. Dispersive waves generated by an underwater landslide. In E. Vazquez-Cendon, A. Hidalgo, P. Garcia-Navarro, and L. Cea, editors, *Numerical Methods for Hyperbolic Equations: Theory and Applications*, pages 245–250. CRC Press, Boca Raton, London, New York, Leiden, 2013.
40. D. Dutykh, R. Poncet, and F. Dias. The VOLNA code for the numerical modeling of tsunami waves: Generation, propagation and inundation. *Eur. J. Mech. B/Fluids*, 30(6):598–615, 2011.
41. K. S. Erduran, S. Ilic, and V. Kutija. Hybrid finite-volume finite-difference scheme for the solution of Boussinesq equations. *Int. J. Numer. Meth. Fluids*, 49:1213–1232, 2005.
42. J. Fenton. A ninth-order solution for the solitary wave. *J. Fluid Mech*, 53(2):257–271, 1972.
43. E. D. Fernandez-Nieto, F. Bouchut, D. Bresch, M. J. Castro-Diaz, and A. Mangeney. A new Savage-Hutter type models for submarine avalanches and generated tsunami. *J. Comput. Phys.*, 227(16):7720–7754, 2008.
44. A. G. Filippini, S. Bellec, M. Colin, and M. Ricchiuto. On the nonlinear behaviour of Boussinesq type models: Amplitude-velocity vs amplitude-flux forms. *Coastal Engineering*, 99:109–123, 2015.
45. J.-M. Ghidaglia, A. Kumbaro, and G. Le Coq. Une méthode volumes-finis à flux caractéristiques pour la résolution numérique des systèmes hyperboliques de lois de conservation. *C. R. Acad. Sci. I*, 322:981–988, 1996.
46. G. Golub and C. Van Loan. *Matrix Computations*. J. Hopkins University Press, 3rd ed. edition, 1996.
47. A. E. Green and P. M. Naghdi. A derivation of equations for wave propagation in water of variable depth. *J. Fluid Mech.*, 78:237–246, 1976.
48. S. T. Grilli and P. Watts. Modeling of waves generated by a moving submerged body. Applications to underwater landslides. *Engineering Analysis with boundary elements*, 23:645–656, 1999.
49. C. B. Harbitz, F. Lovholt, G. Pedersen, S. Glimsdal, and D. G. Masson. Mechanisms of tsunami generation by submarine landslides - a short review. *Norwegian Journal of Geology*, 86(3):255–264, 2006.
50. A. Harten. ENO schemes with subcell resolution. *J. Comput. Phys*, 83:148–184, 1989.
51. A. Harten and S. Osher. Uniformly high-order accurate nonscillatory schemes. I. *SIAM J. Numer. Anal.*, 24:279–309, 1987.
52. N. J. Higham. *Accuracy and Stability of Numerical Algorithms*. SIAM Philadelphia, 2nd ed. edition, 2002.

53. H. Kalisch. Stability of solitary waves for a nonlinearly dispersive equation. *Discrete and Continuous Dynamical Systems*, 10:709–717, 2004.
54. G. S. Khakimzyanov, D. Dutykh, and Z. I. Fedotova. Dispersive shallow water wave modelling. Part III: Model derivation on a globally spherical geometry. *Commun. Comput. Phys.*, 23(2):315–360, 2018.
55. G. S. Khakimzyanov, D. Dutykh, Z. I. Fedotova, and D. E. Mitsotakis. Dispersive shallow water wave modelling. Part I: Model derivation on a globally flat space. *Commun. Comput. Phys.*, 23(1):1–29, 2018.
56. N. E. Kolgan. Finite-difference schemes for computation of three dimensional solutions of gas dynamics and calculation of a flow over a body under an angle of attack. *Uchenye Zapiski TsaGI [Sci. Notes Central Inst. Aerodyn]*, 6(2):1–6, 1975.
57. P. L.-F. Liu, P. Lynett, and C. E. Synolakis. Analytical solutions for forced long waves on a sloping beach. *J. Fluid Mech.*, 478:101–109, 2003.
58. M. S. Longuet-Higgins and J. Fenton. On the Mass, Momentum, Energy and Circulation of a Solitary Wave. II. *Proc. R. Soc. A*, 340(1623):471–493, 1974.
59. J. W. S. Lord Rayleigh. On Waves. *Phil. Mag.*, 1:257–279, 1876.
60. P. A. Madsen, H. B. Bingham, and H. A. Schaffer. Boussinesq-type formulations for fully nonlinear and extremely dispersive water waves: derivation and analysis. *Proc. R. Soc. Lond. A*, 459:1075–1104, 2003.
61. P. A. Madsen and H. A. Schaffer. A review of Boussinesq-type equations for surface gravity waves. *Adv. Coastal Ocean Engng*, 5:1–94, 1999.
62. P. A. Madsen, H. A. Sorensen, and H. A. Schaffer. Surf zone dynamics simulated by a Boussinesq-type model. Part I. Model description and cross-shore motion of regular waves. *Coastal Engineering*, 32:255–287, 1997.
63. O. Nwogu. Alternative form of Boussinesq equations for nearshore wave propagation. *J. Waterway, Port, Coastal and Ocean Engineering*, 119:618–638, 1993.
64. E. A. Okal. Seismic Parameters Controlling Far-field Tsunami Amplitudes: A Review. *Natural Hazards*, 1:67–96, 1988.
65. E. A. Okal and C. E. Synolakis. A theoretical comparison of tsunamis from dislocations and landslides. *Pure and Applied Geophysics*, 160:2177–2188, 2003.
66. E. A. Okal and C. E. Synolakis. Source discriminants for near-field tsunamis. *Geophys. J. Int.*, 158:899–912, 2004.
67. P. J. Olver. *Applications of Lie groups to differential equations*, volume 107 (2nd e of *Graduate Texts in Mathematics*. Springer-Verlag, 1993.
68. F. Pascal. *Sur des méthodes d'approximation effectives et d'analyse numérique pour les équations de la mécanique de fluides*. Habilitation à diriger des recherches, Université de Paris-Sud, 2002.
69. E. Pelinovsky and A. Poplavsky. Simplified model of tsunami generation by submarine landslides. *Physics and Chemistry of the Earth*, 21(12):13–17, 1996.
70. D. H. Peregrine. Long waves on a beach. *J. Fluid Mech.*, 27:815–827, 1967.
71. J. Sandee and K. Hutter. On the development of the theory of the solitary wave. A historical essay. *Acta Mechanica*, 86:111–152, 1991.
72. F. Serre. Contribution à l'étude des écoulements permanents et variables dans les canaux. *La Houille blanche*, 8:374–388, 1953.
73. L. F. Shampine and M. W. Reichelt. The MATLAB ODE Suite. *SIAM J. Sci. Comput.*, 18:1–22, 1997.
74. G. Söderlind. Digital filters in adaptive time-stepping. *ACM Trans. Math. Software*, 29:1–26, 2003.
75. G. Söderlind and L. Wang. Adaptive time-stepping and computational stability. *J. Comp. Appl. Math.*, 185(2):225–243, 2006.
76. C. E. Synolakis. The runup of solitary waves. *J. Fluid Mech.*, 185:523–545, 1987.
77. C. E. Synolakis and E. N. Bernard. Tsunami science before and beyond Boxing Day 2004. *Phil. Trans. R. Soc. A*, 364:2231–2265, 2006.

78. S. Tinti, E. Bortolucci, and C. Chiavettieri. Tsunami Excitation by Submarine Slides in Shallow-water Approximation. *Pure appl. geophys.*, 158:759–797, 2001.
79. V. V. Titov, F. I. Gonzalez, E. N. Bernard, M. C. Eble, H. O. Mofjeld, J. C. Newman, and A. J. Venturato. Real-Time Tsunami Forecasting: Challenges and Solutions. *Natural Hazards*, 35:41–58, 2005.
80. M. I. Todorovska, A. Hayir, and M. D. Trifunac. A note on tsunami amplitudes above submarine slides and slumps. *Soil Dynamics and Earthquake Engineering*, 22:129–141, 2002.
81. E. F. Toro. *Riemann Solvers and Numerical Methods for Fluid Dynamics*. Springer, Berlin, Heidelberg, 2009.
82. F. Ursell. The long-wave paradox in the theory of gravity waves. *Proc. Camb. Phil. Soc.*, 49:685–694, 1953.
83. B. van Leer. Towards the ultimate conservative difference scheme V: a second order sequel to Godunov' method. *J. Comput. Phys.*, 32:101–136, 1979.
84. B. van Leer. Upwind and High-Resolution Methods for Compressible Flow: From Donor Cell to Residual-Distribution Schemes. *Commun. Comput. Phys.*, 1:192–206, 2006.
85. P. Watts, F. Imamura, and S. T. Grilli. Comparing model simulations of three benchmark tsunami generation cases. *Science of Tsunami Hazards*, 18(2):107–123, 2000.
86. T. Y. Wu. Long Waves in Ocean and Coastal Waters. *Journal of Engineering Mechanics*, 107:501–522, 1981.
87. T. Y. T. Wu. Generation of upstream advancing solitons by moving disturbances. *J. Fluid Mech.*, 184:75–99, 1987.
88. Y. Xing and C.-W. Shu. High order finite difference WENO schemes with the exact conservation property for the shallow water equations. *J. Comput. Phys.*, 208:206–227, 2005.
89. J. Yang. *Nonlinear Waves in Integrable and Nonintegrable Systems*. Society for Industrial and Applied Mathematics, Philadelphia, jan 2010.
90. J. A. Zelt. The run-up of nonbreaking and breaking solitary waves. *Coastal Engineering*, 15:205–246, 1991.
91. J. G. Zhou, D. M. Causon, D. M. Ingram, and C. G. Mingham. Numerical solutions of the shallow water equations with discontinuous bed topography. *Int. J. Numer. Meth. Fluids*, 38:769–788, 2002.

Laboratory Modeling of Resonance Phenomena in the Long Wave Dynamics

Nizar Abcha, Efim Pelinovsky and Ira Didenkulova

Abstract Two sets of experiments in a wave flume to demonstrate resonance phenomena in laboratory conditions have been performed. The first set was performed to investigate nonlinear wave run-up on the beach. It is revealed that under certain wave excitation frequencies, a significant increase in run-up amplification is observed Ezersky et al. (Nonlin Processes Geophys 20:35, 2013, [1]). It is found that this amplification is due to the excitation of resonant mode in the region between the shoreline and wave maker. The second set of experiments was performed to model an excitation of localized mode (edge waves) by breaking waves propagating towards shoreline. It is shown that the excitation of edge waves is due to parametric instability similar to pendulum with vibrating point of suspension. The domain of instability in the plane of parameters (amplitude—frequency) of surface wave is found. It was found that for amplitude of surface wave slightly exceeding the threshold, the amplitude of edge wave grows exponentially with time, whereas for the large amplitude, the wave breaking appears and excitation of edge wave does not occur. It was shown that parametric excitation of edge wave can increase significantly (up to two times) the maximal run-up height.

Keywords Resonance · Edge waves · Run-up · Wave breaking · Turbulent viscosity

---

N. Abcha (✉)
Normandie Université, UNICAEN, UNIROUEN, CNRS, UMR 6143, M2C, 14000 Caen, France
e-mail: nizar.abcha@unicaen.fr

E. Pelinovsky · I. Didenkulova
Nizhny Novgorod State Technical University n.a. R.E. Alekseev,
603950 Nizhny Novgorod, Russia

E. Pelinovsky
National Research University – Higher School of Economics, 603950 Nizhny Novgorod, Russia

E. Pelinovsky
Institute of Applied Physics, 603950 Nizhny Novgorod, Russia

I. Didenkulova
Department of Marine Systems, Tallinn University of Technology, 12618 Tallinn, Estonia

N. Abcha et al. (eds.), *Nonlinear Waves and Pattern Dynamics*,
https://doi.org/10.1007/978-3-319-78193-8_2

1 Introduction

The resonance phenomena play significant role in the run-up amplification and lead to different physical effects for tsunamis waves, leading to the long-time weakly damped water oscillations, in coastal areas. Recent huge tsunamis demonstrate the nonlinear behavior on the coast leading to the strong impact. It was also revealed recently that the number of abnormally large and suddenly appearing waves (rogue waves) observed in the coastal zone is sufficiently larger than Gaussian statistics predicts [2, 3]. Analysis of tsunami records showed that reflections due to bottom topography may result in appearance of resonant mode in coastal zone, see for instance [4]. The study of the tsunami and coastal rogue waves is based on the nonlinear theory of shallow water [5, 6]. To characterize the impact of waves on coastal infrastructure, a lot of experimental and analytical studies of run-up processes have been published [7–10].

Recently, [1, 11] on the basis of numerical simulations of the nonlinear shallow water equations, the existence of resonance effects in the process of the long wave run-up was pointed out.

It should be noted that such resonance effect was predicted in the framework of linear theory [12]. The main result [11] is that at a certain frequency of the waves there exists a significant increase in the run-up amplitude. The maximal run-up height can be 50 times greater than the free surface oscillation amplitude used as the boundary conditions in the numerical simulation. Also it was established that the wave period for which maximal run-up amplification appears depends on the slope of the bottom and the depth of water where the waves are excited. This period is much larger than the “natural period”—time needed for perturbations to run from the point of excitation to the shoreline and return back. Results obtained in [11] raise a lot of questions. That is why, we carried out a physical simulation of this process in the wave flume with an inclined bottom [1].

It is known that in the coastal zone, waves coming from the open sea can excite the so-called edge waves which are localized near the shore [13–15]. The edge wave field cannot be represented in the dimensional approximation: edge waves propagate along coastal line and their amplitude decreases in offshore direction.

Characteristics of linear and nonlinear edge waves were studied in numerous theoretical papers [16–21]. Characteristics of edge wave are also investigated in marine experiments and numerical simulations. These studies focus on the investigation of edge wave excitation in coastal zone and correlations between characteristics of edge waves and the spectra of waves propagating toward the shore. The edge waves localized at the shoreline are responsible for the erosion of the shore [22–24]. Therefore, the investigation of the generation mechanisms of edge waves and the study of their run-up are the important problems of wave—coastal zone interaction. One of the edge wave generating mechanisms is discussed here. This mechanism is linked to the parametric excitation of standing edge wave with frequency $\omega/2$ by surface wave with frequency ω propagating perpendicular to the shoreline. Such mechanism was investigated theoretically [22, 25] and it was identified in marine experiments in the coastal zone [26]. The laboratory experiments on parametric excitation of edge wave are described in [27]. It should be noted that in this laboratory experiments, wave breaking was absent meanwhile breaking effects are important in natural conditions. Principal question of the influence of wave breaking on parametric edge wave generation is not investigated yet. Exactly this problem is investigated in our chapter. We concentrate on the influence of wave breaking on characteristics of the edge waves and on run-up amplification occurred in this case.

The chapter is organized as follows. Section 1 presents an introduction, Sect. 2 is devoted to the description of the experimental setup, Sect. 3 presents the results of measurements of resonance phenomena and excitation of edge wave. In Sect. 4, we discuss the experimental data and present a theoretical model to describe the modes of parametric excitation of edge waves and Sect. 5, conclusion.

2 Experimental Setup

Experiments were realized in a long hydrodynamic flume. This flume has a length of 18 m, a width of 0.5 m. The flume is equipped with a wave maker controlled by a computer. To simulate an inclined bottom, a PVC plate with thickness of 1 cm is used. The plate is placed at different angles relative to the horizontal bottom of the flume in the vicinity of the wave maker (Fig. 1).

Three series of experiments have been performed for water depth h_0 near the wave maker and length L: (i) $h_0 = 0.245$ m, $L = 1.458$ m, $\tan\alpha = 0.168$; (ii) $h_0 = 0.26$ m, $L = 1.35$ m, $\tan\alpha = 0.192$ and (iii) $h_0 = 0.32$ m, $L = 1.215$ m, $\tan\alpha = 0.263$. Three resistive probes (P1, P2, P3) are used to measure a displacement of the water surface (Fig. 1). P1 is placed at the distance of 1 cm from the wave maker. P2 and P3 allow us to record run-up at two different points on the plate. Besides, run-up characteristics are determined by processing a movie which is shot by a high-speed

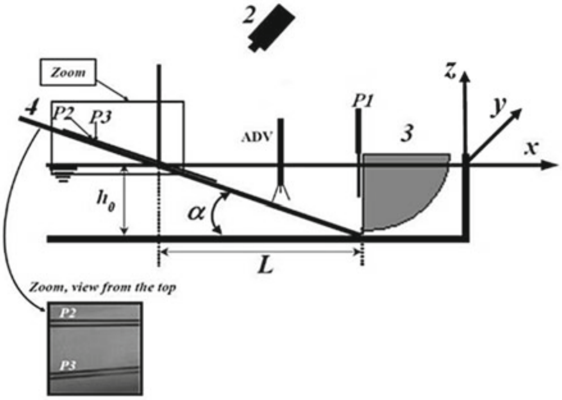

Fig. 1 The experimental setup: resistive probes: vertical probe (P1) and inclined probes (P2, P3), high-speed video camera (*2*), wave maker (*3*), inclined bottom (*4*), and the acoustic Doppler Velocimeter (ADV)

camera mounted as shown in Fig. 1. These characteristics are determined within a precision of 2%.

3 Results of Measurements

3.1 Resonance Phenomena

In Fig. 2 are shown the frequency dependence of the amplitude of free surface displacement near the wave maker (a), maximal run-up (R), and coefficient of run-up amplification ($C = R/a$) for the slope of the bottom $\tan\alpha = 0.263$. It is remarkable that amplitude of free surface displacement has peaks at frequencies $f_1 = 0.44$ Hz and $f_2 = 0.78$ Hz. They are the resonant frequencies of the system. The maximal run-up does not have sharp peaks, only a small increase of R in the vicinity of f_1 and f_2 is observed (Fig. 2b). The coefficient of run-up amplification (Fig. 2c) increases very sharply in the vicinity of $f_3 = 0.28$ Hz and $f_4 = 0.63$ Hz. It is evident that maximal amplification of run-up is observed for frequencies corresponding to the minimal amplitude a. In the vicinity of the wave maker, the amplitude is sufficiently small and the signal is very noisy. That is why the coefficient of run-up amplification requires rather delicate measurements of free surface displacement: a band-pass filter was used to filter the signal of probe in order to measure the amplitude of harmonic corresponding to wave maker forcing.

Amplification coefficient C was investigated for three bottom inclinations. Frequencies of maximal amplification depend on angle α and to compare results obtained for different angles α, the nondimensional frequency F was introduced:

$$F = \frac{f}{f_0},\ f_0 = K^{-1}\sqrt{g/h_0}\,tan\,\alpha, \tag{1}$$

where g is for acceleration of gravity, h_0 is for water depth near wave maker, and $K = 5.23$.

In Fig. 3 are shown the nondimensional frequencies of maximal run-up amplification $F = F_1 = 1$ for different angle α where they coincide very precisely. The coefficient of maximal amplification, corresponding to the frequency $F_1 = 1$ is approximately the same for different inclinations: $C \approx 20 – 25$. The second peak of run-up amplification coefficient is observed for frequency $F_2 = (2.2 – 2.3)\,F_1$. Nondimensional frequency F_2 slightly depends on bottom slope; small peak is observed also for frequency $F_3 \approx 3.5F_1$.

It should be noted that for our experimental conditions, linear run-up is observed for small frequencies of wave excitation $F < 2$. While for higher excitation frequencies $F > 2$ run-up occurs after the wave breaking event. The wave breaking does not prevent precise determination of maximal run-up position. Except high frequencies

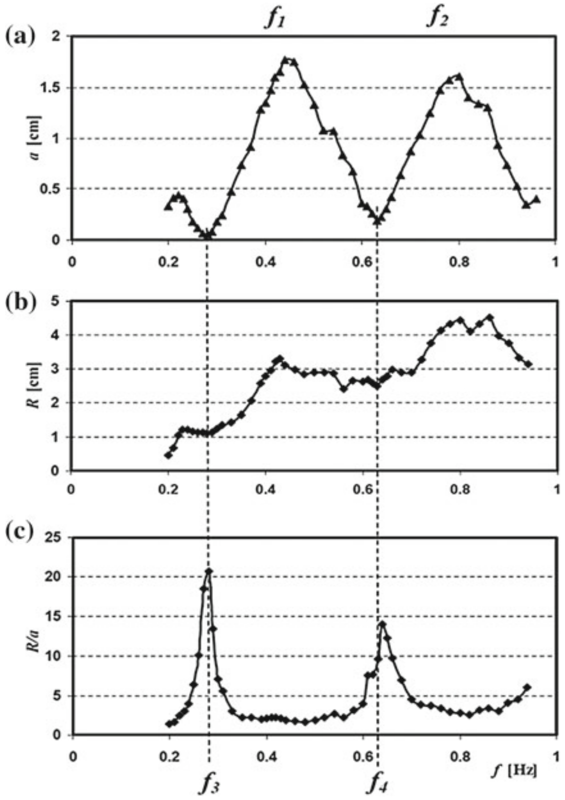

Fig. 2 Dependence of amplitude of free surface displacement on frequency (resonance curve) (**a**), maximal run-up (**b**) and amplification of run-up (ration of maximal run-up and amplitude of surface wave) (**c**) for slope $\tan \alpha = 0.263$

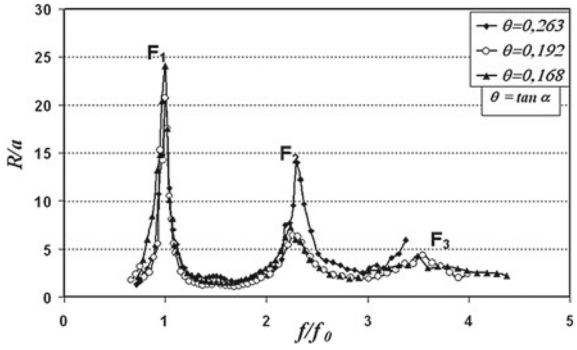

Fig. 3 Dependence of run-up amplification on normalized frequency for different bottom slopes. Frequency. $f_0 = 5.23\sqrt{g/H}\tan\alpha$

$F > 3$ the wave front on a sloping beach was one dimensional and maximal run-up did not depend on coordinate along direction perpendicular to axis x.

3.2 Parametric Excitation of Edge Waves

Wave maker allows us to excite harmonic wave propagating towards the shore with controlled amplitude and frequency and to study the characteristics of edge waves using simultaneous measurements of the amplitude of free surface displacement near the wave maker and run-up height.

The subharmonic instability described above is investigated in the flume for different values of (a_L, f), where a_L is an amplitude of surface waves in the vicinity of the wave maker, $a_L \approx a_0$, and f is the frequency of the wave maker. To understand if instability occurs or not, signals from probes P2 and P3 were analyzed. Before each experiment, we waited certain time during which all the perturbations in the flume decayed, then the wave maker started working. An example of signals from P2 and P3 is shown in Fig. 4a. At the beginning of perturbation, evolution time series are presented in Fig. 4b. One can find that at the beginning of perturbation evolution, $50\ \text{s} < t < 55\ \text{s}$ time series have a frequency of wave maker and the same phase. When instability arises Fig. 4c, $85\ \text{s} < t < 90\ \text{s}$ the period doubling is observed and phase difference between signals recorded by probes P2 and P3 is approximately π. The power frequency spectra for two surface wave regimes are shown in Fig. 5. The first spectrum (Fig. 5a) is the FFT of the beginning of perturbation evolution time series. This is a spectrum in absence of wave breaking, where the first peak indicates the edge wave frequency and the second peak indicates the surface elevation frequency. The second spectrum (Fig. 5b) is plotted in presence of breaking waves and indicates the suppression of the peak for the edge wave frequency.

Water oscillations have been registered by camera. Analysis of movies showed that subharmonic represents mode: maxima of horizontal displacement (antinodes) are near the lateral walls of the channel, zeros of displacement (node) are in the middle of the channel. This mode is a superposition of two edge waves propagating in opposite directions with spatial period twice larger than the width of the flume. In Fig. 6 are shown the snapshots of water surface over the time interval equal to a half of the edge wave period.

Instability of subharmonic begins by exponential growth of small perturbations. To describe the instability in the system, partition of plane (a_L, f) into regions with different stability was performed. The results are presented in Fig. 7.

Instability occurs if the frequency f is close to double frequency of edge wave. Curve 1 represents a border of supercritical instability occurring for points above this curve: generation of edge waves starts from infinitely small perturbations if the amplitude of surface wave increases. If the amplitude of surface wave decreases from finite value, generation of edge wave is observed in small region 3 between curves 1 and 2. It is subcritical instability that is observed when we start from the regime of supercritical instability and decrease the amplitude of surface wave.

Regimes shown in Fig. 7 occur for two qualitatively different conditions of wave excitation. The regions corresponding to the different conditions are schematically shown by boxes (I) and (II). In the region (I) for wave excited by wave maker and propagating towards coast-line, wave breaking (plunging) occurs. In region (II)

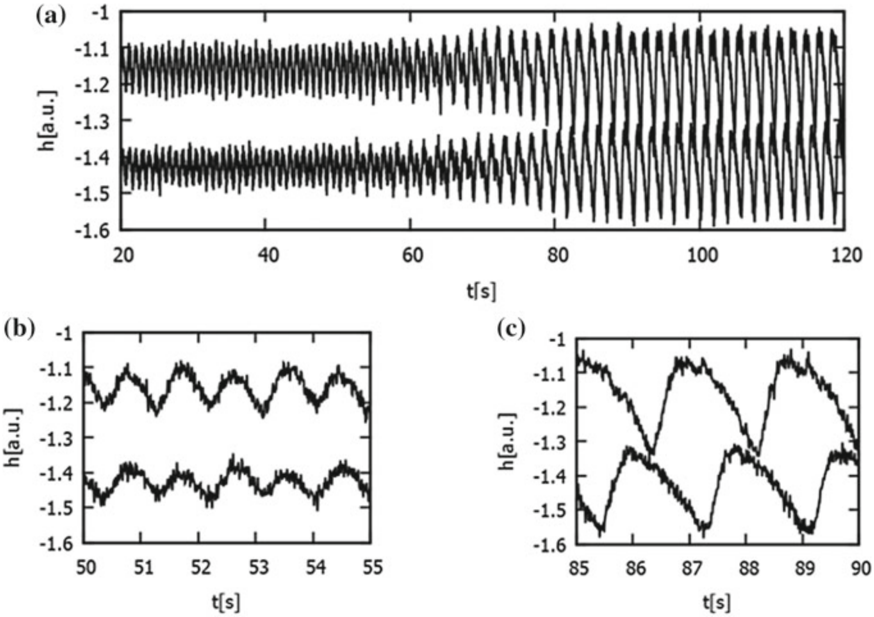

Fig. 4 Temporal evolution of wave instability developing with $f = 1.08$ Hz, $a_L = 0.66$ cm: **a** time series of natural perturbations recorded by probes P2 and P3; **b** zoom of the time series recorded during the time interval 50 s < t < 55 s, and **c** during the time interval 85 s < t < 90 s

wave breaking is absent. Processing of movies obtained by high-speed video camera shows that such excitation occurs when wave breaking parameter $Br > 0.9$. Under wave breaking parameter, we mean $Br = U_{max}^2/gR$, where U_{max} is the maximal flow velocity, and R is the maximal wave run-up height on the shore [17].

Amplitude of edge waves bifurcating from the zero value grows continuously with the amplitude of surface waves a_L near the wave maker. Increase in the wave amplitude leads to generation of wave breaking at the shoreline. When wave breaking is developed, subharmonic instability is suppressed.

The run-up amplitudes before and after the development of parametric instability are measured. The results are shown in Fig. 8, which demonstrates the dependence of run-up amplitude due to edge waves on amplitude of run-up of surface waves, exciting parametric instability. For small amplitude of parametric excitation, one can see that amplitude of run-up is doubled whereas amplification decreases for large amplitude of excitation when wave breaking appears.

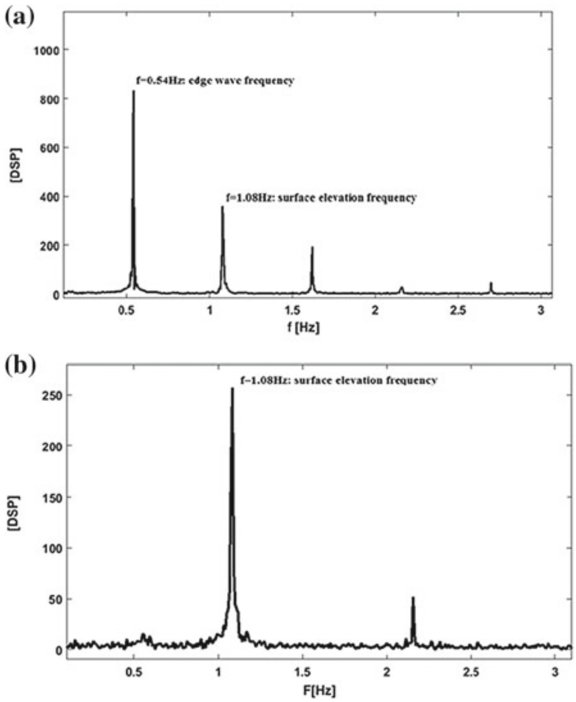

Fig. 5 Power spectrum frequency: **a** in absence of breaking waves: the first peak indicates the edge wave frequency, while the second peak indicates the surface elevation frequency; **b** in presence of breaking waves: the peak for the edge wave frequency is suppressed

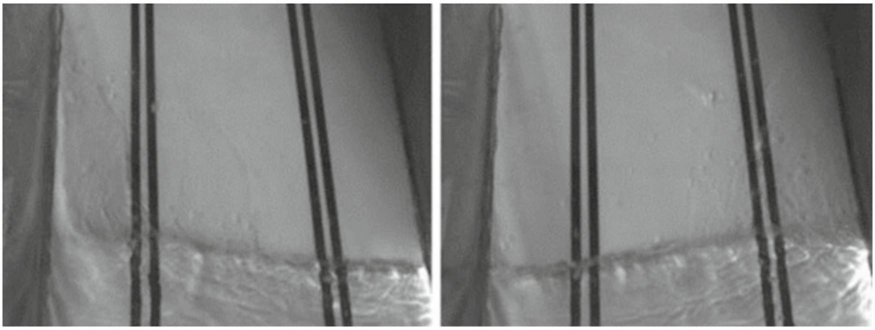

Fig. 6 Snapshots of water surface over the time interval equal to a half of the edge wave period (approximately 1 s), $f = 1.06$ Hz, $a_L = 1.3$ cm

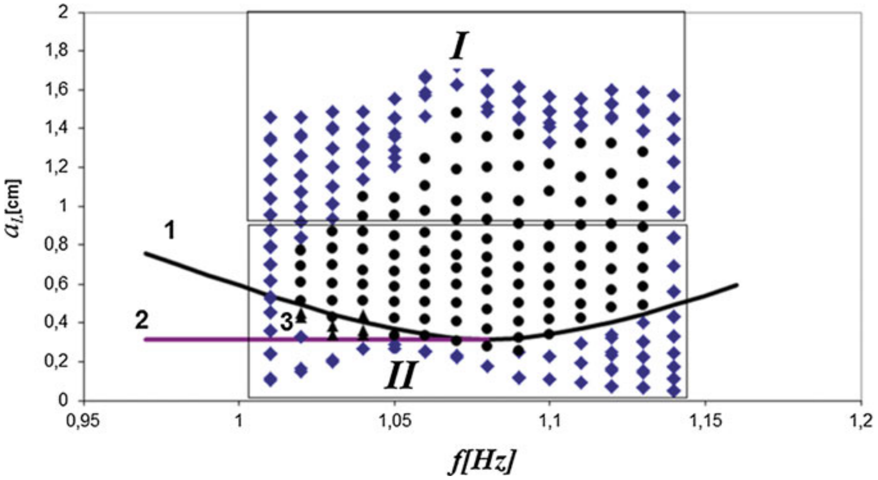

Fig. 7 Partition of a (a_L, f) plane into different stability regions of the system; circles correspond to a parametric instability, diamonds correspond to stability regimes, and triangles are for the regime of subcritical instability

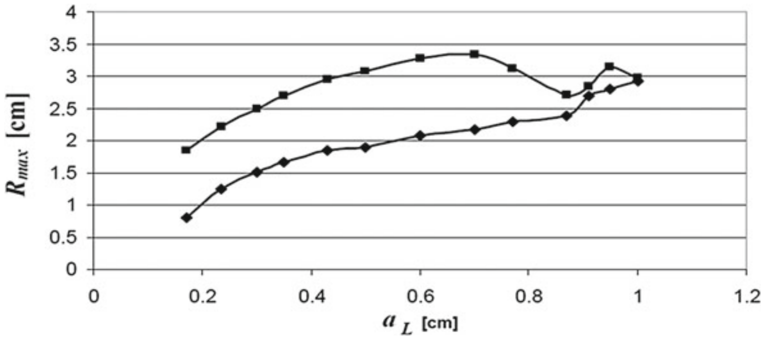

Fig. 8 Dependences of run-up amplitude on wave amplitude near wave maker ($f = 1.06$ Hz) without parametric excitation of edge waves (diamonds) and with parametric excitation of edge waves (squares)

4 Discussion of Experimental Results

4.1 Resonance Phenomena

To study frequency dependence of run-up amplification more precisely, the spatial structures of the free surface oscillations occurring at frequencies corresponding to the resonant frequencies of the system (f_1, f_2) and at frequencies of maximum run-up amplification (f_3, f_4) have been investigated. The results are shown in Fig. 9 for bottom slope $\tan \alpha = 0.168$. Amplitude and phase of free surface displacement

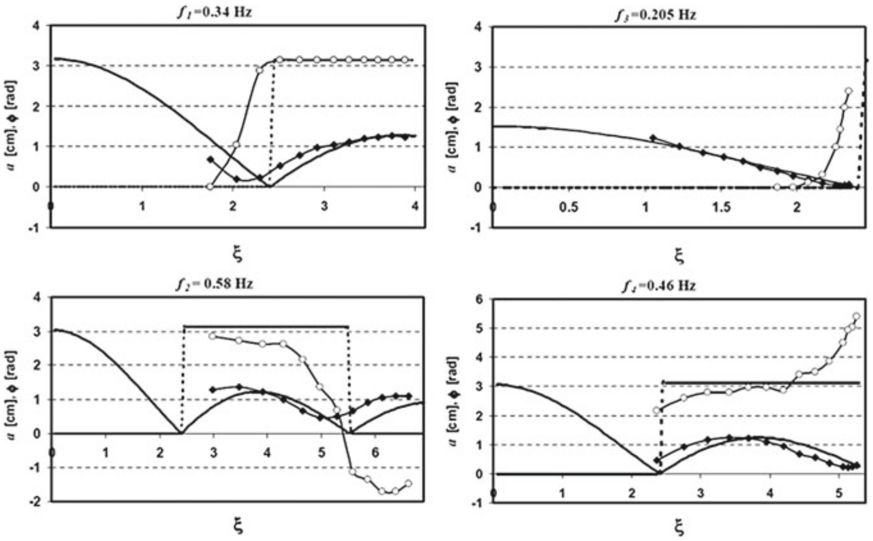

Fig. 9 Comparison of the experimental results of amplitude (diamonds) and phase (circles) with theoretical results of amplitude (thick solid lines) and phase (thick dashed lines) obtained from the equation $\xi = (4\omega^2 x/g.\tan\alpha)^{1/2}$, $\tan\alpha = 0.168$; end of the horizontal axis corresponds to the position of the wave maker edge

are shown by diamonds and circles. Experimental data are compared with the well-known analytical solution for free surface displacement η,

$$\eta = J_0\left(\sqrt{\frac{4\omega^2}{g\,tan\,\alpha}}\right)\cos(\omega t) \tag{2}$$

This solution was obtained in shallow water with linear change in the water depth h_0: $h_0 = x\tan\alpha$. Theoretical dependences are shown in Fig. 9 by thick lines. The amplitude is chosen as $a = |J_0|$, and $\phi = 0$ if $J_0 > 0$ and $\phi = \pi$ if $J_0 < 0$. One can find in Fig. 9 that in the experiment, the amplitude does not go to zero and phase changes smoothly for all frequencies. Note that frequencies of maximal run-up amplification ($f_3 = 0.205$ Hz, $f_4 = 0.46$ Hz) correspond to spatial modes having minimal amplitudes near the wave maker; resonance frequencies (f_1,f_2) have maximum amplitude of free surface displacement near the wave maker. It should be noted that according to solution (2), frequencies of maximal run-up amplification correspond to the spatial modes with boundary condition $\eta|_{x=L} = 0$, and resonant frequencies correspond to mode with boundary conditions:

$$\left.\frac{\partial\eta}{\partial x}\right|_{x=L} \tag{3}$$

In other words, if one uses linear solution (2), the coefficient of run-up amplification in this approximation would be infinite: $a = 0$ at $x = L$. Experimental amplitude is small, but finite. Comparison of curves presented in Fig. 9 shows that difference between theoretical solution and experimental data increase with frequency of excitation. For example, these differences are much more for f_2 than for f_3.

Let us compare the experimental results with numerical simulations [11]. The numerical simulations of wave run-up were carried out for fixed amplitude of free surface displacement as a boundary condition at $x = L$. In the experiment, unlike the numerical calculations, it is not possible to generate waves with fixed amplitude at a definite coordinate. Instead, the simultaneous measurements of the free surface displacement in the vicinity of wave maker and maximal run-up have been performed. In our experiment, the frequencies of maximal run-up amplification are very close to those that were obtained in the numerical calculation. We estimated the frequencies of the first peak as: $f_3 = K^{-1}\sqrt{g/h_0}\,tan\,\alpha,\ K \cong 5.23$; in [11]. Second peak f_4 in the experimental frequency dependence of run-up is more visible than in numerical simulation [11]. Authors [11] did not give any estimates of the second peak frequency, but if one uses their data it is possible to conclude that the frequency of the second peak is 2.5–2.7 times the frequency of the first one. In our experiments, frequency of the second peak exceeds the frequency of the first one in 2.2–2.3 times. Experimental values of frequencies $f_{3\text{-}4}$ practically coincide with frequencies of modes having nodes near the wave maker; numerical values exceed this frequency by 2.5% for all bottom inclinations. Authors [11] do not mention any dissipation of energy neither nonlinear parameter, which they use in numerical simulations. As for the coefficient of run-up amplification, the maximal value that was observed in experiment is $C = 20 - 25$, whereas in [11], this value reaches $C = 50 - 60$. The difference is apparently due to viscous dissipation, which is essential in our experiments.

4.2 Parametric Excitation of Edge Waves

Region of parameters corresponding to parametric excitation of edge waves was found experimentally. Using theoretical formula (4), we are able to estimate the threshold of parametric excitation of edge wave.

$$\frac{\partial b}{\partial t} = -\gamma b + hb^* + i\Delta b + (i\sigma - \rho)\, b\, |b|^2 \tag{4}$$

Here, γ is a wave decrement due to viscose dissipation, $h = a_0\omega^3 S(\alpha)/4g tan^2\alpha$, $S(\alpha)$ is a function of inclination angle α determined in [20], a_0 is for surface wave amplitude at $x = 0$, * means complex conjugation, $\Delta = \Omega - \omega/2$ is for detuning between wave frequency and frequency of external parametric forcing, σ is a nonlinear frequency shift, and ρ is a nonlinear damping coefficient.

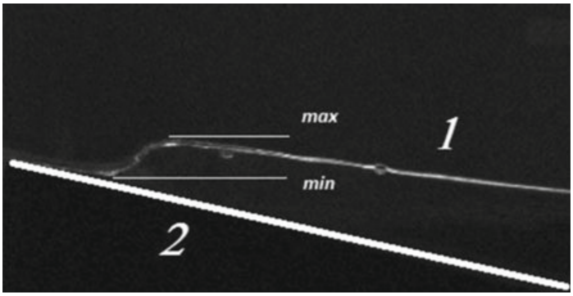

Fig. 10 Visualization of the free surface displacement: 1 is for the water surface, 2 is for the inclined bottom, max and min correspond to the maximum and minimum values of the free surface displacement

To estimate the threshold of parametric excitation of edge waves, we have to find eigenfrequency of the edge waves in the flume. The frequency of edge mode Ω_0 has minimum dissipation that is [28]:

$$\Omega_0 = \sqrt{g\pi \tan \alpha / L} \approx 3.41\,\text{rad/s}\, or\ f_0 = \Omega_0/2 \gg 0.54\,\text{Hz}. \tag{5}$$

To estimate the dissipation rate of harmonic edge wave, we investigate the time evolution of amplitude of edge wave after stopping the parametric excitation. Edge waves decay exponentially and we measured the decay constant γ, which is estimated as $\gamma = 0.1\ \text{s}^{-1}$. For the resonance condition $\Delta = 0$, parametric instability occurs when the wave amplitude exceeds the critical wave amplitude a_0:

$$a_0 = \gamma \frac{4g\beta^2}{\omega^3 S(\beta)} \approx 0.76\,\text{cm} \tag{6}$$

The theoretical value of the parametric instability threshold is calculated using displacement of free surface. To compare the experimental and theoretical values of threshold, we have to measure the displacement amplitude of the free surface of the liquid at $x = 0$ in the wave excited by the wave maker. As it was noted in several studies [5], this value has not been directly measured in experiments. We find the displacement amplitude using flow visualization by laser sheet. The visualization of the free surface displacement with frequency of wave maker was carried out in the center of the flume at a time preceding the development of parametric instability of edge waves. Example of visualization is shown in Fig. 10. Note that when the parametric instability threshold is determined, the wave breaking is absent for all frequencies and amplitudes of waves excited by the wave maker: threshold parameters of surface waves correspond to the region (II) in Fig. 7.

Image of free surface is obtained before development of parametric instability, when amplitude of edge wave is zero. To estimate the amplitude of the surface wave, the distance between maximum and minimum values of the free surface is divided by two (Fig. 10). Comparison of instability thresholds is presented in Fig. 11. Theoretical value is larger than experimental approximately by 30%.

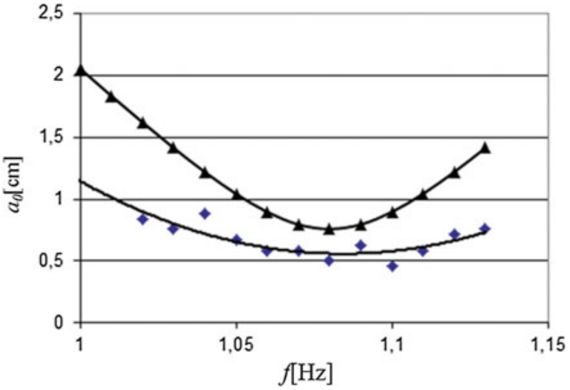

Fig. 11 Comparison of experimental and theoretical values of the instability threshold: triangles correspond to the theoretical formula, diamonds represent experimental data

It is important to note that even when the wave breaking of surface waves takes place, parametric excitation of edge waves occurs. Parametric generation is suppressed for large enough amplitude of surface wave. What is the physical mechanism that is responsible for such suppression? The wave breaking leads also to the appearance of non-regularity in surface wave: amplitude and phase of wave vary chaotically, periodic wave breaking leads to appearance of small-scale turbulence in the nearshore zone. We discuss the impact of these two physical mechanisms to the suppression of parametric instability.

The parametric wave excitation by the irregular oscillating field has been studied in [18, 29]. It was shown that chaotic amplitude and chaotic phase of external wave field caused increase in the threshold of parametric excitation and decrease in the amplitude of parametrically excited oscillations.

We verified if these results may be applied for explanation of decrease in the edge wave amplitude when breaking surface waves appear. For this purpose, we calculate amplitude and phase of surface wave. Surface wave excited by the wave maker may be presented as $\eta_m \cos(\omega t + \Phi)$, where η_m, is a slow varying amplitude, and Φ is a slow varying phase. To extract the amplitude and the phase of the signal, the Hilbert transformation is used:

$$\hat{\eta} = \frac{1}{\pi} PV \left[\int_{-\infty}^{+\infty} \frac{\eta(t,\tau)}{t-\tau} \right] = \eta_m \sin(\omega t + \varPhi), \tag{7}$$

where PV denotes the principal value of the integral. It is also possible to determine the wave amplitude and phase:

$$\eta(t) = Re\{a(t)\exp(i\omega t)\},\ a(t) = |a|\,e^{i\varPhi}, \tag{8}$$

where

$$|a| = \sqrt{\eta^2 + \hat{\eta}^2},\ \varPhi = \arctan\left(\frac{\hat{\eta}}{\eta}\right) - \omega t \tag{9}$$

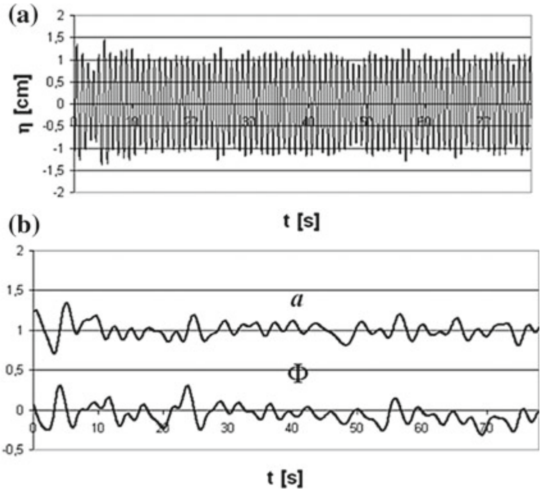

Fig. 12 **a** Time-series measured by P1 with $a_L = 1$ cm, $f = 1.06$ Hz; **b** nondimensional wave amplitude and phase obtained by the Hilbert transformation

Extracted amplitudes and phases for the time-series measured in presence of the surface wave breaking are shown in Fig. 12. The time-series itself is given in Fig. 12a, while the extracted amplitudes and phases are shown in Fig. 12b. The root mean square of phase and amplitude fluctuations for the intensive wave breaking ($a = 1.4$ cm) is

$$\sqrt{\langle \Phi^2 \rangle} \approx 0.1, \; \frac{\sqrt{\left\langle (a - \langle a \rangle)^2 \right\rangle}}{\langle a \rangle} \approx 0.1 \tag{10}$$

It is also possible to estimate the influence of chaotic phases and amplitudes on the parametric wave excitation. It has been revealed that chaotic phases decrease the effective amplitude of the external force [30]. Suppose, that the wave breaking leads to the Gaussian noise, then the corresponding decrease in the external forcing may be estimated as [30]

$$e^{-(\langle \Phi^2 \rangle)/2} \approx 0.995 \tag{11}$$

This small decrease in the effective external forcing cannot explain suppression of the parametric excitation for the wave breaking regime.

The influence of turbulence seems to be more important. Wave breaking generates turbulence and the intensity of turbulent velocity fluctuations increases with the surface wave amplitude. The turbulence leads to the appearance of turbulent shear stresses and eddy viscosity ν_{ed}. We measure experimentally some components of the kinematic turbulent energy in the water appearing on the background of edge wave (Fig. 13b). According to our measurements, the most important components of shear stresses are connected with longitudinal component V_x of turbulent fluctuations (Fig. 13b).

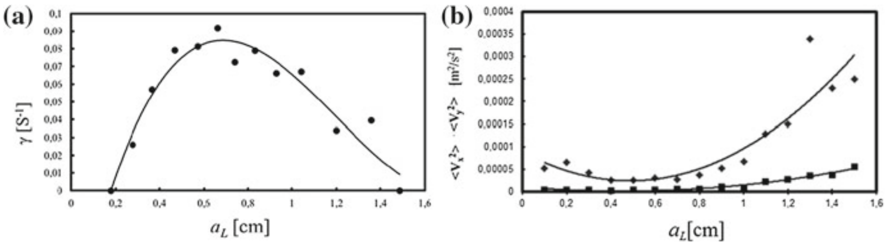

Fig. 13 **a** Dependence of the exponential index of parametric instability γ on the surface wave amplitude a_L, shown by the black dots; **b** dependence of the kinetic turbulent energy components on the surface wave amplitude a_L; V_x is shown by blue diamonds, while V_y is shown by black squares. Solid lines represent a fit to the experimental data

The eddy viscosity is proportional to kinetic energy of turbulence ν_{ed}. For the wave breaking case, it is possible to consider that ν_{ed} is proportional to a^2 (Fig. 13b). In this case, coefficient γ of the exponential decay in Eq. (4) has the following form: $\gamma = \gamma_0 + \gamma_1 a^2$, where γ_0 is the exponential decay of edge waves in the absence of wave breaking, and coefficient γ_1 is responsible for the dissipation of energy due to the eddy viscosity.

Since the external forcing μ grows linearly with the surface wave amplitude and the dissipation grows as the amplitude squared, the parametric instability is suppressed for large surface wave amplitudes. Exactly, this effect is observed in experiment when wave breaking occurs.

5 Conclusion

Amplification coefficients and frequencies, at which run-up amplification maxima are observed, correlate with results of numerical simulations. The most important conclusion is the existence of an abnormally large increase of the coefficient C due to the resonant modes: this coefficient becomes very large because of its determination: the amplitude at the mode node is taken as the amplitude of free surface displacement. This effect is very important for the explanation of rogue waves on the shore and for the prediction of tsunami run-up using the tide-gauge data. It is not sufficient to know the amplitude of free surface displacement in the nearshore zone. Each time, it is necessary to know if this value corresponds to the amplitude A of a propagating wave or to the amplitude a of a standing wave at a fixed point.

Second, parametric generation of edge waves is investigated for different regimes of surface wave propagation. It is shown that the threshold amplitude of parametric excitation is close to the theoretically calculated value.

It was found that for parametrically excited edge waves, there exists region of subcritical instability. In experiments hysteresis is observed: different regimes of edge wave excitation are observed for decreasing and increasing of surface wave amplitude. It should be noted that subcritical instability was not found in [20], although experimental conditions were very close to our experiments.

It is shown experimentally that increase in the surface wave amplitude leads to the appearance of wave breaking. The wave breaking regime does not prevent parametric generation of edge waves. Only the developed wave breaking can suppress parametric generation of edge waves. We compared two mechanisms of parametric instability suppression: phase non-regularity of the parametric force and generation of hydrodynamic turbulence. It was found that the most probable mechanism is the increase in the threshold of parametric excitation and suppression of parametric generation due to hydrodynamic turbulence appearing as a result of wave breaking.

Acknowledgements This work is dedicated to the memory of a dear friend and colleague Professor Alexander Ezersky, who sadly passed away after a long-lasting fight with the cancer. Until his last days, he tried to dedicate his time to work, the results of which are also presented in this Chapter. The present study was supported by the Russian state contract 5.5176.2017/8.9, Russian President Grant NSh-2685.2018.5, RFBR grant 17-05-00067 and ETAG project PUT1378. ID and EP also thank the University of Caen for its visitor program, who allowed this fruitful collaboration.

References

1. Ezersky A., Abcha N. and Pelinovsky E. Physical simulation of resonant wave run-up on a beach. Nonlin. Processes Geophys. 2013;20:35.
2. Nikolkina I. and Didenkulova I. Rogue waves in 2006–2010. Natural Hazards and Earth System Sciences. 2011;11:2913.
3. Nikolkina I. and Didenkulova I. Catalogues of rogue waves reported in media in 2006–2010. Natural Hazards. 2012;61:989.
4. Neetu S., Suresh I., Shankar R., Nagarajan B. and Sharma R. Trapped waves of the 27 November 1945 tsunami: observations and numerical modeling, Natural Hazards and Earth System Sciences. 2011;59:1609.
5. Didenkulova I. and Pelinovsky E. Rogue waves in nonlinear hyperbolic systems (shallow-water framework). Nonlinearity. 2011;24:R1-R18.
6. Slunyaev A., Didenkulova I. and Pelinovsky E. Rogue waters. Contemporary Physics. 2011;52:571.
7. Carrier G.F., Wu T.T. and Yeh H. Tsunami run-up and draw-down on a plane beach. J. Fluid Mech. 2003;475:79.
8. Pelinovsky E. Nonlinear dynamics of tsunami waves. Institute of Applied Physics, Nizhny Novgorod, (in Russian) 1982.
9. Pelinovsky E. and Mazova R. Exact analytical solutions of nonlinear problems of tsunami wave run-up on slopes with different profiles. Natural Hazards and Earth System Sciences. 1992;6:227.
10. Synolakis C. The runup of solitary waves. J. Fluid Mech. 1987;185:523.
11. Stefanakis T.S., Dias F. and Dutykh D. Local run-up amplification by resonant wave interaction. Phys. Rev. Lett. 2011;107:124502.
12. Antuono M. & Brocchini M. Solving the nonlinear shallow-water equations in physical sense. J. Fluid Mech. 2010;643:207.
13. Abcha N., Zhang T., Ezersky A., Pelinovsky E. and Didenkulova I. Subharmonic parametric exitation of edge waves by breaking surface waves. Nonlin. Processes Geophys. 2017;24:157.
14. Johnson R.S.. Some contributions to the theory of edge waves. J. Fluid Mech. 2005;524:81.
15. Johnson R.S. Edge waves: theories past and present. Phyl. Trans. R. Soc. A. 2007;365:2359.

16. Akylas A. R. Large-scale modulations of edge waves. J. Fluid Mech. 1983;132:197.
17. Dubinina V.A., Kurrhin A.A., Pelinovsky E.N. and Poloukhina O.E. Weakly nonlinear periodic Stokes edge waves. Izvestiya, Atmospheric and Oceanic Physics. 2004;40:464.
18. Grimshaw R. Edge waves: a long –wave theory for oceans of finite depth. J. Fluid Mech. 1974;62;775.
19. Kurkin A. and Pelinovsky E. Focusing of edge waves above sloping beach. European Journal of Mechanics—B/Fluid. 2002;21:561.
20. Minzoni A.A. and Whitham G.B. On the excitation of edge waves on beaches. J. Fluid Mech. 1977;79:273.
21. Pelinovsky E. N.., Polukhina O. and Kurkin A. Rogue edge waves in the ocean. European Physical Journal Special Topics. 2010;185:35.
22. Blondeaux P. and Vittori G. The nonlinear excitation of synchronous edge waves by a monochromatic wave normally approaching a plane beach. J. Fluid Mech.1995;301:251.
23. Carter R.W.G. An introduction to the physical, ecological and cultural systems of coastlines. ACADEMIC PRESS, London, San Diego. 2002: 620 p.
24. Coco G., Burnet T.K. and Werner B.T. Test of self-organisation in beach cusp.. J. Geoph. Res. 2003;108: https://doi.org/10.1029/2002jc001496.
25. Guza R.T. and Davis R.E. Excitation of edge waves by waves incident on beach. J Geophys. Research. 1974;79:1285.
26. Huntley D.A. and Bowen A.J. Bach cups and edge waves. Proc. 16th Coastal Engineering Conference, Hamburg. 1978:1378.
27. Buchan S. J. & Pritchard W. G. Experimental observations of edge waves. J. Fluid Mech. 1995;288:1.
28. Yang J. The stability and nonlinear evolution of edge waves. Studies in applied mathematics. 1995;95:229.
29. Ezersky, A. B. and Matusov, P. A. Time-space chaos of capillary waves parametrically excited by noise. Radiophys. Quantum El. 1994;37:828.
30. Petrelis F., Aumaitre S. and Fauve S. Effect of phase noise on parametric instabilities. Phys; Rev. Lett. 2005;94:07060397.

Standing Gravity Wave Regimes in a Shallow-Water Resonator

Alexey Slunyaev, Alexander Ezersky, Dominique Mouaze and Wuttersack Chokchai

Abstract Arising modulations of surface gravity waves in a shallow-water resonator under harmonic forcing is discovered in laboratory experiments. Different types of modulations are found. When certain conditions are satisfied (appropriate frequency and sufficient force of excitation), the standing waves become modulated, and the envelopes of standing waves propagate in the channel. Strongly nonlinear numerical simulations of the Euler equations are performed reproducing the modulational regimes observed in the laboratory experiments. The physical mechanism responsible for the occurrence of modulated waves is determined on the basis of the simulations; quantitative estimates are made with the help of a simplified weakly nonlinear theory. This work was initiated by and performed under the guidance of Prof. A. Ezersky. We dedicate this text to the memory of him.

Keywords Gravity waves · Standing waves · Resonator · Modulations
Three-wave interaction · Shallow water

1 Introduction

Nonlinear instabilities of water waves are the source of large waves and wave pattern formation. The Benjamin—Feir (modulational) instability is suggested by a number of researchers as a possible and regular mechanism of rogue wave formation in the ocean [1]. Meanwhile, theoretically proved instabilities may often be hardly observed in laboratory conditions, and perhaps ineffective in the conditions of a real sea. It takes time to enhance due to nonlinear interactions. Thus, limited sizes of laboratory facilities often make impossible direct observations of the nonlinear focusing effects when progressive waves are considered.

A. Slunyaev (✉)
Institute of Applied Physics, Russian Academy of Sciences,
46 Ulyanov Street Box-120, 603950 Nizhny Novgorod, Russia
e-mail: Slunyaev@appl.sci-nnov.ru

A. Ezersky · D. Mouaze · W. Chokchai
CNRS, M2C, Normandie Univ, UNICAEN, UNIROUEN, 14000 Caen, France

N. Abcha et al. (eds.), *Nonlinear Waves and Pattern Dynamics*,
https://doi.org/10.1007/978-3-319-78193-8_3

Standing waves, which may be understood as two counter-propagating waves, are free of this drawback: the wave fetch may be much more than the size of the laboratory facility. Although the case of two wave systems may exhibit a more complex dynamics [2, 3], in [4] they report that weakly nonlinear standing water waves are modulationally unstable only if the traveling waves are modulationally unstable. The modulational instability is supported by the Lighthill's condition

$$\omega_0''(k)\omega_2(k) < 0, \tag{1}$$

where $\omega_0(k)$ is the dispersion relation for linear waves, k is the wavenumber, and $\omega_2(k)$ is the nonlinear addition to the frequency, $\omega(k) = \omega_0(k) + \omega_2(k)|ka|^2$, a is the wave amplitude. When the water is sufficiently shallow, $kh < 1.363$, where h is the water depth, condition (1) is broken due to the change of sign of the nonlinear frequency correction, ω_2, and the modulational instability vanishes.

In this chapter, we consider a shallow-water case, and the condition for the existence of longitudinal modulation instability (1) is not satisfied. In general, the stability analysis established for deep-water waves becomes trickier for shallow-water conditions [5].

Condition (1) is relevant for weakly nonlinear quasi-sinusoidal progressive waves. As we show in this chapter, nonlinear wave modulations of standing shallow-water waves may significantly grow and lead to the formation of intense traveling envelopes of standing waves. We show that similar to (1), this effect is due to the combination of the shallow-water dispersion and nonlinear frequency shift, what makes short-scale waves in resonance with long perturbations. In contrast to (1), this process is due to the three-wave interaction, which leads to other modulation growth rate as a function of wave amplitude. The action of an external forcing enables resonator waves to get more energy. The described effect was first observed in laboratory (the facility is described in Sect. 2, and the laboratory measurements are summarized in Sect. 3), and then reproduced by means of numerical simulations, which is briefly described in Sects. 4 and 7. A more detailed description of the laboratory measurements and numerical simulations may be found in [6]. Section 5 represents a simplified theory, which gives us a quantitative estimate for the condition of the modulation onset.

2 Experimental Setup

The laboratory tests are carried out in a hydrodynamic channel, see Fig. 1. The length of the channel is $L = 5$ m, its width is 0.5 m, and the depth of the liquid layer is $h = 0.17$ m. A piston type wavemaker consisting of a vertical plate set in motion by a DC motor is placed at one end of the channel. The plate is moved in the horizontal direction by a harmonic law. Amplitude, B, and oscillation frequency, f, of the wavemaker could be changed. Free surface oscillations are registered by resistive wave probe placed at the end of the channel (see Fig. 1). Signals from the

Fig. 1 The scheme of the experiments, (*1*) is the wavemaker, (*2*) is the transducer of horizontal displacement of wavemaker, (*3*) is the resistive probe of a free surface displacement

surface wave transducers and wavemaker displacement are recorded in a computer simultaneously for further data processing.

The channel used during the tests represents a resonator for surface gravity waves. Natural frequencies of resonator modes, f_n, are defined by the dispersion relation as

$$f_n = \frac{1}{2\pi}\sqrt{g\frac{\pi}{L}n \tanh\left(\frac{\pi}{L}nh\right)}, \quad n = 1, 2, 3, \ldots . \tag{2}$$

where n counts the modes and g is the gravity acceleration.

The experiments are accomplished at the frequencies 0.34 Hz $< f <$ 0.48 Hz corresponding to the excitation of modes with numbers $8 < n < 12$, hence, in the experiment we have the depth parameter $0.28 < kh < 0.42$, what makes condition (1) unobtainable.

3 Observation of Modulations in the Laboratory Tank

Three regimes were observed in the experiments. They are as follows: (1) steady-state generation of nonlinear waves with constant amplitude; (2) regime with modulation, including chaotic modulation without wave breaking; and (3) regime with modulation accompanied by wave breaking. A map of these regimes on a plane (amplitude of oscillation of the wavemaker plate, B, versus oscillation frequency, f) is given in Fig. 2.

It is clear from the diagram that the wave modulation and breaking arise at smaller amplitudes of wavemaker oscillations if the excitation frequency does not coincide with the natural frequency of resonator modes (2).

Time series of the free surface displacement corresponding to the regular standing wave regime and regular modulation regime are presented in Fig. 3. An excitation of harmonics with frequencies, multiple of the frequency of external forcing occurs for the regime without modulation. Consequently, a nonlinear steady wave is recorded (Fig. 3a). For the regime with regular modulation, the smallest period of the envelope wave (Fig. 3b) was approximately equal to the period of basic mode of resonator, $1/f_1$, where $f_1 \approx 0.04$ Hz. Besides, double-modulated regular regime was observed, and also irregular (chaotic) wave dynamics with and without wave breaking [6].

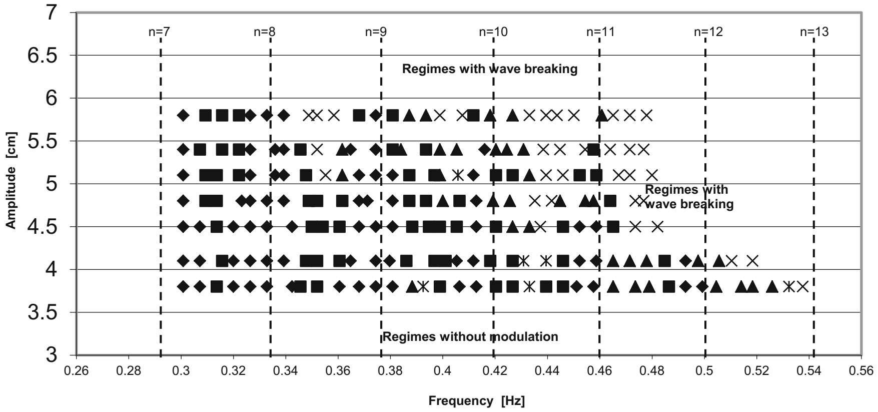

Fig. 2 The diagram of the regimes observed in the laboratory experiments amplitude of the wavemaker, B, versus its frequency, f: rhombs—constant-amplitude standing waves; squares—regular modulated waves; triangles—chaotic wave modulation; stars—double modulation, crosses—wave breaking. The dashed lines show natural mode linear frequencies

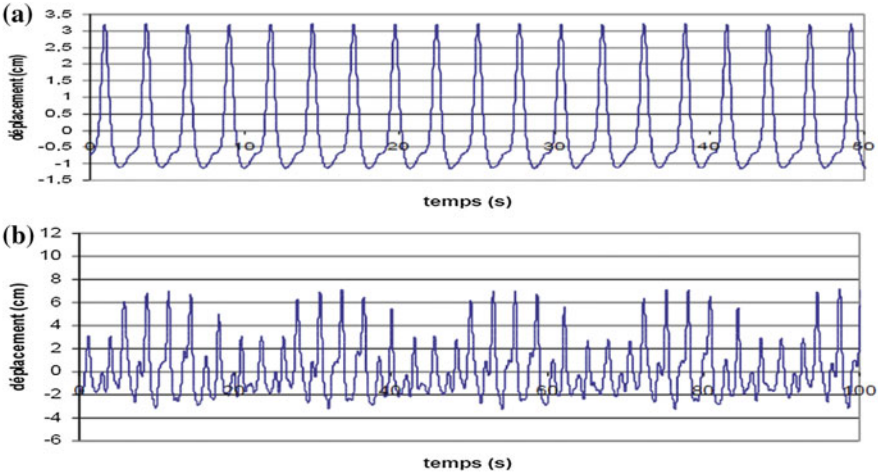

Fig. 3 Time series for different conditions of excitation: **a** the regime without modulation (amplitude $B = 45$ mm, $f = 0.3744$ Hz), **b** the regular modulation ($B = 48$ mm, $f = 0.3616$ Hz)

Sometimes, the appearance of modulation in the channel needs a finite time. At the first stage of wave excitation, steady nonlinear wave are generated. After, some time (as rule 3–5 min) modulation may develop and maximal wave height in resonator becomes about two times more than that before development of instability. Example of such a process is shown in Fig. 4. A band-pass filtering (high and low cutoff frequency) was used to determine growing amplitudes of the spectral harmonics. The harmonics grow in amplitude from very small values, and when they become of

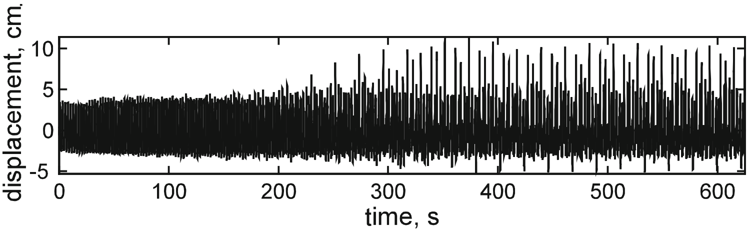

Fig. 4 Development of modulation from steady nonlinear waves. The excitation frequency $f = 0.406$ Hz

the magnitude of the fundamental harmonic, saturation takes place. The exponential function gives us the best-fit approximation for the initial stage of the harmonic growth.

4 Numerical Simulation of the Modulations

The regimes observed in the laboratory experiment are reproduced in numerical simulations of primitive equations of ideal fluid. The potential Euler equations are solved with the help of the High-Order Spectral Method (HOSM), following [7]. The kinematic and dynamic boundary conditions on the free surface are written in form

$$\frac{\partial \eta}{\partial t} = -\frac{\partial \Phi}{\partial x}\frac{\partial \eta}{\partial x} + \left(1 + \left(\frac{\partial \eta}{\partial x}\right)^2\right)\frac{\partial \varphi}{\partial z} + \delta\frac{\partial^2 \eta}{\partial x^2}, \tag{3}$$

$$\frac{\partial \Phi}{\partial t} = -\eta - \frac{1}{2}\left(\frac{\partial \Phi}{\partial x}\right)^2 + \frac{1}{2}\left(\frac{\partial \varphi}{\partial z}\right)^2\left[1 + \left(\frac{\partial \eta}{\partial x}\right)^2\right] - P_a + \delta\frac{\partial^2 \Phi}{\partial x^2}$$

where x and z are horizontal and vertical (upward) coordinates, respectively, and t is time. Conditions $z = -h$ and $z = \eta(x, t)$ specify the waterbed and the free surface displacement correspondingly. The function $\varphi(x, z, t)$ specifies the velocity potential and is obtained at every step of numerical integration through strongly nonlinear iterative solution of the Laplace equation with the potential at the surface specified by $\Phi = \varphi(x, z = \eta(x, t), t)$, see [7]. Term P_a in (3) denotes the atmosphere pressure; its variation in time is used to introduce wave excitation force. Damping effect was found crucial to obtain regular wave patterns. Coefficient δ is chosen to have a better agreement between laboratory registration and simulations; it defines viscous wave dissipation.

A 30 m computational domain with periodic boundary conditions is used in the numerical simulations of the 15 m laboratory resonator. It is supposed that $x = 0$

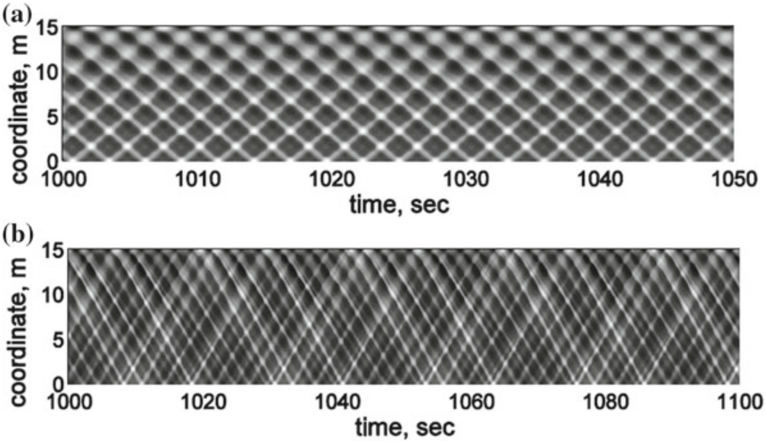

Fig. 5 Spatiotemporal diagrams of regular non-modulated waves **a** and standing wave modulation **b** observed in the numerical simulations

corresponds to the rigid wall of the laboratory resonator (where the gauge is situated, see Fig. 1), while $x = 15$ m corresponds to the other wall (position of the wavemaker).

Regular standing wave (Figs. 3a, 5a) and regular modulated standing wave (Figs. 3b, 5b) regimes are reproduced by means of numerical simulations. On the spatiotemporal diagram in Fig. 5b, the traveling intense wave patterns are clearly seen in contrast to Fig. 5a, where the wave field picture is uniform.

Strongly nonlinear numerical simulation of weakly perturbed standing waves showed that long modulations of standing waves lead to the excitation and subsequent growth of the sidebands, and also to the energy leakage to a number of low modes of the resonator. Many modes of the resonator become excited with time, and the standing waves appear to be strongly modulated. It is found that the growth rate of the excited spectral modes at the early stage corresponds to the three-wave interaction (see [6]). Thus, in contrast to the Benjamin—Feir modulational instability, three-wave interactions, which are common for the shallow-water waves, play the major role in the dynamics of modulated standing waves.

The diagrams of spatiotemporal spectra are obtained on the basis of the numerical simulation data as follows. First, the spatial Fourier transform of the surface elevation as function of space and time is performed. Then, the temporal Fourier transform is applied to the modes of the spatial Fourier spectrum, represented by the complex-valued data time series. Thus, spatiotemporal spectrum $Sp(n, f)$ is obtained, where n is the mode number, and f is frequency. The length of a time series defines the frequency resolution, which is not less than 0.005 Hz for the presented below figures. To render the intensity of the Fourier spectrum, Sp, every value of it (for the grid in the plane of modes and frequencies) is plotted by a filled circle with diameter, D, proportional to the amplitude of Sp in logarithmic scale; too small (insignificant) values of Sp are not plotted.

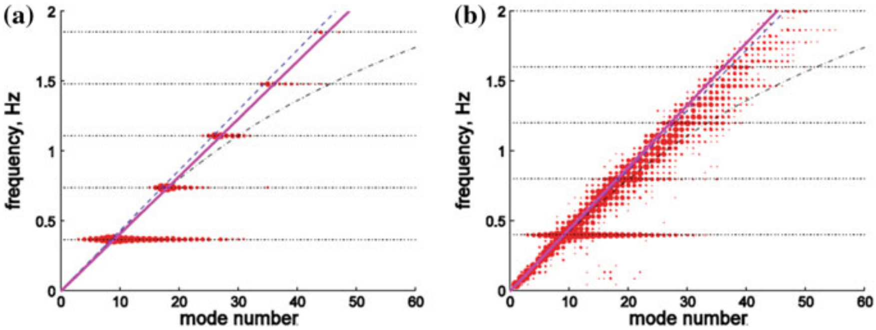

Fig. 6 Spatiotemporal spectral plane for the numerical experiment when standing wave modulations are not observed (**a**) and when regular modulations occur (**b**). The dash-dotted lines represent the exact linear dispersion, its shallow-water limit is given by the dashed straight lines. The horizontal dotted lines show the frequency and multiple frequencies of the excitation. The solid straight lines show the phase velocity of the most energetic standing wave

Figure 6a shows the regime when modulations do not occur, while Fig. 6b demonstrates the case when modulations develop. The horizontal dotted lines in Fig. 6 show the forcing frequency, f, and the multiple values $2f$, $3f$, etc. The dash-dotted lines represent the exact linear dispersion (2), its shallow-water limit is given by the dashed straight lines. The solid straight lines in Fig. 6 pass through the reference origin (0, 0), and through the point (n, f), where $n = 9$ is the most excited mode at the forcing frequency f. Thus, this line on the spectral plane represents the phase velocity of the most excited standing wave.

The spots in Fig. 6a are discrete in both mode and frequency. The frequency discretization is due to the regular character of the record. The driving force at a given frequency excites many modes. Figure 6b represents the regime with modulations and looks quite different from Fig. 6a. There are much more energetic spots; the energy is spread along the curve of the shallow-water dispersion limit, and in a less extent—along the linear dispersion curve. For a given mode number the frequency spectrum is rather wide.

It is known, that in a three-oscillator system with quadratic nonlinearity, lower frequencies may effectively get energy from the high-frequency oscillator (this process is exponential at its early stage, see [8]). It clearly follows from Fig. 6a, b that modulations do not occur when the forcing wave velocity line (the straight lines in Fig. 6) is characterized by the declination smaller than the shallow-water limit of the dispersion. On the contrary, the modulations grow when the forcing wave velocity is higher than the long-wave speed (Fig. 6b). It may be concluded that the three-wave resonance condition becomes fulfilled for the driving wave due to the positive nonlinear frequency shift for a number of low modes. The dynamics involve many wave triplets, thus the nonlinear energy exchange between them may be difficult to interpret. Besides free waves, many bound waves are excited, proving that the waves are essentially cnoidal.

5 Weakly Nonlinear Theory for Shallow-Water Resonances

As it is discussed in the previous part, the nonlinear three-wave interactions are responsible for the dynamics observed in the laboratory experiments, and also in the strong nonlinear numerical simulations. Since the waves are essentially cnoidal, direct application of known theories for weakly nonlinear weakly modulated waves (such as coupled equations describing quasi-sinusoidal waves) is questionable. Meanwhile, let us suppose that the effect of interaction between two counter-propagating wave systems is of secondary importance and that the resonance between long perturbations and shorter nonlinear waves is the most essential effect for the observed instability. Then, let us consider a simplified weakly nonlinear dispersive shallow-water theory for cnoidal waves, the Korteweg—de Vries equation (KdV)

$$\frac{\partial \eta}{\partial t} + c\frac{\partial \eta}{\partial x} + \gamma\eta\frac{\partial \eta}{\partial x} + \mu\frac{\partial^3 \eta}{\partial x^3} = 0,\ c = \sqrt{gh},\ \gamma = \frac{3c}{2h}, \mu = \frac{ch^2}{6} \tag{4}$$

Equation (4) possesses stationary exact solutions, the cnoidal waves, expressed in terms of the Jacobi elliptic functions

$$\eta\left(x,t\right) = \frac{2a}{s^2}\left[dn^2\left(\sqrt{\frac{\gamma a}{6\mu s^2}}\left(x-\left(c+V_{cn}\right)t\right), s\right) - \frac{E\left(s\right)}{K\left(s\right)}\right] \tag{5}$$

(see for instance [9]), where K and E are complete elliptic integrals of the first and the second kinds,

$$K = \int\limits_0^{\pi/2}\left(1-s^2\sin^2\theta\right)^{-\frac{1}{2}}d\theta,\ E = \int\limits_0^{\pi/2}\sqrt{1-s^2\sin^2\theta}d\theta \tag{6}$$

The velocity of the cnoidal wave is defined by

$$V_{cn} = -\frac{\gamma a}{3s^2}\left(3\frac{E\left(s\right)}{K\left(s\right)} + s^2 - 2\right) \tag{7}$$

and the wave amplitude, a, is linked with the wavelength, Λ, through the relation

$$\Lambda = \sqrt{\frac{24\mu}{\gamma a}}sK\left(s\right) \tag{8}$$

The cnoidal waves may have strong vertical asymmetry, and the amplitude parameter a has the meaning that the value $2a$ is equal to the wave height from the trough to the crest.

The "nonlinear" dispersion relation may be obtained from (7) and (8); it is given by formula (see [9])

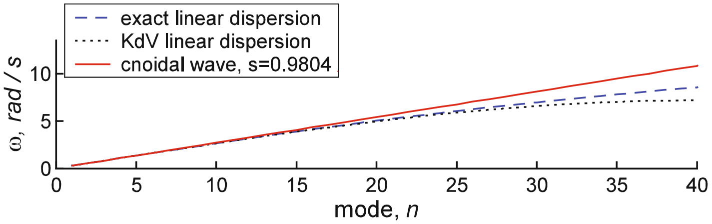

Fig. 7 Dispersion plane in terms of the cyclic frequency versus the mode number

$$\omega(k) - ck = -\mu k^3 \left(\frac{2K\ (s)}{\pi}\right)^2 \left(3\frac{E\ (s)}{K\ (s)} + s^2 - 2\right) \tag{9}$$

Parameter $0 \le s \le 1$ controls the strength of nonlinearity. Linear waves correspond to $s = 0$, then (9) transforms to $\omega(k) - ck = -\mu k^3$, which is the linear dispersive relation of the KdV Eq. (4). The right-hand-side term in (9) becomes zero or even positive when s is large enough. Thus, nonlinearity may give the opposite frequency shift than dispersion, and the condition

$$3\frac{E\ (s)}{K\ (s)} + s^2 - 2 = 0 \tag{10}$$

determines the nonlinear threshold when small-scale cnoidal waves may become resonant with long linear waves.

The dispersion curves for the parameters of the laboratory resonator, when the condition (10) is fulfilled, are shown in Fig. 7. The solid line corresponds to the nonlinear frequency (9) of the cnoidal wave. It is straight and coincides with the long-wave limit of the linear water wave dispersion. The curve of the linear dispersion provided by the KdV model (4) (dotted line) is quite close to the exact linear dispersion (2) shown by the dashed line.

Solution of the threshold condition (10) gives the value of about $s \approx 0.98$; then, the threshold wave amplitude when the nonlinear frequency correction in (9) is positive, may be estimated as

$$a > \frac{2s^2K^2h^3}{3L^2}n^2 \approx 5.9\frac{h^3}{L^2}n^2 \tag{11}$$

The strength of the three-wave nonlinear effects may be estimated with the help of the Ursell parameter, which may be defined as

$$Ur = \frac{a\Lambda^2}{h^3} = \frac{4aL^2}{n^2h^3} \tag{12}$$

The Ursell number is equal to 4, when the soliton solution of the Korteweg–de Vries equation is concerned (when nonlinearity and dispersion are of the same order);

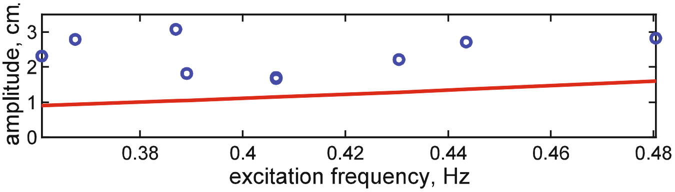

Fig. 8 Comparison of the estimated threshold wave amplitude (the curve) and the laboratory experiment (the circles). Experimental points correspond to the wave amplitude before development of the modulation in the system

estimate (11) results in the value of the Ursell number of about 74, what corresponds to a strongly nonlinear case.

Comparison of the theoretical estimate (11) with the experimental data is given in Fig. 8. The solid line represents the condition (11), and the circles give the heights of measured standing waves divided by factor 4 (we suppose that a wave height is twice the amplitude, and that a standing wave height is twice the progressive wave height). It is important to note that the experimental data displayed in Fig. 8 correspond to the minimum wave amplitudes when modulations occur, thus it tends to overestimate the amplitude threshold. Wave dissipation was clearly observed in the laboratory experiments and may also have effect on the wave amplitude threshold. Thus, although the experimental points lie somewhat higher than the theoretical curve, Fig. 8 reports a reasonable agreement between the theoretical estimate and the laboratory experiments.

6 Extreme States in the Numerical Simulations of the Wave Tank

As it was mentioned in Sect. 4, different regimes of the wave dynamics in the laboratory facility were reproduced in the numerical simulations. In a series of numerical simulations, the action of the wavemaker was modeled by the variable pressure $P_a(x, t)$ in the form

$$P_a = P_0 \sin(2\pi f t) \exp\left[-\left(\frac{x - x_{wm}}{l_{wm}}\right)^2\right]\left(1 - \exp\left(-\frac{t}{t_{wm}}\right)\right) \qquad (13)$$

where P_0 is the pressure amplitude, $x_{wm} = 15$ m is the location of the virtual wavemaker, l_{wm} is its characteristic size, and $t_{wm} = 20$ s provides a smooth start of the excitation. In the numerical experiments, the situation when the forcing frequency, f, at some moment changes the value was considered, and also the situation when the frequency remains the same, but the oscillatory forcing experiences an abrupt phase jump. It could be expected that the frequency change may alter the wave dynamics regime in the entire wave basin. It is more surprising that a sudden change of the

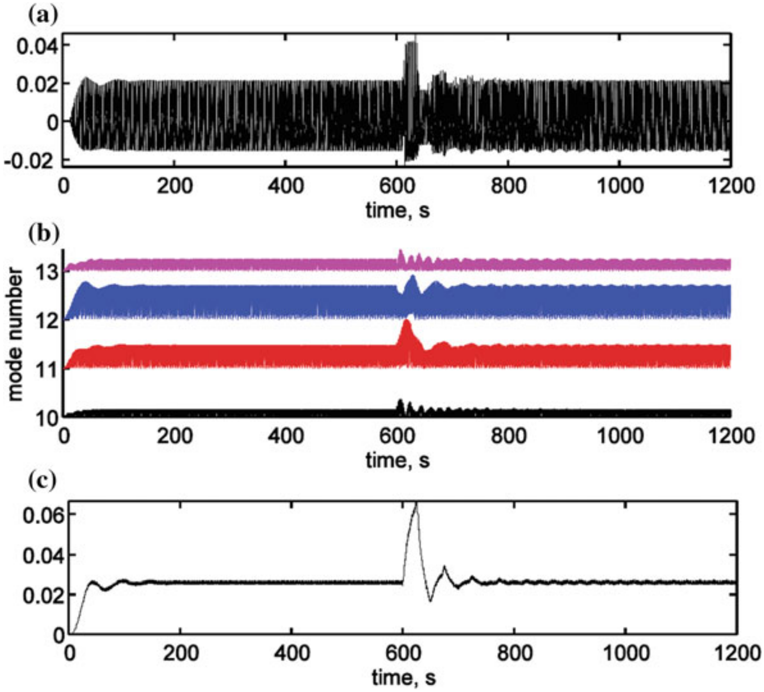

Fig. 9 Time series at the wall (**a**), the evolution of the energy in the most energetic Fourier modes (**b**) and the total energy evolution (**c**) in the numerical simulation with the forcing frequency $f = 0.489$ Hz and $l_{wm} = 0.3$ m

phase may switch the resonator to another dynamical regime. Such a situation is shown in Figs. 9 and 10.

The forcing pressure (13) is characterized by the same frequency, f, and the same amplitude, P_0, in the both cases shown in Figs. 9 and 10, but the length of the virtual wavemaker l_{wm} is larger in the second case. Initially, after a short transition stage, which corresponds to a smooth activation of the forcing, the surface elevation record is characterized by approximately constant wave amplitudes (Figs. 9a and 10a); most of the energy is accumulated in the eleventh and twelfth resonator modes (Figs. 9b and 10b). At the moment, $t = 600$ s the virtual wavemaker's phase experiences an abrupt change. As a result, the maximum surface elevation doubles for a dozen of wave periods, and the balance of energy distributed among the most excited modes gets disturbed. After that, the wave system seems to restore the initial state (Fig. 9a, b) or switches to another regime as shown in Fig. 10a, b. In the latter case, several modes hold significant amounts of energy, which strongly vary in time; they exhibit unsteady behavior. Correspondingly, the surface displacement record exhibits modulated wave patterns. The change of the dynamical regime in the second example is so significant that after the bifurcation the total energy in the resonator is noticeably larger (cf. Figs. 9c and 10c). The wave amplitudes and the accumulated total wave energy

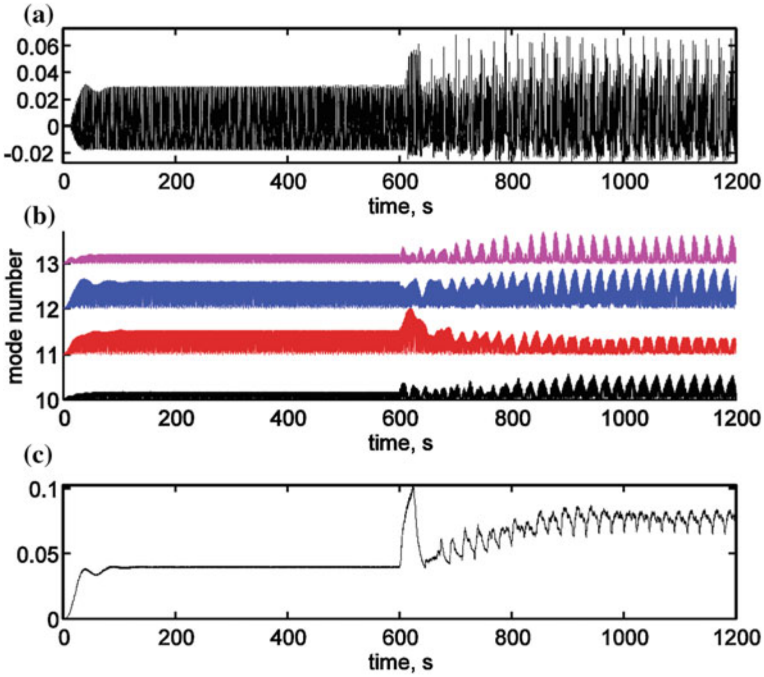

Fig. 10 Similar to Fig. 9, but the size of the virtual wavemaker is larger, $l_{wm} = 0.5$ m

are abnormally large, shortly after the phase change. These extreme events are provoked by almost unnoticeable causes; they possess the attributes of rogue waves.

7 Conclusion

A rich variety of wave regimes is observed in the shallow-water resonator: regular standing waves, modulated and double-modulated wave trains, and also chaotic behavior. The non-breaking regimes have been simulated numerically. The standing wave modulations develop from the initially uniform waves when the certain threshold condition is satisfied providing sufficiently strong nonlinearity. In the leading order, the three-wave nonlinear resonance is responsible for the modulation. Variation of the forcing parameters may lead to the change of the dynamical regime in a nontrivial way, which still desires the further research.

Acknowledgements The experimental tests were supported by a French national scientific program called 'PLAMAR'. AS acknowledges the support from the Russian Foundation for Basic Research (grants No. 16-55-52019, 17-05-00067).

References

1. Kharif, C., Pelinovsky, E., Slunyaev, A.: Rogue Waves in the Ocean, Springer-Verlag Berlin Heidelberg (2009).
2. Vlasov, S.N., Talanov, V.I.: Wave self-focusing. Institute of Applied Physics Press, Nizhny Novgorod (1997) (In Russian).
3. Griffiths, S.D., Grimshaw, R.H.J., Khusnutdinova, K.R.: Modulational instability of two pairs of counter-propagating waves and energy exchange in two-component media. Physica D 214, 1–24 (2006).
4. Bridges, T.J., Laine-Pearson, F.E.: Nonlinear counter propagating waves, multisymplectic geometry, and the instability of standing waves. SIAM J. Appl. Math. 64, 2096–2120 (2004).
5. Francius, M., Kharif, C.: Three-dimensional instabilities of periodic gravity waves in shallow water. J. Fluid Mech. 561, 417–437 (2006).
6. Ezersky, A., Slunyaev, A., Mouazé, D., Chokchai, W.: Occurrence of standing surface gravity waves modulation in shallow water. Eur. J. Mech. B/ Fluids 28, 521–531 (2009).
7. Dommermuth, D., Yue, D.K.P.: A high-order spectral method for the study of nonlinear gravity waves. J. Fluid Mech. 184, 267–288 (1987).
8. Rabinovich, M.I., Trubetskov, D.I.: Oscillations and waves in linear and nonlinear systems. Kluwer Academic Publisher, Dordrecht/Boston/London (1989).
9. Ostrovsky, L.A., Potapov, A.I.: Modulated waves. Theory and applications. Johns Hopkins Univ. Press., Baltimore (1999).

Focusing Wave Group Propagating in Finite Depth in the Presence of Surface Current and Vorticity

Julien Touboul and Christian Kharif

Abstract The kinematics of two-dimensional focusing wave trains on a shearing flow in water of finite depth are investigated analytically. In the absence of waves, the vorticity due to the vertical gradient of the horizontal current velocity is assumed constant. A linear kinematic model based on the spatio-temporal evolution of the frequency is derived predicting the focusing distance and time of a chirped wave packet in the presence of constant vorticity, and surface current. Based on this model, the kinematic behavior of the transient wave packet is analyzed, and described in terms of spreading of the focusing point into a wider area. The effects of bathymetry, vorticity, and surface current are analyzed and discussed. Two main results are obtained: (i) the combined effects of surface current and vorticity, in deep water, are nontrivial, highly depending on the presence of surface current (ii) the effects of bathymetry, in the presence of shear, are also counterintuitive in the presence of vorticity, since significant effects can be observed when considering high values of the depth parameter.

1 Introduction

Freak, rogue, or giant waves are extreme events, localized in time and space. Most of the time, they are defined by a wave height briefly exceeding some statistical properties of the wave field, such as twice the significant wave height. They are characterized by their unpredictability, which explains that they are known as "waves from nowhere". They are responsible for an important number of large damages, caused to ships or offshore rigs, which explains they have focused the attention of the scientific community for the last 30 years.

J. Touboul (✉)
CNRS / INSU, IRD, MIO, Université de Toulon, Aix-Marseille Université,
83957 UM, 110, La Garde, France
e-mail: julien.touboul@mio.osupytheas.fr

C. Kharif
CNRS, Centrale Marseille, IRPHE, Aix-Marseille Université, Marseille, France
e-mail: kharif@irphe.univ-mrs.fr

N. Abcha et al. (eds.), *Nonlinear Waves and Pattern Dynamics*,
https://doi.org/10.1007/978-3-319-78193-8_4

Formation of these waves might be explained through various mechanisms, such as spatio-temporal focusing Kharif et al. [15], Johannessen and Swan [11], Brown [4], Brown and Jensen [5], nonlinear or modulational instability Benjamin and Feir [2], Dyachenko and Zakharov [9], envelope soliton and breather interactions Clamond and Grue [6]. These mechanisms have been reviewed by Kharif and Pelinovsky [14] and by Dysthe [10].

Wave–current interaction contributes also in the freak wave formation and historically; this mechanism was the first to explain the origin of freak waves Lavrenov [20], White and Fornberg [35]. This is due to an important modification of water waves kinematics in the presence of currents reviewed extensively in Peregrine [23] and Jonsson [13].

Since all these mechanisms can exist simultaneously at sea, it is interesting to analyze their robustness when considered together. This, for instance, was achieved for studying the influence of sheared currents on modulational instability in Johnson [12]. The influence of wind on dispersive focusing was studied in Touboul et al. [27], and in Kharif et al. [16], while the evolution of modulation instability under wind action was studied in [17, 30, 31].

Such a question can be asked about the dispersive focusing under the action of currents. This was initially addressed by Touboul et al. [28], who investigated the modification of the dispersive focusing mechanism for water waves propagating in deep water in the presence of uniform currents. But generally, the characteristic length scales of wind waves and swells are much smaller than the spatial scales of horizontal variations in oceanic currents. On the opposite, there are many circumstances in which this claim cannot be applied to current velocity variations in vertical direction. Consequently, the vorticity due to the vertical gradient of the horizontal current velocity which may have an important effect on the dynamics of ocean surface waves cannot be ignored. Various studies of water waves propagating in such conditions can be found in the literature. Among them, one can cite Tsao [33], Dalrymple [8], Brevik [3], Simmen [24], Simmen and Saffman [25] Teles da Silva and Peregrine [26], Kishida and Sobey [19], Pak and Chow [22], Constantin [7], etc. Thus, Touboul and Kharif [32] extended their previous study [28] to this more realistic case of water waves propagating in the presence of vorticity.

Besides, such vortical flows are observed in coastal areas [1, 29]. As pointed out by Professor Ezersky, the effect of bathymetry on dispersive properties should be taken into account. This study was realized experimentally and numerically for water waves propagating in waters of finite depth, in the presence of uniform currents in Merkoune et al. [21].

The purpose of this work is to analyze both the effects of surface current and vorticity for rogue waves propagating in waters of finite depth, extending results presented in [21] to take vorticity into account. To achieve this goal, attention is focused on the kinematic behavior of a focusing wave group. The components should merge at a given point in both time and space, producing a rogue wave. The transformation of this point into a wider area, under the combined effects of surface current, vorticity, and depth is investigated here. The chapter is organized as follows: in Sect. 2, the kinematic model is formulated, focusing on the computation of the coordinates of the focusing point without and with current and vorticity, in finite depth. In Sect. 3, the results are discussed in detail, and briefly summarized in Sect. 4, describing the main conclusions of the work.

2 The Kinematic Model

Since water waves are known to be dispersive, short waves propagating in front of longer ones will be overtaken, and a large amplitude wave can occur at a fixed point. A linear approach of the problem would lead to consider sea surface as a superposition of linear waves of frequencies $\omega(x, t)$. The following nonlinear hyperbolic equation governs the spatiotemporal evolution of these components, as pointed out by Brown [2] and Whitham [34],

$$\frac{\partial \omega}{\partial t} + C_g(\omega) \frac{\partial \omega}{\partial x} = 0, \tag{1}$$

where C_g is the group velocity, defined as $C_g = \partial\omega/\partial k$. The boundary value problem for this equation can be solved using the method of characteristics. Its solution is

$$\omega(x, t) = \omega_0(\tau), \text{ on } t = \tau + x/C_g(\omega), \tag{2}$$

where ω_0 corresponds to the temporal frequency distribution of the wave train at $x = 0$. By differentiating the frequency, it comes

$$\frac{\partial \omega}{\partial t} = \frac{\frac{\partial \omega_0}{\partial \tau}}{1 - \frac{x}{C_g^2}\frac{\partial C_g}{\partial \omega}\frac{d\omega_0}{d\tau}} \tag{3}$$

The latter equation can be solved once the dispersion equation is known, and various examples of solutions can be found in the literature. In the classical formulation of water propagating in deep water, for instance, this dispersion equation reads

$$\omega^2 = gk, \tag{4}$$

where k stands for the wavenumber, and g is the acceleration due to gravity. We can now obtain an expression of the group velocity given by $C_g = g/(2\omega)$. Equation (3) might thus be rewritten

$$\frac{\partial \omega}{\partial t} = \frac{\frac{\partial \omega_0}{\partial \tau}}{1 - \frac{2x}{g}\frac{d\omega_0}{d\tau}}, \tag{5}$$

and one can notice that the case $d\omega_0/d\tau < 0$, which corresponds to the case of short waves emitted before longer waves, leads to a singularity. This singularity corresponds to the focusing of several waves at $t = T_f$ and $x = X_f$. Given the expression of the group velocity in the case at hand, we can find out the frequency to impose to a wave maker located at $x = 0$, and for $0 < t < T$, given by

$$\omega\,(0, t) = \frac{g}{2}\frac{T_f - t}{X_f} \tag{6}$$

This frequency modulation, varying linearly from ω_{min} to ω_{max}, provides the optimal focusing of the linear wave packets in still water of infinite depth, and is very often applied in the laboratory conditions. Such a wave train will involve components which will propagate and all merge at the same place X_f, and at the same time T_f. Coordinates of the focusing point in the $(x - t)$ plane would thus be given by

$$X_f = \frac{gT}{2}\frac{1}{\omega_{max} - \omega_{min}}, \text{ and } T_f = \frac{2\omega_{max}}{g}X_f. \tag{7}$$

If we now consider water waves propagating in deep water, in the presence of uniform currents, the dispersion Eq. (4) can be modified to take a Doppler shift into account, and now reads

$$(\omega - kU)^2 = gk. \tag{8}$$

This specific case was investigated in Touboul et al. [28], where Eq. (5) was demonstrated not to be solution anymore, but to be replaced with

$$\frac{\partial\omega}{\partial t} = \frac{\frac{d\omega_0}{d\tau}}{1 + \frac{2gx}{[g+2U_0(\omega-kU0)]^2}\frac{d\omega_0}{d\tau}} \tag{9}$$

This is true, since the group velocity admits a new expression, $C_g = U_0 + g/\,(2\omega - kU_0)$. Equation (9) shows a difference in the kinematics of the wave group, which becomes more complicated. Indeed, the denominator is now a function of time, and is equal to zero for several values of space and time. The focusing point is not a unique singularity anymore, and the waves present in the group do not merge at a single location of time and space. The singularity is now spread over a focusing area, ranging from L_{min} and L_{max}, where

$$L_{min} = X_f\left(1 + \frac{2U_0\sigma_{min}}{g}\right)^2, \text{ and } L_{max} = X_f\left(1 + \frac{2U_0\sigma_{max}}{g}\right)^2, \tag{10}$$

where σ_{min} and σ_{max} are the intrinsic, Doppler shifted, frequencies, respectively given by $\sigma_{min} = (\omega_{min} - k_{min}U_0) = \sqrt{gk_{min}}$, and $\sigma_{max} = (\omega_{max} - k_{max}U_0) = \sqrt{gk_{max}}$.

In a recent work, Touboul and Kharif [32] investigated the evolution of a chirped wave packet in the presence of a horizontally constant current presenting linear variations with respect to depth, so that

$$U(z) = U_0 + Sz, \tag{11}$$

where U_0 is the current velocity at the undisturbed free surface, and S is the value of the shear of the current. As an immediate consequence, the vorticity vector associated to this flow field is given by $\boldsymbol{\Omega} = \nabla \wedge \boldsymbol{U} = (0, S, 0)$. In such a configuration, the dispersion equation is also known analytically (see, e.g., [13, 18, 29])

$$(\omega - kU_0)(\omega - kU_0 + S) = g|k|, \tag{12}$$

and the related group velocity now reads $C_g = U_0 + g/[\sigma_0 + \sigma_2]$, where σ_0 and σ_2 are respectively the Doppler shifted intrinsic frequencies $(\omega - kU_0)$ and $(\omega - kU_2) = (\omega - k(U_0 - S/k))$. In such configuration, neither Eq. (5) nor Eq. (9) is the solution of Eq. (1) anymore. Instead, the solution (3) reads

$$\frac{\partial\omega}{\partial t} = \frac{\frac{d\omega_0}{dt}}{1 + \frac{2gx}{[g+U_0(\sigma_0+\sigma_2)]^2}\frac{d\omega_0}{dt}}. \tag{13}$$

Here again, the focusing point turns out to be a focusing area, where the values of L_{min} and L_{max} are now given by

$$L_{min} = X_f\left(1 + \frac{U_0\left(\sigma_{0,min} + \sigma_{2,min}\right)}{g}\right)^2, \text{ and} L_{max} = X_f\left(1 + \frac{U_0\left(\sigma_{0,max} + \sigma_{2,max}\right)}{g}\right)^2 \tag{14}$$

where $\sigma_{0,min}$, $\sigma_{2,min}$, $\sigma_{0,max}$ and $\sigma_{2,max}$ are respectively the minimum and maximum of intrinsic frequencies σ_0 and σ_2.

The latter formulation might reduce to both previous cases. Indeed, for S = 0, we find the result $\sigma_0 = \sigma_2$, and Eq. (14) reduces to Eq. (10). Furthermore, with $U_0 = 0$, this equation further reduces to $L_{min} = L_{max} = X_f$, correspondingly to the solution (7) of Eq. (5).

Still, as pointed out in Touboul and Kharif [32], solution (14) also has an interesting behavior, when investigating the only effect of vorticity S, independently of any surface current U_0. Indeed, when considering the absence of surface current, $U_0 = 0$, a nonzero vorticity $S \neq 0$ turns out to change the focusing area in a single point. All frequencies have group velocities affected in such a way that the focusing point is not affected by the value of the vorticity. On the other hand, the focusing time is significantly affected, and all components of the chirped wave packet will reach the focusing point X_f at a time T given by

$$T = T_f + \frac{S}{g}X_f \tag{15}$$

This result is very different from what was observed in the presence of uniform current. Indeed, when uniform current was considered, each component was affected by Doppler shift, so that the focusing was not optimal. Here, the components are also affected, but the focusing point remains unchanged. This means that the focusing of energy remains optimal, even if delayed or leaded.

These three configurations are interesting, since they admit analytical solutions, allowing to emphasize the effect of a uniform current, or a sheared current, on the focusing behavior of a chirped wave packet. But another effect, of possible great significance, was not considered here. This effect is the influence of the water depth, which has, as it is classically known, a significant impact on dispersive properties of water waves. This idea was raised by Pr. Ezersky, and investigated both numerically and experimentally in Merkoune et al. [21]. In this work, we extend this analysis to the presence of a linearly sheared current.

In the latter case, the above derivation of C_g and $\partial C_g/\partial\omega$ can still be performed. The dispersion equation now reads $\sigma_0\sigma_2 = gk\tanh(kh)$, where σ_0 and σ_2 are still the previous Doppler shifted frequencies, but now read respectively $(\omega - kU_0)$ and $(\omega - kU_0 + S\mathrm{th}(kh))$. This new dispersion equation provides the following expression:

$$C_g = U_0 + \frac{g\,tanh\,(kh)}{\sigma_0+\sigma_2} + \frac{gkh+\sigma_0 Sh}{\sigma_0+\sigma_2}\left(1 - tanh\,(kh)^2\right) \tag{16}$$

Starting from this group velocity, and after some algebra, one may derive the expression of $\partial C_g/\partial\omega$. We obtain

$$\frac{\partial C_g}{\partial\omega} = -2\frac{\left(C_g - U_0\right)^2}{(\sigma_0+\sigma_2)C_g} + 2\frac{\left(1 - tanh\,(kh)^2\right)}{(\sigma_0+\sigma_2)\,C_g}\left(gh + \left(gkh^2 + \sigma_0 Sh^2\right) tanh\,(kh)\right) \tag{17}$$

Finally, introducing these values in the denominator of Eq. (3) leads to the following relationship:

$$\frac{x}{C_g^2}\frac{\partial C_g}{\partial\omega}\frac{d\omega_0}{d\tau} = -\frac{gx}{X_f}\frac{\left(C_g + U_0\right)^2}{(\sigma_0+\sigma_2)\,C_g^3} + \frac{gx}{X_f}\frac{\left(1 - tanh\,(kh)^2\right)}{(\sigma_0+\sigma_2)\,C_g^3}\left(gh + \left(gkh^2 + \sigma_0 Sh^2\right) tanh\,(kh)\right) \tag{18}$$

Here again, we notice the complexity of Eq. (18), which is time dependent. Indeed, the denominator of Eq. (3) now admits an infinity of singularities, ranging from

$$\begin{aligned} L_{min} &= X_f\frac{\left(\sigma_{0,min} + \sigma_{2,min}\right) C_g^3\,(\omega_{min})}{g} \times F\,(\omega_{min}, k_{min})\,, \text{ and} \\ L_{max} &= X_f\frac{\left(\sigma_{0,max} + \sigma_{2,max}\right) C_g^3\,(\omega_{max})}{g} \times F\,(\omega_{max}, k_{max})\,, \end{aligned} \tag{19}$$

where the function $F\,(\omega, k)$ is given by

$$F\,(\omega, k) = \frac{1}{\left(C_g\,(\omega) + U_0\right)^2 + \left(gh + \left(gkh^2 + \sigma_0\,(\omega, k)\,Sh^2\right) tanh\,(kh)\right)\left(1 - tanh\,(kh)^2\right)}. \tag{20}$$

3 Results and Discussion

Results presented here aim to describe the influence of bathymetry, surface current, and vorticity on the focusing behavior of a wave packet. To achieve this goal, the chirped wave packet considered here corresponds to the packet studied in a previous work by Touboul and Kharif [32]. The focusing wave group considered had a frequency varying from $f_{max} = 1.3\,\mathrm{Hz}$ to $f_{min} = 0.7\,\mathrm{Hz}$. The peak frequency is thus given by $\omega_{mean} = 2\pi\,(f_{max} + f_{min})\,/2 = 2\pi\,\mathrm{rad/s}$. This chirped wave packet, when propagating in deep water, in the absence of current and vorticity, presented a focusing location of $X_f = 16.26\,\mathrm{m}$ and a focusing time of $T_f = 27\,\mathrm{s}$.

To illustrate the kinematic effects of bathymetry, surface current, and vorticity, we focus in the following subsections on the spreading of the focusing point. Based on the expression of the minimum and maximum distance for caustic formation, L_{min} and L_{max}, provided by Eq. (19), the spreading of the focusing area can be described as

$$A_{spread} = \frac{L_{max} - L_{min}}{X_f} \tag{20}$$

This quantity will provide good insights on how vorticity, surface current, and bathymetry affect dispersion.

a. Effect of vorticity and surface current

In this section, we focus on the combined effects of vorticity and a surface current, homogeneous with depth, on the spreading area A_{spread}. In every case considered, the bathymetry effects are neglected, and water waves propagating in deep water are considered.

Figure 1 depicts the spreading area A_{spread} of the chirped wave packet as a function of the normalized vorticity S/ω_{mean}. In the figure, various lines are represented. These lines are colored as a function of the reference current velocity U_0/c_{mean}. The word "reference" here means the wavenumber considered that corresponds to the wavenumber computed in the absence of vorticity ($S/\omega_{mean} = 0$) for the mean pulsation of the wave packet ω_{mean}.

This figure shows the strong dependence of the focusing area to both the vorticity and the surface current, in a nontrivial coupling. Indeed, it appears that for strong currents, either positive or negative, the width of the focusing area is sensitive to the vorticity. For positive values of the surface current, the width of the area increases with the vorticity, while it decreases when considering negative values of the surface current. Furthermore, when considering counter flowing currents (negative values of U_0/c_{mean}), the spreading of the focusing area tends to be limited. This is connected to the limiting value of the blocking current velocity. When considering positive values of the current, this limiting behavior is not observed, and the focusing area seems to be unbounded. One may observe it is greater than 1, meaning the width of the focusing is as wide as the focusing distance, for relatively weak values of the surface current.

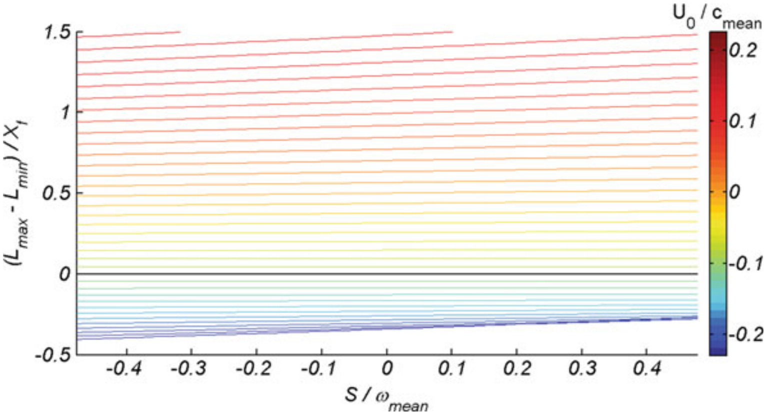

Fig. 1 Spreading area A_{spread} of the focusing wave packet plotted versus normalized vorticity S/ω_{mean}. Various lines are colored as a function of the normalized reference current velocity U_0/c_{mean}

In the meantime, when considering zero surface current (this case is emphasized by the thick black line in Fig. 1), the focusing area turns out to remain a singularity, corresponding to a focusing point, and to be insensitive to the vorticity. This is a confirmation of the result initially obtained in Touboul and Kharif [32]. This result appears not to remain valid for constant, but nonzero values of the surface current.

The dependence of the width of this focusing area can also be analyzed as a function of the normalized effective surface current velocity. The word "effective" here means the phase velocity considered for normalization is still the phase velocity of the average pulsation of the group, ω_{mean}, but now accounts for the actual value of vorticity. This behavior is presented in Fig. 2, where the spreading area is plotted versus the normalized effective current velocity, U_0/c_{mean}. In this figure, various lines appear, colored as a function of the normalized vorticity, S/ω_{mean}.

Confirming the previous result, every curve intersects in $A_{spread} = 0$ for the value of surface current $U_0/c_{mean} = 0$. But beyond this point, it is interesting to notice that the area of focusing always increases with the velocity of the surface current (in modulus). Though, from these curves, it also appears the vorticity has an influence on this behavior, since for strong positive vorticities, the increase rate is smaller than it is when considering strong negative vorticities.

These results are summarized in Fig. 3, where the evolution of the spreading area (in modulus) of the focusing wave packet is presented in the $(U_0/c_{mean}, S/\omega_{mean})$ plane. From this figure, the dependence of the focusing area to both surface current velocity and vorticity might become more intuitive. It appears that for zero values of the surface current, the focusing area is always zero, corresponding to optimal focusing. But this focusing area is found to depend on both surface velocity and vorticity. However, this coupling is nontrivial, since the enlargement of the focusing area is more sensitive to the surface current when considering strong negative

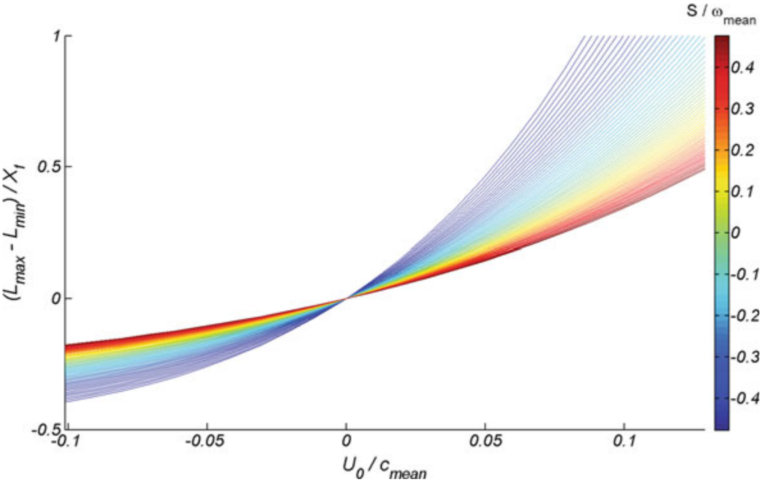

Fig. 2 Spreading area A_{spread} of the focusing wave packet plotted versus normalized effective current velocity U_0/c_{mean}. Various lines are colored as a function of the normalized vorticity S/ω_{mean}

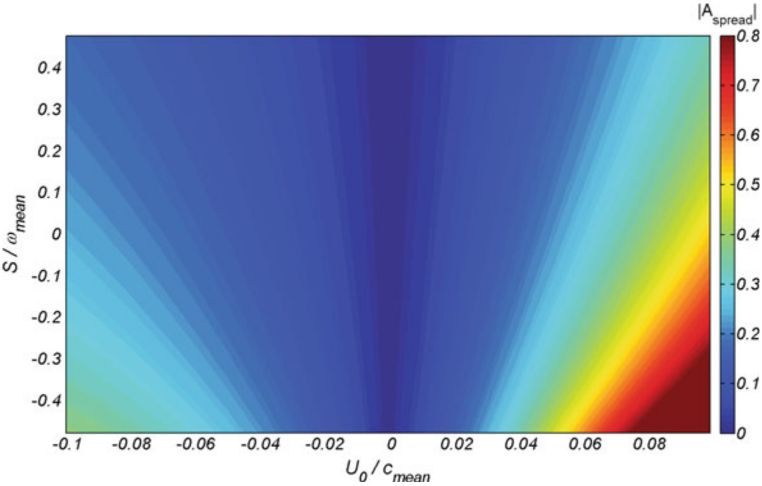

Fig. 3 Evolution of the modulus of the focusing area in the $(S/\omega_{mean}, U_0/c_{mean})$ plane

vorticity. It can also be emphasized that the dependence of this area with vorticity is more important when considering strong values (positive or negative) of the surface velocity.

b. **Effect of Vorticity and Bathymetry**

In this section, we focus on the combined effects of bathymetry and vorticity on the spreading area A_{spread}. In every case considered, the surface current velocity is taken equal to zero.

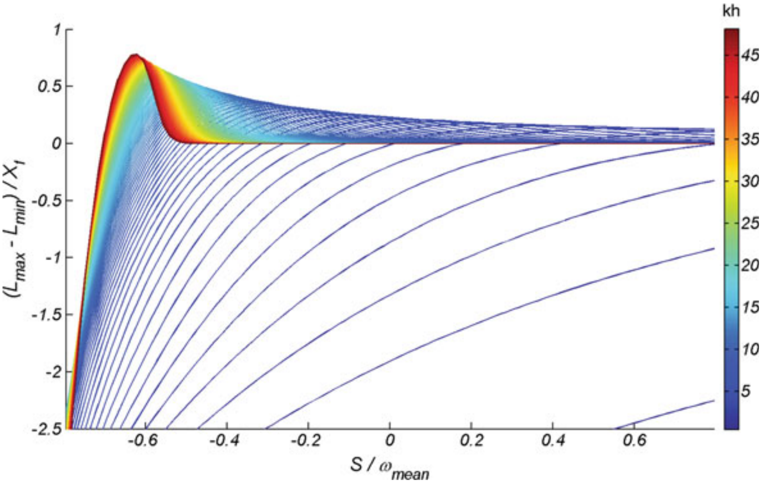

Fig. 4 Spreading area A_{spread} of the focusing wave packet plotted versus normalized vorticity. Various lines are colored as a function of the reference depth parameter *kh*

Figure 4 depicts the spreading area A_{spread} of the chirped wave packet as a function of the normalized vorticity S/ω_{mean}. On the figure, various lines are represented. These lines are colored as a function of the reference depth parameter *kh*. The word "reference" means the wavenumber considered that corresponds to the wavenumber computed in the absence of vorticity ($S/\omega_{mean} = 0$) for the mean pulsation of the wave packet ω_{mean}. From this figure, various behaviors appear for large or small values of *kh*. Indeed, for large values of the depth parameter, the spreading area A_{spread} is zero for almost every value of the vorticity. This is a confirmation of the result initially obtained in Touboul and Kharif [32] for wave packets propagating in deep water. In this study, the focusing location was found to be unaffected, whatever the value of the vorticity. The vorticity, in deep water, has no effect on the dispersive behavior of the chirped wave packet.

On the other hand, for strong negative values of the vorticity S/ω_{mean}, Fig. 4 shows a spreading of the focusing area, even for the strongest values of the *kh* parameter (up to values of $kh = 48$). These values of the vorticity correspond to a strong co-flowing current, which will intuitively result in large values of the wavelength. Thus, the effective wavenumber, taking the influence of the vorticity into account, will be smaller, and the influence of the bathymetry will have a significant effect on the dispersive behavior of the wave packet, resulting in a spreading of the focusing area.

When considering the smallest values of the reference depth parameter *kh*, it turns out that the spreading area is not equal to zero. This means no optimal focusing can be reached in such conditions, and the influence of bathymetry is predominant, regardless to the value of vorticity. Nevertheless, it seems the value of zero will eventually be reached asymptotically, for values of the vorticity large enough.

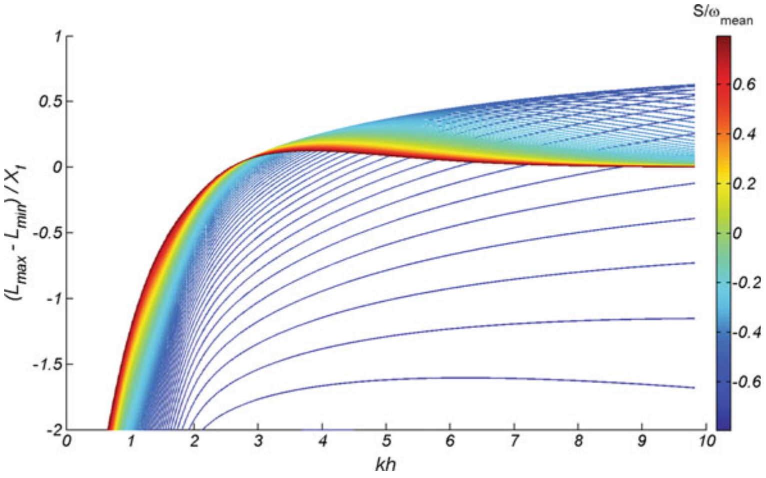

Fig. 5 Spreading area A_{spread} of the focusing wave packet plotted versus depth parameter *kh*. Various lines are colored as a function of the normalized vorticity S/ω_{mean}

Given the previous results, it is also interesting to consider the influence of effective depth parameter *kh* on the focusing area A_{spread}. This is the purpose of Fig. 5, which presents the evolution of the spreading area as a function of the effective depth parameter. The word "effective" here means *kh* is evaluated using the real wavenumber k, computed using the mean pulsation of the wave packet ω_{mean}, and taking the real vorticity value into account. In this figure, several lines are observed, colored as a function of the normalized vorticity magnitude, S/ω_{mean}.

In this figure, we observe various behaviors given the magnitude of the vorticity considered. Indeed, when considering strong vorticity, the spreading area appears to tend to a zero value, meaning the parameter *kh* has less influence when vorticity is important. On the opposite, for strong, but negative values of the vorticity, the parameter *kh* is found to have a strong influence on the focusing area of the chirped wave packet.

The values of the parameter *kh* are striking. Indeed, in the absence of vorticity, depicted by the green lines in Fig. 5, the bathymetry seems to have an influence up to $kh = 7$. This is explained through the frequency width involved in the chirped wave packet. But in the meantime, these values are larger than 10 when vorticity becomes important, but negative.

In Fig. 6, the evolution of the spreading area (in modulus) of the focusing wave packet is presented in the $(S/\omega_{mean}, kh)$ plane. From this figure, it appears that the focusing area is zero, corresponding to optimal focusing, for deep water conditions, and for positive values of the vorticity. On the other hand, the important influence of the depth parameter on the focusing area appears clearly on that figure, when considering important opposing vorticities. This observation is probably explained through a broadening of the spectral width of the group in the presence of vorticity.

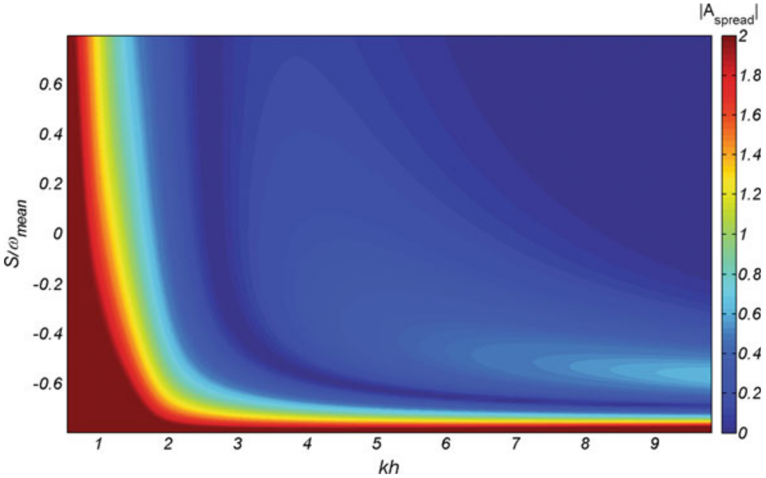

Fig. 6 Evolution of the modulus of the focusing area in the $(S/\omega_{mean}, kh)$ plane

Thus, the mean frequency is not accurate enough to provide a good indicator of the depth effects on the spreading area. Indeed, components involved in the wave packet are now sensitive to finite depth effects, resulting in a spreading of the focusing area. Same remark can be done when considering the vorticity effects for waves propagating in shallow water (small values of the *kh* parameter). When components of the group tend to become nondispersive, due to shallowness, vorticity has no influence anymore, and the focusing cannot be reached anymore.

4 Conclusion

The kinematic behavior of a focusing wave group propagating in finite depth, in the presence of constant vorticity and surface currents is studied analytically. Within the framework of the linear theory we use an approximate kinematic model allowing to describe the focusing point, and its transformation to a focusing area.

Confirming previous results by Touboul and Kharif [34], the effect of vorticity in deep water is found to be surprising, and very different from what is expected in the presence of surface current, varying uniformly with depth. Indeed, when the only vorticity is present, the spreading of the focusing area is not expected anymore. On the other hand, when both current and vorticity are present the focusing area of the wave packets exhibits a dependence on the vorticity. Namely, the modulus of the focusing area always increases with the modulus of the vorticity, whatever its sign. On the other hand, this area is always found to depend on the surface current intensity, with or without vorticity. However, the rate of this dependence is found to be sensitive to the value of vorticity considered.

The effect of bathymetry on the focusing area is also investigated. Here again, results are surprising, since bathymetry turns out to have a strong impact on the focusing area, even for very large values of *kh*. Indeed, this can be explained by a broadening of the wavelength within the wave group. In the presence of strong negative vorticities, the spatial spectral width is increased in such a way the reference wave number might be misleading. Thus, some parts of the components suffer the influence of the bathymetry where we should not expect it. Influence of bathymetry is thus found, indirectly, to have even more significant impact on the dispersive behavior of the chirped wave packet than surface currents do.

Acknowledgements This work is the continuation of a collaboration initiated jointly with Prof. Alexander Ezersky. The authors are also thankful to the editors for organizing such a manuscript. The authors would like to thank the French DGA, who supported this work through the ANR grant ANR-13-ASTR-0007.

References

1. Belibassakis K. A., Simon B., Touboul J. & Rey V. (2017) A coupled-mode model for water wave scattering by vertically sheared currents in variable bathymetry regions, Wave Mot. In Press.
2. Benjamin, T. and Feir, J. (1967). The disintegration of wave train on deep water, J. Fluid Mech. vol. 27, 417–430.
3. Brevik I (1979) Higher-order waves propagating on constant vorticity currents in deep water. Coast Eng 2:237–259.
4. Brown MG (2001) Space-time surface gravity wave caustics: structurally stable extreme events. Wave Mot 33:117–143.
5. Brown MG, Jensen A (2001) Experiments on focusing unidirectional water waves. J Geopys Res 106(C8):16917–16928.
6. Clamond, D. and Grue, J. (2002). Interaction between envelope solitons as a model for freak wave formations. Part I: Long time interaction C. R. Mecanique, vol. 330, 575–580.
7. Constantin A (2011) Two-dimensionality of gravity water flows of constant non zero vorticity beneath a surface wave train. Eur J Mech B/Fluids 30:12–16.
8. Dalrymple RA (1974) A finite amplitude wave on linear shear current. J Geophys Res 79(30):4498–4504.
9. Dyachenko, A.I. and Zakharov, V.E. (2005). Modulation instability of Stokes waves - freak wave, JETP Letters, vol. 81, 6, 255–259.
10. Dysthe, K.B. (2001). Modelling a Rogue Wave – Speculations or a realistic possibility? Rogue Waves, Brest, Ed. by M. Olagnon, and G.A. Athanassoulis, 255–264.
11. Johannessen TB, Swan C (2003) On the nonlinear dynamics of wave groups produced by the focusing of surface water waves. Proc R Soc Lond A 459:1021–1052.
12. Johnson RS (1976) On the modulation of water waves on shear flows. Proc R Soc Lond A 347:537–546.
13. Jonsson IG (1990) Wave-current interactions. In: LeMehaute B, Hanes DM (eds) The sea, vol 9. John, New-York, pp 65–120.
14. Kharif C, Pelinovsky E (2003) Physical mechanisms of the rogue wave phenomenon. Eur J Mech B/Fluids 22:603–634.
15. Kharif C, Pelinovsky E, Talipova T (2001) Focusing of nonlinear wave groups in deep water. JETP Lett. 73(4):170–175.

16. Kharif C, Giovanangeli J-P, Touboul J, Grare L, Pelinovsky E (2008) Influence of wind on extreme wave events: experimental and numerical approaches. J Fluid Mech 594:209–247.
17. Kharif, C. & Touboul, J. (2010) Under which conditions the Benjamin-Feir instability may spawn an extreme wave event: a fully nonlinear approach, Eur. Phys. J. Special Topics, 185, p. 159–168.
18. Kirby JT, Chen TM (1989) Surface waves on vertically sheared flows: approximate dispersion relations, J. Geophys. Res., 94(C1):1013–1027.
19. Kishida N, Sobey RJ (1988) Stokes theory for waves on linear shear current. J Eng Mech 114:1317–1334.
20. Lavrenov, I.V. (1998). The wave energy concentration at the Agulhas current of South Africa, Natural Hazards, vol. 17, 117–127.
21. Merkoune D, Touboul J, Abcha N, Mouaz D, Ezersky A (2013) Focusing wave group on a current of finite depth. Nat Hazards Earth Syst Sci 13:2941–2949.
22. Pak OS, Chow KW (2009) Free surface waves on shear currents with non-uniform vorticity : third order solutions. Fluid Dyn Res 41:1–13.
23. Peregrine DH (1976) Interactions of water waves and currents. Adv Appl Mech 16:9–117.
24. Simmen JA (1984) Steady deep-water waves on a linear shear current. PhD thesis, California Institute of Technology, Pasadena, Californie.
25. Simmen JA, Saffman PG (1985) Steady deep-water waves on a linear shear current. Stud Appl Math 73:35–57.
26. Teles Da Silva AF, Peregrine DH (1988) Steep, steady surface waves on water of finite depth with constant vorticity. J Fluid Mech 195:281–302.
27. Touboul, J., Giovanangeli, J.P., Kharif, C. and Pelinovsky, E. (2006). Freak waves under the action of wind: experiments and simulations, European J. Mech. B/Fluids, vol. 25, 662–676.
28. Touboul J, Pelinovsky E, Kharif C (2007) Nonlinear focusing wave groups on current. J. Korean Soc Coast Ocean Eng 19(3):222–227.
29. Touboul J, Charland J, Rey V, Belibassakis K (2016) Extended mild-slope equation for surface waves interacting with a vertically sheared current. Coast Eng 116:77–88.
30. Touboul, J. & Kharif, C. (2006) On the interaction of wind and extreme gravity waves due to modulational instability, Phys. Fluids, 18, 108103.
31. J. Touboul & C. Kharif, "Nonlinear evolution of the modulational instability under weak forcing and damping", Nat. Hazards Earth Syst. Sci., 10, p. 2589–2597(2010).
32. Touboul J, Kharif C (2016) Effect of vorticity on the generation of rogue waves due to dispersive focusing, Nat. Haz., 84(2):585–598.
33. Tsao S (1959) Behavior of surface waves on a linearly varying current. Tr Mosk Fiz Tekh Inst Issled Mekh Prikl Math 3:66–84.
34. Whitham GB (1974) Linear and nonlinear waves. Wiley, New York.
35. White, B.S. and Fornberg, B. (1998). On the chance of freak waves at sea, J. Fluid Mech., vol. 355, 113–138.

Modeling of Bose–Einstein Condensation in a Water Tank

Germain Rousseaux and Yury Stepanyants

Abstract A theoretical basis for the possibility to emulate Bose–Einstein condensates (BEC) in a water tank is elaborated. It is shown that the equation governing the mean-field BEC dynamics, viz., the Gross–Pitaevskii (GP) equation, can be derived in the same form for surface water waves in a tank with a spatially varying background current. Depending on the wavenumber of the carrier wave, the GP equation for the surface waves is tantamount to the GP equation corresponding to the attractive or repulsive inter-atomic interactions in BEC. The external potential in the effective GP equation can be easily implemented in the water tank with an uneven bottom featuring a well or hump. Examples of particular stable exact solutions of the GP equation with the effective potential are presented. Estimates for physical parameters of the hydrodynamic setting are given.

1 Introduction

The Bose–Einstein condensation (BEC) has drawn a great deal of attention in course of the last two decades. The condensate effect was experimentally demonstrated in various media, including ultracold atomic and exciton-polariton gases, etc. (see, e.g., Refs. [1–4] and references therein). The use of particular external potentials is a necessary ingredient of these experiments, which are run in sophisticated setups. On the other hand, many dynamical matter-wave regimes characteristic to BEC may be emulated, using simpler equipment, in water-wave tanks. To promote this possibility, in the present work we demonstrate that the basic mean-field BEC model, known as

---

G. Rousseaux (✉)
CNRS, Institut Pprime, UPR 3346, Université de Poitiers - ISAE ENSMA,
11 Boulevard Marie et Pierre Curie, Téléport 2, Futuroscope Cedex 30179, 86962, France
e-mail: Germain.Rousseaux@univ-poitiers.fr

Y. Stepanyants
Faculty of Health, Engineering and Sciences, School of Agricultural,
Computational and Environmental Sciences, University of Southern Queensland,
West St., 4350 Toowoomba, QLD, Australia
e-mail: Yury.Stepanyants@usq.edu.au

N. Abcha et al. (eds.), *Nonlinear Waves and Pattern Dynamics*,
https://doi.org/10.1007/978-3-319-78193-8_5

the Gross–Pitaevskii (GP) equation, can be derived for surface water waves in a tank with a spatially varying current. Depending on the wavenumber of the carrier wave, the effective GP equation for the surface waves can be made equivalent to the GP equation with both attractive and repulsive inter-atomic interactions in BEC. External potentials in the GP equation for water waves can be easily emulated in the water tank with an uneven bottom, featuring wells or humps. Particular exact solutions of the effective GP equation are reported here, and estimates for their realization in the water tank are given.

2 Derivation of the Effective Gross–Pitaevskii Equations for Waves on the Surface of Moving Water

Following Ref. [5], we consider water-wave propagation on top of a smoothly varying current along the x-axis, with flow velocity $U(x) = U_0 + U_1(x)$ including a constant mean value U_0 and a small variable component $U_1(x)$, with $\max[|U_1(x)|]/U_0 \ll 1$ (as shown below, the latter term may be induced by a bottom profile of the tank). For a counter-current propagating sinusoidal wave of a small but finite amplitude A, with frequency ω and wavenumber k, the dispersion relation for deepwater in the laboratory reference frame is [5]

$$\omega = -U(x)k + \sqrt{gk\left(1 + Tk^2\right)}\left(1 + \frac{A^2k^2}{2}\right), \tag{2.1}$$

where g is the gravity acceleration, $T = \sigma/\rho\, g$, σ is the surface tension, ρ the water density, and only the term $\sim \varepsilon^2$ with respect to the wave steepnes, $\varepsilon = Ak$, is retained in the respective expression for the Stokes' correction to the wave frequency (see, e.g., Refs. [6, 7]). It is assumed that spatial scale L of the variation of the external current is much greater than the wavelength $\lambda = 2\pi/k$, which makes it meaningful to consider the x-dependent frequency in Eq. (2.1). Figure 1 schematically illustrates the respective configuration of the flow and counter-current propagating wave packet.

We consider a weakly modulated wavetrain with the central wave number k_0 and frequency $\omega_0 = -U_0k_0 + \sqrt{gk_0\left(1 + Tk_0^2\right)}$. Dispersion relation (2.1) can be expanded around the point (ω_0, k_0, $A = 0$) into the Taylor series up to the terms of the order of ε^2 (see Refs. [5, 8, 9])

$$\omega - \omega_0 = \frac{\partial\omega}{\partial k}(k - k_0) - U_1k_0 - \frac{1}{2}\frac{\partial^2\omega}{\partial k^2}(k - k_0)^2 + \frac{\partial\omega}{\partial A^2}(Ak_0)^2, \tag{2.2}$$

where

$$\frac{\partial\omega}{\partial k} = c_g\frac{1 + 3Tk_0^2}{\sqrt{1 + Tk_0^2}} - U_0, \quad \frac{\partial^2\omega}{\partial k^2} = \frac{c_g}{2k_0}\frac{\left(1 - 3Tk_0^2\right)^2 - 12T^2k_0^4}{\left(1 + Tk_0^2\right)^{3/2}},$$

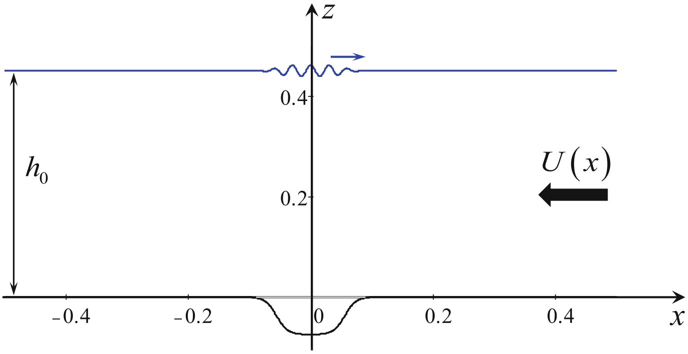

Fig. 1 A sketch of the surface wave train propagating against the current in a water tank with a bottom well

$$\frac{\partial\omega}{\partial A^2} = \frac{c_g k_0}{8}\frac{8 + Tk_0^2 + 2T^2k_0^4}{\left(1 + Tk_0^2\right)^{3/2}\left(1 - 2Tk_0^2\right)}(Ak_0)^2,$$

where $c_g = (1/2)\sqrt{g_0 k_0}$ is the group velocity of a purely gravity wave with the wavenumber k_0 on still water, and

$$\omega{-}\omega_0 \sim k{-}k_0 \sim \varepsilon, \ \max\left[|U_1(x)|\right]/U_0 \sim \varepsilon^2. \tag{2.3}$$

(recall that $\varepsilon \ll 1$ is the small wave steepness).

The evolution equation in the $(x,\ t)$-space corresponding to dispersion relation (2.2) can be easily restored by replacing $\omega - \omega_0 \to i\ \partial/\partial t$ and $k - k_0 \to -i\ \partial/\partial x$ [5, 10, 11]. Thus we obtain the equation for a slowly varying in space and time complex amplitude of a wave train

$$i\left(\frac{\partial A}{\partial t} + V_g\frac{\partial A}{\partial x}\right) = U_1(x)k_0A - \alpha\left|A\right|^2 A - \beta\frac{\partial^2 A}{\partial x^2}, \tag{2.4}$$

where the group velocity of gravity-capillary waves propagating on top of a current is

$$V_g(k_0, U_0) = c_g\frac{1 + 3Tk_0^2}{\sqrt{1 + Tk_0^2}} - U_0, \tag{2.5}$$

and the coefficients in Eq. (2.4) are

$$\alpha = \frac{c_g k_0^3}{8}\frac{8 + Tk_0^2 + 2T^2k_0^4}{\left(1 + Tk_0^2\right)^{3/2}\left(1 - 2Tk_0^2\right)}, \tag{2.6a}$$

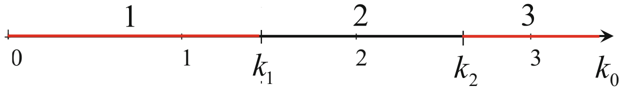

Fig. 2 Intervals of instability (*1* and *3*) and stability (*2*) for sinusoidal surface waves

$$\beta = \frac{1}{2}\frac{d^2\omega}{dk^2}\bigg|_{k=k_0} = \frac{c_g}{4k_0}\frac{\left(1-3Tk_0^2\right)^2 - 12T^2k_0^4}{\left(1+Tk_0^2\right)^{3/2}}. \tag{2.6b}$$

A similar equation was derived in Ref. [12] for purely gravity waves (the rigorous derivation of such equation with the help of the asymptotic expansion method can be found in Rev. [5]).

If we choose for the counter-current propagating wave the speed of the underlying current such that $V_g = 0$, i.e., $U_0 = c_g\ (1+3Tk_0^2)/(1+Tk_0^2)^{1/2}$, then we obtain the standard Gross–Pitaevskii equation [1]

$$i\frac{\partial A}{\partial t} + \alpha\,|A|^2 A + \beta\frac{\partial^2 A}{\partial x^2} - U_1(x)k_0A = 0, \tag{2.7}$$

where $U_1(x)$ plays a role of the external potential, which is shaped as a well, with $U_1(x) < 0$, and as a hump, with $U_1(x) > 0$.

Equation (2.7) without the external potential reduces to the integrable nonlinear Schrödinger (NLS) equation [7–10]. Depending on coefficients α and β, cnoidal-wave periodic solutions of the NLS equation can be stable or unstable against self-modulating perturbations. According to the Lighthill criterion [7, 9], the stability occurs at $\alpha\beta < 0$, and the instability takes place at $\alpha\beta > 0$. The analysis of coefficients α and β shows [8, 9] that, in the case of purely gravity waves, both α and β are positive, hence the sinusoidal wavetrains are unstable, when $Tk_0^2 < 2/\sqrt{3} - 1 \approx 0.155$. In the relatively narrow range, $2\sqrt{3}/3 - 1 < Tk_0^2 < 1/2$, the signs are $\alpha > 0$ and $\beta < 0$, hence the waves are modulationally stable. Finally, when $Tk_0^2 > 1/2$, both α and β are negative, hence the cnoidal waves are again modulationally unstable. The critical wavenumbers, at which coefficients β and α change their signs for clean water at temperature 25 °C are, respectively, $k_1 = 1.452\ \text{cm}^{-1}$ ($\lambda_1 = 4.33$ cm) and $k_2 = 2.61\ \text{cm}^{-1}$ ($\lambda_1 = 2.41$ cm). Note that the group velocity in still water, $V_g(k, 0)$, attains a minimum at the former critical point k_1 [7]. At both critical points $k_{1,2}$, Eq. (2.7) should be replaced with a more complex equation [5] (we do not consider such degenerate cases in detail here). Figure 2 shows the intervals of wavenumbers where the modulational stability and instability occur.

In the next sections we demonstrate that, using various shapes of the bottom well, one can produce different corrections to the main flow $U_1(x)$ in a water tank, via the conservation of the flow rate through the tank's cross-section, $U_1(x)h_1(x) = \mathrm{const}$. For some shapes of the bottom well, exact solutions of the effective GP equation can be constructed both for the repulsive and attractive signs of the nonlinear term. It is easy to make bottom wells of various shapes in the tank, and trapped surface waves on top of the corresponding current can be readily observed in the experiment.

3 An Example of Exact Solution of the Effective Gross–Pitaevskii Equation in the Modulationally Stable Case

In this section, we demonstrate that one of the basic exact solutions of the GP equation can be realized in the laboratory experiment with modulationally stable surface waves belonging to the interval 2 shown in Fig. 2. To this end, we first assume the presence of a constant water flow $U_0 = 0.185$ m/s in the tank of constant depth $h_0 = 0.45$ m. Figure 3 displays the dispersion relation (2.1) for surface waves of infinitesimal amplitude (with $A = 0$) and constant current speed U_0.

Further, we assume the presence of a shallow well in the central part of the tank's bottom, which modifies the total depth so that

$$h(x) = h_0 \left\{ 1 + F \left[\tanh\left(\frac{x}{\Delta} + \phi \right) - \tanh\left(\frac{x}{\Delta} - \phi \right) \right] \right\}, \tag{3.1}$$

where $\phi = \frac{1}{4} \ln \frac{1+\nu}{1-\nu}$, $\Delta = \sqrt{\frac{-6\beta}{\nu F k_0 U_0}}$, $F > 0$ and ν being free parameters ($0 < \nu < 1$), which control the depth of the cavity and its shape. The largest variation of the depth, corresponding to Eq. (3.1), is

$$\delta h = h(0) - h_0 = 2 h_0 F \frac{1 - \sqrt{1 - \nu^2}}{\nu}. \tag{3.2}$$

The front and rear slopes of the well, Δ, depend monotonically on parameter ν, decreasing from infinity to $\Delta_{\mathrm{min}} = \sqrt{-6\beta / (F k_0 U_0)}$, when ν varies from 0 to 1. The characteristic width of the well, L, i.e., the distance between its frontal and rear segments at the half-maximum level, $\delta h/2$, is

$$L = \sqrt{\frac{-6\beta}{\nu F k_0 U_0}} \ln \left(\frac{2\sqrt{1-\nu^2} + 1 + \sqrt{4 - 3\nu^2 + 4\sqrt{1-\nu^2}}}{\sqrt{1-\nu^2}} \right). \tag{3.3}$$

At $\nu \to 0$, the well takes the shape of an inverted bell, whose width increases as $1/\sqrt{\nu}$: $L \approx \sqrt{\frac{-6\beta}{\nu F k_0 U_0}} \ln \left(3 + \sqrt{8} \right)$. In another limit, $\nu \to 1$, the well becomes very wide too, with the width increasing as $L \approx \sqrt{\frac{-3\beta}{2 F k_0 U_0}} \ln \frac{2}{1-\nu}$. The minimum width,

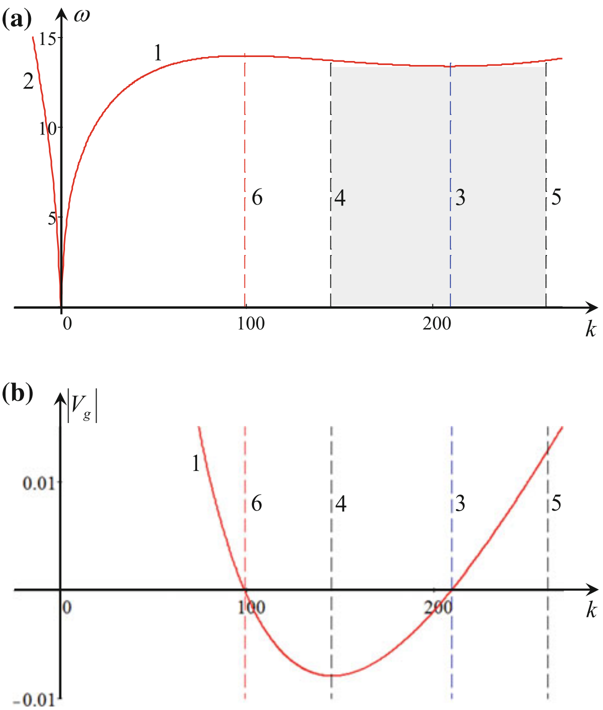

Fig. 3 The dispersion relation for surface waves with an infinitesimal amplitude. Frame **a** shows ω (k) as per Eq. (2.1) with $A = 0$; frame **b** shows the group velocity in the presence of the underlying current. Lines 1 and 2 pertain, respectively, to counter-and co-current propagating waves (the group velocity for the latter branch is not shown). Vertical dashed lines 3 and 6 correspond to the carrier waves with $k_0 = 2.1\ \text{cm}^{-1}$ and $k_0 = 0.985\ \text{cm}^{-1}$, respectively; dashed lines 4 and 5 show the boundaries of the shaded domain where sinusoidal waves are modulationally stable. Line 4 corresponds to k_1, and line 5—to k_2, as per Fig. 2

$L_{\min} \approx 2.2\sqrt{\frac{-6\beta}{Fk_0U_0}}$, is attained at $\nu \approx 0.821$. All such shapes can be readily designed in the experimental setup.

Due to the conservation of the mass flux through any cross-section, the variation of the depth causes the variation of the speed, therefore, above the bottom well, the current varies as follows:

$$U(x) = \frac{U_0}{1 + F\left[\tanh\left(\frac{x}{\Delta} + \phi\right) - \tanh\left(\frac{x}{\Delta} - \phi\right)\right]} \approx U_0\left\{1 - F\left[\tanh\left(\frac{x}{\Delta} + \phi\right) - \tanh\left(\frac{x}{\Delta} - \phi\right)\right]\right\}, \tag{3.4}$$

where the condition $F \ll 1$ is assumed, hence the effective potential in Eq. (2.7) is

$$U_1(x) = -U_0F\left[\tanh\left(\frac{x}{\Delta} + \phi\right) - \tanh\left(\frac{x}{\Delta} - \phi\right)\right]. \tag{3.5}$$

To realize the dynamical regime corresponding to the GP equation with the self-attraction, we chose a surface mode with wavelength $\lambda_0 = 3$ cm ($k_0 = 2\pi/\lambda_0 = 2.1$ cm^{-1}) and amplitude $A \approx 1$ mm, hence the corresponding wave steepness, $\varepsilon = Ak_0 = 0.21$, may be considered as a small parameter. For such a wave, even in a relatively shallow section of the tank we have $k_0h_0 = 135 \gg 1$, which means that the deepwater condition is achieved. The absolute value of the group velocity of such a wave in the absence of the underlying current is $V_g(k_0, 0) = 18.5$ cm/s, whereas the minimal group velocity for given parameters is $V_{\min} = -0.79$ cm/s, see Fig. 3b. An obviously interesting possibility is to observe a "standing water soliton", i.e., to bring the wavetrain, traveling counter-current, to a halt in the laboratory frame. To this end, we set $U_0 = c_g\left(1 + 3Tk_0^2\right)/\sqrt{1 + Tk_0^2}$; according to Eqs. (2.5), and (2.6a, 2.6b) this determines the nonlinearity and dispersion coefficients in GP Eq. (2.7): $\alpha = 3.348 \times 10^2$ cm^{-2} s^{-1}, $\beta = -1.806 \times 10^2$ cm^2 s^{-1}.

As has been shown in Ref. [13], the GP equation with the potential given by Eq. (3.5) admits the exact solution in the form of

$$A(x,t) = \exp\left(-i\Omega t\right)\sqrt{\frac{\nu F k_0 U_0}{3\alpha}}\left[\tanh\left(\frac{x}{\Delta} + \phi\right) - \tanh\left(\frac{x}{\Delta} - \phi\right)\right], \tag{3.6}$$

where $\Omega = 2\nu\ F\ k_0U_0/3$ is a nonlinear correction to the wave frequency ω_0, and the amplitude of the localized state is

$$A\max = 2\sqrt{\frac{F k_0 U_0}{3\alpha\nu}}\left(1 - \sqrt{1 - \nu^2}\right). \tag{3.7}$$

The total norm of this solution (which gives a scaled number of atoms in the application to BEC) is

$$N = \int\limits_{-\infty}^{+\infty} |A(x)|^2 dx = \frac{4\nu F k_0 U_0 \Delta}{3\alpha}\left[2\phi\ \coth(2\phi) - 1\right]. \tag{3.8}$$

The normalized squared absolute value of solution (3.6), corresponding to the local density of atoms in BEC, along with the normalized potential, $U_1(x)/(U_0F)$, are shown in Fig. 4 for several values of free parameter ν. As demonstrated in Ref. [13], this exact solution is actually the ground state of the GP equation with the repulsive nonlinearity and potential well (3.5), hence this solution is definitely stable.

Thus, a surface gravity-capillary wave with carrier wavelength $\lambda_0 = 3$ cm can be trapped in the water flow over the bottom well. If one takes, for example, the value of the free parameter $F = 0.15$, the largest depth of the well at $\nu = 0.999$ is $\delta h \equiv h_{\max} - h_0 = 12.9$ cm, so that $\delta h/h_0 = 0.29$. The width of the well is $L \approx 53$ cm, according to Eq. (3.2), the envelope of the trapped wavetrain having the same width, see Fig. 4. The amplitude of the wave is $A_{\max} = 1.5$ mm, hence $(k_0A_{\max})^2 = 0.3$, whereas $(|U_1(x)/U_0|)_{\max} = 0.29$, which agrees with the assumption of the smallnesses of the

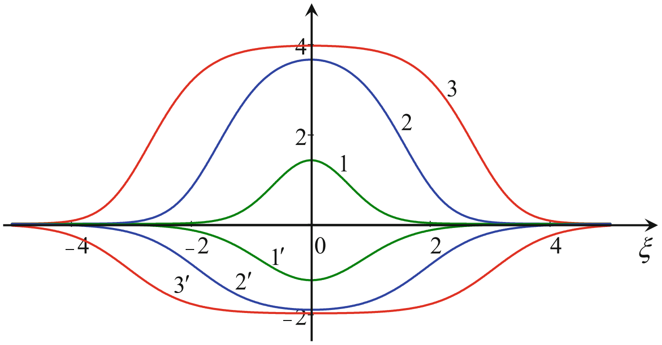

Fig. 4 Normalized solution (3.6) in terms of $3\alpha\ |A(x)|^2/(FU_0k_0)$ (lines labeled 1, 2, 3), and the corresponding normalized potentials $U_1(x)/(U_0F)$ (lines labeled 1′, 2′, 3′) as functions of dimensionless coordinate $\xi = x/\Delta$. Lines 1 and 1′ pertain to $\nu = 0.9$; lines 2 and 2′ to $\nu = 0.999$; lines 3 and 3′ to $\nu = 0.99999$

wave steepness and modulation of the basic current, $(|U_1(x)/U_0|)_{\max}$ and ε^2 being of the same order of magnitude, in agreement with Eq. (2.3).

It has been shown in Ref. [13] that there are many other exact stable solutions of the GP equation with the corresponding potentials, which can be easily realized in a water tank.

4 An Example of Exact Solution of the Effective Gross–Pitaevskii Equation in the Modulationally Unstable Case

We now consider the situation with a small bell-shaped well in the central part of the tank's bottom which modifies the depth as [cf. Eq. (3.1), which represented another well's profile]

$$h(x) = h_0\left[1 + \frac{F}{1 + B\ \cosh(x/\Delta)}\right], \tag{4.1}$$

where Δ and $B > 1$ are free parameters, which control the depth and width of the cavity, and F is a function of Δ, to be specified below. The maximal variation of well's depth is

$$\delta h \equiv h(x) - h_0 = \frac{h_0 F}{1 + B}. \tag{4.2}$$

where it is assumed that second term in the square brackets is small in comparison with 1.

To consider the effective GP equation with the self-attraction, i.e., modulational instability of the surface wave, we choose it with wavelength $\lambda_0 = 6.4$ cm ($k_0 = 2\pi/\lambda_0 = 0.985$ cm^{-1}) and amplitude $A \approx 3.24$ mm, so that the wave steepness $\varepsilon = Ak_0 \approx 0.32$ may again be treated as a small parameter. For such a wave, even in a relatively shallow section of the tank we have $k_0h_0 = 44.33 >> 1$, which means that the deepwater approximation remains valid. The group velocity of such a wave in the absence of the underlying current is the same as in the previous example, viz., $V_g(k_0, 0) = 18.5$ cm/s, see Fig. 3b. To bring a counter-current traveling wavetrain to a halt in the laboratory frame (as done above, to produce a "standing water hump") we again set $U_0 = V_g(k_0, 0)$, pursuant to Eq. (2.5). Then Eq. (2.6a, 2.6b) produces the nonlinearity and dispersion coefficients of GP Eq. (2.7): $\alpha = 18.6$, cm^{-2} s^{-1}, $\beta = 2.385 \times 10^2$, cm^2 s^{-1}, and the effective potential,

$$U_1(x) = \frac{-U_0 F}{1 + B\ \cosh(x/\Delta)}. \tag{4.4}$$

It is easy to check that the GP equation with this potential and self-attractive cubic term has an exact localized solution (a soliton pinned to the potential well) in the form of

$$A(x,t) = \frac{R\ \exp(-i\Omega t)}{1 + B\ \cosh(x/\Delta)}, \tag{4.5}$$

where $\Omega = \beta/\Delta^2$ is a nonlinear correction to the wave frequency ω_0, and R and F are expressed in terms of free parameters B and Δ:

$$R = \frac{1}{\Delta}\sqrt{\frac{2\beta}{\alpha}\left(B^2 - 1\right)}, \quad F = \frac{-3\beta}{U_0 k_0 \Delta^2}. \tag{4.6}$$

The amplitude of this pinned soliton is

$$A\text{max} = \frac{R}{1 + B} = \frac{1}{\Delta}\sqrt{\frac{2\beta}{\alpha}\frac{B-1}{B+1}}. \tag{4.7}$$

The stability of this solution was verified in Ref. [13]. The profile of its squared absolute value, corresponding to the local density of atoms in BEC, along with the respective normalized potential, $U_1(x)/(U_0b)$, are shown in Fig. 5 for dimensionless parameter $B = 2.5$ and $\Delta = 25$ cm.

Thus, we see that the surface gravity wave with the carrier wavelength $\lambda_0 = 6.4$ cm can be trapped in the water flow over the bottom well considered here. For the chosen free parameters B and Δ we find that the maximal depth of the well is $\delta h \equiv h_{\max} - h_0 = 0.8$ cm ($\delta h/h_0 \approx 0.018$). The number of periods of the carrier wave within the envelope of the localized trapped mode is $2\Delta/\lambda_0 \approx 8$. The same width has the envelope of the trapped wave train. The amplitude of the mode is $A_{\max} \approx 1.3$ mm, hence the corresponding wave steepness is $\varepsilon \equiv k_0A_{\max} \approx 0.13$. The largest variation of the mean flow, induced by the bottom well, is $|U_1(x)/U_0|_{\max} \approx 0.018$. This agrees

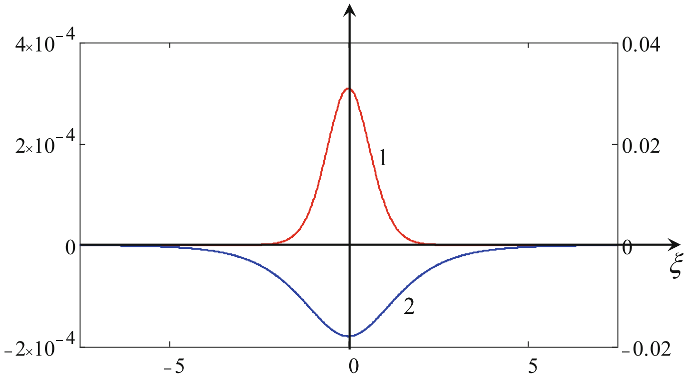

Fig. 5 The squared absolute value of solution (4.5) (line 1) and the corresponding normalized potential $U_1(x)/(U_0)$ (line 2), as functions of dimensionless coordinate $\xi = x/\Delta$. The left and right scales pertains, respectively, to lines 1 and 2

well with our underlying assumptions about the smallnesses of the wave steepness, and $|U_1(x)/U_0|_{\max} \sim \varepsilon^2$, see Eq. (2.3).

In the case of purely gravity waves, when the GP equation has the attractive nonlinearity, many other exact solutions with the corresponding potentials are available [13]; they can be relatively easy realized in the water tank, using the surface waves with $\lambda > 4.3$ cm.

5 Conclusion

In this chapter we have shown that surface waves propagating against the external current, slowly varying in the horizontal direction in deepwater, are governed by the equation which is tantamount to the GP (Gross–Pitaevskii) equation modeling the mean-field BEC dynamics. The repulsive or attractive sign of the cubic term is controlled by the choice of the carrier wavelength of the surface waves, while the spatial variation of the current plays the role of the external potential in the GP equation. The current profile can be easily controlled in the experiments by small variation of bottom profile, so that the corresponding effective potential in the GP equation can be made in the form of a well or hump. We assume that the free surface remains flat when water flows around a bottom obstacle which is simplification of course because the current induces in general a standing free surface perturbation. But at certain conditions the surface perturbation can be made small.

For some particular bottom profiles the effective GP equation admits exact solutions, which can be experimentally implemented in the water tank with the background current. Thus, the phenomenon of the Bose–Einstein condensation can be effectively emulated in relatively simple laboratory setups for water waves. Generating perturbations with an appropriate carrier wavelength, one can create patterns in the form of trapped waves which correspond to pinned states of the GP equation with local potentials. Our estimates presented in the chapter demonstrate that the parameters of bottom profile, background current, and surface waves are quite accessible to laboratory experiments.

Finally, we note that, formally speaking, in addition to what is elaborated above, the GP equation can be also implemented in the domain 3 in Fig. 4 for purely capillary waves with $\lambda < 2.4$ cm. However, for such short waves water viscosity becomes important, which would complicate the comparison between the theoretical results predicted by the GP equation and observations.

Acknowledgements The authors are thankful to B. Malomed for the comments and helpful advices. This work was initiated when one of the authors (Y.S.) was an invited Visiting Professor at the Institut Pprime, Université de Poitiers in August–October, 2016 thankful to the grant from Region Poitou–Charentes. G.R. acknowledges funding from the ANR grant HARALAB No ANR-15-CE30-0017-04.

References

1. Pitaevskii, L.P., and Stringari, S. (2003). *Bose–Einstein Condensation*, Clarendon, Oxford.
2. Kasprzak, J., Richard, M., Kundermann S., Baas, A., Jeambrun, P., Keeling, J.M.J., Marchetti, F.M., Szymańska, M.H., André, R., Staehli, J.L., Savona, V., Littlewood, P.B., Deveaud, B., and Le Si Dang. (2006). Bose–Einstein condensation of exciton polaritons. Nature, v. 443, 409–414.
3. Byrnes, T., Kim, N. Y., and Yamamoto, Y. (2014). Exciton–polariton condensates. Nature Phys., v. 10, 803–813.
4. Pethick, C.J., and Smith, H. (2008). *Bose–Einstein Condensation in Dilute Gases*. Cambridge University Press, 2nd Edition.
5. Stocker, J.R., and Peregrine, D.H. (1999). The current-modified nonlinear Schrödinger equation. J. Fluid Mech., v. 399, 335–353.
6. Lamb, H. (1932). *Hydrodynamics*, 6th edn. Cambridge University Press.
7. Whitham, G.B. (1974). *Linear and nonlinear waves*, Wiley Interscience Publ., John Wiley and Sons, N. Y.
8. Djordjevic, V.D., and Redekopp, L.G. (1977). On two-dimensional packets of capillary-gravity waves. J. Fluid Mech., v. 79, pt. 4, 703–714.
9. Ablowitz, M.J., and Segur, H. (1981). *Solitons and the Inverse Scattering Transform*, SIAM, Philadelphia.
10. Yuen, H.C., and Lake, B.M. (1982). Nonlinear dynamics of deep-water gravity waves. Adv. Appl. Mech., v. 22, 67–229.
11. Korpel. A., and Banerjee, P.P. (1984). A heuristic guide to nonlinear dispersive wave equations and soliton-type solutions. Proc. IEEE, v. 72, n. 9, 1109–1130.
12. Bakhanov, V.V., Kemarskaya, O.N., Pozdnyakova, V.I., Okomel'kova, I.A., and Shereshevsky, I.A. (1996). Evolution of surface waves of finite amplitude in field of inhomogeneous current. Proc. Intl. Geoscience & Remote Sensing Sympos. v. 1, 609–611.
13. Malomed, B.A., and Stepanyants, Y.A. (2010). The inverse problem for the Gross – Pitaevskii equation. Chaos, v. 20, 013130, 14 p.

Laboratory and Numerical Modeling of Stably Stratified Wind Flow Over Water Surface

O. A. Druzhinin, D. A. Sergeev, Yu I. Troitskaya, W.-T. Tsai and M. Vdovin

Abstract The objective of this chapter is to perform laboratory and direct numerical modeling of turbulent wind over water surface under stable stratification conditions. Laboratory and numerical experiments are performed under the same bulk Reynolds and Richardson numbers which allow a direct comparison between the measurements and calculations. The laboratory experiments are performed in a wind-wave flume on the basis of a thermostratified tank facility at IAP RAS. A sufficiently strong stable stratification (with the air–water temperature difference of up to 18 K) and a comparatively large bulk Richardson number (up to Ri $\approx$ 0.04) in the experiment are created by heating the incoming air flow while maintaining a relatively low wind speed (up to 3 m/s) and the corresponding bulk Reynolds number up to Re $\approx$ 60000. The air velocity field is retrieved by employing both contact (Pitot tube) and PIV methods, and the air temperature profile is measured simultaneously by a set of contact probes. The same bulk Ri and Re are prescribed in direct numerical simulation where turbulent Couette flow is considered as a model of the near water constant stress atmospheric boundary layer. The mean velocity and temperature profiles obtained in our laboratory and numerical experiments agree well and also are well predicted by the Monin–Obukhov similarity theory. The results show that sufficiently strong stratification, although allowing a statistically stationary turbulent regime, leads to a drastic reduction of both turbulent momentum and heat fluxes. Under this regime, the flow turbulent Reynolds number (based on the Obukhov length scale and friction velocity) is found to be in agreement with known criteria characterizing stationary strongly stratified turbulence.

O. A. Druzhinin (✉) · D. A. Sergeev · Yu I. Troitskaya · M. Vdovin
Institute of Applied Physics, Russian Acad. Sci, Nizhny Novgorod, Russia
e-mail: druzhinin@hydro.appl.sci-nnov.ru

D. A. Sergeev
e-mail: sergeev4758@gmail.com

Yu I. Troitskaya
e-mail: yuliyatrinity@mail.ru

W.-T. Tsai
Taiwan National University, Taipei, Taiwan

N. Abcha et al. (eds.), *Nonlinear Waves and Pattern Dynamics*,
https://doi.org/10.1007/978-3-319-78193-8_6

1 Introduction

Detailed knowledge of the properties of small-scale processes occurring in atmospheric boundary layer over water surface is important for correct parameterization of turbulent exchange in marine atmospheric boundary layer in large-scale weather and climate prognostic models. Under the conditions of relatively small (about several degrees of K) air–water temperature difference and sufficiently high wind speed (typically, about several m/s) the air flow in the boundary layer (BL) is weakly stratified and turbulent, and its properties are well predicted by the Monin–Obukhov similarity theory (MOST) [7]. Of special interest are subcritical regimes under a sufficiently strong stratification, where the flow is still statistically stationary and turbulent although turbulent momentum and heat fluxes are drastically reduced as compared to the weakly stratified flow. In practice, such BL regime can be realized, for example, when a relatively warm inland air is advected over a cooler sea or lake in the spring season wherein the air–water temperature difference can become quite significant (more than 10 K) to render stratification effects to become strong at sufficiently low winds (about or below 3 m/s) [1, 2].

Available field observations and laboratory experimental measurements show that strong stable stratification effectively suppresses turbulent momentum and heat fluxes in the boundary layer as compared to the weakly stratified turbulent regime under which MOST parameterization is still applicable [3]. Detailed experimental measurements of the velocity and temperature profiles in the stably stratified boundary layer, both for weakly stratified and strongly stratified regimes, were performed by Ohya et al. [4]. In this experiment, the air flow over a cooled flat solid floor in thermally stratified wind tunnel was investigated. The bulk inflow air velocity U_0 was in the range from 0.8 m/s to 3 m/s and the difference between the air and surface temperatures ΔT was in the range from 46 to 53 K with the resulting bulk Reynolds number $\mathrm{Re} = \mathrm{O}(10^4 \div 10^5)$ and bulk Richardson number $\mathrm{Ri} = \mathrm{O}(0.1 \div 1)$. These experimental results suggest that under the influence of stable stratification the air velocity in the boundary layer, normalized by the free-stream air velocity, is decreased as compared to the non-stratified flow. The results also show that turbulent momentum flux was reduced by strong stable stratification as compared to the neutrally stratified flow case. However, there was no comparison given between the experimental results obtained under strong stratification conditions and predictions of MOST.

In our earlier study, we investigated stably stratified turbulent flow over water surface by performing direct numerical simulation (DNS) for a range of bulk Richardson and Reynolds numbers [5]. DNS does not require any parameterization and resolves all physically relevant flow scales up to viscous dissipation (Kolmogorov) length. At sufficiently small Ri, DNS reproduces statistically stationary turbulent regime with vertical profiles of mean velocity and temperature obeying the Monin–Obukhov similarity theory. At large Ri turbulence degenerates. We investigated the transition from turbulent to laminar regime as dependent on both Reynolds and Richardson numbers, and compared our results with those of the previous study by Flores and Riley [6]. These authors compiled available laboratory and numerical data and performed

DNS of their own to analyze the transition from turbulent to laminar regime in terms of a *turbulent Reynolds number*, Re_L, based on the Obukhov length scale and friction velocity. The basic result obtained by Flores and Riley [6] is that the stationary turbulent regime is maintained at $\mathrm{Re}_L > 100$; otherwise turbulence degenerates and the flow becomes laminar. Our DNS confirmed this conclusion. However, there is still an insufficient knowledge of a threshold regime, where BL can still be regarded in a statistically stationary turbulent regime, where MOST predictions still correctly predicts the flow properties. This study aims at laboratory and numerical study of such regimes.

We perform both laboratory modeling and DNS of turbulent air wind over water surface under both weak and strong stable stratification conditions. The laboratory and numerical experiments are performed under the same bulk Reynolds and Richardson numbers which allow a direct comparison between the measurements and DNS results. The laboratory experiment is performed in a wind-wave flume on the basis of a thermostratified tank facility at IAP RAS. A sufficiently strong stable stratification (with the air–water temperature difference up to 18 K) and a comparatively large bulk Richardson number (up to $\mathrm{Ri} \approx 0.04$) in the experiment is created by heating the incoming air flow while maintaining a relatively low wind speed (up to 3 m/s) and the corresponding bulk Reynolds number up to $\mathrm{Re} \approx 60000$. The air velocity field is retrieved by employing both contact (Pitot) and PIV methods, and the air temperature profile is measured simultaneously by a set of contact probes. The same bulk Ri and Re are prescribed in DNS. The mean velocity and temperature profiles obtained in laboratory and numerical experiments, for both regimes of weak and strong stratification, agree well and also are well predicted by the Monin–Obukhov similarity theory. The results also show that under strong stratification conditions, both turbulent momentum and heat fluxes are drastically reduced as compared to the weak stratification regime.

The chapter is organized as follows. In the next Sect. 2, for convenience, we briefly formulate the predictions of Monin–Obukhov similarity theory (MOST) for weakly stratified BL flow. In Sect. 3, laboratory and numerical experimental settings are presented, and the results are discussed. Section 4 contains discussion and conclusions.

2 MOST Predictions for Velocity and Temperature Profiles in Weakly Stratified BL Flow

Stably stratified boundary layers typically are classified as *weakly stable* if buoyancy effects are weak enough to allow a statistically stationary turbulent regime [3]. In this weakly stratified boundary-layer flow, the dependence of the mean velocity $U(z)$ and the deviation of mean temperature from its surface value, on height z in the region of constant turbulent stresses are described by the Monin–Obukhov similarity theory (MOST) (cf. [7]) as

$$\frac{U(z)}{u_*} = \frac{1}{\kappa}\left(\ln\frac{z}{z_{0U}} + C_U\frac{z}{L}\right), \tag{1}$$

$$\frac{T(z) - T_0}{T_*} = \frac{\mathrm{Pr}_t}{\kappa}\left(\ln\frac{z}{z_{0T}} + C_T\frac{z}{L}\right), \tag{2}$$

where κ is the von Karman constant, C_U and C_T are empirical dimensionless constants and Pr_t is the turbulent Prandtl number. The common estimates are $\kappa = 0.4$, $C_U = 2$, $C_T \sim C_U$, and $\mathrm{Pr}_t = 0.85$ as observed in most laboratory and field experiments. The turbulent velocity and temperature scales, namely, u_* (friction velocity measured in m/s) and T_* (measured in K) are expressed through turbulent stresses (i.e. momentum and heat fluxes), τ and F, as

$$u_* = \sqrt{\tau}, T_* = F/\sqrt{\tau}, \tag{3}$$

where τ and F are taken at sufficiently large distance from the surface, where they reach asymptotically constant values. The turbulent Prandtl number, Pr_t, is defined as

$$\underset{t}{\mathrm{Pr}} = \frac{u_*}{T_*}\frac{dT}{dz}\left(\frac{dU}{dz}\right)^{-1} \tag{4}$$

The Obukhov turbulent length scale L (measured in m) is

$$L = \frac{u_*^2}{(g/T_0)T_*}, \tag{5}$$

where g is the gravitational acceleration and T_0 the reference temperature. (Note that our definition of the Obukhov length scale L, Eq. (5), does not include the von Karman constant, κ, whereas the popular version of this scale, $\tilde{L}$, includes κ in the denominator, so that $\tilde{L} = L/\kappa$. Then the second term on the right-hand side in brackets in Eqs. (1) and (2) becomes $C_U\frac{\eta}{\kappa\tilde{L}} = \tilde{C}_U\frac{\eta}{\tilde{L}}$ where $\tilde{C}_U = \frac{C_U}{\kappa} = 5$.)

Roughness lengths z_{0U} and $z_{0\Theta}$ in the case of an aerodynamically smooth flat surface are determined by conventional relations (e.g., [7])

$$z_{0U} = \frac{\nu}{u_*}\exp(-5\kappa), \tag{6}$$

$$z_{0\Theta} = \frac{\nu}{u_*}\exp(-2.5\kappa), \tag{7}$$

where ν is the kinematic viscosity of the air.

The bulk Reynolds and Richardson numbers are conventionally defined as

$$\mathrm{Re} = \frac{U_0\delta}{\nu}, \tag{8}$$

$$\mathrm{Ri} = g\frac{\Delta T}{T_0}\frac{\delta}{U_0^2}. \tag{9}$$

Note that Eq. (1) does not give a direct answer to the question whether the air velocity will be enhanced or reduced, relative to bulk velocity, if the stratification strength (measured by the bulk Richardson number, Ri) is increased, since the turbulent stress (measured by the friction velocity) as well as the Obukhov length L both depend on the stratification strength.

3 Laboratory and Numerical Experiments

The laboratory experiment was performed in a Thermostratified wind-wave tank (TSWiWaT) of IAP over a smooth water surface (Figs. 1 and 2). Experiments were carried out for two cases: weakly stratified and strongly stratified air flow. In order to simulate stable temperature stratification of the air boundary layer, the input wind flow was heated before income but the temperature of the water surface remained unchanged. Thus in the weakly stratified case, the bulk temperature difference between air and water was about 4 K whereas in the strongly stratified case the temperature difference was about 20 K, and the wind bulk velocity was from 2 to 3 m/s in both cases. This setting of the laboratory experiment provides the bulk Reynolds and Richardson numbers in the range Re $\approx$ 40000–60000 and Ri $\approx$ 0.01–0.04, respectively. The measurements of the air velocity in the working section at the distance of 7.5 m from the inlet were performed with the use of Pitot tubes at different heights above the water surface (Fig. 1). Hotwire installed together with Pitot tubes was used for simultaneous air temperature measurements. In order to reduce statistical errors an ensemble averaging was performed over five different experimental realizations.

PIV technique was applied for retrieving instantaneous wind velocity fields. 20 μm polyamide seeding particles were injected in the flow at the first section of the channel (Fig. 2). Over the working section (with fetch 7.5 m) a continuous laser (1.5 Wt, 527 nm) was installed. Vertical laser sheet parallel to side walls of the channel was formed by a cylindrical lens. Motions of illuminated particles were recorded by a high-speed camera Videoscan Videosprint (3012 fps, exposure time 100 μs, frame size 1280 × 166 px (250 × 32 mm), scale 195 μm/px). For each regime, 20 records were obtained, and each record has the duration of 0.5–2 s. Instantaneous velocity fields were retrieved by comparison of consequent frames with the use of a correlation postprocessing analysis where mean visible displacement of particles corresponded to shift peak of cross-correlation function. Calculations were carried for interrogation window of 64 × 32 px evenly distributed on a rectangular grid with 50% overlap. Sub-pixel interpolation of CCF peak position by three points was used. Due to high levels of peak-locking (since whole values of displacement were more probable to retrieve) comparison between neighbor frames provided wrong results for velocity fluctuations and turbulent fluxes. So each frame was compared to the frame separated by three, five, and seven frames after it. Using this method increased visible particle displacement and reduced peak-locking influence. The resulting profiles were similar for different frame distances. These velocity fields were filtered by difference between

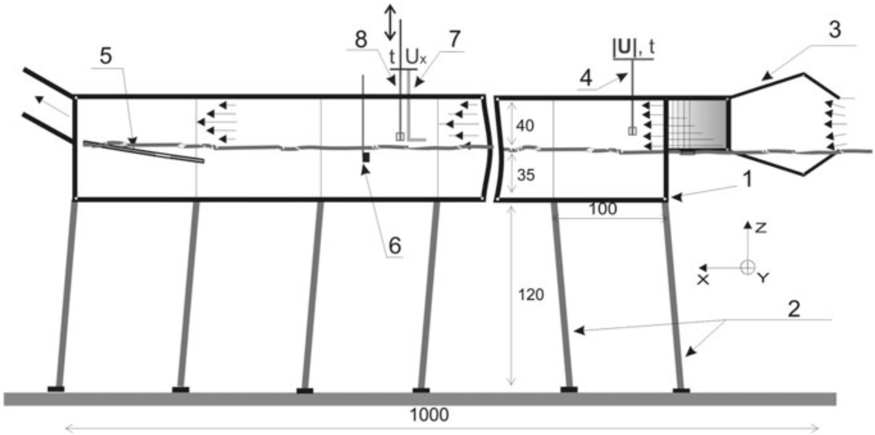

Fig. 1 Schematic of the laboratory experiment on the TSWiWaT (side view). All dimensions given in cm. 1—the wind channel 2—vertical beds 3—expanded-narrow section 4—hotwire controlling the incoming flow 5—wave damping beach 6—surface water temperature gauge 7—Pitot gauge installed on the scanning probe in the working section on the 8 m length from the income 8—hot wire installed together with Pitot

local velocity value and the median value at the given height. Mean velocity profiles were retrieved by averaging of the filtered velocity fields over time and horizontal coordinate. Mean velocity profiles were used for evaluation of the velocity fluctuation field which was also averaged in a similar way. By these means, the mean velocity and turbulent momentum flux profiles were retrieved for each record.

Direct numerical simulations of stably stratified Couette flow were performed at the same Re and Ri as in the laboratory experiment. The setup of the numerical experiment was similar to the one considered by Druzhinin et al. [5]. A Cartesian framework was considered where x-axis was oriented along the mean wind, z-axis is directed vertically upwards and y-axis was orthogonal to the mean flow. Periodical boundary conditions were considered in the x and y directions. The no-slip boundary conditions were prescribed at the top and bottom horizontal boundary planes separated by distance D and moving in the opposite directions along the x-axis with velocities $\pm 0.5\,U_0$. The stable density stratification was specified by prescribing the air temperature at the bottom surface as $T = T_0$ and the top boundary plane as $T = T_0 + \Delta T$, where $\Delta T > 0$.

Numerical algorithm was based on the integration of full, 3D Navier–Stokes equations for incompressible fluid under the Boussinesq approximation [5]. The governing parameters in DNS were the bulk Reynolds and Richardson numbers defined as

$$\mathrm{Re} = \frac{U_0 D}{\nu}, \tag{10}$$

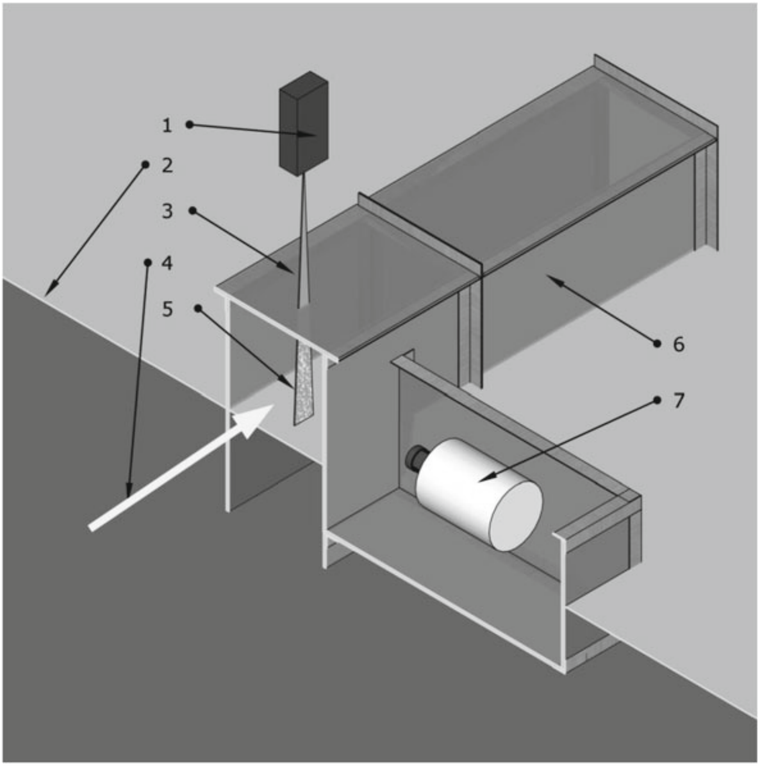

Fig. 2 Cross-wind section of the channel: 1—continuous laser; 2—water surface; 3—laser sheet; 4—wind direction; 5—PIV-particles; 6—underwater part of the channel; 7—high-speed camera in semi-submerged box

$$\mathrm{Ri} = g\frac{\Delta T}{T_0}\frac{D}{U_0^2}. \tag{11}$$

In DNS we prescribed $\mathrm{Re} = 40000$ and $\mathrm{Ri} = 0$, in the non-stratified case, and $\mathrm{Ri} = 0.04$, in the stratified case, which are in agreement with the parameters of the laboratory experiment. The organization of DNS procedure was similar to the one discussed by [5]. The velocity field in DNS was initialized as a weakly perturbed laminar Couette flow with the initial temperature deviation field put to zero. The integration was advanced in time until a statistically stationary flow regime was established. Then the sampling of the velocity and temperature fields was performed, and the mean vertical profiles of all fields were obtained by averaging over time and x and y coordinates.

Figure 3 compares mean velocity and temperature profiles obtained in the laboratory experiment and DNS. The figure also shows theoretically predicted profiles of mean velocity and temperature obtained with the use of Eqs. (1)–(5). Figure 3

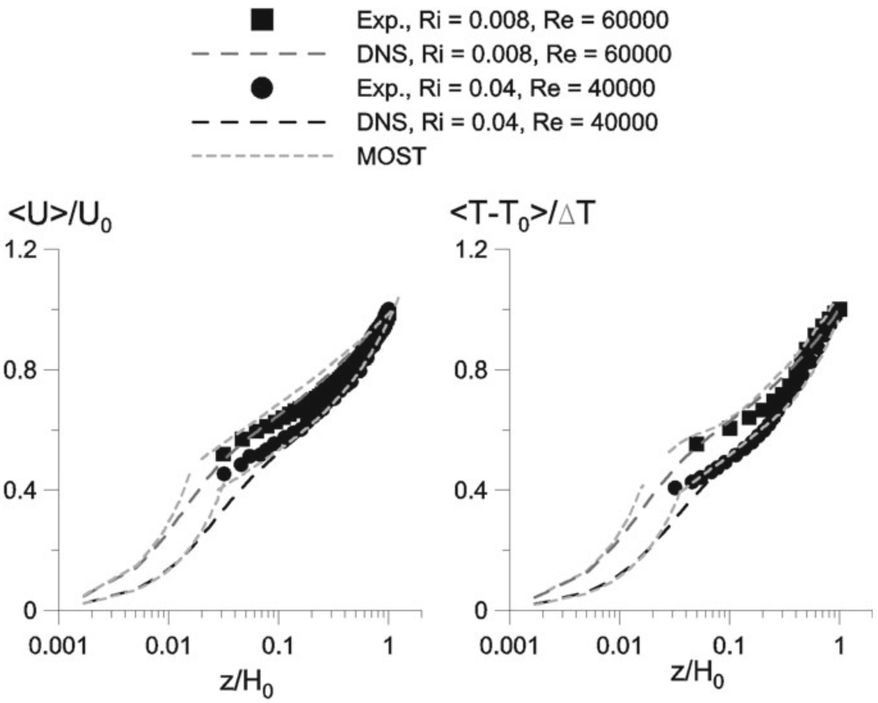

Fig. 3 Vertical mean velocity (left panel) and temperature (right panel) profiles in weakly- and strongly stratified boundary layer over smooth water surface obtained in laboratory experiment (symbols) and DNS (dashed curves). Theoretical predictions of MOST are in dotted line

presents profiles of turbulent fluxes, τ and F, and turbulent Prandtl number, Pr_t, evaluated as described in (4), obtained in DNS. The experimental velocity profiles are normalized by the maximum (bulk) velocity $U_0 = U(z = H_0)$, approximately in the middle of the flume at height $z = H_0 \approx 24$ cm. The mean temperature profile was normalized with $T_0 = T(H_0)$. The DNS profiles are normalized by the mean velocity and temperature in the middle of the computational domain at $z = 0.5D$.

Figure 3 shows very good agreement between the experimental and numerical results and theoretical prediction. Note that the best agreement for the mean temperature profile was obtained for constant coefficient $C_T = 6$.

Note also that the flow in DNS is in statistically stationary turbulent regime according to characterization developed by Flores and Riley [6]. These authors compiled available laboratory and numerical data and performed DNS of their own to analyze the transition from turbulent to laminar regime in terms of the *turbulent Reynolds number*, Re_L, based on the Obukhov length scale and friction velocity

$$\mathrm{Re}_L = \frac{L u_*}{\kappa \nu}. \tag{12}$$

Fig. 4 Vertical profiles of turbulent momentum flux, normalized by the bulk velocity, τ/U_0^2, obtained in the laboratory experiment in weakly stratified regime (squares), and the reduction of the momentum flux in the experiment and DNS (circles and dashed curve, respectively) under the strong stratification conditions

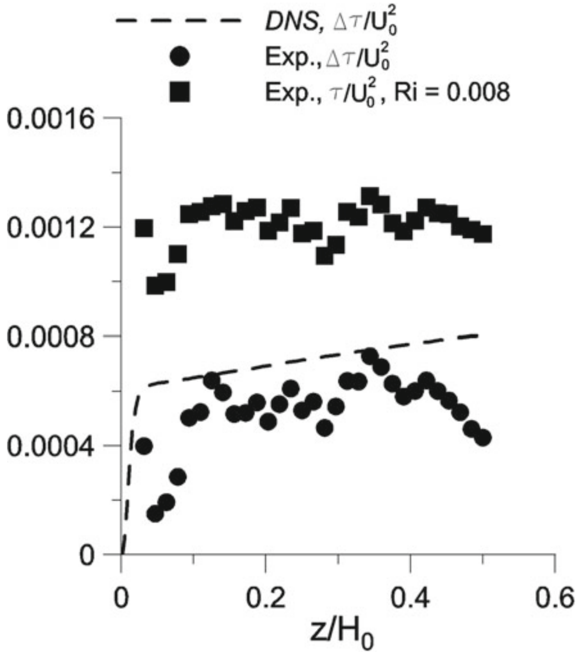

The basic result obtained by Flores and Riley [6] is that the stationary turbulent regime is maintained at $\mathrm{Re}_L > 100$; otherwise turbulence degenerates and the flow becomes laminar. In our numerical experiment $u_* \approx 0.018U_0$ and $L \approx 0.37D$, so that $\mathrm{Re}_L \approx 270$.

Figure 4 presents vertical profiles of turbulent momentum flux, normalized by the bulk velocity, τ/U_0^2, obtained in the laboratory experiment in weakly stratified regime with Ri $\approx$ 0.01 (squares), and the reduction of the momentum flux $\Delta\tau/U_0^2$ obtained in the experiment and DNS for bulk Rishardson and Reynolds numbers Ri $\approx$ 0.04 and Re $\approx$ 60000 (circles and dashed curve, respectively). The figure shows a drastic reduction of turbulent momentum flux (by more than 50%) under the strong stratification regime.

4 Conclusions

We have performed laboratory experiment and direct numerical modeling of turbulent wind over water surface under stable stratification conditions. The laboratory and numerical experiments have been performed under the same bulk Reynolds and Richardson numbers which allowed a direct comparison between the measurements and calculations. Laboratory study and DNS considered both regimes of weak and strong stable stratification. Under the latter regime, the air–water temperature difference created in the laboratory experiment was of up to 18 K and a relatively low wind speed of about 3 m/s which allowed us to reach a comparatively large bulk Richardson number (up to Ri $\approx$ 0.04) and the corresponding bulk Reynolds number up to Re $\approx$ 60000. Both contact (Pitot tube) and PIV methods were employed to measure the air velocity whereas the air temperature profile was measured simultaneously by a set of contact probes. The same bulk Ri and Re were prescribed in direct numerical simulation where turbulent Couette flow was considered as a model of the near water constant-stress atmospheric boundary layer.

Both experimental and DNS results show that mean velocity and temperature profiles obtained in our laboratory and numerical experiments agree well and also are well predicted by the Monin–Obukhov similarity theory. Although under strong stratification conditions a drastic reduction of both turbulent momentum and heat fluxes was observed, the prediction of MOST was still found to be a good approximation for the wind velocity and temperature profiles.

Acknowledgements This work is supported by RFBR (16-55-52022, 17-05-00703, 18-05-00265, 16-05-00839) and by the grants of the President (MK-2041.2017.5, SP-1740.2016.1). Postprocessing of the experimental data and numerical simulations were supported by the Russian Science Foundation (15-17-20009). Laboratory experiments were carried out on the Unique Scientific Facility "Complex of Large-Scale Geophysical Facilities" (http://www.ckp-rf.ru/usu/77738/).

References

1. Melas D. 1989. The temperature structure in a stably stratified internal boundary layer over a cold sea. *Boundary-Layer Meteorol.* 48: 361–375.
2. Mulhearn P.J. 1981. On the formation of a stably stratified internal boundary layer by advection of warm air over a cooler sea. Boundary-Layer Meteorology, 21: 247–254.
3. Mahrt L. 2014. Stably stratified atmospheric boundary layers. Annu. Rev. Fluid Mech. 46: 23–45, https://doi.org/10.1146/annurev-fluid-010313-141354.
4. Ohya Y., Neff D., Meroney R. N. "Turbulence structure in a stratified boundary layer under stable conditions", *Boundary-Layer Meteorology* **83:** 139–161, 1997.
5. Druzhinin O.A., Troitskaya Yu. I., Zilitinkevich S.S. 2016. Stably stratified air flow over waved water surface. Part 1: Stationary turbulent regime. Q.J.R.M.S.
6. Flores O., Riley J.J. Analysis of turbulence collapse in the stably stratified surface layer using direct numerical simulation. *Boundary-Layer Meteorol*. 139: 241–259.
7. Monin A. S., Yaglom A.M. 1971. *Statistical Fluid Mechanics: Mechanics of Turbulence*. V. 1. MIT Press: Cambridge, Massachusetts, and London, England; 769 pp.

Formation of Sand Bedforms Under Surface Waves

François Marin and Armelle Jarno

Abstract Surface waves often generate bedforms at the seabed. Small structures such as ripples with a typical wavelength between ten centimeters and one meter are very common structures in the coastal zone. The formation of these structures under nonlinear surface waves is considered in this chapter. Under regular waves, two modes of pattern formation from a flatbed in a wave flume are reported for well-sorted grains and mixtures of grains. Sand ripples can form uniformly or from isolated ripples spreading on the bed while growing. In this latter case, front propagation speed is measured and a simple model based on the quintic complex Ginzburg-Landau equation can explain features of front propagation on the granular bed. The profile of surface waves propagating in shoaling water approaches the solitary waveform before wave breaking. The main characteristics of solitary waves are presented. The effect of the high nonlinearity of these waves may be very significant on bedforms induced in the nearshore zone. The interaction between solitary waves and a sandy bed is reported. Sandy ripples induce a strong energy dissipation of solitary waves. When solitary waves propagate on the background of a standing harmonic wave, bars are formed with crests located beneath the nodes of the harmonic surface wave. In the case of harmonic standing waves alone, the bar crests are positioned beneath the antinodes of the harmonic surface wave. Grains with different densities may be found on the seabed. The concentration of light sedimenting particles on ripple crests is explained by a simple theoretical model.

Keywords Solitary waves · Surface waves · Bedforms · Ripples · Bars

---

F. Marin (✉) · A. Jarno
Normandie Université, Unilehavre, CNRS, UMR 6294, LOMC,
53 Rue de Prony BP 1123, 76063 Le Havre Cedex, France
e-mail: francois@univ-lehavre.fr

A. Jarno
e-mail: jarnoa@univ-lehavre.fr

N. Abcha et al. (eds.), *Nonlinear Waves and Pattern Dynamics*,
https://doi.org/10.1007/978-3-319-78193-8_7

1 Introduction

Bedforms are often generated on the seabed. These sedimentary structures result from a complex interaction between the flow and the sediments. The knowledge of the size of these structures is necessary for the estimate of their equivalent roughness, of the bed shear stress, and of the sediment transport. Numerous studies have been carried out on sand bedforms induced by surface waves. However, due to the complexity of the involved processes, many questions remain unsolved, in particular, in the case of nonlinear surface waves. Nonlinearity may generally not be neglected for surface waves. The formation of sand bedforms under weakly nonlinear waves is first considered in this chapter. In other respects, long waves such as tsunamis often behave like solitary, highly nonlinear waves. After a brief introduction on these waves, the interaction between solitary waves and a sandy bed will be considered.

2 Ripple Pattern Formation Under Regular Surface Waves

In a wave flume, ripple pattern formation from an initial plane bottom depends on the forcing conditions applied to grains. Two distinct modes are identified and characterized by two nondimensional parameters: the Reynolds number $Re = U_\infty a/\nu$ and the Froude number $Fr = U_\infty/\sqrt{(s-1)gd_{50}}$, where a and U_∞ are the fluid particle semi-excursion and the fluid velocity amplitude at the edge of the bed boundary layer, respectively, s is the relative density of sediment, g the gravity, and ν the water kinematic viscosity. Either ripples form on the whole bed or several isolated rippled zones named patches first appear. In the latter case, ripples grow from a defect of small amplitude on the initial flat bottom. This mode of formation is exhibited in Fig. 1 for well-sorted sands and also for mixing of sands [1].

The two modes of pattern formation are represented in the (Fr, Re) plane (Fig. 2) for tests performed with sands (111 μm < d_{50} < 375 μm) [2] and PVC particles (d_{50} = 170 μm) [12]. The dotted line on Fig. 2 delineates the domain of the two modes of pattern formation. For a fixed Re number, if Froude number remains lower than a critical Froude number Fr_c, ripples form from localized sites and the perturbation necessary to initiate ripple growth must be of finite amplitude, whereas if $Fr > Fr_c$, a perturbation of infinitesimal amplitude is enough to trigger ripple formation and ripples can form spontaneously on the whole bottom. A rough estimate of the number of cycles for observation of isolated systems of ripples before invasion on the whole bottom n_c is represented on Fig. 3. The dimensionless bed shear stress (Shields

Fig. 1 Example of bed image in grayscale for mixing of sands forming by patch for n = 2000 cycles (d_m = 350 μm; Re = 4715; Fr = 1.7)

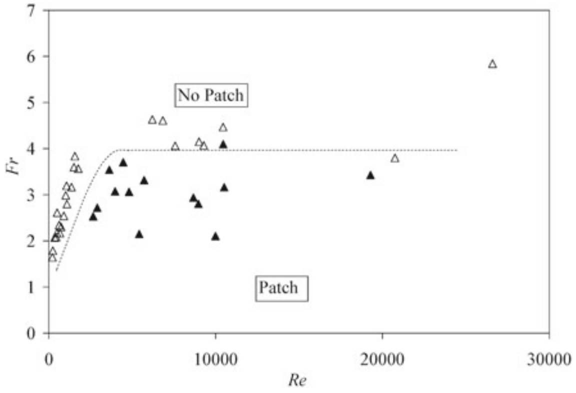

Fig. 2 Delineation of the two modes of pattern formation in the (Re, Fr) plane

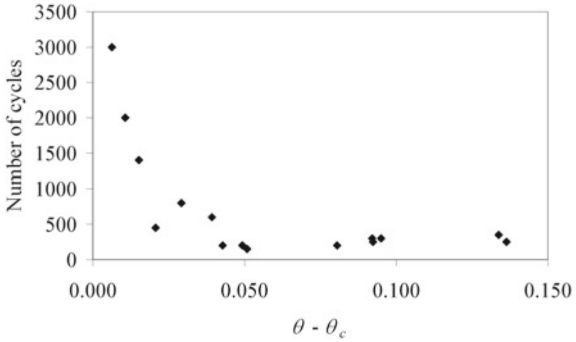

Fig. 3 Number of cycles for observation of isolated systems of ripples before invasion on the whole bottom n_c as a function of the deviation to the threshold of ripple formation

parameter) is defined with Jonsson formulae [3] for the skin friction factor f_w by: θ $\theta = 0.5\, f_w Fr^2$, and θ_c is the critical Shields number. When the deviation to the threshold for ripple formation $(\theta - \theta_c)$ increases, the amplitude of the perturbation necessary to destabilize the bottom decreases, the number of observed initial sites of ripples nucleation increases and the time of observation of these ripple patches decreases.

2.1 Dynamics of Propagation Fronts

Experimental determination

Ripples form by a mechanism of amplification of initial perturbations of small amplitude. When ripples form from isolated nucleation sites, the front propagation on the granular bed plays an important role in the pattern formation processes. The work performed with A. B. Ezersky [2] was focused on a test with a well-sorted sand with a slow dynamics (Test *B*, *Re* = 5512; *Fr* = 2.2), where isolated systems of ripples can be observed for more than 1000 excitation cycles before total invasion on the whole

Fig. 4 Longitudinal position of detected ripple fronts for Test B (Re = 5512, Fr = 2.2) as a function of number of excitation cycles. Estimated front propagation velocities

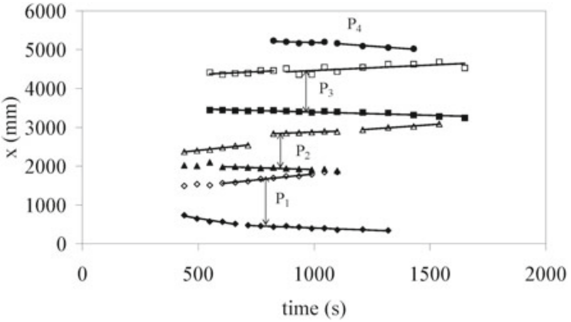

bed. For each patch, the two fronts are processed separately. Fourier spectrum of the bed elevation signal $\eta(x, t)$ is calculated for a selected y-transverse line along the x-longitudinal direction in the front zone and harmonics are filtered to conserve only $\eta_m(x, t)$, the slow-varying amplitude, and $\phi(x, t)$, the slow-varying phase. After the filtering process, we get: $\eta(x, t) = \eta_m(x, t)\ \cos(kx + \phi(x, t))$. In the next step of the processing, Hilbert transform is processed and the module of the complex amplitude $a(x)$ and unwrapped phase $\phi(x)$ of the envelope wave of the front are extracted. The wavefront is localized in the region, where a transition from a low amplitude to a high nearly constant value is detected. The chosen detection threshold is fixed to 15% of the maximum amplitude of the selected patch. An example of detected mean ripple fronts is presented in Fig. 4. The upflow v_{p-} and down flow front v_{p+} velocities designate, respectively, a front propagation in the direction opposite to the surface wave propagation and in the same direction of surface waves. Fronts propagate linearly with time with a good regression coefficient and a greater velocity for the fronts propagating in the direction of surface waves. The difference between the two mean front velocities has been attributed to the drift along the direction wave propagation induced by surface waves in the bed boundary layer [4].

$$(\mathrm{P}_1) : v_{p-} = -0.23 \text{ mm s}^{-1};\ v_{p+} = +0.62 \text{ mm s}^{-1};$$

$$(\mathrm{P}_2) : v_{p-} = -0.19 \text{ mm s}^{-1};\ v_{p+} = +0.53 \text{ mm s}^{-1};$$

$$(\mathrm{P}_3) : v_{p-} = -0.16 \text{ mm s}^{-1};\ v_{p+} = +0.45 \text{ mm s}^{-1}$$

Model for propagation of ripple fronts

The quintic complex Ginzburg-Landau equation was used to model the propagation of sandy ripples fronts:

$$\frac{\partial A}{\partial t} = (1 + ic_1)\,\frac{\partial^2 A}{\partial x^2} + \varepsilon A + (1 + ic_3)\,|A|^2\,A - (1 - ic_5)\,|A|^4\,A \qquad (1)$$

where A is the complex amplitude of sand ripples, ε is criticality and c_1, c_2, c_3 are real coefficients. Equation (1) is a model equation for subcritical bifurcation as observed for sand ripple dynamics. Indeed, experiments showed us that there is a threshold value of the amplitude: an amplification of the perturbations occurs for amplitudes more than a threshold value and a decay with time is observed for amplitudes less than threshold value. The analytical solution of Eq. (1) [5] can be expressed in the form: $A = e^{-i\omega t} a(\xi) e^{i\varphi(\xi)}$, $\xi = x \mp Vt$, where V is the front velocity and ω the frequency of sand ripples. The analytical solution for the amplitude and phase of propagating fronts (see [1] for more details) can be written as follows:

$$a = a_N \frac{e^{K_{L\mp\xi}}}{\sqrt{1 + e^{2K_{L\mp\xi}}}} \tag{2}$$

and

$$\phi = q_N \xi - \frac{(q_N - q_L)}{K_{L\mp\xi}} lna \tag{3}$$

The ξ sign "+" corresponds to a front, which propagates in the positive direction, $K_{L+} < 0, a(x = -\infty, t = 0) = a_N$ is the limit of the exponential growth, $a(x = +\infty, t = 0) = 0$, and the sign "−" corresponds to a front propagating in the opposite direction: $K_{L-} > 0, a(x = -\infty, t = 0) = 0$, $a(x = +\infty, t = 0) = a_N$. In the phase expression (Eq. 3), q_L, q_N may be considered as the contributions to the wave number for waves of bottom profile with infinitesimal and finite amplitudes.

Excluding the linear growing phase in space for a given instant, Eq. 3 can be simplified in the form $\phi(x) = \frac{q_L - q_N}{K_{L\pm}} \ln a$, predicting a theoretical local linear dependence between the wave phase and logarithm of the wave amplitude $a(x)$.

Experimental data were used to check if this correlation occurs for wavefronts in sand ripples. The linear dependence between lna and φ was found and the coefficients $\frac{q_L - q_N}{K_{L\pm}}$ were estimated at different instants for one patch and for fronts propagating in both directions. This result validates the model prediction.

2.2 *Ripple Growth in Pattern*

Complex demodulation by Hilbert transformation was used to extract geometric characteristics of each ripple and to build distributions of ripple characteristics of patterns while they form. Three examples of growth of dominant ripple wavelength in the pattern are presented in Fig. 5. For the test performed with light PVC particles (Test *A*, $Re = 214$; $Fr = 1.4$; $d = 1.35$; $D_{50} = 0.17$ mm), ripples form on the whole bottom from an initial network of short fragments of three-dimensional ripples and they grow by coalescence processes. Ripples initially formed are rolling-grain ripples. During this stage, the pattern is characterized by a constant dominant ripple length and a low steepness ($h/L < 0.1$) in agreement with Sleath empirical criterion [6]. For Test *B* conducted with a well-sorted sand characterized by a pattern formation from nucleation sites, rolling-grain ripples are not detected. Vortex ripples grow with an exponential relaxation law. The equilibrium length is reached before the whole bottom is

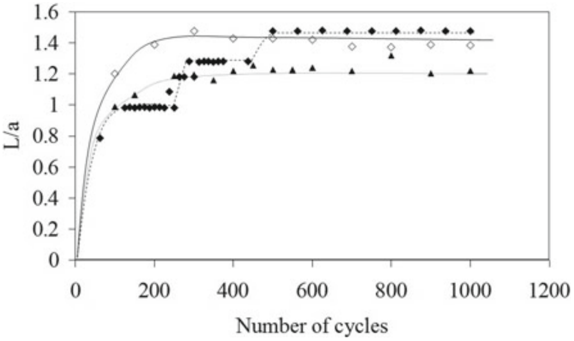

Fig. 5 Dominant ripple wavelength versus the number of excitation cycles for Test A: solid diamonds, *Re* = 214, *Fr* = 1.4, PVC particles; Test B: open diamonds, *Re* = 5512, *Fr* = 2.2, well-sorted sand and Test C: solid triangles, *Re* = 4640, *Fr* = 2.2, sand mixture

covered by ripples. Thus, the selection of the dominant equilibrium wavelength is not significantly influenced by the initial mode of pattern growth. A similar exponential relaxation law is found in the case of a mixing of sands (Test C, $Fr = 2.2$, $Re = 4640$, median diameter $d_m = (d_{16}.d_{50}.d_{84})^{1/3} = 350\ \mu\text{m}$). Grain heterogeneity does not influence significantly the growth law for pattern dominant length.

3 Sand Bedforms Induced by Strongly Nonlinear Surface Waves

3.1 Solitary Waves

Solitary waves have been the object of attention from Prof. Alexander Ezersky. The solitary water wave, localized wave that propagates along one space direction only with undeformed shape has been experimentally discovered in 1834 by John Scott Russell. A model equation representing the dynamics of solitary waves was obtained by Korteweg and de Vries [7]. This well-known KdV equation, which has been obtained for shallow water under the assumption of wave propagation in one direction, may be written as follows:

$$\frac{\partial \eta}{\partial t} + V_0 \frac{\partial \eta}{\partial x} + \frac{3}{2}\frac{V_0}{H}\eta\frac{\partial \eta}{\partial x} + \frac{1}{6}V_0 H^2 \frac{\partial^3}{\partial x^3} = 0 \tag{4}$$

where η is the displacement of free surface, t the time, $V_0 = \sqrt{gH}$ the velocity of surface waves of infinitely small amplitude in shallow water, H the water depth, and x the wave propagation direction. The localized solution resulting from the balance of nonlinearity and dispersion has the form of a single hump as observed by Russell:

$$\eta_s\left(x - V_s t\right) = A_s \cosh^{-2}\left(\sqrt{\frac{3A_s}{4H^3}}\left(x - V_s t\right)\right) \tag{5}$$

$$V_s = V_0 \left(1 + \frac{A_s}{2H}\right) \tag{6}$$

where V_s is the velocity of the solitary wave which depends linearly on its amplitude, A_s. The duration of this wave is proportional to $A_s^{-1/2}$.

As an oscillatory wave moves into shoaling water, the wave amplitude becomes higher, the trough becomes flatter, and the surface profile approaches the solitary waveform before wave breaking [8]. The cnoidal wave theory approaches the solitary wave theory as the wavelength becomes very long. In other respects, long waves such as tsunamis and waves resulting from large displacements of water caused by landslides and earthquakes often behave like solitary waves. Ezersky et al. [9] studied the generation of solitary waves (solitons) in a 10 m long hydrodynamic resonator used in shallow water. Surfaces waves were produced by an oscillating paddle at one end of the flume, and a near-perfect reflection took place at the other end. The frequency of the wavemaker was chosen close to the resonant frequency of the mode whose wavelength is equal to the flume length. For small values of the amplitude of displacement of the wavemaker, only standing harmonic waves are generated in the channel. For values of this amplitude greater than a critical value, pulses propagating from one end of the flume to the other end are excited on the background of the standing wave. The characteristics of such pulses are close to those of the theoretical soliton. In particular, the soliton width decreases with increasing values of its amplitude, as illustrated in Fig. 6. Moreover, these pulses resulting from the excitation of high harmonics are not altered by collision with other pulses. They are called solitons by Ezersky et al. [9]. The KdV equation does not describe the interaction of contra-propagative waves. The Boussinesq equations can be used to depict counter-propagating solitary waves.

3.2 Formation of Sand Bedforms Under Solitary Waves

The effect of the high nonlinearity of solitary waves may be very significant on bedforms induced in the nearshore zone. Let us consider the formation of sand bedforms under solitary waves.

Numerous studies have been carried out on bedforms under linear or weakly nonlinear waves [6, 10–13]. In the nearshore zone, bars consisting of ridges of sediments running roughly parallel to the shore are common features on sandy beaches. These structures provide a possible mechanism of natural beach protection from the energy of incident waves. The mode of sediment transport has a key role on the bar position under partially standing waves, the bars having spacing equal to half the surface wavelength. This spacing corresponds to the Bragg condition for which strong reflection of the incident waves may occur. The bar position is a very significant parameter as far as the ability of bars to reflect wave incident energy is concerned. The effect of solitary waves on the bar position, and more generally on bedforms generation has been carefully studied by Prof. A. E. Ezersky. Experimental and theoretical work has

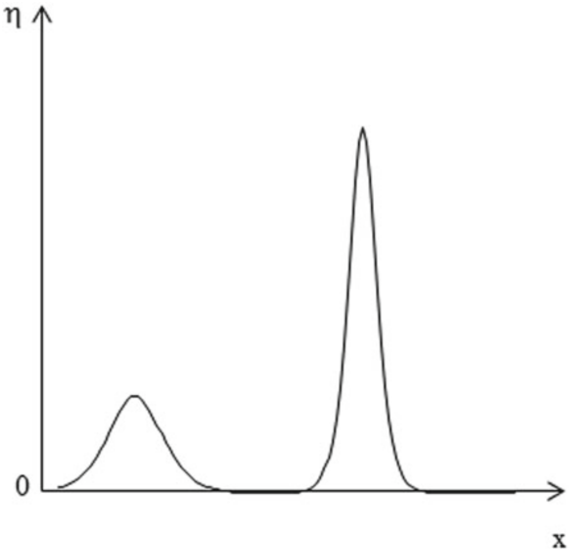

Fig. 6 Schematic comparison between the size of two theoretical solitons (solutions of the KdV equation)

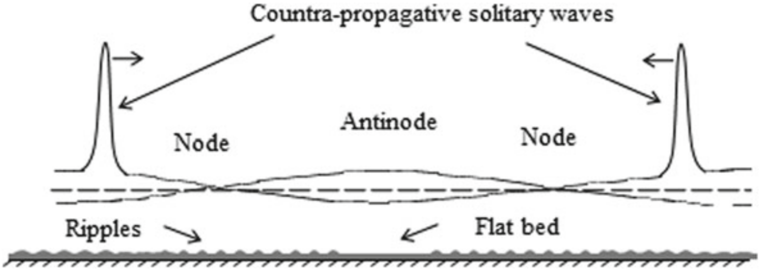

Fig. 7 Sketch of ripples formation under solitary waves propagating on the background of a standing harmonic wave

been carried out at this aim. As far as the experimental work is concerned, Ezersky chose to use the original method of solitary waves generation in a hydrodynamic resonator described in the previous section and considered the interaction between solitary waves and a loose sandy bed. When high nonlinear waves are excited in the resonator, small ripples form rapidly everywhere in the flume, except in the central part, where the bed remains flat as illustrated in Fig. 7. This region corresponds to the zone of collision of counter-propagating solitons, which have horizontal velocities of opposite sign, leading to a horizontal velocity close to zero in the collision zone [14]. The value of bed shear stress is then close to zero, anyway below the critical value θ_c for incipient motion given by Soulsby and Whitehouse [15]:

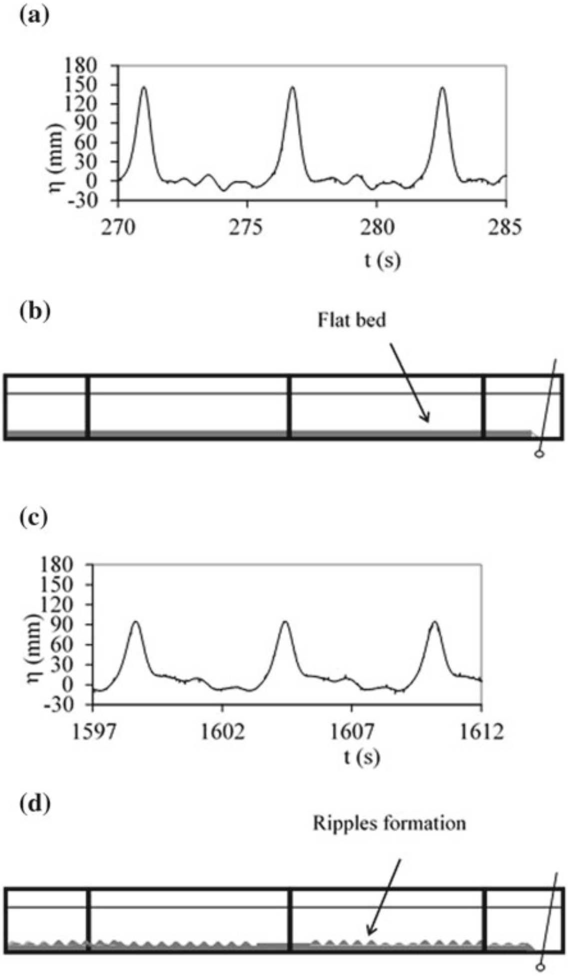

Fig. 8 Interaction between the free surface and the sandy bed. Frequency of the oscillating paddle: f = 0.173 Hz. Amplitude of the horizontal displacement of the oscillating paddle averaged over depth: a = 6 cm. H = 0.26 m; s = 2.65; D = 0.15 mm. **a** and **b** Beginning of the test, just after the solitary waves formation. **c** and **d** After ripple formation

$$\theta_c = \frac{0.24}{D_*} + 0.055\left[1 - \exp\left(-0.020 D_*\right)\right] \tag{7}$$

where $D_* = \left[g\left(s-1\right)/\nu^2\right]^{1/3} D$, s is the sediment relative density, D, the sediment median diameter, and ν the kinematic viscosity. A strong interaction between the sandy bed and the free surface occurs, as shown in Fig. 8, where the temporal evolution of the free surface η at the reflective end of the flume is depicted with a sketch of the sand distribution in the flume. The level 0 mm corresponds to the water level at rest. The peaks in the free surface elevation correspond to the passage of solitary waves. Neglecting the interaction of contra-propagative waves, the free surface displacement at the fixed end of the flume can be described by

Fig. 9 Variation of the amplitude of the solitary wave with time. Same test conditions as for Fig. 8

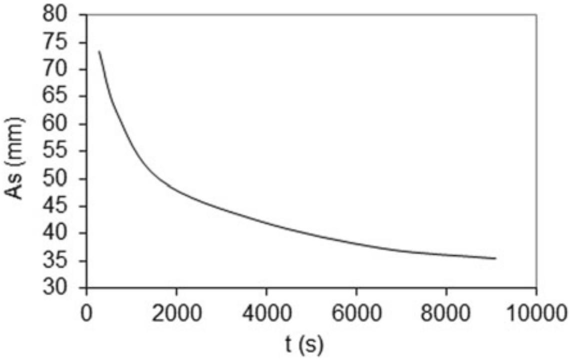

Fig. 10 Variation of the mean ripple height with time. Same test conditions as for Fig. 8

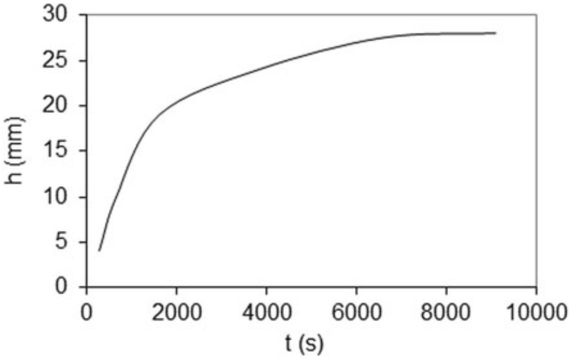

$$\eta\left(t\right)=2\eta_s\left(t\right)+2A_0\sin\left(\omega t-\varphi_s\right) \tag{8}$$

where ω is the angular pulsation of the flow, A_0 the harmonic wave amplitude, and φ_s the phase shift between the soliton and the harmonic waves. The sandy bed is initially flat (Fig. 8b).

Figure 8c, d shows that after about 27 min, that is when the dimensionless time $\tau = t\omega \cong 1760$, the bed is rippled and the peak values of the free surface are significantly lower than at the beginning of the test. This results from the dissipation at the now rippled bed.

The variation of the soliton amplitude A_s with the time t is depicted in Fig. 9 for the same test as in Fig. 8. The decrease of A_s is particularly marked during the beginning of ripple formation. The temporal variations of the ripple height h and wavelength L, averaged over the flume length, are exhibited in Figs. 10 and 11, respectively. The ripple dimensions forming on the bed increase for increasing values of time, when the soliton amplitude decreases, as shown in Fig. 8. Let us consider the soliton energy E_s:

Fig. 11 Variation of the mean ripple wavelength with time. Same test conditions as for Fig. 8

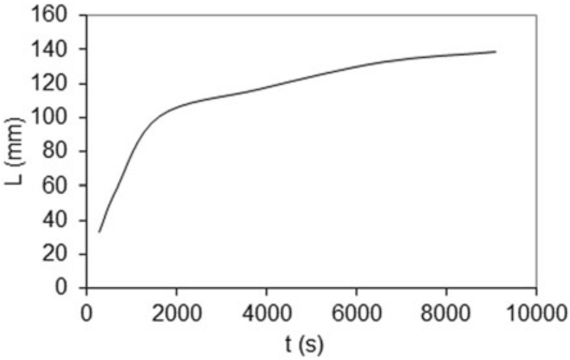

$$E_s = \int_{-\infty}^{+\infty} \eta_s^2 dx \sim A_s^{3/2} \tag{9}$$

Taking into account the energy dissipation due to ripples, the temporal variation of the soliton energy may be written as follows:

$$\frac{dE_s}{dt} = \frac{3}{2}\frac{\omega A_0}{H} E_s \cos\varphi_s - (\beta + \alpha h)\, E_s \tag{10}$$

In this equation, β is a coefficient describing the part of the damping of the soliton, which is independent of the scale of the perturbations, and α a phenomenological coefficient for the dissipation of the soliton due to sand ripples. This part of dissipation is supposed to be proportional to the ripple height, as a linear function is the simplest parameterization.

Once the ripples are formed, two sand accumulation zones progressively appear (Fig. 12). At the equilibrium state, that is for $t \cong 60$ h, they form bars with crests located beneath the nodes of the harmonic surface wave. In the case of harmonic standing waves (without solitons), the bar crests are positioned beneath the antinodes of the surface elevation when the suspended load transport is dominant [16]. In the present case, where solitons are excited on the background of a standing harmonic wave, ripples generate vortices, which lift into suspension a lot of sand, leading to a significant amount of suspended load transport. Present bar positions may be explained by the variation of the time window between the passage of the contra-propagating solitons with the distance along the flume [17].

Grains with different physical characteristics (size, shape, and density) are often found on the seabed. This led Ezersky to study the segregation of sedimenting grains of different densities on a rippled bed under a velocity field induced by solitary waves. These waves were excited in a hydrodynamic resonator as described above in the section "solitary waves". The hydrodynamic forcing was stopped, the water waves damped, and sedimentation of suspended particles occurred. The grain mixture consisted of particles of different densities: sand grains (s = 2.65) and PVC grains

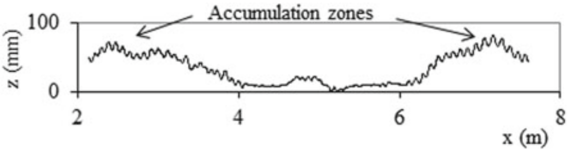

Fig. 12 Sand accumulation zones with superimposed ripples. Same test conditions as for Fig. 8. Equilibrium state; z: altitude from the flume bottom

(s = 1.35). It was found that light particles (PVC grains) accumulate on the ripple crests. This can be explained as follows. Taking into account the Stokes force and neglecting the turbulent drag, the grain velocity $\vec{V}$ may be obtained from the flow velocity $\vec{U}$ [18]:

$$\vec{V} = \vec{U} + \frac{S_t}{\omega}\frac{\rho_w}{\rho_{gr}}\frac{d\vec{U}}{dt} + \left(\frac{\rho_{gr} - \rho_w}{\rho_w}\right)\vec{g} - \frac{S_t}{\omega}\frac{d\vec{V}}{dt} \tag{11}$$

where $S_t = D^2\rho_{gr}\omega/18\upsilon\rho_w$ is the Stokes number, ρ_w the fluid density, and ρ_{gr} the grain density. For small values of the Stokes number, it is possible to use S_t as an expansion parameter for the grain velocity:

$$\vec{V} = \vec{V}^{(0)} + S_t\vec{V}^{(1)} + S_t^2\vec{V}^{(2)} + \cdots \tag{12}$$

Let us consider in the first approximation a very simple model defined in the vicinity of each sand crest by the stream function $\psi = -a\,(\alpha x + z)\,z$, with α a nondimensional coefficient and a a coefficient corresponding to an angular frequency. While the flow direction changes periodically, a stationary hyperbolic point takes place. After some transformation, the time-averaged velocity of particles may be expressed in the horizontal direction in the following way:

$$\langle V_x \rangle = -x\left(\frac{s'}{2}a_0\alpha_0 e^{-\gamma t} + \frac{S_t}{4\omega}a_0^2\alpha_0^2 e^{-2\gamma t}\right) \tag{13}$$

where $s' = 1 - \rho_w/\rho_{gr}$, γ is the rate of exponential decay of surface waves, a_0 and α_0 the amplitudes of a and α, respectively. The expression of $\langle V_x \rangle$ is such as whatever the side of the ripple crest, where the particles are, the grains move toward the ripple top. The sand grains which are heavier than the PVC grains settle faster than the PVC grains. When most sand grains have settled on the bottom, only PVC grain concentrate near the ripple crests.

4 Conclusions

Seabed is rarely flat. Sand bedforms are very common. Many studies have been carried out on these sedimentary structures, in particular under the assumption of linear waves. However, the nonlinearity of surface waves cannot be neglected in most of practical cases, and the physical processes involved in the bedforms generation, in this case, are poorly understood. Prof. A.B. Ezersky carried out pioneering work in this field, and he has significantly contributed to the emergence of new approaches. The interaction between a sandy bed and extreme waves propagating in the shoaling zone is one of the subjects he outlined the need for further work, owing to the significance of the practical applications for the evolution of the shore. In order to bring a contribution to this topic, a PhD project was launched in October 2016 between the LOMC (CNRS, University Le Havre Normandie) and M2C (CNRS, University Caen Normandie) laboratories, started in the end of 2016 with the financial support of the Normandie Regional Council. A PhD was hired and Prof. A. E. should have been his co-advisor together with us.

Acknowledgements The authors thank the Normandie Regional Council for its contribution for financing this work.

References

1. Lebunetel-Levaslot J., Dynamique de formation des réseaux de rides de sable en canal à houle, Thèse de doctorat, Université du Havre (2008).
2. Lebunetel-Levaslot, J., Jarno-Druaux A., Ezersky A.B. and Marin F., Dynamics of propagating front into sand ripples under regular waves, *Phys. Rev. E* 82, 032301 (2010).
3. Jonsson I.G., Wave boundary layers and friction factors, in Coast. Eng. Proc. 10th Conf. Tokyo 1, ASCE, pp. 127–146 (1966).
4. Longuet-Higgins M.S., Mass transport in water waves, *Philos. Trans. R. Soc. Lond.*, A 245 903, 535–581 (1953).
5. van Saarloos W., Hohenberg P.C, Pulses and fronts in the complex Ginzburg – Landau equation near a subcritical bifurcation, *Phys. Rev. Let..,* 64 749–752 (1991).
6. Sleath J.F.A., On rolling-grain-ripples, *J. Hydraul. Res.*, 14, 69–81 (1976).
7. Korteweg D.J., de Vries G., On the change of form of long waves advancing in a rectangular channel, and on a new type of long stationary waves, *Phil. Mag.*, 39 (5), 442–443 (1895).
8. Munk W.H., The solitary wave theory and its application to surf problems, *Ann. N.Y. Acad. Sci.*, 51, 376–423 (1949).
9. Ezersky A.B., Polukhina O.E., Brossard J., Marin F., Mutabazi I., Spatio-temporal properties of solitons excited on the surface of shallow water in a hydrodynamic resonator, *Phys. Fluids,* 18 (6), 067104 (2006).
10. Bagnold R.A., Motion of waves in shallow water: Interaction of waves and sand bottoms, *Proc. Roy. Soc. London*, Ser. A 187, 1–15 (1946).
11. Blondeaux, P., Sand ripples under sea waves: Part 1. Ripple formation, *J. Fluid Mech., 218*, 1–17 (1990).
12. Jarno-Druaux, A., J. Brossard, and Marin F. Dynamical evolution of ripples in a wave channel, *Eur. J. Mech. B/Fluids, 23*(5), 695–708 (2004).
13. Vittori G., and P. Blondeaux, Sand ripples under sea waves: Part 2. Finite-amplitude development, *J. Fluid Mech., 218*, 19–39(1990).

14. Marin F., Abcha N., Brossard J., Ezersky A.B., Laboratory study of sand bedforms induced by solitary waves in shallow water, *J. Geophys. Res.*, 110, F04S17 (2005).
15. Soulsby, R.L. and R.J.S.W. Whitehouse, Threshold of sediment motion in coastal environments, *Pacific Coasts and Ports '97 Conf.*, 1, 149–154, Christchurch, Univ. Canterbury, New Zealand (1997).
16. Nielsen P., Some basic concepts of wave sediment transport, *Ser. Pap. 20*, 160 pp., Inst. of Hydrodyn. and Hydraul. Eng., Tech. Univ. Denmark, Lyngby, Denmark (1979).
17. Marin F., Ezersky A.B., Formation dynamics of sand bedforms under solitons and bound states of solitons in a wave flume used in resonant mode, *Eur. J. Mech. - B/Fluids*, 27 (3), pp 251–267 (2008).
18. Ezersky A.B., Marin F., Segregation of sedimenting grains of different densities in an oscillating velocity field of strongly nonlinear surface waves, *Phys. Rev. E*, 78 (2), 022301 (2008).

Aggregation of Fibers by Waves

Gautier Verhille and Patrice Le Gal

Abstract Sea balls also called aegagropila, can be found on Mediterranean beaches. They are made of *Posidonia* fibers, which aggregate on the seabed due to the sea motions. To understand the mechanism of aggregation and compaction of these structures, we have performed a laboratory investigation on the dynamics of aggregation of fibers by surface gravity waves generated in a water tank. Amazingly, depending on the flexibility of the fibers, two different sites of aggregation are observed. Following our experiments, we propose an analytical derivation of the clustering of particles by the Stokes drift. This theoretical calculation is quite general and emphasizes the respective roles of the Stokes number and the density of the particles; it also underlines the importance of the fiber flexibility in their drift and explains our experimental observations.

Keywords Fiber aggregation · Fiber dynamics in flow · Stokes drift

1 Introduction

Aegagropila are sea balls composed of *Posidonia* fibers, which can be found along the Mediterranean beaches. *Posidonia* are aquatic plants that fade in autumn. Their roots then release on the seabed a large quantity of fibers that will get caught by the sea water flows and waves. After a certain time (still unknown), clusters of entangled fibers are deposited on the beaches in the form of compact balls. These structures have a large size dispersion (a few millimeters for the smaller ones to about ten centimeters for the larger ones). Figure 1a presents a photograph of these sea balls constituted by one to two centimeter long fibers having a diameter around 100 μm. A statistical study of the size and mass of aegagropila shows that these distributions obey a lognormal law,

---

G. Verhille (✉) · P. Le Gal
Aix-Marseille Univ, CNRS, Centrale Marseille, IRPHE, Technopôle de Château Gombert, 49 Rue F. Joliot Curie, BP 146, 13384 Marseille Cedex 13, France
e-mail: verhille@irphe.univ-mrs.fr

P. Le Gal
e-mail: legal@irphe.univ-mrs.fr

N. Abcha et al. (eds.), *Nonlinear Waves and Pattern Dynamics*,
https://doi.org/10.1007/978-3-319-78193-8_8

Fig. 1 **a** Photographs of *Posidonia* aegagropila (Plage du Prophète, Marseille). **b** Close up of the extremities of a marine rope piece, where some fibers have been agglomerated on the nylon fiber bundles. **c** Two aegagropila that have aggregated on a textile thread

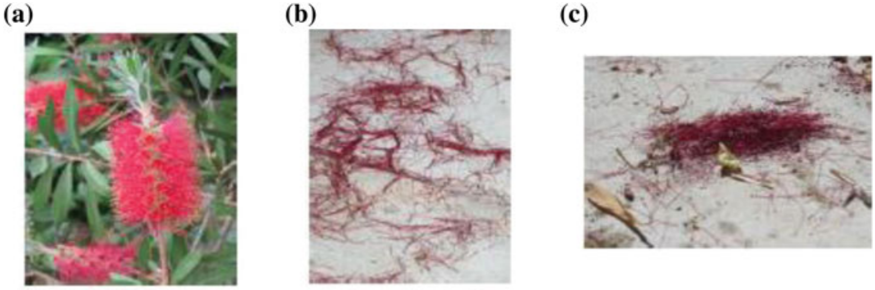

Fig. 2 **a** Photograph of a bottlebrush flower (Marseille). **b** Bottlebrush flower stamens fallen on the floor in the course of aggregation under the action of a turbulent wind. **c** An aggregate of bottle brush flower fibers

which is compatible with an aggregation of fibers trapped randomly by the forming balls [1]. Some of these fiber aggregates can also be encountered around *Posidonia* rhizome fragments or even foreign bodies as it is the case in Figs. 1b, c, where the fibers have been trapped on the extremities of a marine rope piece or along a textile thread. These examples show if the aggregation process does not need any nucleus, some of the sea balls possess synthetic or natural nuclei that may help their formation.

More generally, natural fibers have the tendency to agglomerate to form bundles or balls when agitated by fluid turbulent motions. Figure 2 presents an example of aggregation of fibers in air: under the action of wind, bottlebrush (*Callistemon*) flower stamens whose length is around 3 cm for a diameter about 300 μm aggregate when they fall on the floor. Figure 3 gives another example of natural fiber accretion by the sea, but this time of living seaweeds. Contrary to the short fibers of *Posidonia* or bottlebrush flower fiber aggregates, in the case of these long seaweeds, fiber self-entanglements are certainly at the origin of the bundles that can be seen along the shore.

These different structures pose several questions ranging from their formation (physical mechanisms, duration of the aggregation process, etc.) to the understanding of the observed size distributions. In the absence of in situ measurements, we propose to study in the laboratory, the dynamics of formation of fiber clusters in a simple flow generated by the periodic excitation of surface waves in a tank. Then, we will

Fig. 3 Photographs of seaweed aggregates along the Pacific seashore (Gator beach, San Diego, California). The length of the seaweeds, between ½ and 1 m, enhances self-entanglements that sustain the aggregates (pen length ~15 cm)

propose a nonlinear model that explains the observed transport of the fibers by a flow.

2 Experimental Observation of Fiber Aggregation in a Flow

2.1 Experimental Device

In order to stay close to the back and forth movement that exists at the bottom of the sea, we choose to study the dynamics of fibers in a flow induced by the oscillation of a plate in a basin of length L = 80 cm (along the x direction). The basin is 28 cm wide (y direction) and 40 cm deep in the vertical z direction. When oscillating at angular frequency ω, the plate drives a stationary wave in a $h = 10$ cm deep layer of water. The two-dimensional flow field can then be approximated by a periodic potential ϕ:

$$\phi = U_0 \cos(kx) \cosh((z + h)/\lambda) \sin(\omega t), \tag{1}$$

where $k = 2\pi/\lambda$ is the wave number of the surface gravity wave and λ its wavelength. The resonance frequency of the basin is close to 0.8 Hz. In order to test the influence of fiber stiffness on the formation of aggregates, we used two types of fiber material: nylon and cotton. The length of the threads is around 5 cm and the diameter of the cotton threads is 150 and 400 μm for the nylon threads. Therefore, the aspect ratio of the fibers that we use in the experiment is between 100 and 300, i.e., in the same order of magnitude of the aspect ratio of the *Posidonia* fibers found in natural aegagropila (50–100). The cotton fibers are very flexible and can be easily deformed in the flow while the nylon fibers are rigid and do not deform. In both cases, the density of the fiber material is greater than the one of the fluid and since the flow velocities are relatively small, all the dynamics occurs on the smooth bottom of the basin. Finally, only a unique concentration of threads (500 threads in total) will be considered here.

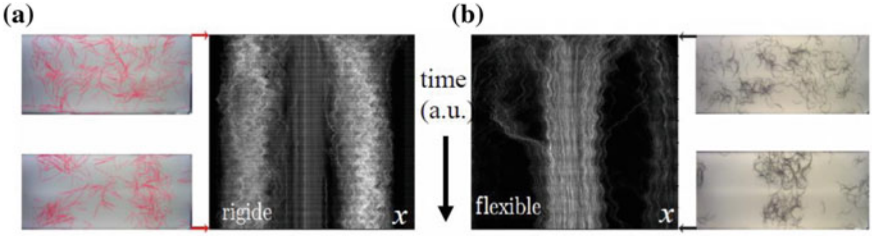

Fig. 4 Comparison of the dynamics of rigid fibers (**a**) and flexible fibers (**b**) in the experiments. Above and below on each side, are the initial and final conditions of the experiment, respectively. In the center, the space-time diagrams visualize the dynamics of fiber agglomeration toward the quarter and three-quarters of the basin for the rigid nylon fibers and toward the center for the flexible cotton fibers

2.2 Localization of the Fiber Aggregates

Consider first, a forcing frequency below the resonance frequency. The amplitude of the surface wave at the free surface is around 1 cm with a wavelength of 0.8 m. At initial time, the threads are arranged randomly (in position and orientation) on the bottom of the basin. After several hours, once the equilibrium is reached, we see in Fig. 4 that the threads have migrated toward some particular locations in the basin: the rigid nylon fibers (on the left of Fig. 4) are mainly located at a quarter and three-quarters of the tank length, whereas the flexible cotton fibers (on the right of Fig. 4) go mainly to the center of the basin. It is found that in both cases, at least during the 5–10 h of the experimental run duration, the clusters are not very tight and compact.

In order to understand the localization of these clusters, we propose in the following a one-dimensional model since Fig. 4 shows that the system is almost invariant over the width of the tank (this is expected because of the symmetries of the forcing and because of the random initial conditions). Because each fiber is first rapidly oriented in the flow before it drifts, it is fully justified to model it by a point particle moving in a velocity field as described by the potential flow given by Eq. (1). By neglecting the history terms (Basset terms) and the interactions between particles, the equation of evolution of the velocity of a spherical particle v_p is simply [2]:

$$dv_p/dt = \alpha Du/Dt + \left(u - v_p\right)/St, \tag{2}$$

where d/dt and D/Dt represent the Lagrangian derivative when following a solid particle and the Lagrangian derivative when following a fluid particle, respectively. The density coefficient α is equal to $3\rho_f/(2\rho_f + \rho_p)$, where ρ_f and ρ_p are the fluid and the solid particle density. When α is less than unity the particles sink at the bottom of the fluid layer contrary to the cases when α is larger than 1, where particles float on the fluid surface. The Stokes number characterizes the relative importance of inertia to viscous effects. For instance, for a spherical particle of radius a, immersed in a fluid of kinetic viscosity ν_f, the Stokes number reads:

$$St = 2a^2\omega/3\nu_f\alpha$$

In Eq. (2), all magnitudes are made dimensionless using the wavelength λ for the lengths, the inverse of the angular frequency $1/\omega$ for the time and U_0 for the velocities. Thus, the forcing velocity field at a fixed depth z near the bottom of the tank is simply $u = \sin(x)\ \sin(t)$. Using these quantities, and the fact that the flow is essentially one-dimensional at the bottom of the basin along its length, the Lagrangian total derivatives can be cast under the form:

$$d/dt = \partial_t + \varepsilon v_p \partial_x \quad \text{and} \quad D/Dt = \partial_t + \varepsilon u \partial_x,$$

where ε is equal to $U_0/\omega\lambda$. Using the orders of magnitude of the experimental parameters (observed velocity $U_0 \sim 1$ cms^{-1}, frequency $\omega \sim 1$ Hz and $\lambda \sim 1$ m), we can estimate that the order of magnitude of ε is around 10^{-2}. Therefore, ε can be considered as a small parameter and this will allow studying the solutions of the particle transport Eq. (2) and their stability by making a perturbative development in power of ε:

$$v_p = v_p^0 + \varepsilon v_p^1 + \varepsilon^2 v_p^2 + \ldots$$

At order 0 in ε, introducing the shape of the fluid velocity field in Eq. (2), leads to the determination of v_p^0 with the condition that $v_p = 0$ at initial time:

$$v_p^0 = (A \sin t + B (\cos t - e^{-t/St}))\sin x, \tag{3}$$

where the analytical expressions of the coefficients A and B are:

$$A = (1 + \alpha St^2)/(1 + St^2),\ B = St(\alpha - 1)/(1 + St^2)$$

The two first terms in (3) represent the stationary oscillatory response of the particle to the oscillatory forcing of the flow. This stationary oscillation will be reached after a transient represented by the third term, which is parametrized by the Stokes number St. We can see on formula (3) that the fixed points, i.e., the positions in the basin, where the particles will always stay at the same place are $x_e = 0$ or $x_e = \pm\ \pi$, thus at the center and near the sidewalls of the tank. At this order, we can also see that after the transient, the time-averaged velocity of any particle will be zero: $\langle v_p^0 \rangle = 0$. The drift of the particles, which is here at the origin of aggregation in our experiment does not appear at this zero order in ε and will only be recovered when taking into account the nonlinearity of Eq. (2) as expected for a Stokes drift. The integration of Eq. (2) at first order in ε, leads to the analytical expression of v_p^1:

$$v_p^1 = \sin 2x[St(\alpha - A^2 - B^2)/2 + C \cos 2t + D \sin 2t$$

$$+ (B^2 \sin t + 2AB \cos t + \delta)\, e^{-t/St} + e^{-2t/St} B^2 St/2)]/2$$

with the following constants:

$$C = [4ABSt^2 + St(A^2 - B^2 - \alpha^2)]/2(1 + 4St^2),$$
$$D = (A^2 - \alpha - B^2St^2 - ABSt)/2(1 + 4St^2)$$

and δ, a constant of integration that allows to set $v_p = 0$ at initial time.

The transients having disappeared, the mean velocity in time $\langle v_p^1 \rangle$ is non zero now because of the first term in the expression of v_p^1. This nonzero drift velocity $Vs = \langle v_p^1 \rangle$ gives rise to what is classically called the Stokes drift of the particles. The physical meaning of this drift comes from the fact that the oscillating flow is nonhomogeneous as its amplitude varies along the x axis of the tank. Therefore, after one period of oscillation, a particle never comes back exactly at the same position in space and as a consequence slowly drifts in time. This phenomenon should be similar to the drift of sand grains by steady streaming that forms seabed ripples under shallow water waves [3, 4]. In our case, this drift velocity can be analytically calculated:

$$Vs = \sin 2x(1 - \alpha)(\alpha St^2 - 1)/4\left(1 + St^2\right)^2$$

So, depending on the sign of Vs, the equilibrium positions $x_e = 0$ or $x_e = \pm\,\pi$ can be either stable or unstable. The calculation of the sign of Vs leads to the diagram presented in Fig. 5 that presents the repulsive or attractive characteristics of the positions x_e as a function of St and α. When $\alpha < 1$ (particles denser than the fluid), the aggregates are located in $x_e = 0$ or $x_e = \pm\,\pi$, that is at the center and the sidewall of the container. This case is stable for $St^2 < 1/\alpha$ (white area on Fig. 5) and corresponds to the situation, where the friction force $(u\text{-}v_p)/St$ acting on the particle is greater than the pressure force. In the opposite case, the drift of the particle is dominated by inertia effects (gray areas). Note that this criterion is exactly the same as the one found by Xu and Nadim in the case of the drift of particles under the action of the Coriolis force in a librating flow [5].

The numerical integration of the particle dynamics Eq. (2) confirms the previous stability analysis result. As an initial condition, we consider 128 particles homogeneously distributed on a line between $-\pi$ and π. Integration in time of Eq. (2) reproduces the two cases that we have discovered analytically. In the first case, where the equilibrium positions are stable, we observe that the particles slowly drift and merge at the expected locations $x_e = 0$ or $x_e = \pm\,\pi$. The numerical space-time plot of Fig. 5a illustrates this case. In the other case, when the drift velocity expels the particles from the equilibrium positions x_e, we found that the nonlinear solution converges toward limit cycles, where the particles oscillate indefinitely around $x_c = \pm\,\pi/2$. Figure 5b illustrates this computation.

The comparison of the space-time diagrams of Figs. 4 and 6 shows that the dynamics of the rigid nylon fibers correspond to case, where $x_e = 0$ or $x_e = \pm\,\pi$ are repulsive, whereas the dynamics of the flexible (cotton) fibers correspond to that of the case,

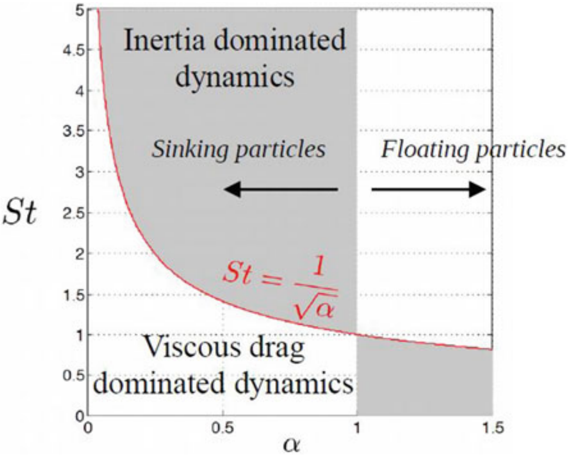

Fig. 5 Stability diagram of the equilibrium positions x_e as function of the Stokes number *St* and the density parameter α. The gray areas correspond to cases, where x_e are unstable and the white areas to cases, where x_e are stable

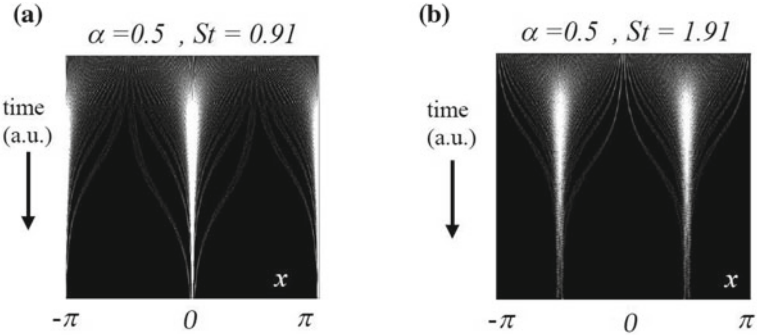

Fig. 6 Numerical simulations of the drift of 128 particles (without interaction) in a periodic flow $U_0 \sin(x) \sin(t)$. Space-time diagram of the dynamics: **a** attraction of the particles in locations $x_e = 0$ or $x_e = \pm\pi$; **b** repulsion of the particles from locations $x_e = 0$ *or* $x_e = \pm\pi$ and attraction by limit cycles around $x_c = \pm\pi/2$

where $x_e = 0$ or $x_e = \pm\pi$ are attractive. Since the geometry and density of the two types of fibers are very close (ρ_p ~ 1.2 kg m^{-3} for nylon and ρ_p ~ 1.4 kg m^{-3} for cotton), it seems that the difference in behavior is more likely associated with the stiffness of the two different fibers. Indeed, we think that flexible fibers are less sensitive to inertia effects as they can deform under the action of pressure forces. Therefore, it is logical to observe the drift of the flexible cotton fibers toward $x_{e.}$ On the contrary, the rigid, nondeformable nylon fibers are more sensitive to pressure, and thus drift away from x_e as expected from the model.

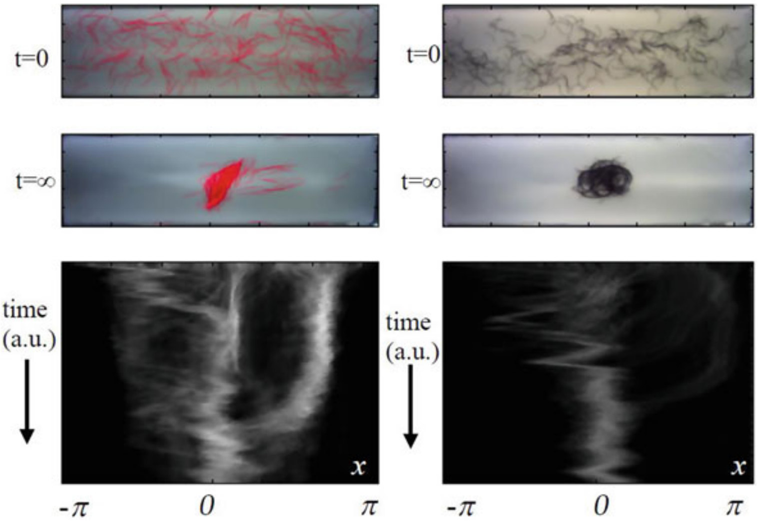

Fig. 7 Pictures of the initial and final states in the case of compaction of rigid nylon fibers (left) and flexible cotton fibers (right). Corresponding spatiotemporal diagrams revealing the compaction dynamics

Let us consider now a forcing with a frequency ω around the resonance frequency resulting in a wave having an amplitude larger than in the previous experiments. Moreover, a transverse mode of oscillation appears also in the tank. We see in Fig. 7 that relatively compact clusters are formed now and that whatever the nature of the fibers, these balls stand in the center of the basin after the experiments have run several hours. The associated space-time diagrams of Fig. 7 show, however that, in the case of the rigid nylon wires, the aggregation occurs initially (and as before) at $x_c = \pm\, \pi/2$ before the cluster drifts to the equilibrium location $x_e = 0$. This original phenomenon can be understood using our model as presented earlier. A time $t = 0$, the rigid nylon fibers are expelled from the fixed points toward attractors located at $x_c = \pm\, \pi/2$. The forcing being sufficiently strong this time and three-dimensional because of the presence of basin transverse mode, the fibers will form a deformable cluster of fibers, which in consequence increases the influence of the viscous force and reduces the effects of pressure. After a certain time, the cluster behaves as a deformable particle and migrates as a whole to the fixed equilibrium points as expected for flexible particles by our model and as observed in the experiments.

Finally, to follow the compaction rate in time, we have defined the ratio β of the projected areas occupied by the fibers on the bottom of the tank (the black pixels on the video images) to the total horizontal section of the basin. β is a function of time and the ratio of β by the initial β_0 represents the compaction rate of the system. The temporal evolution of the averages on ten independent realizations of the ratio β/β_0 is represented in Fig. 8 for both cotton and nylon fibers. As can be seen, clear power laws are visible for both rigid fibers and flexible fibers clustering. Power laws fit of

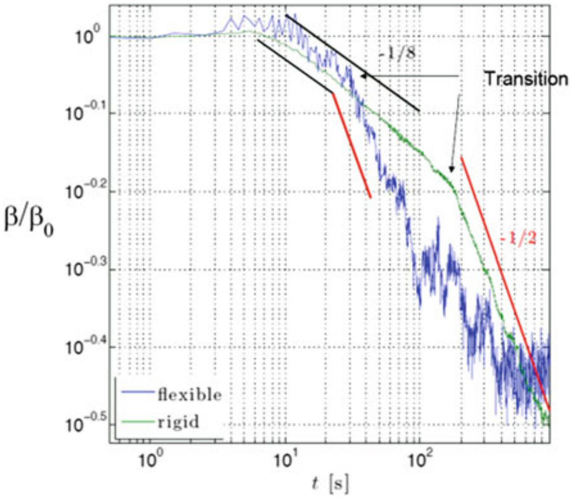

Fig. 8 Evolution of the compaction rate β/β_0 as a function of time. An average of 10 independent realizations have been performed. Power laws are clearly visible in both cases with a transition in the exponent values

the experimental curves give an exponent close to $-1/8$ at the beginning of the run (up to 10 s for the flexible fibers, and up to 100 s for the rigid ones). A transition then occurs and a regime with power laws with an exponent equal to $-1/2$ takes place in both cases. We suspect that the appearance of fiber interactions to be at the origin of these power laws that escape our modeling.

3 Conclusion

Inspired by the observation of natural aggregates formed by the motions of air or sea water, our studies on the dynamics of formation of fiber aggregates show that the Stokes drift is at the origin of the movement of the fibers and finally of their clustering in our set-up. The location of the clusters in the experiment is understood by the study of the stability of the fixed points of the particle dynamics equation when forced by a simple periodic (in space and time) fluid velocity field. A criterion based on the relative magnitude of the pressure effects compared to the viscous drag is deduced from a simple one-dimensional point particle model. This criterion based on the zeroing of the Stokes drift is quite general and may be useful to understand and even promote particle segregation. Our experiments, using flexible or rigid fibers confirmed the predicted attractive (where the aggregates form) or repulsive locations. This model even leads to the interpretation of the difference in behavior between rigid and flexible fibers. Finally, we observe that the aggregation process obeys temporal power laws that escape our modeling and are probably related to fiber interactions.

Acknowledgements This work has received funding from the Labex MEC Project (No. ANR-10-LABX-0092) and from Excellence Initiative of Aix-Marseille University—A*MIDEX, a French "Investissements d'Avenir" programme.

References

1. Verhille G., Moulinet S., Vandenberghe N., Adda-Bedia M. and Le Gal P. (2017) Structure and Mechanics of Aegagropilae Fiber Network. PNAS x: pp-pp.
2. Maxey M.R. and Riley J.J. (1983) Equation of motion for a small rigid sphere in a non uniform flow. Phys. Fluids 26: 883–889.
3. Blondeaux P. (1990) Sand ripples under sea waves. Part 1. Ripple formation. J. Fluid Mech. 218: 1–17.
4. Larrieu E, Hinch J. and Charru F (2009) Lagrangian drift near a wavy boundary in a viscous oscillating flow. J. Fluid Mech. 630: 391–411.
5. Xu S. and Nadim A. (2016) Oscillatory counter-centrifugation. Physics of Fluids 28 (2), 021302.

Part II
Patterns in Nonequilibrium Media

Order and Chaos in 2D Nonequilibrium Media: Review of Ezersky's Experiments

Mikhail Rabinovich and Patrick Weidman

1 Introduction

As emphasized in our joint publication with Aleksandr Ezersky of the book *The Dynamics of Patterns* [12], regular and chaotic pattern formation has traditionally been studied in nonequilibrium physics from the viewpoint of describing the basic structures and their interactions in different media. Particular attention has been paid to the analysis of generic properties of certain simple planforms, such as periodic (cellular) structures, quasiperiodic structures, as well as the dynamics and interactions of localized structures, topological defects, and features of 2D turbulence; see François et al. [8]. While this is still an important area of research, the emphasis in the past few years has been shifting toward analysis of specific properties of patterns in various complex media. In the past two decades in addition to "conventional" pattern formation, scientists have focused much attention on novel phenomena occurring in "smart" brain-like media that are characterized by highly nontrivial local dynamics and complex networks with nonlocal interactions. Scientists have addressed the dynamics and studied the general principles of learning and memory, and so forth. The ideas and principles also are used in modern technology; see François et al. [7].

Aleksandr Ezersky became interested in the nonlinear dynamics of patterns more then 30 years ago. He has focused mainly on the following three aspects: patterns on parametrically excited capillary waves; patterns in a cell with Rayleigh-Bénard and Bénard-Marangoni convection; and vortices in the vibrated soap film. Although his convection experiments are of great importance (see, for example, [2]), in this

---

M. Rabinovich (✉)
BioCircuits Institute, University of California, San Diego,
9500 Gilman Drive #0328, La Jolla, CA 92093-0328, USA
e-mail: mrabinovich@ucsd.edu

P. Weidman
Department of Mechanical Engineering,
University of Colorado, Boulder, CO 80309-0427, USA
e-mail: patrick.weidman@colorado.edu

N. Abcha et al. (eds.), *Nonlinear Waves and Pattern Dynamics*,
https://doi.org/10.1007/978-3-319-78193-8_9

tribute we will discuss his contributions to parametrically excited liquid layers and soap films. It is important at this point to note here that Ezersky's experimental results are still in demand.

2 Faraday Ripples

Ezersky's first experiments on spatiotemporal chaos in parametrically excited capillary waves were published in 1985 [4]. These seminal experiments form the basis for a series of deep investigations into the transition to spatiotemporal disorder in 2D media and the origin of 2D turbulence.

The primary patterns and the secondary chaotic instabilities of parametrically forced surface waves (Faraday ripples) in a large system have been observed by Ezersky and coauthors for the first time. In general, the symmetry of the primary pattern (stripes, squares, or hexagons) depends on the kinematic viscosity ν and driving frequency f_0. A lot of new phenomena have been analyzed in subsequent publications [5, 6]. Hexagons are observed at low f_0 over the whole viscosity range. Boundary-induced distortion is absent for the hexagonal and square patterns, but present for stripes. Phase defects occur between hexagonal domains differing in phase by π (with respect to the forcing). Patterns of different symmetries coexist and produce patterns with defects in certain parameter ranges; see Fig. 1 reproduced here from Kiyashko et al. [10] with panels (a), (b), (c) separated by 2.0 s. The transition to spatiotemporal chaos depends on the symmetry of the primary patterns; see Ezersky et al. [5] and Kudrolly and Gollub [11].

The development of 2D turbulence has been investigated both experimentally and theoretically. It was shown that modulation in the form of quasiperiodic "focusing" appears with an increase of the supercriticality e on the background of the Faraday ripples, and with further increase of e this focusing goes over (via intermittency) to spatiotemporal chaos. The dynamical nature of the observed chaos is established. Two examples are given. First, in Fig. 2, the complexity of the patterns of the capillary ripple on the surface of a vibrating layer of silicone oil increases with the supercriticality as shown in panels (a) $e = 0.4$, (b) $e = 0.53$, and (c) $e = 1.13$. Second, in Fig. 3, the transverse modulation of a standing ripple wave outside the region with square cells is found at $e = 0.1$.

The onset of parametric turbulence of capillary waves is an example of the creation, in a real nonequilibrium medium, of spatiotemporal chaos that is dynamical in nature and does not require for its explanation any prior "chaotic hypotheses". The transition to chaos and its finite-dimensional description are determined by the resonance character of the parametric excitation of waves and do not depend on the boundary conditions on the periphery of the medium.

To describe the 2D turbulence theoretically one can derive a parametric variant of the well-known Ginzburg–Landau equation (GLE). The experimentally observed two-dimensional chaos on a background of elementary cells near the threshold for the onset of turbulence is almost a superposition of one-dimensional mutually

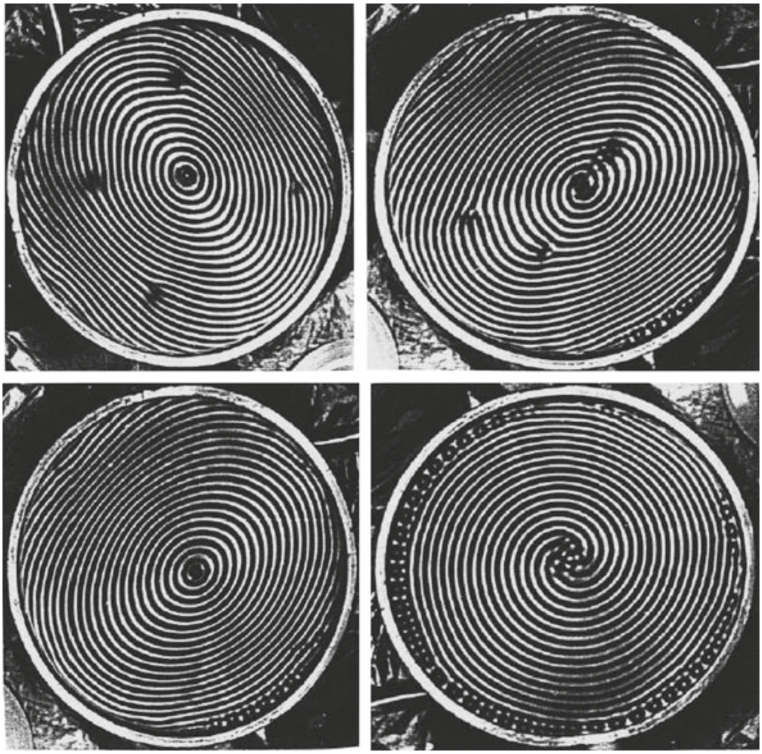

Fig. 1 Faraday ripples in a laboratory experiment: **a** a target with four dislocations (two positive and two negative); **b** one dislocation is attracted to the target core, spiral is formed; **c** all dislocations have been attracted to the center and annihilated, a perfect target reappeared; **d** asymptotic state of another experiment where a three-armed spiral was formed and rotated for a long time

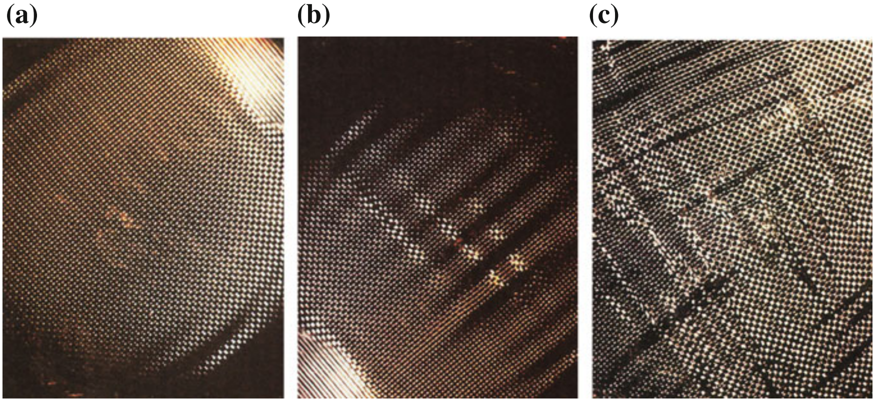

Fig. 2 Increasing complexity e of patterns of the capillary ripple in the Faraday experiment with silicone oil. **a** $e = 0.4$; **b** $e = 0.53$; **c** $e = 1.13$

Fig. 3 Transverse modulation of a standing ripple wave outside the region with square cells at supercriticality $e = 0.1$

orthogonal structures with random modulation, and is justified by the constructed one-dimensional theory. As the numerical experiments have shown, the GLE with the same parameter values can describe different steady-state chaotic regimes. This implies that in its phase space several different chaotic attractors exist simultaneously, and which of these is eventually reached is determined by the initial conditions. Visually, in an experiment, a set of spatial forms (patterns) is established on the background of the capillary ripples at the same supercriticality. The transition to chaos is investigated experimentally in a system of capillary waves parametrically excited in a thin layer of fluid in a cavity oscillating in the vertical direction. In a certain range of fluid depths, when the amplitude of oscillation is increased, a regular wave system is replaced quasiperiodically in time by a chaotic field.

The above-discussed experiments have shown that the low-frequency oscillations appearing in the large system can be the result of subsequent intermittency of chaos and explained by the resonance between capillary ripples and gravity waves. According to the estimates, the group velocity of capillary waves at 70 Hz is close to the velocity of gravity waves. If the fluid depth is such that the velocity of gravity waves does not belong to this range, neither the excitation of low-frequency waves nor the temporal intermittency of chaos occurs (details of the spectra are presented in Fig. 3a of [6]).

Ten years after the observation and analyses of spatiotemporal chaos, Kiyashko et al. [10] discovered rotating spirals in a large Faraday experiment. Spirals in such media are waves. These may be waves of density or temperature, or waves of amplitudes and phases of oscillating fields. Figure 1a–c shows Faraday ripples in a laboratory experiment with production and annihilation of dislocations and Fig. 1d shows an asymptotic state in which a three-armed spiral was formed and rotated for a long time.

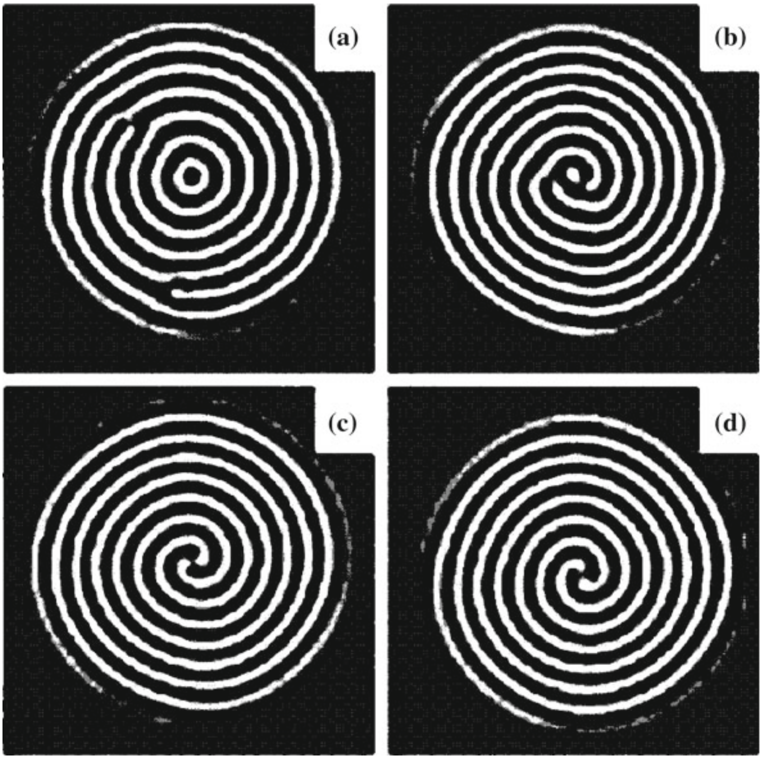

Fig. 4 Snapshots of multiarmed spiral formation in numerical simulation with parameters $\gamma = 1.0$, $\nu = 0.5$, $\alpha = 0.0$, $\kappa = 1.0$, $k_0 = 1.0$, $\xi = 0.1$. A target with two dislocations on the periphery was taken as the initial condition. **a** $t = 10$, **b** $t = 100$, **c** $t = 200$, **d** $t = 300$

Multiarmed spiral waves are found in a Faraday experiment performed in a thin layer of viscous liquid placed in a vessel subjected to the oscillating gravity field normal to the quiescent free surface of the liquid. These objects are standing capillary waves with spiral-like fronts slowly rotating around the core. Examples of spiral structures and their formation from a target pattern via defect dynamics are given in Fig. 4 reproduced here from Kiyashko et al. [10]. Spirals having different topological charges born as a result of the motion of a defect toward the center of cylindrical pattern were observed. Experiments indicated that the existence of capillary spirals is sustained by the mean flow generated near the walls of the cell by rapidly damped viscous surface waves.

A theoretical description of these spiral waves was devised using a model equation for the complex order parameter ψ that takes into account the principal features of parametrically excited structures [10], viz.,

$$\frac{D\psi}{Dt} = i\gamma\psi^* - \nu\nabla^2\psi - (1 + i\alpha)|\psi|^2\psi + i\kappa(\nabla^2 + k_0^2)\psi \tag{2.1}$$

Here, $D/Dt = \partial/\partial t + \mathbf{u} \cdot \nabla$ is the substantial derivative where $\mathbf{u}$ is the velocity of the induced mean flow, ψ is the complex amplitude of surface oscillations at the parametric frequency ω_0 (half of the driving frequency), γ is the amplitude of external forcing, κ is the dispersion parameter, and the superscript * denotes complex conjugate. Linear terms in this equation can be derived from the dispersion relation for capillary waves under parametric excitation, expanded near $\omega = \omega_0$ and wavenumber $k = k_0$. The nonlinear term is written here in its simplest possible form and describes two mechanisms of stabilization of parametric instability—one due to nonlinear energy dissipation ($|\psi|^2\psi$) and the other due to a nonlinear mismatch from parametric resonance ($i\alpha|\psi|^2\psi$).

Equation (2.1) with periodic boundary conditions was studied numerically using a pseudospectral split-step method with 256×256 collocation points, domain size $d = 200$, and integration time step 0.05. To simulate waves in a circular cavity, we ramp the linear dissipation outside the circle of radius $r_0 = 86$, i.e., $v = v_0, r < r_0$, and $v = v_0[1 + k(r - r_0)], r > r_0$, where k varied between 0.5 and 1.0. It is assumed that the flow is directed radially and is azimuthally symmetric, i.e., $u = u(r)\,\hat{\mathbf{r}}$. The profile for flow velocity, $u(r) = u_0\, exp[\xi(r - r_0)]$ is used. For $\gamma > \nu k_0^2$ the trivial state $\psi = 0$ is unstable with respect to perturbations with wavenumbers near k_0. Numerical simulations show that at the nonlinear stage, these perturbations give rise to various cellular patterns, including plane waves, targets, and spirals. Without the mean flow term ($u_0 = 0$), these patterns remain stationary even when nonlinear coefficient in (2.1) is complex. A nonlinear frequency shift proportional to α only leads to deviation of the selected wavenumber from $k = k_0$. In systems with ordinary (nonparametric) pattern forming instabilities, non-potential effects usually lead to wave propagation. However, when the near-wall flow is introduced in (2.1), standing waves comprising targets and spirals begin to drift slowly toward the center. The multiarmed spirals are born due to dislocation motion toward the core of the structure. The topological charge of the spiral is equal to the sum of topological charges of the dislocations.

Recent advances in the physics of parametric fluid sloshing and related problems are discussed in a very good review paper written by Ibrahim [9]. Parametric liquid sloshing, i.e., Faraday waves, has been a long standing subject of interest. The development of the theory of Faraday waves has witnessed a number of controversies regarding the analytical treatment of sloshing modal equations and mode competition. One of the significant contributions is that the energy is transferred from lower to higher harmonics and the nonlinear coupling generates static components in the temporal Fourier spectrum, leading to the contribution of a non-oscillating permanent sinusoidally deformed surface state. These also include the boundary value problem of parametric liquid sloshing, like Kiyashko at al. [10] have emphasized. The physics of Faraday wave competition together with pattern formation under single-, two-, three-, and multi-frequency parametric excitations is a very promising area of research. Significant efforts have been expended to understand and predict the pattern selection using analytical and numerical tools. Mechanisms for selecting the main frequency responses, different from the first sub-harmonic, were identified in the literature. Nontraditional sources of parametric excitation like earthquake and Faraday waves of ferromagnetic films and ferrofluids also have attracted a lot of attention.

3 Vortices in Oscillating Soap Films

Realizing the wealth of studies available on the Faraday problem for a liquid layer, Weidman, while on sabbatical leave visiting the International Center for Advanced Studies in Nizhny Novgorod during the summer of 1996, conceived the idea to apply the Faraday problem to a soap film. The results reported here may be found in Afenchenko et al. [1].

The experimental apparatus used to vibrate soap films supported on circular (8 cm diameter) and square (7 cm on a side) support frames is depicted in Fig. 5. The cavity was made of clear Plexiglass with the lower half attached to the vibrator. The support frames were rigidly located inside the upper half the cavity to minimize evaporation and protect the film from external air currents and surface contamination. The upper half of the cavity could be removed to form a soap film composed of 5% glycerin, 1% Russian baby soap, and 94% tap water. With both halves assembled, the soap film was symmetrically disposed between the upper and lower Plexiglas boundaries. Figure 5 shows the overhead lighting, accelerometer, and small ports open to the atmosphere to adjust the pressure drop across the film so as to obtain a flat film

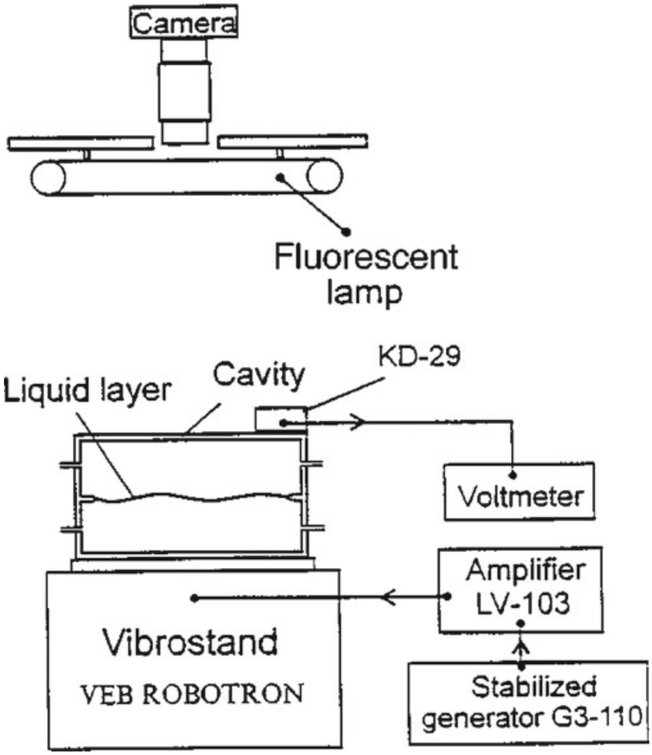

Fig. 5 Schematic of the experiment to vertically vibrate a soap film

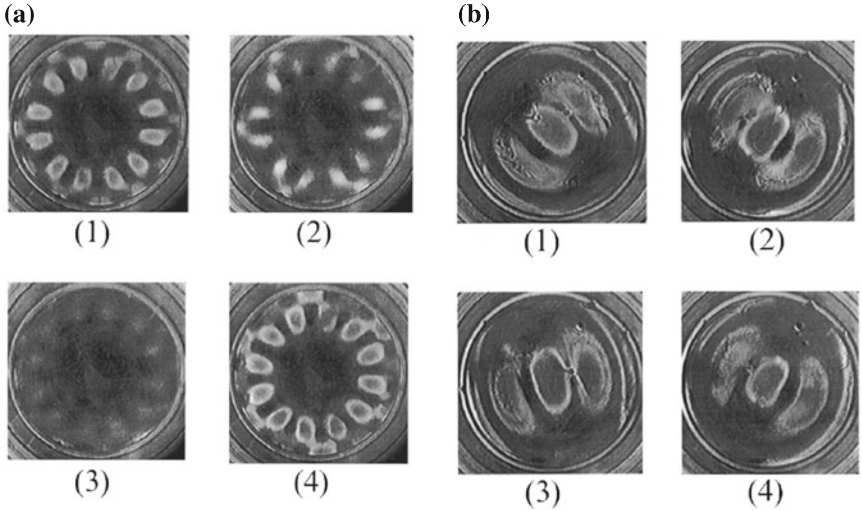

Fig. 6 Shadowgraphs of nonstationary flexural wave patterns in circular and rectangular support frames: **a** amplitude modulation at $f = 75$ Hz; **b** quasiperiodic rotation at $f = 45$ Hz

prior to vibration. Vortex structures were excited in the frequency range 20–200 Hz with accelerations 3–18 g_0, where g_0 is Earth's gravity. For future reference, we denote the film thickness as $h(x, y)$ and the film deflection as $\eta(x, y)$ where (x,y) are coordinates in the horizontal plane of the undisturbed film.

Early in the experiment incoherent light interference by the relatively thick $O(\mu\text{m})$ films produced clear shadowgraph images of the planforms of transverse oscillation. These membrane modes formed interesting spatiotemporal patterns as shown in Fig. 6. Pulsations of mode amplitude with pulsation frequencies in the range 0.3–1.0 Hz are shown in Fig. 6a and the quasiperiodic rotation of harmonic modes with angular frequencies in the range 0.5–1.0 Hz are shown in Fig. 6b. The frequencies f of excitation are noted in the figure captions. Also, in the square support frame, rolls parallel to the x-axis alternating with rolls parallel to the y-axis at frequencies in the range 0.3–0.6 Hz were observed at excitation frequency $f = 59$ Hz. Through evaporation and by internal redistribution of liquid in the film, very thin $O(n\text{m})$ regions evolved. The organized interference patterns of colored fringes associated with these thin films afforded a means of tracking the horizontal fluid motion and also of estimating thickness variations across the film surface.

The photographs in Fig. 7 reveal that transverse periodic vibration of the cavity can induce in the film quasi-steady motion in the form of counter-rotating vortices. Two types of regular vortex structures were observed: (i) counter-rotating vortex pairs with continuous rotation to the center of each vortex as in Fig. 7b, and (ii) counter-rotating vortex pairs whose cores evolve to stationary black islands—a small elliptical black core may be seen at the center of the vortex on the right in Fig. 7a. It should be noted that this counter-rotating vortex pair was formed by a sudden change in amplitude at

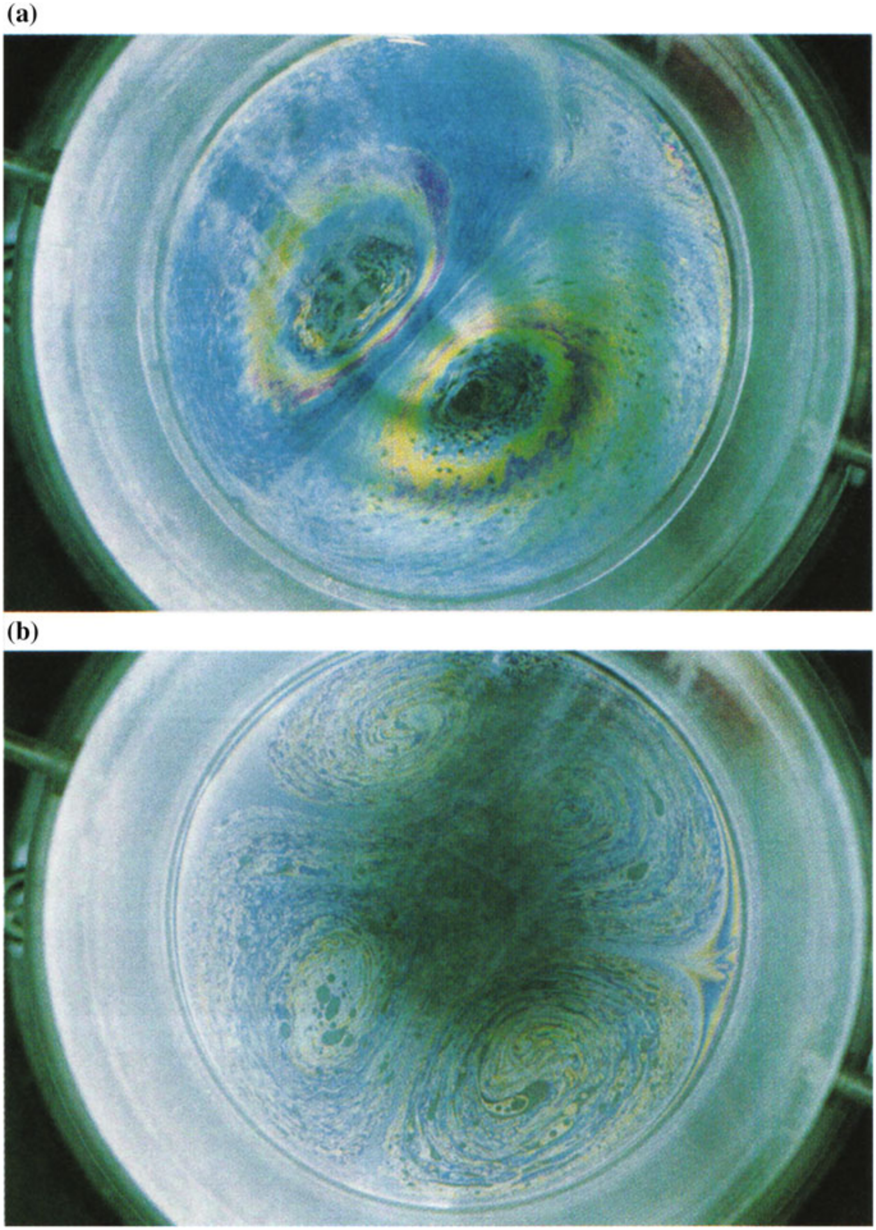

Fig. 7 Vortex motion in a circular cell: **a** single counter-rotating vortex pair at $f = 127$ Hz with feint dark circles indicating nodes of the background flexural mode pattern; **b** two counter-rotating vortex pairs at $f = 50$ Hz

the fixed frequency $f = 127$ Hz. The thinnest films ($h = 4.5\ n$m) are called *black films* and the next largest ($h = 30\ n$m) has a distinct silver hue [3]. Once formed, these ultrathin films are irreversibly stable, i.e., they cannot reinflate. At high-forcing frequencies many pairs of counter-rotating vortices, periodically distributed around the perimeter of the circular cell were observed as in Fig. 8a. These vortices ultimately coalesce to form larger vortices; a snapshot during this vortex merging process is given in Fig. 8b where the flow in a square cell has evolved for some time leading to the appearance of black film patches forming the vortex cores.

Not all vortices are linked to the film boundary; they often appear spontaneously at internal positions as shown in Fig. 9a for a circular cell and Fig. 9b for a square cell. At weak-forcing amplitude, the films take on one of two characteristic patterns depending on the excitation frequency. At low frequencies, one observes a stable symmetric pattern of thin films with vortex structures separated by thick bladders as in Fig. 10a; counting the fringes in this pictures gives an estimate of the ratio of bladder to black film thickness greater than 1000:1. At higher frequencies, the evolution of black films inevitably breaks the pattern symmetry as in Fig. 10b; here the flow is forced to meander around isolated black islands and thick bladders that appear irregularly over the film surface.

Two models have been developed to explain the vortex patterns observed in the experiments. One is a wave-boundary interaction model that neglects the presence of the surrounding air. The other is a model accounting for the complicated interaction between the liquid film and the surrounding air that neglects the wave-boundary interaction. These models are described in the following sections.

3.1 Marangoni Wave Model

Three types of waves are known to exist in soap films. In addition to the hydrodynamical transverse waves of symmetric (varicose) and antisymmetric (sinuous) type, there exists a longitudinal Marangoni wave produced by the variations in the surface concentration of soap molecules. Ezersky (in [1]) modeled the interaction between the Marangoni waves and the circular boundary of the soap film using the assumption of zero deflection $\eta(x, y) = 0$ and neglected the role of air. For this flat liquid layer, Marangoni waves in the absence of dissipation are described by the inviscid film equations [3]

$$\frac{Dh}{Dt} = -h(\nabla \cdot \mathbf{u}), \qquad \frac{D\mathbf{u}}{Dt} = -\frac{E(h)}{\rho h^2}\nabla h, \tag{3.1a, b}$$

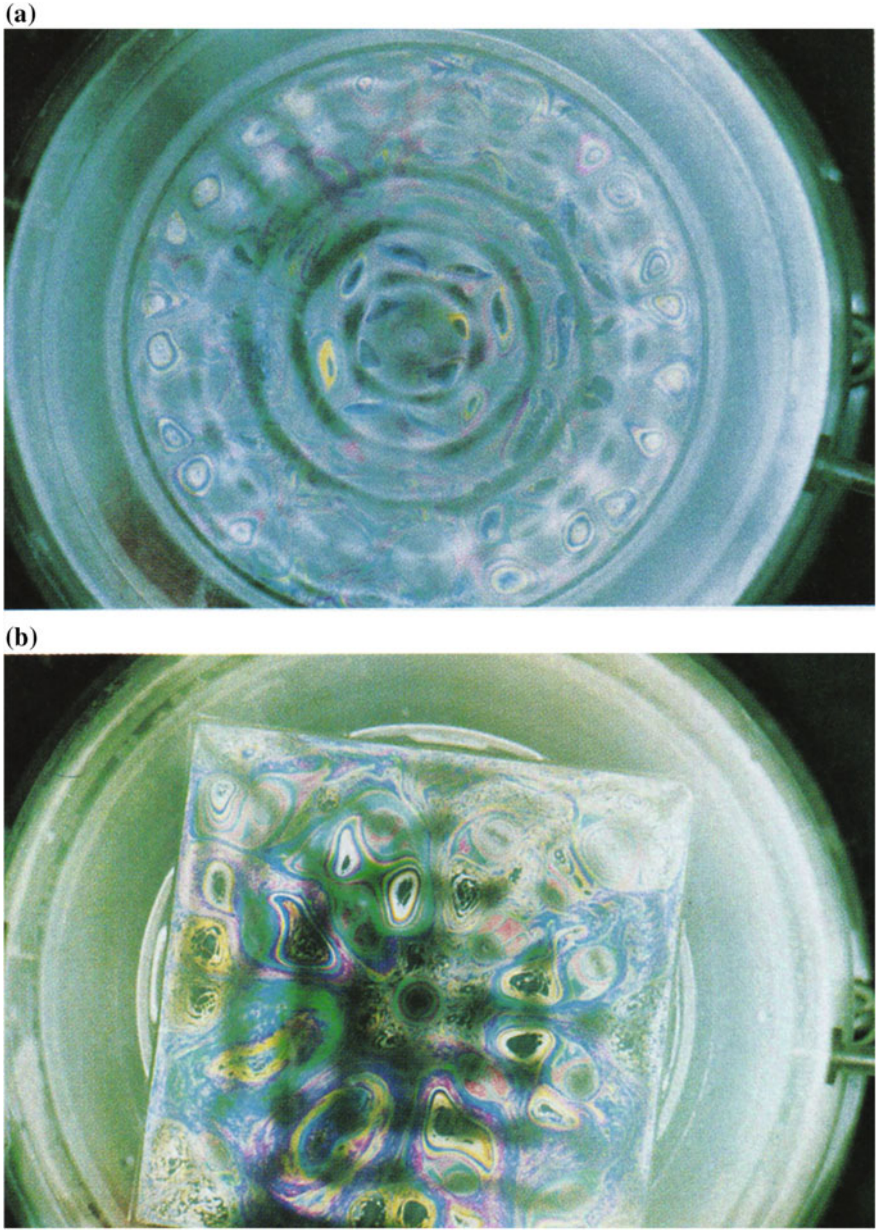

Fig. 8 High-frequency patterns: **a** 14 pairs of counter-rotating vortices adjacent to the perimeter of a circular cell at $f = 199$ Hz; **b** vortex pattern in a square cell at $f = 176$ Hz showing vortex pairing and the evolution of black films at vortex centers

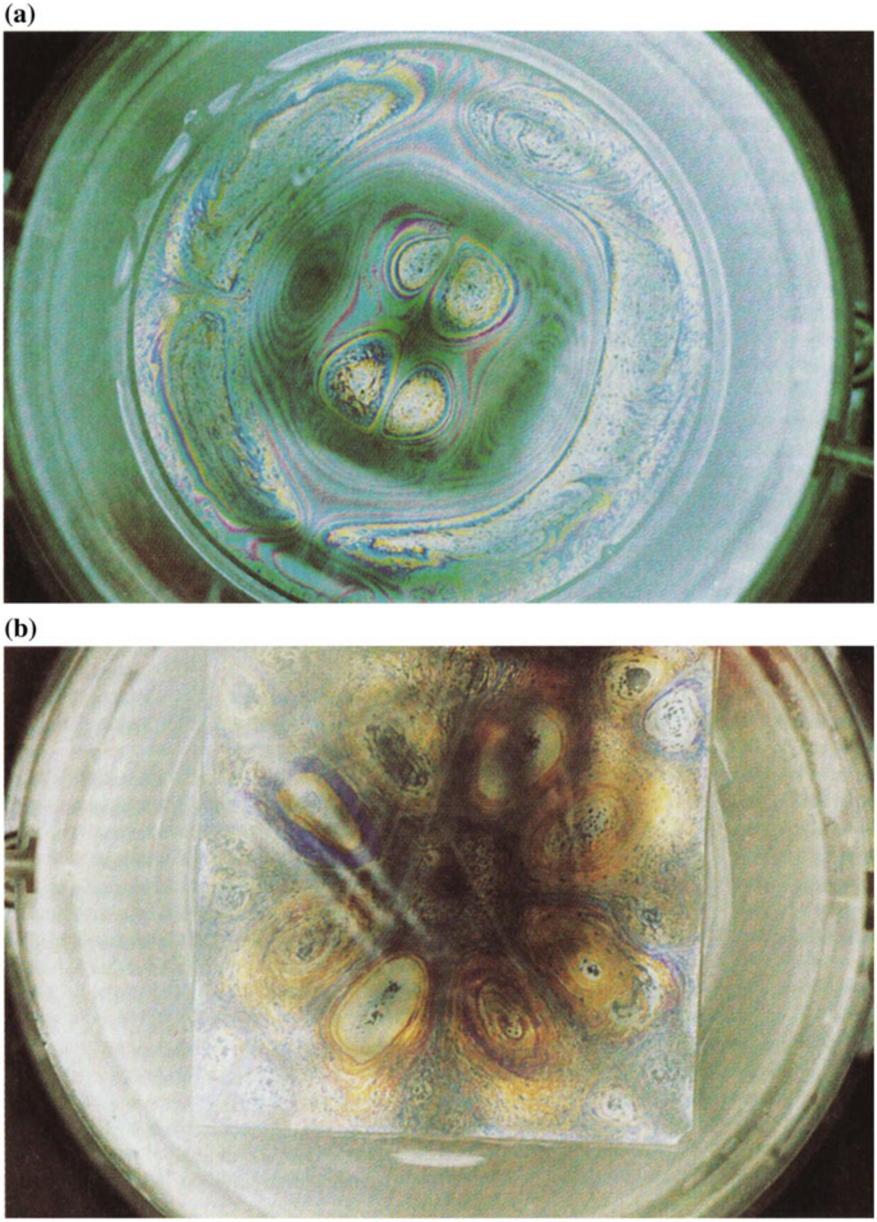

Fig. 9 Vortex patterns generated away from soap film boundaries: **a** two counter-rotating vortex pairs in a circular cell at $f = 65$ Hz; **b** four counter-rotating vortex pairs symmetrically disposed around the center of a square cell at $f = 180$ Hz

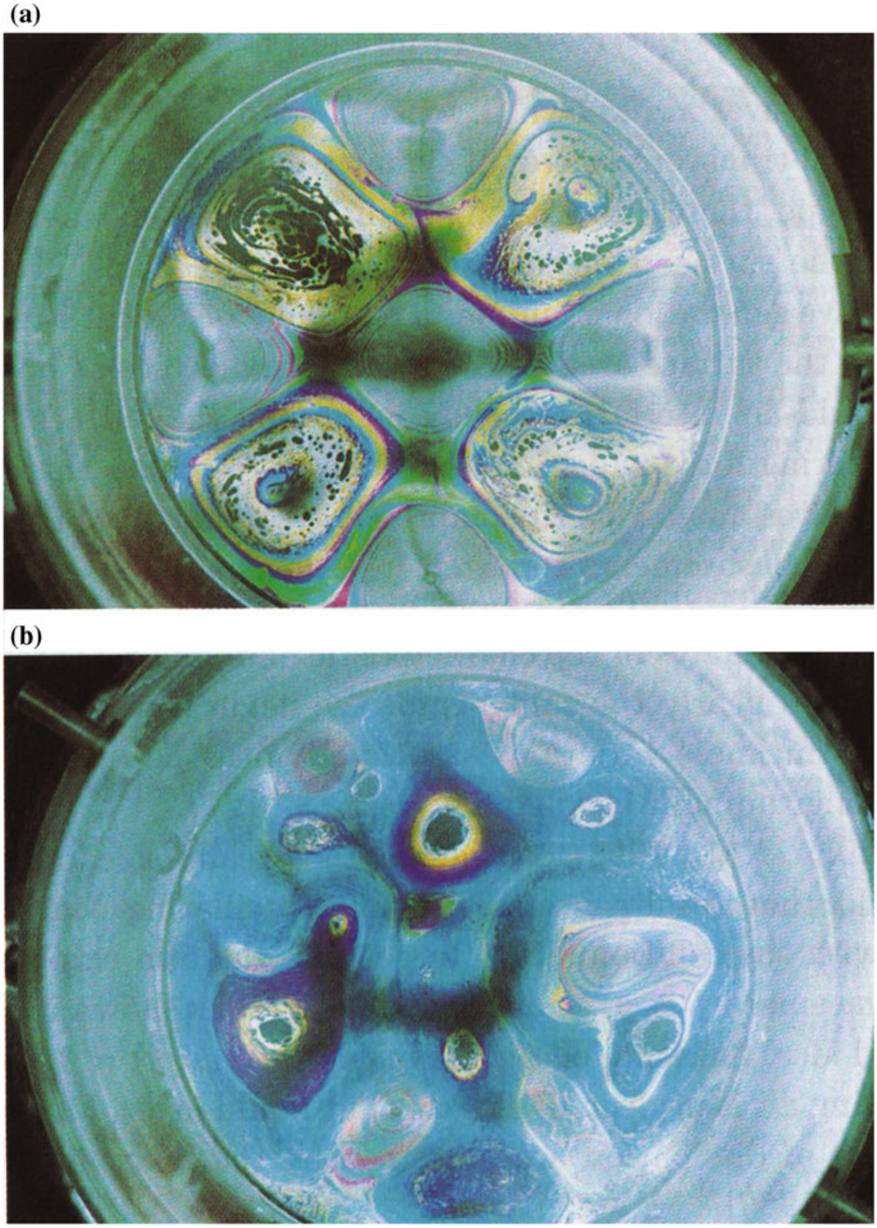

Fig. 10 Late time features of vibrating soap films: **a** four vortices symmetrically disposed between four thick fluid bladders at $f = 53$ Hz—each vortex around the circle rotates opposite to its neighbor and a thick bladder resides in the center of the cavity; **b** symmetry breaking of a regular pattern due to vortex pairing and the formation of black films at $f = 84$ Hz

where $\mathbf{u}(x, y)$ is the two-dimensional velocity field in the plane of the film, ρ is the liquid density, and $E(h)$ is the film elasticity. Small disturbances of $\tilde{\mathbf{u}}$ and $\tilde{h}$ of a stationary film of uniform thickness h_0 lead to the linear wave equation

$$\frac{\partial^2 \tilde{h}}{\partial^2 t} - c^2 \nabla^2 \tilde{h} = 0, \qquad c = \sqrt{\frac{E_0}{\rho h_0}} \tag{3.2}$$

where $E_0 = E(h_0)$ and c is the Marangoni wave speed.

The Marangoni waves torsionally rotate in the plane of the liquid creating a thin Stokes layer at the film boundary. The thickness of the Stokes layer scales as $\delta \sim (\nu/\Omega)^{1/2}$, where ν is the effective kinematic film viscosity (soap films possess both bulk and surface viscosities) and Ω is the frequency of Marangoni wave oscillation. To analyze what mean flows are produced by the Marangoni waves, Afenchenko et al. [1] consider the simple geometry of a film supported by a circular frame of radius R_0. In (r, θ) cylindrical coordinates, the disturbance velocities are $(\tilde{u}_r, \tilde{u}_\theta)$. Solution of (3.2) for $\tilde{h}$ is readily obtained and then $\tilde{u}_\theta$ is computed from $\tilde{h}$ using Eq. 3.1a, b giving

$$\tilde{u}_\theta = U_\tau(r, \theta)\cos(\Omega t), \qquad U_\tau = -\left(\frac{nE_0}{\rho\Omega h_0^2}\right)\frac{1}{r}J_n\left(\frac{\Omega r}{c}\right)\sin[n(\theta + \theta_0)], \tag{3.3}$$

where $J_n(z)$ is the Bessel function of order $n \geq 1$ and Ω is the intrinsic frequency of the Marangoni mode found from the impermeability condition $J_n'(\Omega R_0/c) = 0$. Following [13], the steady-streaming velocity induced at the edge of the Stokes layer is given by

$$U_\theta = -\frac{3}{4\Omega}U_\tau(R_0, \theta)\frac{\partial U_\tau(R_0, \theta)}{\partial \tau} = -V_0 \sin[2n(\theta + \theta_0)]. \tag{3.4}$$

where $\tau = R_0\theta$ and

$$V_0 = \left(\frac{3n^3 E_0^2}{8\rho^2\Omega^3 h_0^4 R_0^3}\right) J_n^2\left(\frac{\Omega R_0}{c}\right). \tag{3.5}$$

Finally, for the small disturbances $\tilde{h} \ll h_0$, a Stokes streamfunction Ψ exists which in cylindrical coordinates is related to the velocities (u_r, u_θ) by $(r^{-1}\partial\Psi/\partial\theta, -\partial\Psi/\partial r)$. For the weak flows observed in the experiment, Ezersky assumed it was sufficient to consider only the zero Reynolds number two-dimensional Navier–Stokes equations

$$\nabla^4 \Psi = 0. \tag{3.6}$$

The solution of (3.6) regular at the origin and satisfying the steady-streaming boundary condition $u_\theta = U_\theta$ is given by

$$\Psi(r, \theta) = -\frac{1}{2} V_0 R_0 \left(\frac{r}{R_0}\right)^{2n} \left[1 - \left(\frac{r}{R_0}\right)^2\right] \sin[2n(\theta + \theta_0)]. \qquad (3.7)$$

Flow patterns for $n = 1, 2, 3$ are displayed in Fig. 11.

As the azimuthal mode number increases, the vortex cores, lying at discrete points on the circle $r_c = \sqrt{n/(n+1)}R_0$, shift toward the cell boundary in agreement with experiments. Note that the lowest mode shown in Fig. 11a produces two pairs of counter-rotating vortices; hence this simple model cannot describe the vortex pattern shown in Fig. 7a. This single counter-rotating vortex pair was observed in both circular and square cells. Ezersky showed, however, that a crude model of such a configuration in the circular cell is obtained if two Marangoni waves of neighboring

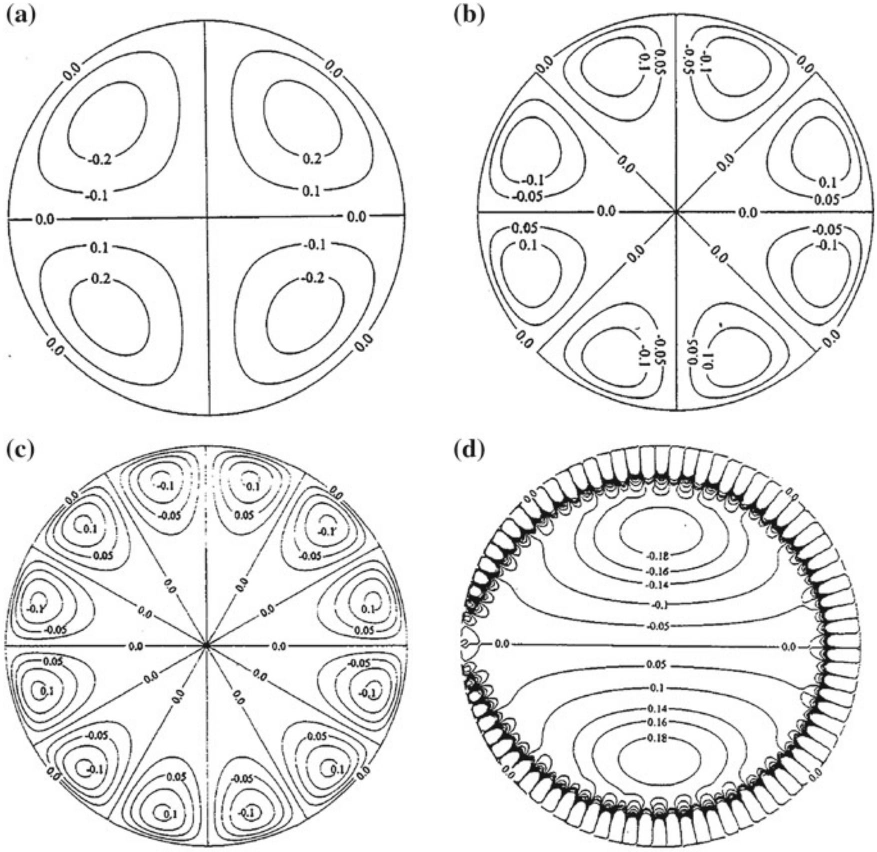

Fig. 11 Two-dimensional vortices generated by Marangoni wave-boundary interaction in a circular domain according to Eq. (3.7): **a** mode n=1; **b** mode n=2; **c** mode n=3; and **d** a vortex pair induced by a superposition of equal amplitude, in-phase modes $n = 20$ and $n = 21$

large angular mode numbers n and $(n+1)$ are excited. Then, by virtue of nonlinearity, the mean flow may be a pair of intense vortices. An example of computed streamlines for stationary vortices generated in this manner is presented in Fig. 11d.

3.2 *The Role of Air*

Assuming no evaporation from the film surfaces, no formation of black films, and no wave-boundary interaction, Vega et al. [14] modeled the oscillatory and non-oscillatory interaction of the liquid with the surrounding air. The analysis is very subtle and tedious, and also because this is not a contribution of Ezersky, only an outline of the methodology leading to the final governing equations will be presented.

The motion of the air above and below the film obeys the incompressible continuity and Navier–Stokes equations with continuous velocity and pressure conditions at the liquid–air interfaces. Here $\mathbf{x} = (x, y)$ are Cartesian coordinates in the plane of the unperturbed film, $\nabla = (\partial/\partial x, \partial/\partial y)$, $\mathbf{u} = (u, v)$ is the horizontal velocity of the liquid averaged across the film thickness, and z is the coordinate from the center plane of the quiescent horizontal film. The film interfaces lie at $z = \eta \pm h/2$ and satisfy $h \ll \eta \ll l$, where l is the characteristic horizontal length of the flow in the film. The full three-dimensional equations for the liquid motion are written in a coordinate system attached to the film. Averaging the equations across the film gives, to an approximation sufficient for the analysis, the governing equations

$$\frac{Dh}{Dt} + h(\nabla \cdot \mathbf{u}) = 0 \tag{3.8}$$

$$h\frac{D\mathbf{u}}{Dt} = \frac{2}{\rho}\nabla\sigma - h\left(\frac{\partial^2\eta}{\partial t^2} + g\right)\nabla\eta + \frac{1}{\rho}\nabla\cdot\boldsymbol{\tau}' + 2\nu\nabla(h\nabla\cdot\mathbf{u}) + \frac{1}{\rho}\boldsymbol{\tau}_b \tag{3.9}$$

$$\rho h\left(\frac{\partial^2\eta}{\partial t^2} + g + 2\mathbf{u}\cdot\nabla\frac{\partial\eta}{\partial t}\right) = 2\sigma\nabla^2\eta - \Delta p_g. \tag{3.10}$$

Eqs. (3.8) and (3.9) are the continuity and momentum equations for the thin liquid layer and Eq. (3.10) governs the deflection of the layer. Here g is gravity, and the subscript g is attached to stresses produced on the film by the gas phase. The surface tension coefficient σ is a function of the local surface concentration of soap which depends only on the local film thickness h; these variations are linear if the soap concentration is below the critical micelle limit. Here $\tau'_{ij} = \rho(h\nu + \nu^s)(\partial u_i/\partial x_j + \partial u_j/\partial x_i)$ is the viscous stress tensor containing contributions from the bulk liquid and its interfaces, with respective kinematic viscosities ν and ν^s, $\boldsymbol{\tau}_g$ is the sum of the shear stresses of the air on both sides of the film, and $\Delta p_g = p_g^+ - p_g^-$ is the difference of air pressures across the film.

The velocity and pressure in the air and the deflection of the film are decomposed into oscillatory ($e^{i\omega t}$) and non-oscillatory (subscript s) parts

$$(\mathbf{u}_g, w_g, p_g) = (\mathbf{U}_g, W_g, P_g)e^{i\omega t} + c.c. + (\mathbf{u}_{gs}, w_{gs}, p_{gs}) + \dots \tag{3.11a}$$

$$\eta = \Lambda e^{i\omega t} + c.c. + \eta_s + \dots \tag{3.11b}$$

where complex notation is used with c.c. denoting complex conjugate. The gas velocities and pressure depend on ($\mathbf{x}$, z) and Λ and η_s depend on $\mathbf{x}$ only. These quantities may also depend on time, in a characteristic time scale much larger than ω^{-1}, so these terms are described as being quasi-steady. Using the same notation as in Eq. (3.11), the liquid velocity and film thickness are decomposed as

$$\mathbf{u} = \mathbf{U}e^{i\omega t} + c.c. + \mathbf{u}_s + \dots, \qquad h = He^{i\omega t} + c.c. + h_s + \dots \tag{3.12a, b}$$

where $\mathbf{U}$, H, $\mathbf{u}_s$, and h_s depend on $\mathbf{x}$ only.

The analysis is divided into four parts: the oscillatory problems for the gas and the liquid and the quasi-steady problems for the gas and the liquid. For the oscillatory gas problem, the leading order gas variables and film deflection ($\mathbf{U}_g$, W_g, P_g, Λ) of expansions (3.11) satisfy linearized continuity and momentum equations in the air, Eq. (3.10) across the film and continuity of normal velocity at each liquid–air interface. Solution of this inviscid gas-phase problem gives the flexural modes of the air-film system and the potential oscillatory horizontal velocity of the air outside the thin viscous Stokes layers adjacent to the film surfaces, the structure of which is determined to within the unknown horizontal velocity $\mathbf{U}$ of the liquid in the film. Turning now to the oscillatory liquid problem, the leading oscillatory terms ($\mathbf{U}$, H) of expansions (3.12a, b) satisfy linearized forms of the liquid film continuity and momentum equations (3.8) and (3.9) with appropriate interfacial boundary conditions. Elimination of H then gives a single-vector equation for $\mathbf{U}$ which describes *Marangoni waves* in the liquid film forced by vertical oscillations of the air and the film.

Next, omitting details found in Vega et al. [14], solution of the quasi-steady gas problem yields the governing equation

$$2\sigma\nabla^2\eta_s = -\rho\omega[\Lambda^*\nabla\cdot(h_s\mathbf{U}) + 2h_s\mathbf{U}\cdot\nabla\Lambda^* + c.c.] - \rho_s(|\mathbf{U}_g^+|^2 - |\mathbf{U}_g^-|^2) - \rho g h_s \tag{3.13}$$

where $\mathbf{U}_g^{\pm} = \mathbf{U}_g(x, y, 0^{\pm})$ and the superscript * denotes complex conjugate. Finally, again omitted details, the leading order equations governing the quasi-steady streaming in the liquid film are found to be

$$\frac{Dh_s}{Dt} + h_s(\nabla\cdot\mathbf{u}_s) = 0 \tag{3.14a}$$

$$h_s\frac{D\mathbf{u}_s}{Dt} = -c_s^2\nabla h_s + \frac{1}{\rho}\nabla\cdot\boldsymbol{\tau}_s' + 2\nu\nabla(h_s\nabla\cdot\mathbf{u}_s) + \mathbf{G} + \mathbf{L}. \tag{3.14b}$$

The term $c_s^2 = c^2(h_s) = -2[d\sigma(h_s)/dh_s]/\rho$ is the square of the Marangoni wave speed. Several contributions to the quasi-steady viscous stress *surface forcing* terms

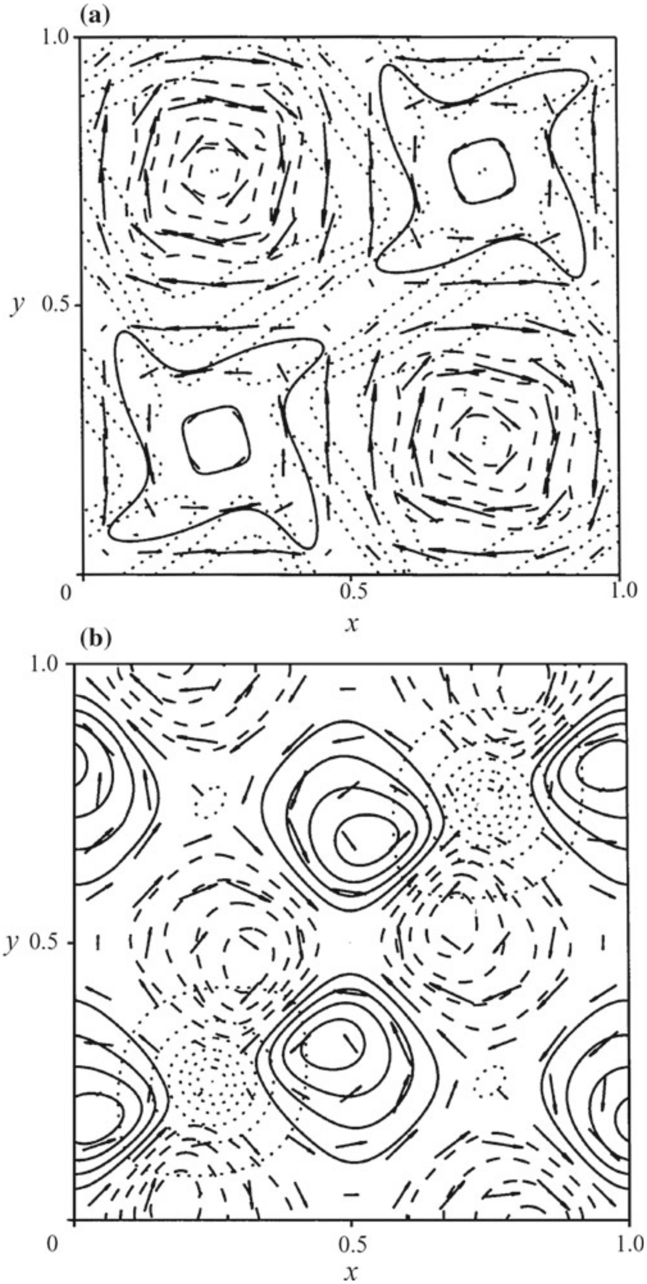

Fig. 12 **a** Solution of Eq. (3.14) with the dominant volume forcing term given in the text. Plotted are six equispaced contours of h_s between 0.15 and 2.02 (dotted), six contours of vorticity ω_s between -20 and 10 (solid for $\omega_s > 0$ and dashed for $\omega_s < 0$, and velocity arrows). **b** Solution of Eq. (3.14) with both volume and surface-forcing terms given in the text. Plotted are eight equispaced contours of h_s between 0.44 and 5.83 (dotted), eight contours of vorticity ω_s between -4 and 4 (solid for $\omega_s > 0$ and dashed for $\omega_s < 0$, and velocity arrows)

are lumped into the single vector $\mathbf{G}$ and the non-oscillatory contributions appearing from time-averaging the nonlinear terms in Eq. (3.9) are *volume forcing* terms lumped into the single vector $\mathbf{L}$, both containing components derivable from a potential Φ and components not derivable from a potential. In summary, the leading order quasi-steady evolution of film deflection and thickness, η_s and h_s, and of the the liquid velocity $\mathbf{u}_s$ are governed by the coupled system of equations (3.13) and (3.14) supplemented by appropriate initial and boundary conditions.

Rather than solve the entire system of steady and unsteady equations in both the air and the liquid film, the type of flows allowed by Eq. (3.14) may be found by choosing typical, but simplified, forcing terms $\mathbf{L}$ and $\mathbf{G}$ and prescribing periodic boundary conditions. Before integration, the variables are normalized so that the undisturbed thickness is $h_s = 1$ and the spatial domain lies in the square region $0 \leq x \leq 1$ and $0 \leq y \leq 1$. In the first simulation $\mathbf{L} = h_s \nabla \Phi_L$ is represented by $\Phi_L = 0.5 \sin(2\pi x) \sin(2\pi y)$. The dominant volume forcing term does not induce any motion by itself, but leads to a spatial thickness that enables or enhances the action of other terms. Thus, in order to mimic the strong recirculation regions sometimes observed in variable thickness regions around patches of black films, a non-potential forcing $\mathbf{G} = (\partial \Phi_g/\partial x, -\partial \Phi_g/\partial y)$ with $\Phi_G = 0.2\Phi_L$ is added to $\mathbf{L}$. Contours of constant film thickness and of vorticity along with some velocity vectors are shown in Fig. 12a. One observes two strong clockwise-rotating vortices in quadrants two and four in regions of small film thickness, and two weak counter-clockwise-rotating vortices in quadrants one and three where the film is relatively thick.

We now look at the combined effects of volume plus surface forcing by choosing the same volume potential $\Phi_L = 0.5 \sin(2\pi x) \sin(2\pi y)$ as above, but now taking the surface potential as $\Phi_G = 0.1 \sin(2\pi x + \pi/2) \sin(2\pi y + \pi/2)$. The result displayed in Fig. 12b shows four vortices of alternate signs appearing around each of the two bladders of large thickness on the main diagonal; two vortices with positive circulation at the left and right and two with negative circulation above and below. Again the velocity is higher outside the bladders than inside. The two counter-rotating vortex pairs in this square cell computation bear resemblance to the vortex system observed at the interior of the circular cell in Fig. 9a. Replacing Φ_G by Φ_G^2 gives a flow with eight vortices around each bladder, similar to what is observed at the interior of the square cell in Fig. 9b.

References

1. Afenchenko, V. O., Ezersky, A. B., Kiyashko, S. V. and Rabinovich, M. I., The generation of two-dimensional vortices by transverse oscillation of a soap film, *Phys. Fluids*, **10**, 390–399 (1998).
2. Afenchenko, V. O., Ezersky, A. B., Nazarovsky, A. V. and Veladre, M. G, Experimental evidence on the structure and evolution of the penta hepta defect in hexagonal lattices due to Rayleigh-Bénard and Marangoni convection, *Int. J. Bif. Chaos*, **11**, 1261–1273 (2001).
3. Couder, Y., Chomaz, J. M. and Rabaud, M., On the hydrodynamics of soap films, *Physical D*, **37**, 384–405 (1989).

4. Ezersky, A. B., Korotin, P. I. and Rabinovich, M. I., Spatiotemporal chaos in the parametric excitation of a capillary ripple, *Sov. Phys. JETP*, **41**, 157–160 (1985).
5. Ezersky, A. B., Rabinovich, M. I., Reutov, V. P. and Starobinets, I. M., Spatiotemporal chaos in the parametric excitation of a capillary ripple, *Sov. Phys. JEPT*, **64**, 1228–1236 (1986).
6. Ezersky, A. B., Temporal intermittency of chaos in parametrically excited capillary ripples, *Europhys. Lett.*, **16**, 661–666 (1991) and corrigendum published in *Europhys. Lett.*, **17**, 571 (1992).
7. François, N., Xia, H., Punzmann, H., Fontana, P. W. and Shats, M., Wave-based liquid-interface metamaterials, *Nature Communications*, **8**, 14325 (2017).
8. François, N., Xia, H., Punzmann, H. and Shats, M., Inverse energy cascade and emergence of large coherent vortices in turbulence driven by Faraday waves, *Phys. Rev. Lett.*, **110**, 194501 (2013).
9. Ibrahim, R. A., Recent advances in physics of fluid parametric sloshing and related problems, *J. Fluids Engrg.*, **137**, 090801 (2015).
10. Kiyashko, S. V., Korzinov, L. N., Rabinovich, M. I. and Tsmiring, L. S., Rotating spirals in a Faraday experiment, *Phys. Rev. E.*, **54**, 5037–5040 (1996).
11. Kudrolli, A. and Gollub, J. P., Localized spatiotemporal chaos in surface waves, *Phys. Rev. E*, **54**, R1052 (1996).
12. Rabinovich, M. I., Ezersky, A. B. and Weidman P. D. *The Dynamics of Patterns*, (World Scientific, Singapore, 2000).
13. Schlichting, H., *Boundary Layer Theory* (McGraw Hill, New York, 1960), p 226.
14. Vega, J. M. Higuera, F. J. and Weidman, P. D., Quasi-steady vortical structures in vertically vibrating soap films, *J. Fluid Mech.*, **372**, 213–230 (1998).

Chimera Patterns in One-Dimensional Oscillatory Medium

L. A. Smirnov, G. V. Osipov and A. Pikovsky

To the memory of our colleague and friend Sasha Ezersky.

Abstract Kuramoto and Battogtokh [Nonlinear Phenom. Complex Syst. 5, 380 (2002)] described chimera states as a coexistence of synchrony and asynchrony in a one-dimensional oscillatory medium. After a reformulation in terms of a local complex order parameter, the problem can be reduced to a system of partial differential equations. We further reduce finding of uniformly rotating, spatially periodic chimera patterns to solving a reversible ordinary differential equation, and demonstrate that the latter has many solutions. In the limit of neutral coupling, analytical solutions in the form of one- and two-point chimera patterns as well as localized chimera solitons are found. Based on these analytic results, patterns at weakly attracting coupling are characterized by virtue of a perturbative approach. Stability analysis reveals that only the simplest chimeras with one synchronous region are stable.

L. A. Smirnov (✉)
Institute of Applied Physics, Ul'yanov Street 46, 603950 Nizhny Novgorod, Russia
e-mail: smirnov_lev@appl.sci-nnov.ru

G. V. Osipov
Department of Control Theory, Nizhny Novgorod State University, Gagarin Av. 23, 603950
Nizhny Novgorod, Russia
e-mail: osipov@vmk.unn.ru

A. Pikovsky
Institute for Physics and Astronomy, University of Potsdam, Karl-Liebknecht-Street
24/25, 14476 Potsdam-Golm, Germany
e-mail: pikovsky@uni-potsdam.de

A. Pikovsky
Institute of Supercomuting Technologies, Nizhny Novgorod State University, Gagarin Av. 23,
603950 Nizhny Novgorod, Russia

N. Abcha et al. (eds.), *Nonlinear Waves and Pattern Dynamics*,
https://doi.org/10.1007/978-3-319-78193-8_10

1 Introduction

Chimera states in oscillatory media have attracted great attention since their first observation and theoretical explanation by Kuramoto and Battogtokh [1]. The surprising feature of chimera is the breaking of the translational symmetry: although a homogeneous fully symmetric synchronous state exists, yet another nontrivial state combining synchrony and asynchrony is possible and can even be stable. In terms of the local complex order parameter, chimera is a solution wherein a part of the space this parameter has absolute value one (full local synchrony), and in another part its absolute value is less than one (partial local synchrony). This description links chimera patterns to a general problem of pattern formation in media described by a complex field [2].

Chimeras (see [3] for a recent review) can be found at interaction of several populations of oscillators [4–7], or in an oscillatory medium [8–11]. Here, formulation in terms of a local coarse-grained complex order parameter indeed allows one to reduce the problem to that of evolution of a complex field [10, 11].

The goal of this chapter is to present a theory of chimera patterns in a one-dimensional (1D) medium. The main questions we address are: (i) How complex can be chimera states? (ii) Do solitary chimera states exist in an infinite medium? (iii) Is there a way of an analytical description of chimera patterns? (iv) What are the stability properties of chimera patterns?

This chapter extends a short communication [12] and is organized as follows. In Sect. 2, we briefly summarize the key provisions of the studied model. This will make it possible to introduce the required equations and reformulate the problem of chimera patterns in a 1D medium of coupled oscillators as a system of partial differential equations (PDEs). This allows us to represent uniformly rotating chimera states as solutions of ordinary differential equations (ODEs). Spatially periodic chimeras correspond to periodic orbits, of different complexities, of these ODEs. In Sect. 4, we develop the analytical approach for chimera states. First of all (in Sect. 4.1), we show that in the limit of neutral coupling, the obtained system of ODEs is integrable, yielding singular solitary "one-point" and "two-point" chimeras. Then (in Sect. 4.2), for a weakly attracting coupling we find the properties of the chimera states by a perturbation analysis of these solutions. The developed perturbation theory allows us to estimate typical sizes of the synchronous regions for simplest chimera patterns. In Sect. 5, we describe the numerical calculation procedure based on ODEs of the spatial structure of stationary chimera states. Here, we demonstrate a variety of chimera patterns. However, within the framework of this paper, we mainly concentrate on the analysis of chimeras in which no more than two synchronous regions are singled out with allowance for periodic boundary conditions. Furthermore, in Sect. 6, we study the stability of the found chimera patterns by employing a numerical method allowing one to disentangle essential continuous and discrete (point) parts (see [13, 14] and Sect. 6.1) of the stability spectrum. The proposed numerical method (see Sect. 6.2) is based on variation of a starting point of discretization and calculating eigenvalues of matrix several times. This allows us to determine all the point eigenvalues for chimera states. Based on the location of point spectrum, we can make a conclusion regarding the temporal stability of the stationary chimeras.

2 Formulation of the Problem. Basic Approaches and Equations

The original Kuramoto–Battogtokh (KB) model [1] is formulated as a 1D field of weakly nonlocally coupled identical phase oscillators, which are continuously distributed on an infinite domain. In this system, there are spatially periodic patterns of the distribution of the phases, which are called chimera states and characterized by the existence of a region or regions of coherent, phase-locked elements embedded in a background of incoherent oscillators.

In this chapter, as in most of the works, dedicated to the chimera phenomenon, we study the system of nonlocally coupled identical phase oscillators, which are continuously distributed on a finite interval $[0, L)$ and satisfy periodic boundary conditions. Such a configuration is completely equivalent to the case where the phase oscillators are equally spaced on a ring of length L.

In the discussed situation, the system of nonlocally coupled identical phase oscillators with the natural frequency ω (which can be, without loss of generality, set equal to zero) is mathematically described using the dynamic phase variable $\phi(x, t)$, which is defined at each point x of the interval $[0, L)$ and obeys the following integral-differential equation:

$$\frac{\partial \phi}{\partial t} = \omega - \int_0^L G(x - \tilde{x}) \sin\big(\phi(x, t) - \phi(\tilde{x}, t) + \alpha\big) d\tilde{x}, \quad (1)$$

where the constant α describes the phase shift effects. The last term on the right-hand side of Eq. (1) is an integral operator with the kernel $G(y)$. This kernel described the effects of nonlocal interaction inside the considered 1D oscillatory medium and satisfies the normalization condition, according to which the integral of $G(y)$ within the limits of 0 to L is equal to unity.

The KB model [1] exactly corresponds to Eq. (1) if the integration is performed in the infinite domain with the exponential kernel

$$G_{KB}(y) = \kappa \exp\big(-\kappa |y|\big)/2, \quad (2)$$

while the 1D field of phase oscillators $\phi(x, t)$ are assumed to have a period L.

In our case, when the integration over the domain of size L is performed, we use the kernel

$$G(y) = \frac{\kappa}{2\sinh\big(\kappa L/2\big)} \cosh\big(\kappa\left(|y| - L/2\right)\big), \quad (3)$$

which is the Green's function of the inhomogeneous Helmholtz equation (7) with the source on the right-hand side and periodic boundary conditions at the points $x = 0$ and $x = L$. It appears that $G(y)$ in the form (3) is more adequate for a periodic 1D oscillatory medium of size L, compared to the original purely exponential kernel. Note that Eq. (3) in the limit $\kappa L \to +\infty$ converges to the exponential kernel $G_{KB}(y)$ of the original KB paper [1].

Using the procedure of averaging over a small δ-vicinity of the point x, one can reformulate this setup as a continuous oscillatory medium described by the complex field $Z(x,t)$ [10, 11], which represents a coarse-grained order parameter of the phases:

$$Z(x,t) = \frac{1}{2\delta} \int\limits_{x-\delta}^{x+\delta} \exp\big[i\phi(\tilde{x},t)\big] d\tilde{x}. \tag{4}$$

This complex relatively smooth function of the coordinate x and time t satisfies the condition $|Z(x,t)| \le 1$. In the regions where $|Z(x,t)| = 1$, the neighboring phase oscillators move synchronously (local distribution of the phases is a delta function). For a smooth local distribution of the phases, which corresponds to partial synchrony, $|Z(x,t)| < 1$. The dynamics of such a function $Z(x,t)$ follows locally the Ott–Antonsen equation [3, 15]

$$\frac{\partial Z}{\partial t} = i\omega Z + \frac{1}{2}\Big(e^{-i\alpha} H - e^{i\alpha} H^* Z^2\Big). \tag{5}$$

Here, $H(x,t)$ is a coupling field defined via a temporarily instantaneous, spatially integral linear operator:

$$H(x,t) = \int\limits_{0}^{L} G(x-\tilde{x})\; Z(\tilde{x},t)\, d\tilde{x}. \tag{6}$$

In the considered case, using a specific form (3) for the kernel $G(y)$, it is easy to proceed from the integral coupling (6) between $Z(x,t)$ and $H(x,t)$ to the equivalent differential equation

$$\frac{\partial^2 H}{\partial x^2} - \kappa^2 H = -\kappa^2 Z \tag{7}$$

with periodic (for finite values of L) boundary conditions:

$$H(0) = H(L), \quad \frac{\partial H}{\partial x}\Big|_{x=0} = \frac{\partial H}{\partial x}\Big|_{x=L} \tag{8}$$

Note that in an infinite medium $|x| < \infty$, the solution of (7) is $H(x,t) = \int G_{KB}(x-\tilde{x})\, Z(\tilde{x},t)\, d\tilde{x}$ as in Ref. [1]. It is also worth mentioning that the same nonlocal coupling stems from the following model for the interaction of oscillators via the “auxiliary” field $H(x,t)$ (cf. Refs. [9, 16, 17]):

$$\tau \frac{\partial H}{\partial t} = \frac{1}{\kappa^2}\frac{\partial^2 H}{\partial x^2} - H + Z. \tag{9}$$

In this case, parameter τ indicates the characteristic time scale of the relaxation of $H(x,t)$. In the limit of the infinitely fast relaxation of the auxiliary field, where $\tau \to 0$, Eq. (9) reduces to Eq. (7).

The reformulated problem (5), (7), as the initial problem (1), (3) contains two parameters having the dimension of length: L and κ^{-1}. By rescaling x, we can set one of these parameters to one. Therefore, we assume, without loss of generality, that $\kappa = 1$. Then the only parameter is the size of the system L.

3 Stationary Chimera States as Solutions of ODE

We look for the rotating wave solutions of system (5), (7), which are stationary in a rotating reference frame. For this purpose we assume, that the complex functions $Z(x,t)$ and $H(x,t)$ have the following form:

$$Z(x,t) = z(x)\, e^{i(\omega+\Omega)t}\,, \quad H(x,t) = h(x)\, e^{i(\omega+\Omega)t}\,, \tag{10}$$

where Ω is some unknown frequency, depending on the period of the solution (here our definition of the frequency Ω is the same as in the KB paper [1]). This frequency will be negative, if $\alpha \lesssim \pi/2$. It is convenient, however, not to fix the period L, but to fix the frequency of the rotating chimera Ω and then find periodic patterns as solutions of the equations to be formulated below; period L of these solutions depends on Ω. This will, after the inversion the yield dependence $\Omega(L)$.

After the substitution of Eq. (10) into relation (5), we obtain an algebraic equation

$$e^{i\alpha} h^* z^2 + 2i\Omega z - e^{-i\alpha} h = 0, \tag{11}$$

which can be treated as a quadratic equation with respect to z with two solutions that can be written formally as

$$z(x) = \frac{-\Omega \pm \sqrt{\Omega^2 - |h(x)|^2}}{h^*(x)\exp(-i\beta)}. \tag{12}$$

Here, for convenience of the further notation, we define the parameter measuring deviation of α from $\pi/2$:

$$\beta = \pi/2 - \alpha. \tag{13}$$

Which sign (plus or minus) in the relation between $z\left(x\right)$ and $h\left(x\right)$ has to be chosen in Eq. (12), is determined by the physical meaning of the complex order parameter $Z(x,t)$. First, the amplitude of $Z(x,t)$ cannot be greater than unity, i.e., $\left|Z\left(x,t\right)\right| \leq 1$. It follows from relation (12) that for $\left|h\left(x\right)\right| \geq \left|\Omega\right|$ the equality $\left|z\left(x\right)\right| = 1$ is always fulfilled. But if $\left|h\left(x\right)\right| < \left|\Omega\right|$, then $\left|z\left(x\right)\right| \leq 1$ only when in expression (12) the negative sign in chosen. In other words, $z\left(x\right)$ is uniquely related to $h\left(x\right)$ as follows:

$$z\left(x\right) = -\frac{\Omega + \sqrt{\Omega^2 - \left|h\left(x\right)\right|^2}}{h^*\left(x\right)\exp\left(-i\beta\right)}. \tag{14}$$

Substituting Eq. (10) into Eq. (7) and making use of Eq. (14), for the complex function $h\left(x\right)$ we obtain an ODE of the second order:

$$h'' - h = \frac{\Omega + \sqrt{\Omega^2 - |h|^2}}{h^*\exp\left(-i\beta\right)}. \tag{15}$$

Hereafter, by primes at the functions of the variable x we will denote derivatives with respect to the spatial coordinate x. Equation (15) is complemented by boundary conditions $h\left(0\right) = h\left(L\right)$ and $h'\left(0\right) = h'\left(L\right)$.

Let us represent $h\left(x\right)$ in the form

$$h\left(x\right) = r\left(x\right)e^{i\theta(x)}, \tag{16}$$

where $r\left(x\right)$ and $\theta\left(x\right)$ are real functions. However, unlike the classical definition of the amplitude and the phase of a complex function, we assume that $r\left(x\right)$ can reverse sign and take both positive and negative values. In this case, $\theta\left(x\right)$ will not undergo $\pm\pi$ jumps at the points where $r\left(x\right)$ vanishes and retain its smoothness when passing through such points. It should be mentioned that $Z\left(x,t\right)$ and $H\left(x,t\right)$, and therefore both $z\left(x\right)$ and $h\left(x\right)$ are defined up to a constant phase shift (gauge invariance $\theta\left(x\right) \to \theta\left(x\right) + \theta_0$). Hence, without loss of generality, we can put $\theta\left(0\right) = 0$.

Substituting Eq. (16) into Eq. (15) and separating real and imaginary parts, we arrive at a real system of ODEs of the third order:

$$r'' = r + \frac{q^2}{r^3} + \frac{\Omega}{r}\cos\beta - \frac{\sqrt{r^2 - \Omega^2}}{r}\sin\beta, \tag{17}$$

$$q' = \Omega\sin\beta + \sqrt{r^2 - \Omega^2}\cos\beta \tag{18}$$

in the domain where $\left|r\left(x\right)\right| \geq \left|\Omega\right|$, i.e., in the region of synchronous motion of phase oscillators, and

$$r'' = r + \frac{q^2}{r^3} + \frac{\Omega + \sqrt{\Omega^2 - r^2}}{r}\cos\beta, \tag{19}$$

$$q' = \left(\Omega + \sqrt{\Omega^2 - r^2}\right)\sin\beta \tag{20}$$

in the domain where $|r(x)| < |\Omega|$, i.e., in the region characterized by partially synchronous behavior. Here, for convenience, we defined a new variable

$$q(x) = r^2(x)\,\theta'(x)\,. \tag{21}$$

Below, we confine ourselves to the analysis of stationary solutions without the phase gradient, i.e., we discuss only cases where $\theta(L) = \theta(0)$ (in general also solutions with $\theta(L) = \theta(0) + 2\pi n$ are admissible).

4 Analytical Approach for Chimera States

In this section, we describe an analytical approach to find nontrivial solutions of system (17)–(20). In the next section, numerical approaches are presented.

4.1 One- and Two-Point Chimeras

Remarkably, it is possible to describe basic chimera profiles analytically, for $\alpha \lesssim \pi/2$ ($\beta \ll 1$). Let us first consider the limiting case of a purely neutral coupling between the phase oscillators, where $\alpha = \pi/2$ ($\beta = 0$). In this situation, from Eq. (18) it follows that $q'(x)$ is nonnegative in the synchronous state, i.e., $q'(x) \geq 0$ for $|r(x)| \geq |\Omega|$. In turn, according to Eq. (20), the derivative $q'(x)$ vanishes in the partially synchronous state. Therefore, $q(x)$ does not depend on x and remains constant in partially synchronous regions, i.e., $q(x) = \text{const}$ for $|r(x)| < |\Omega|$. Thus, a periodic solution with $q(x) = q(x + L)$ should be everywhere partially synchronous, possibly except for one or two points at which $r(x)$ achieves an extremum $|r| = |\Omega|$. This allows us to set in Eqs. (20) and (19) $q = 0$, so that Eq. (19) reduces to an integrable second-order equation

$$\begin{gathered} r'' = -dU(r)/dr, \\ U(r) = -r^2/2 - \sqrt{\Omega^2 - r^2} - \Omega \ln\left(\sqrt{\Omega^2 - r^2} - \Omega\right). \end{gathered} \tag{22}$$

Potential $U(r)$ is depicted in Fig. 1. In Eq. (22) there are two types of trajectories having the maximum at $r_{\max} = |\Omega|$, depending on the value of Ω. For $-1 < \Omega < \Omega_* = 2(\ln 2 - 1)$ this is a periodic orbit with $0 < r_{\min} \leq r \leq |\Omega|$. It reaches the boundary of the partially synchronous region at one point and corresponds to a degenerate "one-point chimera" [which can be considered as the limiting case of curve A in Fig. 3], where the synchronous region shrinks to a point. For $\Omega_* < \Omega < 0$ there is a symmetric periodic orbit with $-|\Omega| \leq r(x) \leq |\Omega|$. This degenerate "two-point chimera" corresponds to curve B in Fig. 3. These two types of solutions merge in a homoclinic orbit with infinite period at $\Omega = \Omega_*$, which can be named "chimera

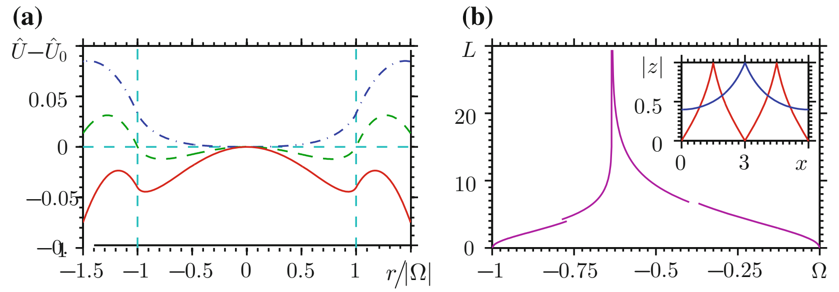

Fig. 1 **a** Effective potential $\hat{U}(r)$ (see Eq. (28)) for different values of Ω: $\Omega = -0.4$ (dash-dotted blue curve), $\Omega = \Omega_* = -2(\ln 2 - 1) \approx -0.77$ (dashed green curve), $\Omega = -0.8$ (solid red curve). Here $\hat{U}_0 = -\Omega \ln(2|\Omega|) - |\Omega|$. **b** The period of the one- and two-point chimera solutions vs parameter Ω. **b** Dependence of the chimera spatial period on the rotation frequency Ω. The inset shows examples of one -and two-point chimeras

soliton" (one- or two-point, depending on which side of the criticality the orbit is considered). Physically, chimera solitons correspond to localized states of enhanced synchrony in an infinite medium, with full synchrony (maximal coarse-grained order parameter $|z| = 1$) being achieved just at one (or two) point. The dependencies Ω versus (L) for these solutions are shown in Fig. 1b. Note that additionally there is a branch of synchronous solutions with $\Omega = -1$ which are steady states $r(x) = 1$.

4.2 Perturbation Theory Near One- and Two-Point Chimeras

Now, we consider the case where the parameter α is slightly different from $\pi/2$. In this limit, a small parameter $\beta \ll 1$ appears in the problem, and it becomes possible to construct a perturbation theory allowing to estimate typical sizes of the synchronous and the partially synchronous areas for solutions directly related to the one-and two-point chimera states mentioned above.

Besides $\beta \ll 1$, we assume that Ω is not too close to the value $\Omega_{syn} = -\sin\alpha$, which corresponds to a stable, purely synchronous motion of the phase oscillators. Then it can be stated (based on the structure of system (17)–(20)) that: (i) the typical sizes of the synchronous regions are much smaller than the sizes of partially synchronous regions; (ii) the maximum value $r_{\max}$ of the function $r(x)$ only slightly exceeds $|\Omega|$, and (iii) the quantity $q(x)$ is small for all $0 \leq x < L$. Using these properties and keeping only the main terms in relations (17)–(20), we obtain approximate equations

$$r'' = r + \Omega r^{-1}, \tag{23}$$

$$q' = \Omega\beta + \sqrt{r^2 - \Omega^2} \tag{24}$$

if $|r(x)| \geq |\Omega|$ and

$$r'' = r + \left(\Omega + \sqrt{\Omega^2 - r^2}\right) r^{-1}, \tag{25}$$

$$q' = \left(\Omega + \sqrt{\Omega^2 - r^2}\right) \beta \tag{26}$$

if $|r(x)| < |\Omega|$. In Eqs. (23) and (25), we have neglected the small terms having an order β^2 or higher, including the term q^2/r^3.

Thus, in the first approximation, the equations for the function $r(x)$, both in the synchronous and asynchronous domains, cease to depend on β and $q(x)$, making it possible, as for $\beta = 0$, to rewrite them in the form of a unified equation of motion in the potential field

$$r'' = -d\hat{U}(r)/dr, \tag{27}$$

where the effective potential $\hat{U}(r)$ extends potential U to the domain $|r| > |\Omega|$:

$$\hat{U}(r) = \begin{cases} -r^2/2 - \Omega \ln |r|, & \text{if} \quad |r| \geq |\Omega|, \\ U(r), & \text{if} \quad |r| < |\Omega|. \end{cases} \tag{28}$$

Fig. 1 shows characteristic profiles $\hat{U}(r)$ for three values of Ω in the interval $-1 < \Omega < 0$. In addition to the discussed above point chimera solutions with $r_{\max} \leq |\Omega|$, now the solutions with $r_{\max} \geq |\Omega|$ are possible. The reason is, that unlike to the case of vanishing $\beta = 0$, according to Eq. (26), the derivative $q'(x)$ is nonzero and proportional to β, which leads to a variation in the function $q(x)$ not only for $|r(x)| \geq |\Omega|$, but also for $|r(x)| < |\Omega|$. This circumstance makes it possible to satisfy the periodic boundary conditions, not only for $r(x)$ and $r'(x)$, but also for $q(x)$, even if there are areas where $|r(x)| > |\Omega|$.

As a result, the problem for a fixed Ω can be formulated as follows. First, one finds periodic solutions $r(x)$ in potential $\hat{U}$ as solutions of the second-order ODE (27), with one or two synchronous regions with $|r(x)| > |\Omega|$. We stress once again that when $\beta \ll 1$ and Ω are not too close to $\Omega_{syn} = -\sin\alpha$, the sizes of these regions can be assumed small compared with the total period $L(r_{\max})$. Then one substitutes $r(x)$ in relations (24) and (26) and finds $q(x)$. Finally, the periodicity condition $q(x + L(r_{\max})) = q(x)$, which is equivalent to

$$\int\limits_0^{L(r_{\max})} q'\big(r(x)\big)dx = 0, \tag{29}$$

should be fulfilled which fixes the chimera state. If in Eq. (29), we consistently integrate over synchronous and asynchronous areas, replacing $q'\big(r(x)\big)$ by expressions (24) or (26), respectively, in each of them, then we obtain

$$N_{SR}\int\limits_0^{L_{syn}}\sqrt{r^2-\Omega^2(x)}\,dx=-\beta\Omega L(r_{\max})-\beta N_{SR}\int\limits_0^{L_{psyn}}\sqrt{\Omega^2-r^2(x)}\,dx. \tag{30}$$

When deriving Eq. (30) we used the fact that we are interested first of all in the simplest stationary chimera states, which in the limit $\beta \to 0$ convert directly either to a "one-point chimera" or a "two-point chimera". This means that for a small, but nonzero β the solutions of interest have one ($N_{SR}=1$) or two ($N_{SR}=2$) identical synchronous regions (by virtue of symmetry and periodicity the number of partially synchronous states is the same). Here, L_{syn} is the size of a separate synchronous area and L_{asyn} is the individual length of the partially synchronous interval, i.e., $N_{SR}\left(L_{syn}+L_{asyn}\right)=L(r_{\max})$. We also note that L_{syn} and L_{asyn} depend on $r_{\max}$.

We assume that the maximum value $r_{\max}$ of the function $r(x)$ exceeds $|\Omega|$ only slightly. Therefore, we represent $r_{\max}$ in the form $r_{\max}=|\Omega|+\Delta r_{\max}$, where $0<\Delta r_{\max}\ll|\Omega|$. Assuming $\Delta r_{\max}\sim\beta$, it is possible to calculate the right-hand side of equality (30) approximately, neglecting terms having an order β^2 or higher:

$$-\beta\Omega L(r_{\max})-\beta N_{SR}\int\limits_0^{L_{asyn}}\sqrt{\Omega^2-r^2(x)}\,dx\approx-\beta\Omega L\big(|\Omega|\big)-\beta\int\limits_0^{L(|\Omega|)}\sqrt{\Omega^2-R^2(x)}\,dx=$$
$$-\beta\oint\Big(\Omega+\sqrt{\Omega^2-R^2(x)}\Big)dx=\beta\oint\left(R'^2+R^2\right)dx\,. \tag{31}$$

When making transformations in Eq. (31) we took into account that

$$L(r_{max})=L\big(|\Omega|+\Delta r_{\max}\big)\approx L\big(|\Omega|\big)+\left.\frac{dL}{dr_{\max}}\right|_{|\Omega|}\Delta r_{\max}, \tag{32}$$

$$L_{asyn}(r_{max})=L_{asyn}\big(|\Omega|+\Delta r_{\max}\big)\approx\frac{L\big(|\Omega|\big)}{N_{SR}}+\left.\frac{dL_{asyn}}{dr_{\max}}\right|_{|\Omega|}\Delta r_{\max}. \tag{33}$$

Moreover, in the considered case, $r(x)$ is close (all the differences are of the same order as $\Delta r_{\max}\sim\beta$) to the trajectory $R(x)$ corresponding to the case $\beta=0$, which totally lies in the partially synchronous region, except for one ($N_{SR}=1$) or two (when $N_{SR}=2$) turning points where $|r|=|\Omega|$ in modulus. Actually, in the first approximation, for estimates of the integrals in Eq. (31) it suffices to take, instead of $r(x)$, the solution $R(x)$ at $\beta=0$, i.e. solution of the equation

$$R''=R+\Big(\Omega+\sqrt{\Omega^2-R^2}\Big)R^{-1} \tag{34}$$

with boundary conditions

$$R(0)=R\left(L\big(|\Omega|\big)\right)=|\Omega|\,,\quad R'(0)=R'\left(L\big(|\Omega|\big)\right)=0\,. \tag{35}$$

Using relations (34) and (35), it is easy to perform the last transition in Eq. (31). Note that by a cyclic integral we denote the integral over the period $L\big(|\Omega|\big)$ of the function $R\,(x)$.

We now analyze the left-hand side of relation (30). For this, we consider in more detail the behavior of $r\,(x)$ on the synchronous area where $|\Omega| \le r\,(x) \le r_{\max}$. Since the sizes L_{syn} of this region are assumed small, $r_{\max} = |\Omega| + \Delta r_{\max}$, and $\Delta r_{\max} \ll |\Omega|$, the solution of Eq. (23) can be sought in the form

$$r\,(x) = |\Omega| + r_{syn_1}\,(x) + r_{syn_2}\,(x) + \dots, \tag{36}$$

where by identical indices we denoted the terms having the same order of smallness. After the substitution of Eq. (36) into Eq. (23), for the main x-dependent term of expansion $r_{syn_1}\,(x)$ we obtain

$$r''_{syn_1} = |\Omega| - 1. \tag{37}$$

Allowing for the fact that the corrections to $|\Omega|$ of any order should become zero at the boundaries of the considered area, while at its center the function $r_{syn_1}\,(x)$ should reach the maximum value $\Delta r_{\max}$, we find

$$r_{syn_1}\,(\xi) = \Delta r_{\max} + \big(|\Omega| - 1\big)\xi^2\big/2 \tag{38}$$

Here, for convenience, instead of x, we introduced the spatial coordinate ξ reckoned from the central point of the synchronous region, i.e., $\xi = 0$, when $r\,(x) = r_{\max}$. For $r\,(x) = |\Omega|$, ξ takes the values $\pm\xi_0$, where

$$\xi_0 = \sqrt{2\Delta r_{\max}\big/\big(1 - |\Omega|\big)} \tag{39}$$

Now it is easy to directly calculate the integral on the left-hand side of expression (30) in the first approximation:

$$\int\limits_0^{L_{syn}} \sqrt{r^2\,(x) - \Omega^2}\,dx \approx \int\limits_{-\xi_0}^{\xi_0} \sqrt{2\,|\Omega|\,r_{syn_1}\,(\xi)}\,d\xi =$$

$$\sqrt{|\Omega|\,\big(1-|\Omega|\big)} \int\limits_{-\xi_0}^{\xi_0} \sqrt{\xi_0^2-\xi^2}\,d\xi = \frac{\pi}{2}\sqrt{|\Omega|\,\big(1-|\Omega|\big)}\,\xi_0^2\,. \tag{40}$$

Finally, substituting Eqs. (31) and (40) into relation (30), we find, with accuracy up to corrections of the first order of smallness in β, that

$$\pi N_{SR}\sqrt{|\Omega|\,(1 - |\Omega|)}\,\xi_0^2 = 2\beta\,\mathscr{I}_0\,(\Omega)\,, \tag{41}$$

Here, we introduced a notation

$$\mathscr{I}_0(\Omega) = \oint \left(R'^2 + R^2\right) dx, \tag{42}$$

and the integration was performed over the period $L\big(|\Omega|\big)$ of the function $R(x)$, which is the solution of Eq. (34) with boundary conditions (35). From Eq. (42) estimates follow for the sizes of the synchronous region

$$L_{syn} \approx 2\xi_0 = \sqrt{\frac{8\beta\,\mathscr{I}_0(\Omega)}{\pi N_{SR}\sqrt{|\Omega|\,(1-|\Omega|)}}} \tag{43}$$

and for the maximum value $r_{\max}$, which is reached on the trajectory $r(x)$ "trapped" by the potential (28):

$$r_{\max} = |\Omega| + \Delta r_{\max} = |\Omega| + \beta\sqrt{\frac{1-|\Omega|}{|\Omega|}}\,\frac{\mathscr{I}_0(\Omega)}{\pi N_{SR}}. \tag{44}$$

It is also possible to find the corresponding expression for characteristic scales of the whole stationary chimera and its partially synchronous parts for a given Ω and small β:

$$L_{ch} \approx L\,(r_{max}) \approx L_0 + \beta\,\frac{dL}{dr_{\max}}\bigg|_{|\Omega|}\sqrt{\frac{1-|\Omega|}{|\Omega|}}\,\frac{\mathscr{I}_0(\Omega)}{\pi N_{SR}}, \tag{45}$$

$$L_{asyn} = \frac{L_{ch}}{N_{SR}} - L_{syn}, \tag{46}$$

where $L_0 = L\big(|\Omega|\big)$ is the length of the one- or two-point chimera for a given Ω.

The result of the developed perturbation theory is that the size L_{syn} of synchronous regions becomes finite for $\beta > 0$. Physically, the constructed solutions are periodic in space patterns, where oscillators are partially synchronized almost everywhere, except for one or two small regions of enhanced coherence, which is full in small core zones. It should be mentioned that for Ω close to $\Omega_{syn} = -\sin\alpha$, the presence of a stable, purely synchronous state has a strong effect, and the approach we proposed ceases to work. However, the chimeras found for such values of Ω are strongly unstable and deteriorate rapidly. Therefore, the case where Ω differs very slightly from Ω_{syn} was not considered in detail.

Figure 2 demonstrates a comparison of the results of the developed perturbation theory and the data obtained numerically (see Sect. 5 for more details). A fairly good agreement between the line and the markers indicates the validity of the analytical description presented in this section.

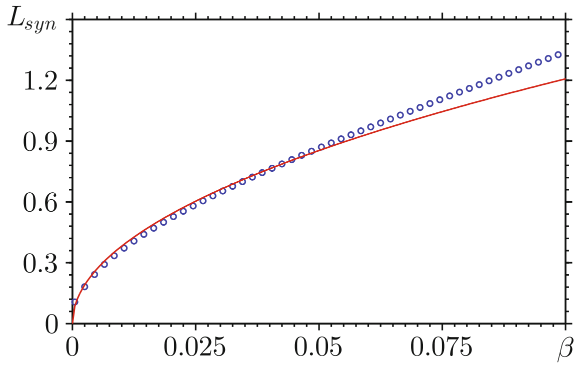

Fig. 2 Dependence of the size L_{syn} of a separate synchronous area on β for $\Omega = -0.8$. Here, the unshaded markers show the results obtained by direct numerical simulation immediately within the framework of the system of ODEs (17)–(20) and the solid lines show the law determined by the analytical formula (43)

5 Numerical Calculation of Spatial Structure of Stationary Chimera States

In this section, we find numerically stationary rotating periodic chimera patterns described by Eqs. (17)–(20) satisfying the periodicity condition $r(x + L) = r(x)$, $q(x + L) = q(x)$ in the form of chimeras, which consist simultaneously of synchronous and partially synchronous parts. Before discussing the proposed numerical procedure based on the ODEs (17)–(20), we would like to mention that Eqs. (17)–(20) are invariant with respect to a shift of variable x, as well as to the involution $x \to -x$, $r\,(x) \to r\,(x)$, and $q\,(x) \to -q\,(-x)$. The latter property implies that the system is reversible and thus has properties similar to Hamiltonian dynamical systems. This means that the simplest partial solutions can be sought in the class of symmetric $r\,(x)$ and antisymmetric functions $q\,(x)$ with respect to the point $x = L\big/2$. For such solutions, by virtue of the periodic boundary conditions, the equalities $r'\,(0) = r'\,(L)$ and $q\,(0) = q\,(L)$ should be fulfilled only if $r'\,(x)$ and $q\,(x)$ vanish at the points $x = 0$, $x = L\big/2$, and $x = L$. Also recall that we are interested in stationary states in the form of chimeras, which on the spatial interval $[0, L)$ have regions with $|r\,(x)| \geq |\Omega|$ and $|z\,(x)| = 1$, where the nonlocally coupled phase oscillators are locked, as well as regions with $|r\,(x)| < |\Omega|$ and $|z\,(x)| < 1$, where the elements of the considered oscillatory medium are partially synchronous. The aforementioned constraints determine the value of Ω and the possible form of the functions $r\,(x)$ and $q\,(x)$ (and therefore also $h\,(x)$) for a given length L.

Below, we describe the used numerical chimera-seeking approach on the example of a chimera state with one synchronous region. First of all, we choose the value of Ω and fix it, assuming that L is arbitrary. The system of ODEs (17)–(20) is solved numerically (using the Runge–Kutta method of fourth order) with the starting point $r\,(0) = r_0$, $r'\,(0) = 0$, and $q\,(0) = 0$. Integration ends at a point $x = \ell$, where the conditions $r'\,(\ell) = 0$ and $q\,(\ell) = 0$ are fulfilled, at this point $r(\ell) = r_1$. We have to satisfy the condition $r_1 = r_0$; this is a one-dimensional root-finding problem which is easy to accomplish. At the final stage, we put $L = 2\ell$, substitute the previously

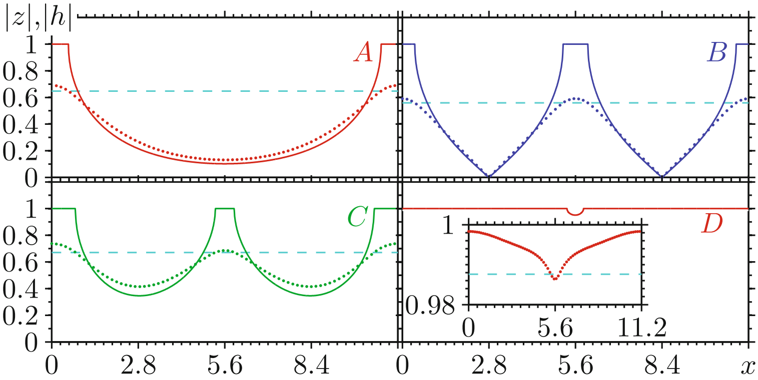

Fig. 3 Spatial profiles of the simplest chimera patterns (with at most two synchronous regions) for $\alpha = 1.457$, $|z|$: solid lines, $|h|$: dotted lines. A: the KB chimera with one synchronous region for $\Omega = -0.648$, B: symmetric chimera with synchronous regions for $\Omega = -0.558$, C: asymmetric chimera with two synchronous regions (here, the sizes of the synchronous domains are different, and their phases differ not by π, unlike in case B) for $\Omega = -0.672$, D: nearly synchronous chimera with one synchronous region for $\Omega = -0.98762$. The colors correspond to coding of the solutions in Fig. 4

chosen value of Ω into Eq. (15) and solve it numerically on the interval of 0 to L, taking $h(0) = r_0$ and $h'(0) = 0$ as “initial” conditions. Here, we use the fact that without loss of generality we can assume $\theta(0) = 0$. Finally, we find the spatial distribution $h(x)$, and using Eq. (12) we retrieve the complex coarse-grained order parameter $z(x)$, which corresponds to the stationary state in the form of a chimera with one synchronous region for the locally interacting phase oscillators distributed continuously over an interval of length $L = 2\ell$. The described method can also be easily generalized to the case of chimeras with a large number of synchronous regions, by choosing not the first point where $r'(x)$, $q(x)$ vanish, but the second one, third one, etc. If one seeks for solutions with a fixed period L, then the corresponding value of Ω (and then the corresponding profiles $z(x)$ and $h(x)$) is determined by an additional root-finding procedure.

We show in Fig. 3 typical solutions for $\alpha = 1.457$ (the value used in [1]) with period $L \approx 11.2$. These patterns (types A and B have been already discussed in the literature [1, 3, 14]) are just the simplest possible chimeras with at most two synchronous regions.

In Fig. 4 we compare the the periods of the found chimeras with the results of the analytical approach above, for several values of α. Panel (a) shows that for small β chimera states (of types A and B in Fig. 3) are close to degenerate regimes at $\beta = 0$. One can see in panels (a) and (b) that the two analytic solutions at $\alpha = \pi/2$ (the one-point chimera and the synchronous state) merge into one branch at $\alpha \lesssim \pi/2$ with a nonmonotonic dependence Ω on L, cf. chimeras (with one synchronous region) A and D in Fig. 3. In panel (b) one can see an additional branch corresponding to the asymmetric chimera (with two synchronous regions) C in Fig. 3. As a result, in (b)

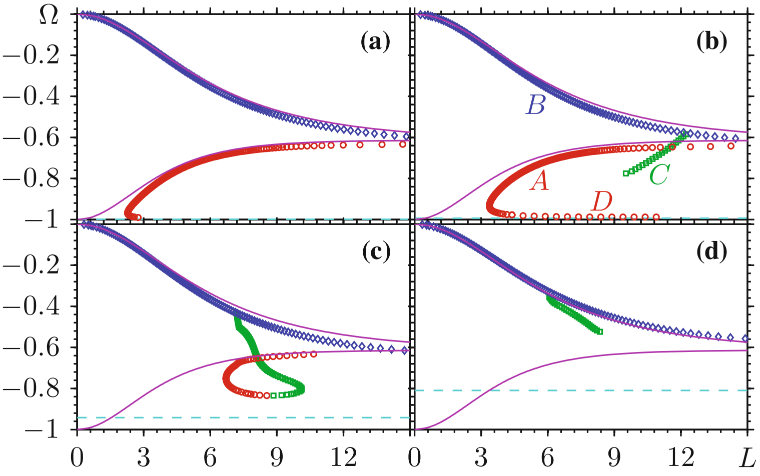

Fig. 4 Periods of chimera patterns L versus parameter Ω for $\alpha = 1.514$ (**a**), $\alpha = 1.457$ (**b**), $\alpha = 1.229$ (**c**), and $\alpha = 0.944$ (**d**). Chimera states for $\alpha = \pi/2$, obtained by integration equation (22), are shown with violet solid lines (cf. Fig. 1b). Different markers correspond to the chimera types shown in Fig. 3, as specified in panel (**b**). Cyan dashed lines show the frequency of the synchronous state $\Omega = -\sin\alpha$

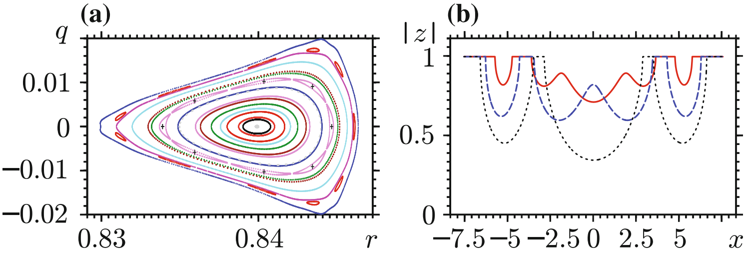

Fig. 5 **a** Poincaré map for system (17)–(20) for $\alpha = 1.457$ and $\Omega = -0.8$. The condition for the surface of section: $r' = 0, r'' < 0$. **b** Complex patterns with three synchronous regions for $L \approx 15.1$ and $\Omega = -0.796$ (solid red line), $\Omega = -0.726$ (dashed blue line) and $\Omega = -0.674$ (dotted black line)

and (c) one has four solutions in some range of periods L. Only two of them survive for small α; diagrams for $\alpha < 0.9$ are qualitatively the same as panel (d) in Fig. 4.

In a more general context, the system (17)–(20) as a reversible (with respect to involution $r \to r$, $q \to -q$) third-order system of ODEs may possess a plethora of solutions, including chaotic ones. We illustrate this by constructing a two-dimensional Poincaré map in Fig. 5a. It shows a typical picture of tori and periodic orbits of different periods for nearly integrable Hamiltonian systems. Not all points on the Poincaré surface lead to physically relevant solutions: the trajectories which resulted in values $|r| > 1$ should be discarded. Therefore only in a small region of initial values (r, q) the Poincaré map is well defined, outside of this region there are only isolated periodic orbits.

The fixed point of the map Fig. 5a at $q = 0$, $r \approx 0.84$ describes the one-hump chimera state A in Fig. 3. The Poincaré map is constructed for a fixed value of Ω. It provides several branches of periodic orbits having different periods. Collecting solutions at a fixed period L, we obtain many coexisting long-periodic chimera patterns; several chimeras with three synchronous regions are illustrated in Fig. 5b. Similar complex patterns appear also in other physical setups (e.g., multi-peak solitons in nonlinear optics), a special feature of chimera patterns is that they are non-smooth in terms of the order parameter $|z|$ and look like sharp zebra stripes "order-disorder". Our aim in this study is not to follow all possible periodic and chaotic solutions of this reversible system. Below in exploring the stability properties, we focus on the simplest ones illustrated in Fig. 3, corresponding to fixed points and period-two orbits of the Poincaré map. In other words, we focus on solutions with the number of extreme values of $|r\,(x)|$ not exceeding four (one or two minima, or one or two maxima).

6 Temporal Stability of the Chimera Patterns

6.1 Linear Stability Analysis. Fundamental Properties of the Corresponding Spectral Problem

In this section, we discuss stability of the obtained chimera patterns. Contrary to the problem of finding chimera solutions, this analysis cannot be reduced to that of differential equations, rather we have to consider the integral-differential equation (5), (6) for $Z\,(x, t)$ with the kernel (3). Temporal stability of the chimera state with a certain value of Ω can be studied by linearizing this integral-differential equation near the stationary rotating solution (10). To this end, we use an ansatz

$$Z\,(x, t) = \Big(z\,(x) + \tilde{Z}\,(x, t)\Big)\, e^{i(\omega+\Omega)t}, \tag{47}$$

where $\tilde{Z}\,(x, t)$ represents a generic small deviation from $z\,(x)$. Substituting (47) into Eq. (5) and linearizing the result with respect to the variations $\tilde{Z}\,(x, t)$, we obtain

$$\frac{\partial \tilde{Z}}{\partial t} = -\big[i\Omega + e^{i\alpha} z\,(x)\, h^{*}(x)\big]\tilde{Z} + \frac{e^{-i\alpha}}{2}\tilde{H} - \frac{e^{i\alpha}}{2} z^{2}(x)\,\tilde{H}^{*}\,, \tag{48}$$

where $\tilde{H}(x, t)$ is the coupling force for $\tilde{Z}(x, t)$ as in (6).

Now we rewrite this integro-differential equation for the complex function $\tilde{Z}\,(x, t) = \zeta_1\,(x, t) + i\zeta_2\,(x, t)$ as a system for two real components $\zeta_1\,(x, t)$ and $\zeta_2\,(x, t)$ which are periodic in space with period L:

$$\frac{\partial \zeta_1}{\partial t} = \mu_1(x)\zeta_1 - \mu_2(x)\,\zeta_2 + \frac{1}{2}\big(\cos\alpha - \eta_1(x)\big)\int_0^L G(x-\tilde{x})\,\zeta_1(\tilde{x},t)\,d\tilde{x} + \frac{1}{2}\big(\sin\alpha - \eta_2(x)\big)\int_0^L G(x-\tilde{x})\,\zeta_2(\tilde{x},t)\,d\tilde{x}\,, \tag{49}$$

$$\frac{\partial \zeta_2}{\partial t} = \mu_2(x)\,\zeta_1 + \mu_1(x)\,\zeta_2 - \frac{1}{2}\big(\sin\alpha + \eta_2(x)\big)\int_0^L G(x-\tilde{x})\,\zeta_1(\tilde{x},t)\,d\tilde{x} + \frac{1}{2}\big(\cos\alpha + \eta_1(x)\big)\int_0^L G(x-\tilde{x})\,\zeta_2(\tilde{x},t)\,d\tilde{x}\,. \tag{50}$$

Here we introduce four real functions of spatial coordinate x:

$$\mu_1(x) = -\big(h_{\mathrm{Re}}(x)\,z_{\mathrm{Re}}(x) + h_{\mathrm{Im}}(x)\,z_{\mathrm{Im}}(x)\big)\cos\alpha - \big(h_{\mathrm{Im}}(x)\,z_{\mathrm{Re}}(x) - h_{\mathrm{Re}}(x)\,z_{\mathrm{Im}}(x)\big)\sin\alpha, \tag{51}$$

$$\mu_2(x) = -\Omega - \big(h_{\mathrm{Re}}(x)\,z_{\mathrm{Re}}(x) + h_{\mathrm{Im}}(x)\,z_{\mathrm{Im}}(x)\big)\sin\alpha + \big(h_{\mathrm{Im}}(x)\,z_{\mathrm{Re}}(x) - h_{\mathrm{Re}}(x)\,z_{\mathrm{Im}}(x)\big)\cos\alpha, \tag{52}$$

$$\eta_1(x) = \big(z_{\mathrm{Re}}(x)\big)^2\cos\alpha + \big(z_{\mathrm{Im}}(x)\big)^2\cos\alpha - 2z_{\mathrm{Re}}(x)\,z_{\mathrm{Im}}(x)\sin\alpha, \tag{53}$$

$$\eta_2(x) = \big(z_{\mathrm{Re}}(x)\big)^2\sin\alpha + \big(z_{\mathrm{Im}}(x)\big)^2\sin\alpha + 2z_{\mathrm{Re}}(x)\,z_{\mathrm{Im}}(x)\cos\alpha. \tag{54}$$

The symbolic indices "Re" and "Im" denote the real and imaginary parts of a complex variables $z(x)$ and $h(x)$, respectively. Using relation (14) one can transform (51) and (52) to the following expressions:

$$\mu_1(x) = \begin{cases} -\sqrt{|h(x)|^2 - \Omega^2}, \text{ if } |h(x)| \ge |\Omega|, \\ 0, \text{ if } |h(x)| < |\Omega|, \end{cases} \tag{55}$$

$$\mu_2(x) = \begin{cases} 0, \text{ if } |h(x)| \ge |\Omega|, \\ -\sqrt{\Omega^2 - |h(x)|^2}, \text{ if } |h(x)| < |\Omega|. \end{cases} \tag{56}$$

It is easy to see that (49) together with (50) can be reformulated in the form of an operator equation for the two-component vector function $\boldsymbol{\zeta}(x,t) = \big(\zeta_1(x,t)\,,\,\zeta_2(x,t)\big)^T$ (see, e.g., [13, 14]):

$$\frac{\partial \boldsymbol{\zeta}}{\partial t} = \Big(\hat{\mathbf{M}} + \hat{\mathbf{K}}\Big)\boldsymbol{\zeta}, \tag{57}$$

where $\hat{\mathbf{M}}$ is a multiplication operator

$$\hat{\mathbf{M}} = \begin{pmatrix} \mu_1(x) & -\mu_2(x) \\ \mu_2(x) & \mu_1(x) \end{pmatrix}, \tag{58}$$

and $\hat{\mathbf{K}}$ is an integral operator

$$\hat{\mathbf{K}}\boldsymbol{\zeta} = \begin{pmatrix} \int\limits_0^L \Big[G_{11}(x,\tilde{x})\,\zeta_1(\tilde{x}) + G_{12}(x,\tilde{x})\,\zeta_2(\tilde{x}) \Big] d\tilde{x} \\ \int\limits_0^L \Big[G_{21}(x,\tilde{x})\,\zeta_1(\tilde{x}) + G_{22}(x,\tilde{x})\,\zeta_2(\tilde{x}) \Big] d\tilde{x} \end{pmatrix} \tag{59}$$

with a (2×2)-matrix kernel given by

$$\hat{\mathbf{G}}\,(x,\tilde{x}) = \begin{pmatrix} G_{11}\,(x,\tilde{x}) & G_{12}\,(x,\tilde{x}) \\ G_{21}\,(x,\tilde{x}) & G_{22}\,(x,\tilde{x}) \end{pmatrix} =$$
$$\frac{1}{2} \begin{pmatrix} \cos\alpha - \eta_1\,(x) & \sin\alpha - \eta_2\,(x) \\ \sin\alpha + \eta_2\,(x) & \cos\alpha + \eta_1\,(x) \end{pmatrix} G\,(x - \tilde{x})\,. \tag{60}$$

Moreover, definitions (59), (60) imply that the integral operator $\hat{\mathbf{K}}$ is compact for any piecewise-smooth coupling function $G\,(y)$, particularly, for our default choice (3), and continuous in x stationary profiles $z\,(x)$ and $h\,(x)$.

Solution of Eq. (57) is sought in the form $\boldsymbol{\zeta}\,(x,t) = \mathrm{Re}\big[\boldsymbol{\varXi}\,(x)\,e^{\lambda t}\big]$ leading to the eigenvalue problem

$$\lambda\boldsymbol{\varXi} = \Big(\hat{\mathbf{M}} + \hat{\mathbf{K}}\Big)\boldsymbol{\varXi}, \tag{61}$$

where $\boldsymbol{\varXi}\,(x) = \big(\varXi_1\,(x)\,,\,\varXi_2\,(x)\big)^T$. Therefore, the stability properties of the chimera states can now be investigated by analyzing the spectrum of the linear time-independent operator $\hat{\mathbf{M}} + \hat{\mathbf{K}}$. It is reasonable to expect that this spectrum consists of two different parts, a continuous spectrum λ_c and a (possibly empty) point spectrum λ_p (see, e.g., [13, 14, 18]). Note that each part is symmetric with respect to the real axis.

Continuous spectrum is invariant under compact perturbations [13, 14], hence the continuous spectrum λ_c of the composed operator $\hat{\mathbf{M}} + \hat{\mathbf{K}}$ is given just by the continuous spectrum of $\hat{\mathbf{M}}$. Since $\hat{\mathbf{M}}$ is a multiplication operator, it only has an essential continuous spectrum consisting of all complex values λ_c with

$$\det \begin{pmatrix} \mu_1(x) - \lambda_c & -\mu_2(x) \\ \mu_2(x) & \mu_1(x) - \lambda_c \end{pmatrix} = 0 \tag{62}$$

for some $x \in [0, L)$. For a stationary chimera solution, we have synchronous regions, where $|h\,(x)| \geq |\varOmega|$, and partially synchronous domains, where $|h\,(x)| < |\varOmega|$. Therefore, according to formulas (55) and (56), for such a pattern the multiplication operator $\hat{\mathbf{M}}$ has a T-shaped continuous spectrum with a symmetric interval of purely imaginary (with their zero real parts) eigenvalues λ_c corresponding to the partially synchronous areas. In contrast, for the other intervals corresponding to synchronous regions, eigenvalues λ_c are real and lie in the left complex half-plane. Notably, this is one more argument supporting for our choice of the solution branches in relation (12): choosing the opposite sign there, the real branch of λ_c is located in the positive half-plane and the corresponding stationary rotating wave with coherent domains would be unstable.

Thus, the continuous spectrum λ_c is either stable (negative) or neutrally stable (purely imaginary). The temporal stability of the chimera states is determined by the point spectrum λ_p of the composed operator $\hat{\mathbf{M}} + \hat{\mathbf{K}}$, but the remaining point eigenvalues λ_p have no simple representation, and it is not easy to calculate this part of the spectrum λ numerically using only standard spatial discretization procedure and replacing in (61) integral operators with $M \times M$ matrix.

6.2 Numerical Calculation of the Point Spectrum

There are some difficulties in numerical calculation of stability properties of the stationary chimera states. The main difficulty here is that, according to Sect. 6.1, the original eigenvalue problem (61) has an essential continuous T-shaped spectrum λ_c consisting of eigenvalues on the imaginary and the negative real axes, but stability is determined by the point spectrum λ_p. After spatial discretization, we get a matrix eigenvalue problem. Unfortunately, it is not easy to discriminate essential and point parts of the spectrum λ in the eigenvalues of the approximate matrix, because the eigenvalues representing the T-shaped essential part λ_c of spectrum λ lie not exactly on the imaginary and the negative real axes.

We suggest the following approach to identify the point spectrum λ_p. For a chimera state in the domain $x \in [0, L)$, we discretize the linearized system (61) by using a set of points $x_0 + j\Delta$, $j = 0, 1, \ldots, M-1$, where $\Delta = L\big/M$ and $0 \le x_0 \le \Delta$ is an arbitrary continuous parameter. This leads to an $2M \times 2M$ real matrix, the eigenvalues λ of which we obtained numerically. The main idea is to vary the offset of the discretization x_0. We find that while the components of the essential spectrum vary with x_0, the point spectrum λ_p components vary extremely weakly with x_0. This allows us to determine the point spectrum λ_p reliably for most values of the parameters.

In Fig. 6 we present the results of the stability analysis for $\alpha = 1.457$, for branches A, B, C, D (see Fig. 4b). Four characteristic types of spectra are shown in panels (a–d). Only case (c) where the point spectrum λ_p has a negative real part corresponds to a stable chimera pattern, while all other patterns are unstable (oscillatory instability for cases (a) and (b) and monotonous instability for case (d)). The dependence of the point spectrum λ_p on parameter Ω for $\alpha = 1.457$, for branches A, B, D, is shown in Fig. 6e, f. One can see that in the region $-0.68 \lesssim \Omega \lesssim -0.64$ there are four points of λ_p; for other values of Ω, there is only one pair of eigenvalues (or one real eigenvalue

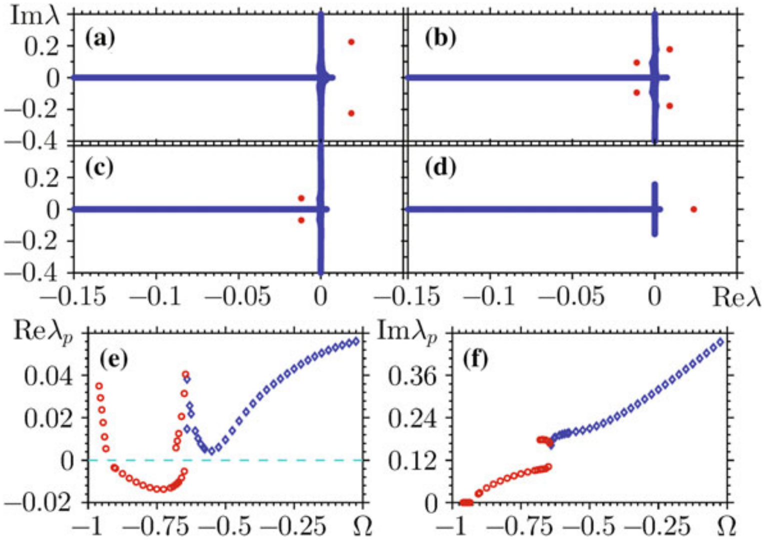

Fig. 6 Panels **a**–**d**: Essential (blue markers) and point (red markers) spectra for chimera states at $\alpha = 1.457$ and four values of Ω: **a** $\Omega = 0.45$, **b** $\Omega = 0.675$ and **c** $\Omega = 0.8$, **d** $\Omega = 0.95$. In these diagrams, all $2MN$ eigenvalues with $M = 2048$ and $N = 128$ are plotted. **e**, **f**: real and imaginary parts of the point spectrum λ_p for solutions A, D (red circles) and B (blue diamonds) in Fig. 4b.

for branch D). This property may be explained by closeness to the homoclinic orbit $\Omega \approx \Omega_*$, where the length of the patterns is large, so two discrete modes are possible here. The only stable chimera state is of type A (we refer here to Figs. 3 and 4b) with $-0.91 \lesssim \Omega \lesssim -0.69$. On the contrary, chimera states with two synchronous regions (type B) are unstable. Most difficult was the analysis of the solutions of type C with two synchronous regions (Fig. 7), here the unstable branch of the point spectrum λ_p is real, and there are up to three stable complex pairs. In some cases, only a very fine discretization with $M = 6144$ allowed us to reveal unstable point eigenvalues λ_p. We attribute this to a complex profile of this solution, requiring a high resolution of perturbations.

Stability properties described above are confirmed by direct numerical simulations of the ensemble governed by Eq. (1), (3), see Fig. 8 for space-time plots of field

$$\left|H\left(k,t\right)\right| = \left|\sum_j G\big(|k-j|\,/KL\big)\exp\left(i\phi_j\right)\right| \tag{63}$$

We initialize the chimera patterns as the periodic solutions of ODEs; in the unstable regions these patterns are eventually destroyed, while a stable chimera persists. Remarkably, for weakly unstable chimeras with two synchronous regions for $\Omega \approx -0.58$, where the real part of the point eigenvalue λ_p has a minimum (see Fig. 6e), the life time of the initial chimera pattern is relatively large.

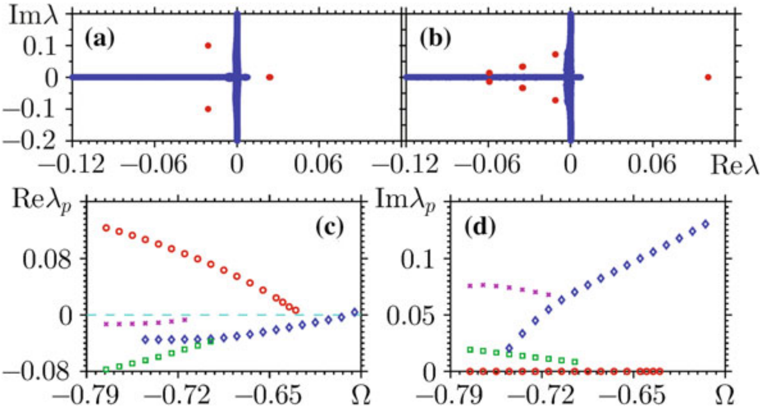

Fig. 7 Eigenvalues [**a** $\Omega = -0.645$, **b** $\Omega = -0.735$, here $M = 4096$, $N = 64$] of continuous and point spectra in dependence on Ω (**c**, **d**) for the asymmetric branch C

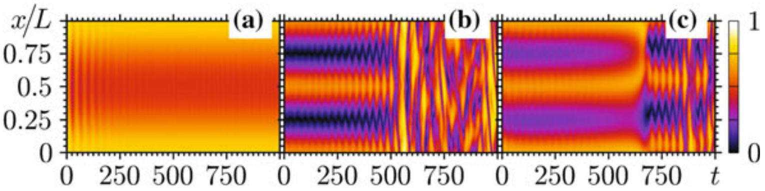

Fig. 8 Direct numerical simulations of the evolution of stable and unstable chimeras for $\alpha = 1.457$. **a** Chimera of type A for $\Omega = -0.71377$, $L = 6.03$; **b** chimera of type B for $\Omega = -0.575$, $L = 12.06$; **c**: chimera of type C, $\Omega = -0.6$, $L = 12.06$. The number of oscillators was $K = 700$ per length unit

7 Conclusion

In this chapter, we described a PDE-based approach to the problem of chimera patterns in a 1D medium of coupled oscillators. The equations resemble those typical for the pattern formation problem (e.g., the complex Ginzburg–Landau equation), but have several peculiarities stemming from the synchronization setup. For example, the complex order parameter cannot exceed one. This leads to a coexistence of synchronous and partially synchronous regions in the chimera patterns. The uniformly rotating chimera states are found as solutions of an ODE. We demonstrated a variety of patterns with different profiles and periods, but focused on the simplest ones, with at most two synchronous domains. Remarkably, these profiles can be analytically described in the limit of neutral coupling between oscillators. For a coupling close to the neutral one, we developed a perturbation theory which yields approximate solutions. Exploring the stability of the found solutions appears to be a nontrivial numerical problem. We describe an approach to characterize the essential and the point parts of the spectrum via finite discretizations. The calculations show that only chimeras of the type originally studied by Kuramoto and Battogtokh are stable, while others are linearly unstable.

This chapter presents a novel object in a zoo of patterns, so nicely described by Sasha Ezersky with co-workers in the book [2]. He made seminal contributions also to nonlinear phenomena in hydrodynamics and acoustics. All who knew S.E. enjoyed discussions and collaborations with him, he was an inspiration for many of us.

Acknowledgements We are thankful to O. Omelchenko, M. Wolfrum, and Yu. Maistrenko for useful discussions. L. S. was supported by ITN COSMOS (funded by the European Unions Horizon 2020 research and innovation programme under the Marie Sklodowska Curie grant agreement No 642563). Stability studies were supported by the Russian Science Foundation (Project No. 14-12-00811). Poincaré section study was supported by the Russian Science Foundation (Project No. 17-12-01534).

References

1. Y. Kuramoto, D. Battogtokh, Nonlinear Phenom. Complex Syst. **5**, 380 (2002)
2. M.I. Rabinovich, A.B. Ezersky, P.D. Weidman, *The Dynamics of Patterns* (World Scientific, Singapore, 2000)
3. M.J. Panaggio, D.M. Abrams, Nonlinearity **28**(3), R67 (2015)
4. D.M. Abrams, R. Mirollo, S.H. Strogatz, D.A. Wiley, Phys. Rev. Lett. **101**, 084103 (2008)
5. A. Pikovsky, M. Rosenblum, Phys. Rev. Lett. **101**, 264103 (2008)
6. M.R. Tinsley, S. Nkomo, K. Showalter, Nature Physics **8**(9), 662 (2012)
7. E.A. Martens, S. Thutupalli, A. Fourrière, O. Hallatschek, Proc. Natl. Acad. Sci. **110**(26), 10563 (2013)
8. D.M. Abrams, S.H. Strogatz, Phys. Rev. Lett. **93**(17), 174102 (2004)
9. S.I. Shima, Y. Kuramoto, Phys. Rev. E **69**(3), 036213 (2004).
10. C.R. Laing, Physica D: Nonlinear Phenomena **238**(16), 1569 (2009).
11. G. Bordyugov, A. Pikovsky, M. Rosenblum, Phys. Rev. E **82**(3), 035205 (2010)
12. L. Smirnov, G. Osipov, A. Pikovsky, Journal of Physics A: Mathematical and Theoretical **50**(8), 08LT01 (2017).
13. M. Wolfrum, O.E. Omel’chenko, S. Yanchuk, Y.L. Maistrenko, CHAOS **21**(1), 013112 (2011).
14. O.E. Omel’chenko, Nonlinearity **26**(9), 2469 (2013)
15. E. Ott, T.M. Antonsen, CHAOS **18**(3), 037113 (2008)
16. C.R. Laing, Physica D: Nonlinear Phenomena **240**(24), 1960 (2011).
17. C.R. Laing, Phys. Rev. E **92**, 050904 (2015).
18. J. Xie, E. Knobloch, H.C. Kao, Phys. Rev. E **90**, 022919 (2014).

Radial Propagation of the Instability Modes Observed in a Viscoelastic Couette–Taylor Flow

Nizar Abcha, Fayçal Kelai, Noureddine Latrache, Olivier Crumeyrolle and Innocent Mutabazi

Abstract Experimental investigation of the flow of a high-molecular-mass polymer solution in the Couette–Taylor system with fixed outer cylinder was performed using visualization and particle image velocimetry (PIV) techniques. Spatiotemporal diagrams of the reflected light intensity and of velocity data allow to describe the flow dynamics in the meridional cross section. When the elasticity and inertia effects are comparable (inertioelastic regime), the circular Couette flow bifurcates to standing waves—in the axial direction—called ribbons. These critical waves also propagate in the radial direction toward the outer cylinder. The higher instability mode manifests in form of domains with disordered oscillations separated by fluctuating walls characterized by strong radial inflow.

Keywords Couette–Taylor flow · Viscoelasticity · Inertio-elastic waves · PIV

N. Abcha (✉)
Normandie Université, UNICAEN, UNIROUEN, CNRS, UMR 6143, M2C, 14000 Caen, France
e-mail: nizar.abcha@unicaen.fr

F. Kelai · O. Crumeyrolle · I. Mutabazi
Normandie Université, Unihavre, CNRS, UMR 6294, LOMC, 76600 Le Havre, France
e-mail: kelaifafa@hotmail.com

O. Crumeyrolle
e-mail: olivier.crumeyrolle@univ-lehavre.fr

I. Mutabazi
e-mail: innocent.mutabazi@univ-lehavre.fr

N. Latrache
FRE CNRS 3744 IRDL, Université de Brest, 29200 Brest, France
e-mail: noureddine.latrache@univ-brest.fr

N. Abcha et al. (eds.), *Nonlinear Waves and Pattern Dynamics*,
https://doi.org/10.1007/978-3-319-78193-8_11

1 Introduction

Flows of viscoelastic liquids exhibit features that are very different from those of Newtonian flows. One can cite the Weissenberg effect which consists of a liquid climb along with a rotating vertical rod partially immersed in a viscoelastic liquid, or the turbulent drag reduction due to polymer additives to Newtonian flows. The late case seems counterintuitive if one considers that, for example, the turbulent flow in a pipe requires a lower pressure gradient for viscoelastic fluid at the same flow rate and viscosity than for a viscous fluid. An important class of viscoelastic liquids is formed by high molecular weight polymer solutions such as polyethyleneoxide (PEO) or polyacrylamide (PAM) solutions [1, 2]. A small amount of these polymers in aqueous solutions may significantly alter the transition scenario from laminar to turbulent flows, the nature of flow structures and the torque exerted by the fluid on rotating surface or the pressure drop in pipe flows, compared to the Newtonian flows. Since the observation of the turbulent drag reduction effect by Toms in 1948 [3], the use of polymer additives has been tested in different applications such as the increase of flow rate in pipe flows for firefighting or drainage, the design of ships and submarines with an increased speed and a reduced energy cost, the transportation of oil pipelines over long distances, wastewater treatment or inkjet printer [1]. Despite these different applications, theoretical investigations of viscoelastic flows are much limited because of the lack of universal equations that can describe their dynamics. Different constitutive equations that are available in literature to model viscoelastic fluids depend on the rheological properties of the solutions: dependence of viscosity on shear rate, elasticity and relaxation time spectrum. This situation limits the predictability of these models and has motivated a large number of experimental studies since the second half of the last century [4–8].

Flows of viscoelastic fluids can be characterized by the following dimensionless numbers [9]: the Reynolds number $Re = \rho\dot{\gamma}d^2/\eta$, the Weissenberg number $Wi = \dot{\gamma}\lambda$, the elasticity number $E = \lambda/\tau_\nu$ and the viscosity ratio $S = \eta_p/\eta$, where ρ is the density of the solution, d is the gap between the cylinders, $\dot{\gamma}$ is the shear rate, λ is the polymer relaxation time, η is the solution viscosity, η_p is the polymer contribution to the solution viscosity, $\tau_\nu = \rho d^2/\eta$ is the viscous diffusion time. The solvent viscosity is $\eta_s = \eta - \eta_p$. The Weissenberg number is the analog of the Reynolds number, while the elasticity number is a property of the fluid and geometry.

One of the privileged flow set up to investigate the transition to turbulence in closed flows is the Couette–Taylor system which consists of a flow in the gap between two coaxial cylinders that can rotate independently. Flows in the Couette–Taylor system are well documented for Newtonian fluids [10]. This system was also used to investigate flow structures developing in viscoelastic fluids, and the features peculiar to non-Newtonian character of the fluid can be easily identified. Flows of fluids with very weak values of the elasticity number behave like the Newtonian flows with the identical transition scenario [10]. Flows with very high elasticity become unstable to disordered oscillatory waves which correspond to the elastic response of polymer molecules to the applied shear. This elastic instability was first reported in the study of Boger fluids (highly viscoelastic liquids with constant viscosity) for low shear rate [7]. Higher modes of this instability can lead to elastic turbulence [7, 8, 11–14] in conditions for which a Newtonian fluid with comparable viscosity would remain laminar. For solutions with $E \sim 10^{-1}$, the base circular Couette flow becomes unstable and transits to the ribbons, inertio-elastic modes formed of counter-propagating spirals with equal amplitude and frequency [11–13, 15–19], resulting in standing waves in the axial direction. Among previous experimental results on the stability of the Couette flow in inertio-elastic regime, the experimental study by Groisman and Steinberg [12] reported the observation of an instability mode called Radial Waves (RW) propagating both axially and radially, which was not fully characterized.

In this chapter, we present the results on the rotating radial waves observed in the Couette–Taylor flow of a viscoelastic fluid when the inner cylinder is rotating while the outer one is fixed. The flow was visualized using reflective Kalliroscope flakes, or seeded with glass particles for particle image velocimetry (PIV) in order to measure the radial and axial velocity components. Space-time diagrams extracted from reflected light intensity and from the velocity fields provide a good representation of the flow dynamics.

The chapter is organized as follows: after the description of experimental setup and procedure (visualization, PIV) in Sect. 2, we present the main results in Sect. 3. The last section contains discussion and concluding remarks.

2 Experimental Setup and Polymer Characterization

Polymer solutions were prepared by mixing a solution of polyethyleneoxide (PEO) of large molecular mass ($M \sim 10^6$ g/mol) with 100 ml of isopropyl alcohol in 1900 ml of water (with the pH = 7) at room temperature. Viscosity measurements revealed a shear-thinning behavior, i.e., the solution viscosity is constant for low shear rates and then decreases according to a power law when the shear rate of the flow increases (Fig. 1). The viscosity data were fitted with the Carreau formula [9]: $\eta = \eta_0 \left(1 + (\lambda\dot{\gamma})^2\right)^{-n}$, from which we extracted the viscosity at zero shear η_0, the relaxation time λ of the solution and the shear-thinning index n. We found $\eta_0 = 26$ mPa × s, $\lambda = 0.69$ s and $n = 0.26$ for c = 1200 ppm. The validity of Carreau equation has been tested on solutions with eight different concentrations. The solutions have sufficiently low viscosities to avoid the viscous heat-induced patterns that can occur in high viscosity polymer solutions [14].

The experimental system consists of two vertical coaxial cylinders immersed in a large rectangular plexiglass box filled with water for thermal insulation (Fig. 2). The inner cylinder has a radius $a = 4$ cm, the gap between the cylinders is $d = 1$ cm and the cylinder working length is $L = 45.9$ cm. The radius ratio is $\mu = a/(a + d) = 0.8$ and the aspect ratio is $L/a = 45.9$. Such an aspect ratio is sufficiently large for the system to be considered as an extended one, i.e., for the end plates to have

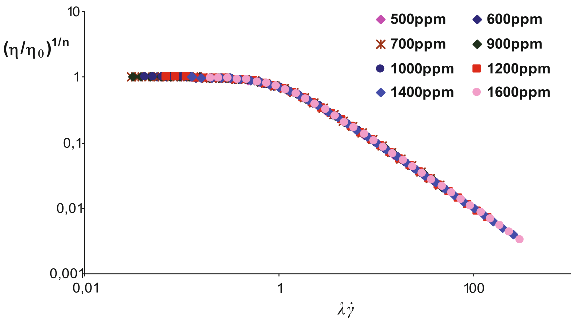

Fig. 1 Master viscosity curve from Carreau equation

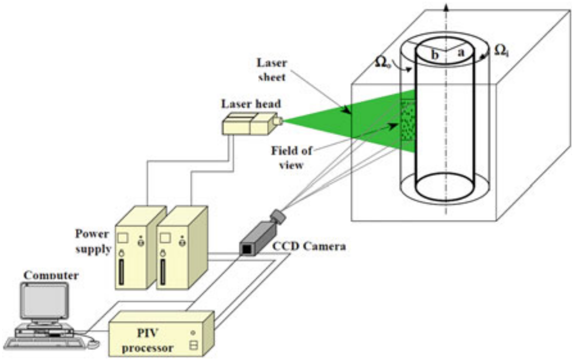

Fig. 2 Experimental apparatus: scheme of visualization and data acquisition system

negligible effects on the flow dynamics. Both cylinders may rotate independently at angular frequencies Ω_i and Ω_o for inner and outer cylinder, respectively. For the visualization of flow structures, we have added 2% by volume of Kalliroscope AQ1000, which is a suspension of 1–2% of reflective flakes [20, 21]. The amount of this added suspension is small enough that it does not affect the rheology of the resulting solution.

In the present experiment, the outer cylinder is fixed. The average shear rate is defined as $\dot{\gamma}_c = \Omega_i a/d$. We introduce a zero-shear rate Taylor number Ta_0 and an effective Taylor number Ta: $Ta_0 = \frac{\dot{\gamma} d^2 \rho}{\eta_0}\sqrt{d/a}$ and $Ta = \frac{\dot{\gamma} d^2 \rho}{\eta}\sqrt{d/a}$.

Optical flow visualization was made in the $(r,\ z)$ cross section with a He–Ne laser sheet (1 mm wide beam), spread by a cylindrical lens (Fig. 2). A 2-d CCD camera (A641f, Basler) was used to record intensity of the reflected light by the flow structures at regular time intervals, more precisely, every 1/25th of a second, yielding signal denoted I (z, r, t). The signal was recorded over a length of 12 cm in the central part of the system (Fig. 3). The axial distribution of the light intensity, at regular time intervals on the line $r = a + d/2$ can be plotted in the space-time diagram $I(z,\ t)$

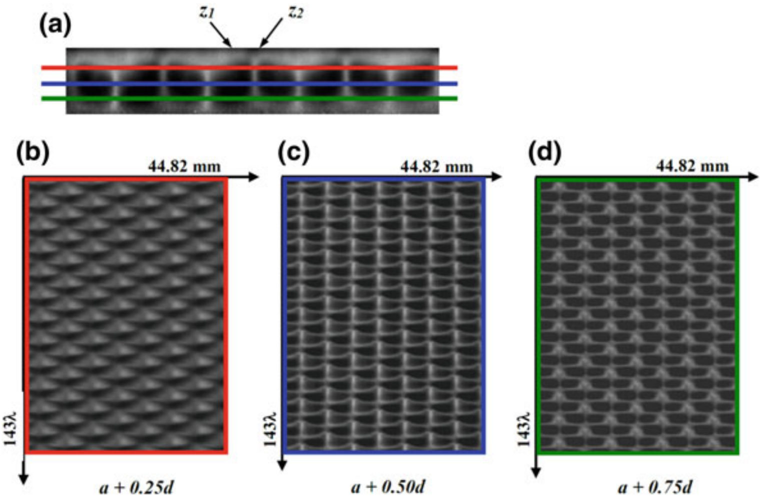

Fig. 3 Flow patterns in the (r, z) plane over a length of 4.482 cm in the central part of the flow system and time duration of 60 s: **a** a cross section of the flow structures, **b** space-time diagram near the inner cylinder ($x = 0.25$), **c** $I(z, t)$ at the mid-gap ($x = 0.5$), **c** $I(z, t)$ at $x = 0.75$ where x = (r − a)/d

(Fig. 3b–d). We also recorded the intensity at different radial positions in the plane $z = \Gamma/2$ and then plotted the space-time diagram $I(r, t)$ (Fig. 4). Space-time diagrams from reflected light intensity allow for the precise measurements of spatiotemporal properties of the patterns (Fig. 5). However, they do not provide any quantitative data of velocity. The latter can be obtained by PIV measurements, which allow for the estimate of energy and momentum transfer in different flow regimes.

For PIV measurements, the working fluid was seeded with spherical glass particles of mean diameter 12.9 μm (standard deviation between particles of 5.5 μm) and a density of 1.6 g/cm^3, with a concentration of about 1 ppm and with a relatively large refractive index of 1.85.

The PIV system (from Tecflow) features two Nd-YAG laser sources, a MasterPIV processor and a CCD camera (Kodak) with 1034 × 779 pixels. The time delay between two laser pulses varies from 0.5 to 25 ms, depending on the values of Re. In the PIV technique, the flow in the test area of the plane (r, z) is visualized with a thin light sheet that illuminates the glass particles, the positions of which can be recorded at short time intervals. We have recorded 195 pairs of images of size 1034 × 779 pixels. Each image of a pair was sampled into windows of 32 × 32 pixels with an overlapping of 50%. The velocity fields were computed using the intercorrelation function, which is implemented in the software "Corelia-V2IP" (Tecflow). From velocity fields, we have deduced the azimuthal component of the vorticity $\omega_\theta = (\partial v_r/\partial z - \partial v_z/\partial r)$. We have performed PIV measurements in the circular Couette flow (CCF), in the Taylor vortex flow (TVF), and Wavy vortex flow (WVF) regimes in order to calibrate our data acquisition system and to fit data available in the

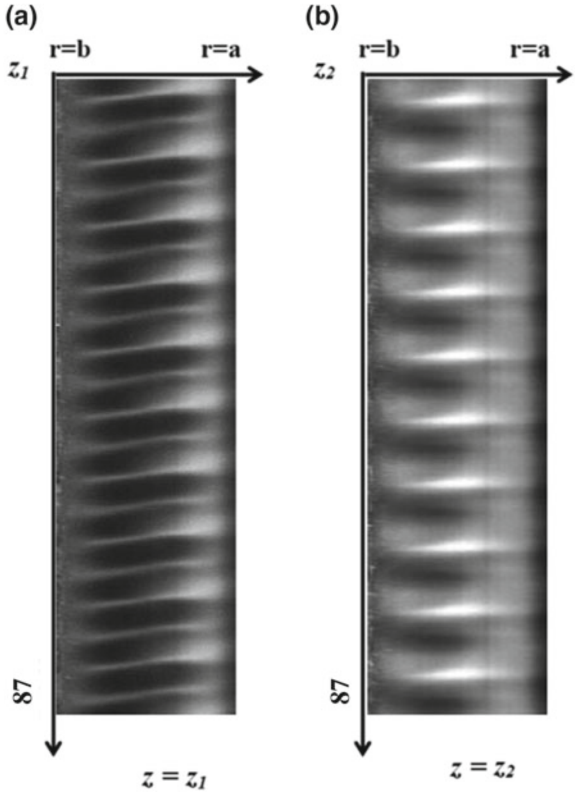

Fig. 4 Spatiotemporal diagrams I (r, t) obtained at two different axial positions: **a** $z = z_1$, **b** $z = z_2$

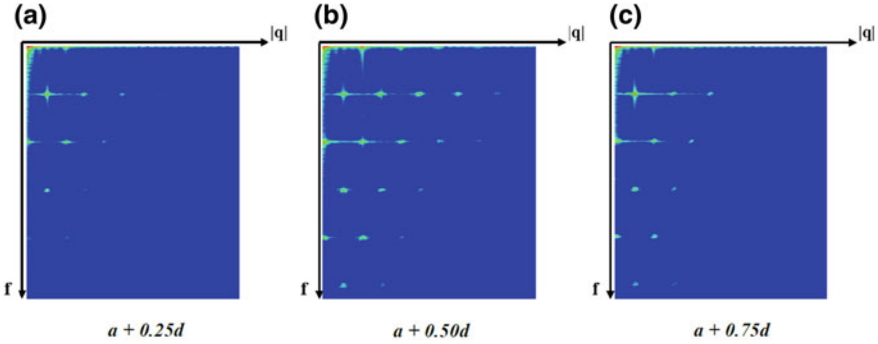

Fig. 5 Two-dimensional power spectra of spatiotemporal diagrams I (z, t) obtained at different radial positions: **a** $x = 0.25$, **b** $x = 0.5$, **c** $x = 0.75$

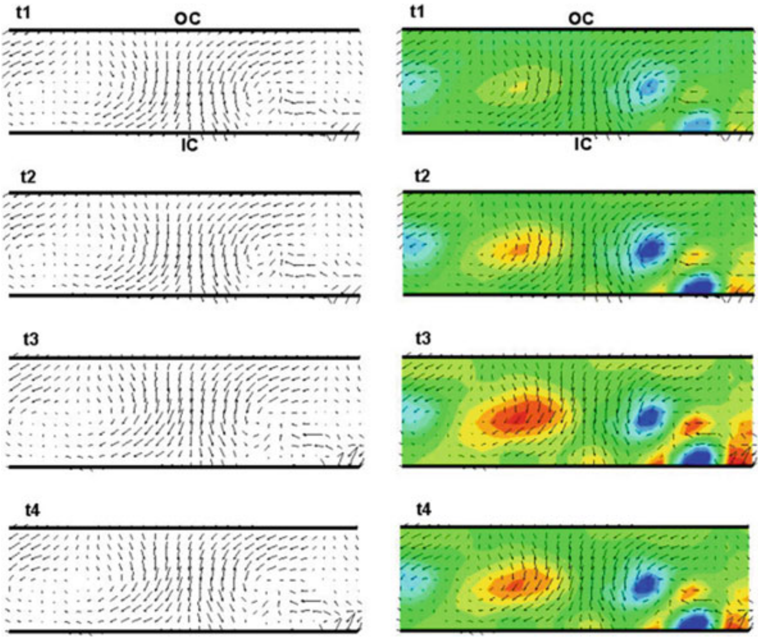

Fig. 6 Instantaneous velocity and vorticity of the flow regime at $\dot{\gamma}_c = 12.6s^{-1}$ ($\mathrm{Ta_c} = 41.8$) for 4 consecutive records ($t_{i+1} = t_i + 0.5$ s)

literature for these regimes [22–25]. The PIV allows for the visualization of velocity and vorticity fields in the cross section (r, z) (Fig. 6). From the instantaneous data, we have plotted the space-time diagrams of velocity components, as illustrated for the radial V_r component in the axial (Fig. 7a, b) and radial directions (Fig. 7c, d) and extracted from them the amplitudes and phases using the complex demodulation technique described in Bot et al. [26, 27].

3 Results

We describe results obtained for a polymer solution with a fixed concentration c = 1200 ppm of PEO. Results for concentrations below c = 1200 can be found in our previous works [15–19]. Increasing the angular frequency of the inner cylinder, i.e., the shear rate$\dot{\gamma}$, leads to the bifurcation of the circular Couette flow to regular time-dependent structures. The threshold occurs at the shear rate $\dot{\gamma}_c = 12.56s^{-1}$. The shear viscosity corresponding to this critical shear rate is $\eta = 15$ mPa × s and the viscous diffusion time is $\tau_\nu = \rho d^2/\eta = 6.66$ s. Thus, the critical value of the effective Taylor number is $Ta_c = 41.8$ and the critical Weissbenberg number computed with the solution relaxation time $Wi_c = \dot{\gamma}_c \lambda = 8.7$.

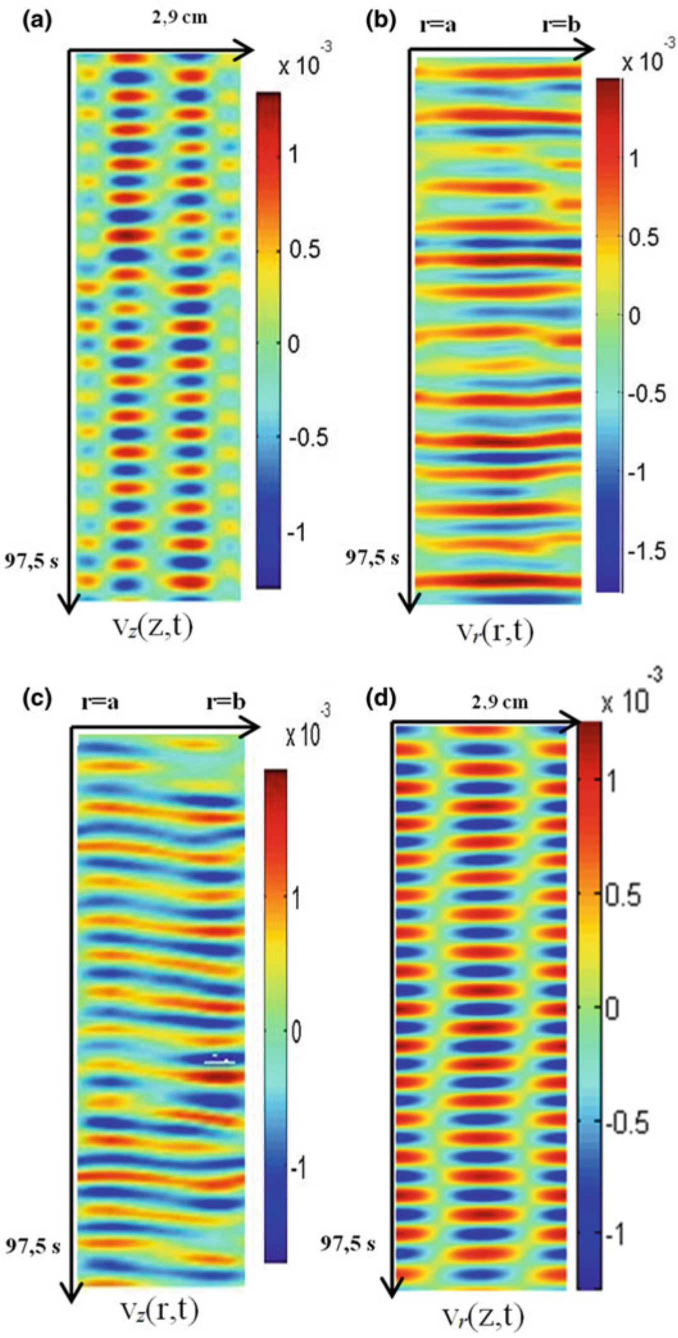

Fig. 7 Space-time diagrams of the flow velocity components for $\dot{\gamma}_c = 12.6\,s^{-1}$ ($\mathrm{Ta_c} = 41.8$): **a** V_z(z, t), **b** V_r(r, t), **c** V_z(r, t), **d** V_r(r, t)

Critical flow structures

The critical structures are axially counter-propagating waves called *inertio-elastic waves* (Fig. 3). Their critical wavelength and frequency are $\lambda_c = 1.96$ cm $\simeq 2d$ and $f_{\mathrm{c}} = 0.178$ Hz, respectively, yielding a dimensionless critical wavenumber $q_c = 2\pi d/\lambda_c = 3.21$ and a dimensionless critical frequency $\omega_{\mathrm{c}} = 2\pi f_c \tau_\nu = 7.45$. The critical structures also propagate in the radial direction. Their space-time diagrams are shown in Figs. 3b–d and 4. The elasticity number corresponding to this solution is $E = \lambda/\tau_\nu = 0.10$ and the viscosity ratio $S = \eta_p/\eta = 0.93$. Linear stability analysis of the viscoelastic solutions with such parameters shows that the critical modes are oscillatory modes [9].

The space-time diagrams I (r, t), shown in Fig. 4, are extracted from I (z, r, t) at the positions z_1 and z_2 mentioned in Fig. 3a. These diagrams show the radial propagation of the critical mode toward the outer cylinder. We noted clear difference between the pattern of Fig. 3b and the other two diagrams (Fig. 3c, d). The first pattern, Fig. 3a, for $r = a + 0.25d$, is close to the pattern associated with strongly coupled contra-propagative modes [15], while the other two correspond to patterns with lower coupling.

The two-dimensional Fourier power spectra of the space-time diagrams are presented in Fig. 5. The spectra exhibit finite peaks, corresponding to the left and right propagating spirals located at $(-q_c, \omega_c)$ and (q_c, ω_c), respectively. Second harmonic modes $(-2\mathrm{q}_c, 2\omega_c)$ and $(2q_c, 2\omega_c)$ propagate with the same phase velocity as the fundamental modes. The spectrum exhibits, aside from these peaks, two large peaks corresponding one to a stationary spatial harmonic mode $(2q_c, 0)$, and the other to a temporal homogeneous harmonic mode $(0.2\ \omega_c)$. These unlocked harmonic modes result from a multiplicative coupling between right and left spirals [15], and exhibit a power 3.1 times greater than that of the fundamental mode (q_c, ω_c) at $r = a + 0.25d$, while for the other investigated radial positions, the powers of the unlocked harmonics and the fundamental mode are closer. This confirms the above remark about $I(z, t)$ patterns of Fig. 3a. The spectra in Fig. 5 show from a general point of view the significant coupling between fundamental modes, harmonics and mean flows. The amplitudes of the different harmonics can be obtained from complex demodulation technique. Locked harmonics $(\pm 2q_c, 2\omega_c)$ and higher modes can be ignored in the following as their magnitude in the power spectrum is relatively small. The real signal can then be represented as follows:

$$I(z,t) = \mathrm{Re}\left\{A(z,t)\exp(i\phi_A) + B(z,t)\exp(i\phi_B) + U_\omega(z,t)\exp(2i\omega t) + U_q(z,t)\exp(2iqz)\right\}, \tag{1}$$

where $A(z, t)$, $B(z, t)$, $U_\omega(z, t)$, and $U_q(z, t)$ are the amplitudes of right- and left-traveling modes, the temporal and spatial harmonics, respectively; $\phi_A = \omega_A(z, t)t - q_A(z, t)z$, and $\phi_B = \omega_B(z, t)t + q_B(z, t)z$ represent the phases of the right- and left-traveling waves, respectively. The amplitudes A, B, U_ω, and U_q satisfy a system of coupled nonlinear equations that were developed in [17].

Analysis of the variations of the amplitudes, frequencies, and wavenumbers shows that the right-and left-traveling waves have approximately the same amplitudes, frequencies, and wavenumbers i.e.

$$|A\,(z,t)| \cong |B\,(z,t)|\,,\omega_A \cong \omega_B \, and \; q_A \cong q_B \tag{2}$$

meaning that the inertia-elastic waves are ribbons (standing waves) [23]. The estimate of the hysteresis shows that the inertio-elastic waves occur via a supercritical bifurcation. In the neighborhood of the threshold, they can be described by the coupled Landau equations:

$$\begin{cases} \dfrac{dA}{dt} = \left[a\varepsilon - b\,|A|^2 + c\,|B|^2\right] A \\ \dfrac{dB}{dt} = \left[a\varepsilon - b\,|B|^2 + c\,|A|^2\right] B \end{cases}, \tag{3}$$

where $\varepsilon = (Ta - Ta_c)\big/ Ta_c$ is the criticality, a, b, c are complex coefficients; the spatial and temporal harmonics are ignored. The amplitudes of ribbons are given by:

$$\begin{cases} |A|^2 = |B|^2 = \varepsilon\big/ (c_r - b_r) \\ \omega_A = \omega_B = \left[-a_i + (b_i - c_i)\big/ (b_r - c_r)\right] \varepsilon \end{cases} \tag{4}$$

For further investigations of observed amplitudes |A| and |B|, the PIV technique was used.

Velocity fields

The instantaneous velocity and vorticity fields of the flow regime in the meridional cross section, just above the transition to supercritical flow for 4 records ($t_{i+1} = t_i + 0.5$ s) are shown in Fig. 6. The inner cylinder corresponds to the bottom line of the images and the values of the vorticity are coded colors: red for positive values and blue for negative values. From the velocity fields, we have extracted radial and axial velocity components $V_r(z)$, $V_z(z)$ at a given a radial position $r = a + 0.5d$ and to an axial position $V_r(r)$ and $V_z(r)$.

The instantaneous velocity components can also be superposed chronologically at regular time intervals in order to obtain space-time diagrams (Fig. 7) of the velocity field. The resulting diagrams are color-coded as follows: the red color corresponds to positive values and blue to the negative values of the velocity. The diagrams of radial velocity for different positions in the axial direction V_r(z, t) show that the first mode of instability manifests as a pattern of two counter-propagating waves (Fig. 7a, b). The space-time diagrams of the two velocity components V_r(r, t) and V_z(r, t) are presented in Fig. 7c, d. It is visible on V_z(r, t) that the waves propagate in the radial direction from the inner cylinder to the outer cylinder. We have observed that the vortices occupy the whole gap. Fourier two-dimensional filtering of the space-time diagrams allowed us to extract (Fig. 8) time variations of $V_r(z, t)$ for the left and right

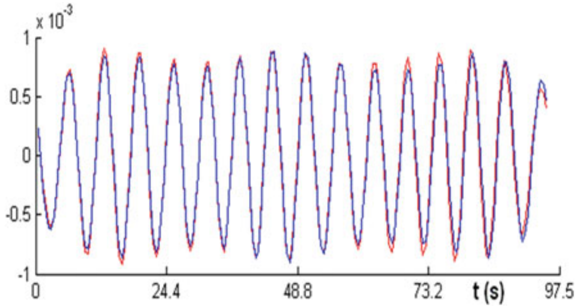

Fig. 8 Temporal variation of $V_r(z, t)$ for right-traveling mode **a** (blue curve) and left-traveling mode **b** (red curve), in the mid-gap ($r = a + d/2$)

modes separately, and the common amplitude, $|A| = |B|$, as expected for ribbons, is observed.

4 Disordered Wave Domains and Fluctuating Walls

When the control parameter is increased above $Ta = 1.113\ Ta_c$, the pattern of counter-propagating spirals becomes disordered while forming domains separated by fluctuating in time and space walls. These walls represent zones with a strong inflow (i.e., a strong flow toward the inner cylinder). To follow the dynamics of the walls, we have plotted in Fig. 9a, b the time-averaged intensity of light reflected by the pattern as a function of the axial coordinate $\bar{I}\,(z) = \sum_{t_1}^{t_1+\Delta t} I(z, t)/\Delta t$. We measured the velocity field in the neighborhood of the domain wall. The domain walls appear as holes in light intensity (Fig. 9c) or as zones in which the radial velocity is strong toward the inner cylinder (Fig. 9d, f). The pattern exhibits a disorder more pronounced in the time than in space. In fact, the frequency spectrum of the pattern is completely noisy while the wavenumber spectrum exhibits a peak (with its harmonics), corresponding to a wavelength $\lambda = 5.36$ cm. The maximal radial velocity in the wall is approximately equal to the ratio of the gap width to the characteristic viscous time $V_{\mathrm{r,max}} \approx d/t_{\mathrm{vis}} = 0.97$ cm/s. The walls observed in our experiment are fluctuating in space and in time, they can disappear or be generated erratically in space and in time. To investigate their statistical distribution with their duration and spatial width, we have performed a digitalization as follows (Fig. 10): walls have been represented as black (value 0) and inertia-elastic waves as white (value 1). In order to reduce the noise of the processing, only the skeleton of the resulting pattern was used for statistics. Then, the histograms of walls with respect to their size and their duration have been constructed (Fig. 11) and they allow for the determination of the mean width and lifetime of the walls.

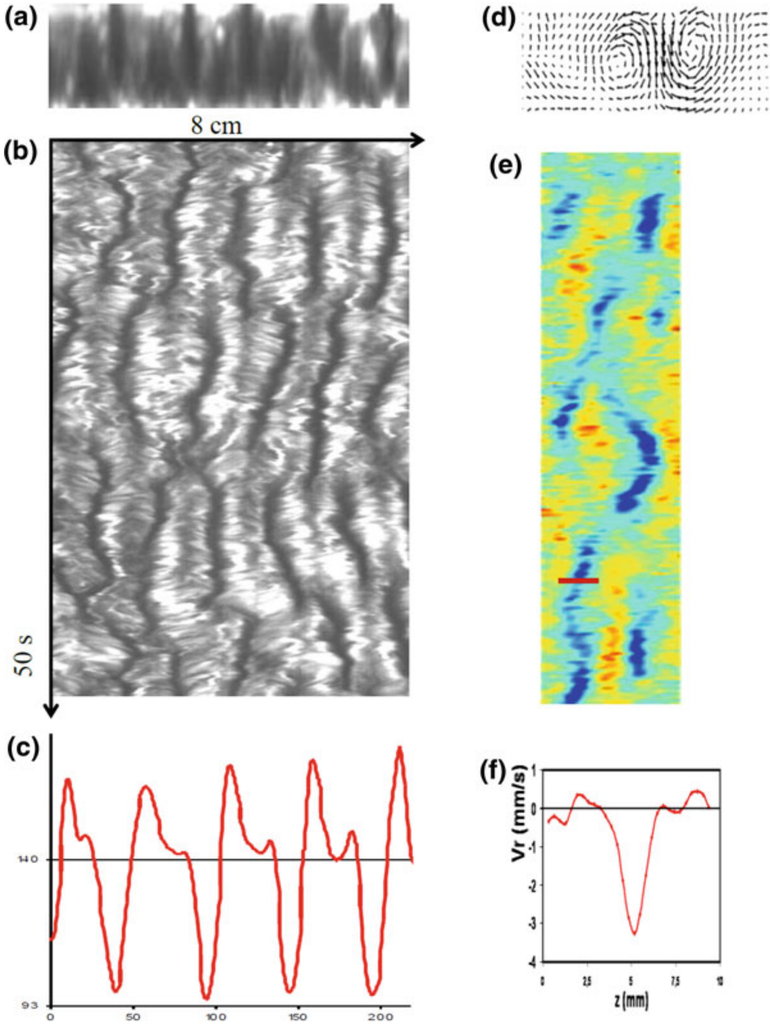

Fig. 9 Disordered wave domains with fluctuating walls for Ta $= 1.122$ Ta$_c$: **a** r-z cross section of the flow, **b** space-time diagrams of the pattern, **c** Time-averaged profile of the intensity $\bar{I}\,(z)$, **d** velocity field in the r-z plane near the wall, **e** space-time diagram of the radial velocity near the wall and **f** time-averaged radial velocity profile focused on the wall

5 Discussion

The destabilization of the circular Couette flow of a viscoelastic shear-thinning aqueous solution of polyethylene oxide of $c = 1200$ ppm appears at the effective Taylor number $Ta_c = 41.8$ and the Weissenberg number of $Wi_c = \dot{\gamma}_c\lambda = 8.7$. The critical pattern is composed of counter-propagating spirals in the axial direction with radial

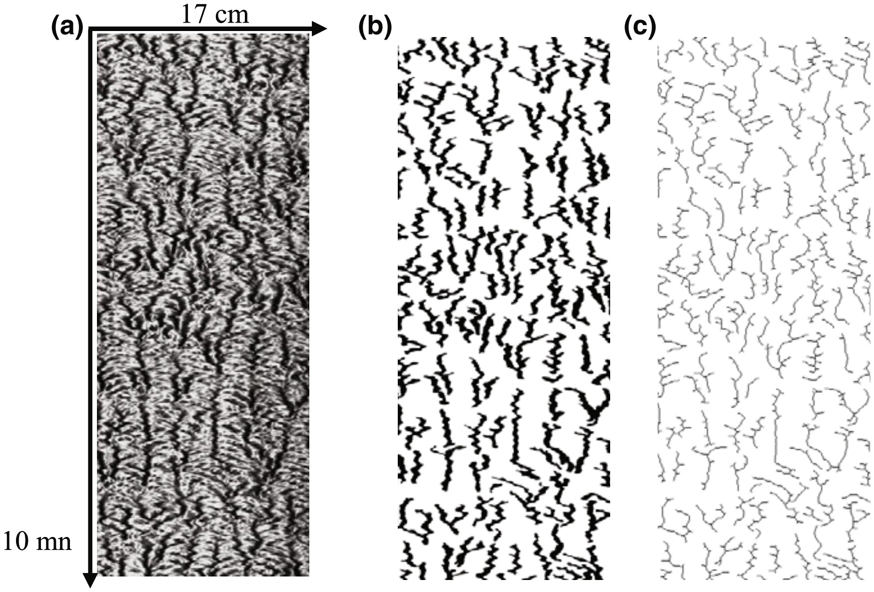

Fig. 10 Digitalization procedure: **a** space-time diagram of the pattern of inertia-elastic waves with fluctuating walls, **b** digitalized pattern (black: 0, white = 1), **c** skeleton of the walls

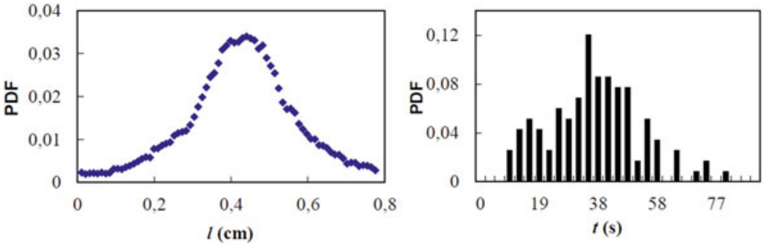

Fig. 11 Distribution of the wall in size and in duration for Ta = 1.122 $\mathrm{Ta_c}$: the mean width of the walls is $\langle l \rangle = 0.44$ cm and their lifetime is $\langle \Delta t \rangle = 35.3$ s

propagation to the outer cylinder, in agreement with the linear stability theory [9]. The instability in a Newtonian liquid appears at $Ta_c = 47.4$ and the critical pattern is formed by stationary axisymmetric vortices of Taylor. The difference between the two thresholds and the nature of critical structures is associated with the elasticity of the solution. The elasticity of polymer solution may lead to the destabilization of the flow through a Hopf bifurcation leading to inertio-elastic waves. The shear-thinning also is destabilizing but it does not necessarily lead to oscillatory modes. In fact, the shear-thinning effect can be estimated by the ratio of the polymer viscosity to the solution viscosity $S = \eta_p/\eta$. Linear stability analysis for Oldroyd B model (i.e., for solution with constant viscosity) shows that the threshold decreases with increasing S and for shear-thinning solution, the threshold decreases with the increase of shear-thinning index. The working solution with $c = 1200$ ppm is semi-dilute as the critical concentration is $c^* \simeq 180$ ppm. In the same flow geometry, but for dilute solution, i.e., with $c \ll c^*$, the critical state occurs in form of stationary vortices (Taylor vortices) and the secondary modes are wavy vortices [15].

We note that the spatiotemporal diagrams of the radial velocity component are very similar to those obtained by the visualization with the Kalliroscope flakes. This confirms the result obtained in the comparison of PIV data and the visualization patterns from Kalliroscope aqueous suspension in the Newtonian Couette–Taylor flow [24].

The fundamental frequency of the pattern in units of the effective time of viscous diffusion is $f_c \times \tau_\nu = 1.19$, roughly in agreement with the predictions of Larson et al. [7], the regime seems more inertial than elastic. radial waves, but toward the inner cylinder, were observed by Groisman and Steinberg [11] using high molecular weight polyacrylamide dissolved in 58% solution of saccharose in water in a Couette–Taylor cell with radius ratio $\mu = 0.829$. The spatial period, for example, in the axial direction of a regime with radial propagation observed by Groisman and Steinberg [11], was much smaller than the characteristic size of the gap size. Moreover, the wave regime reported in [11] contained many sinks and sources, whereas the wave regime observed in the present experiment is very regular. The disordered inertio-elastic waves with walls have been observed in the experiment of Baumert and Muller [14] in non-shear-thinning dilute polymer solutions (polyisobutylene/polybutene) in a Taylor–Couette system with radius ratio $\mu = 0.827$, where the walls were called *flame patterns* because of their resemblance with the combustion flames.

6 Conclusion

The present chapter was concerned with the experimental study of the instability modes observed in viscoelastic Couette–Taylor flow with a shear-thinning semi-dilute high molecular weight polymer aqueous solution. Flow visualization was made by either adding 2% Kalliroscope aqueous suspension or by Particle Image Velocimetry (PIV). Space-time diagrams for different radial positions have allowed following the flow dynamics in the radial and axial directions. The critical modes are ribbons, which are superposition of equal amplitude right- and left- traveling waves. These critical modes propagate in the radial direction toward the outer cylinder. The secondary instability is characterized by domains of disordered waves separated by fluctuating in time and in space walls, which are characterized by strong radial inflow.

Acknowledgements During this work, we have benefited from the theoretical enlightening discussions with A. B. Ezersky who has introduced the modeling of the harmonic interaction within the coupled complex Ginzburg-Landau equation. The present work was partially supported by the Normandie Regional Council under the projects THETE and BIOENGINE (CPER-FEDER).

References

1. A. Gyr & H-W. Bewersdorff, *Drag reduction of Turbulent flows by Additives*, Vol. 32 Fluid Mechanics and its Applications (Kluwer Academic, New York, 1995).
2. R.B. Bird, R.C. Armstrong & O. Hassaguer, *Dynamics of Polymer Liquids*, Vol 1 & 2, (Wiley, New York, 1987).
3. B. A. Toms, Some observations on the flow of linear polymer solutions through straight tubes at large Reynolds numbers. *Proceedings of the 1st International Congress on Rheology*, Vol. 2, pp. 135–141. (North-Holland 1948).
4. R.F. Ginn & M.M. Denn, Rotational stability in viscoelastic liquids: Theory, *AIChE J*. **15**, 450 (1969).
5. M.M. Denn & J.J. Roisman, Rotational stability and measurement of normal stress functions in dilute polymer solutions, *AIChE J*. **15**, 454 (1969).
6. G.S. Beavers & D.D. Joseph, Tall Taylor cells in polyacrylamide solutions, *Phys. Fluids* **17**, 650 (1974).
7. R.G. Larson, E.S. G. Shaqfeh & S.J. Muller, A purely elastic instability in Taylor-Couette flow, *J. Fluid Mech*. **218**, 573 (1990).
8. R.G. Larson, Instabilities in viscoelastic flows, *Rheol. Acta* **31**, 213 (1992).
9. Y. Bai, "Study of the viscoelastic instability in Taylor-Couette system as an analog of the magnetorotational instability", Ph.D. thesis, Université du Havre (2015).
10. C.D. Andereck, S.S. Liu & H.L. Swinney, Flow regimes in a circular Couette system with independently rotating cylinders. *J. Fluid Mech*. **164**, 155 (1986). See also R. Tagg, The Couette–Taylor problem, *Nonlinear Sci. Today* **4,** 1 (1994).
11. A. Groisman & V. Steinberg, Elastic turbulence in a polymer solution flow, *Nature*, **405**, 53–55 (2000).
12. A. Groisman & V. Steinberg, Mechanism of elastic instability in Couette flow of polymer solutions: experiment, *Phys. Fluids* **10** (10), 2451–2463 (1998).
13. A. Groisman & V. Steinberg, Couette-Taylor flow in a dilute polymer solution, *Phys. Rev. Lett*. **77** (8), 1480–1483 (1996).
14. B. M. Baumert & S. J. Muller, Axisymmetric and non-axisymetric elastic and inertio-elastic instabilities in Taylor-Couette flow, *J. Non-Newt. Fluid Mech.* **83**, 33–69 (1999).
15. O. Crumeyrolle, I. Mutabazi & M. Grisel, Experimental study of inertioelastic Couette-Taylor instability modes in dilute and semidilute polymer solutions, *Phys. Fluids* **14** (5), 1681–1688 (2002).
16. N. Latrache, N. Abcha, O. Crumeyrolle, I. Mutabazi, Defect-mediated turbulence in ribbons of viscoelastic Taylor-Couette flow*, Phys. Rev. E* **93**, 043126 (2016).
17. O. Crumeyrolle, N. Latrache, I. Mutabazi, A.B. Ezersky, Instabilities with shear-thinning polymer solutions in the Couette-Taylor system, *J.Phys. Conf. Ser.* **14**, 78 (2005).
18. N. Latrache, O. Crumeyrolle, N. Abcha, and I. Mutabazi, Destabilization of inertio-elastic mode via spatiotemporal intermittency in a Couette-Taylor viscoelastic flow, *J. Phys. Conf. Ser*. **137**, 012022 (2008).
19. N. Latrache, O. Crumeyrolle, I. Mutabazi, Transition to turbulence in a flow of a shear-thinning viscoelastic solution in a Taylor-Couette cell*, Phys. Rev. E* **86**, 056305 (2012).
20. P. Matisse, M. Gorman, Neutrally buoyant anisotropic particles for flow visualization, *Phys. Fluids* **27**, 759 (1984).
21. M. A. Dominguez-Lerma, G. Ahlers, D.S. Cannell, Effects of Kalliroscope flow visualization particles on rotating Couette–Taylor flow, *Phys. Fluids* **28**, 1204 (1985).
22. S.T. Wereley, R.M. Lueptow, Spatio-temporal character of nonwavy and wavy Taylor–Couette flow, *J. Fluid Mech*. **364**, 59 (1998).
23. P. Chossat & G. Iooss, The Couette-Taylor problem, Springer-Verlag, New York (1994).

24. N. Abcha, N. Latrache, F. Dumouchel, I. Mutabazi, Qualitative relation between reflected light intensity by Kalliroscope flakes and velocity field in the Couette-Taylor flow system *Exp. Fluids* **45**, 85 (2008).
25. I. Mutabazi, N. Abcha, O. Crumeyrolle, and A. Ezersky, Application of the particle image velocimetry to the Couette-Taylor flow, in *The PIV Characteristics, Limits and Possible Applications*, edited by G. Cavazzini (InTech, Rijeka, 2012), Chap. 7, pp. 177–202.
26. P. Bot, I. Mutabazi, Dynamics of spatio-temporal defects in the Taylor-Dean system*, Eur. Phys. J. B* **13**, 141 (2000).
27. P. Bot, O. Cadot, I. Mutabazi, Secondary instability mode of a roll pattern and transition to spatiotemporal chaos in the Taylor-Dean system, *Phys. Rev. E* **58**, 3089 (1998).

The Heated Bénard–Kármán Street: A Review of the Effective Reynolds Number Concept

Pierre Paranthoën and Jean-Claude Lecordier

Abstract This chapter focuses on the wake flow behind a heated circular cylinder in the laminar vortex shedding regime where the Bénard–Kármán street appears. This flow is of fundamental importance both from the viewpoint of the hydrodynamic stability theory and engineering applications. Even in absence of buoyancy forces, this wake flow is more complicated than in the isothermal case due to temperature differences generated within the fluid leading to variations of its physical properties. In this situation, experiments showed that heat is never a passive contaminant. Due to the respective thermal dependence of the kinematic viscosity, heating the cylinder stabilizes the flow in air while it destabilizes the flow in water. This phenomenon led to the definition of an effective Reynolds number that is associated to an effective temperature. Value of the effective temperature is shown to depend on the nature of the fluid. In air, global and local flow similarities between wake flows of the same "effective" Reynolds numbers are pointed out, underlying the physical significance of this concept.

1 Introduction

Since the early works of Bénard [1] and von Karmàn [2], the regular pattern of the vortex street behind circular cylinders at low Reynolds numbers ($30 < Re = U_\infty d/\nu < 180$) has always attracted considerable attention of researchers because of its theoretical interest as well as practical importance. Here, U_∞ is the velocity of the oncoming flow, d is the diameter of the cylinder and ν is the kinematic viscosity of the fluid. From a theoretical point of view, flows over a bluff body represents an important class of problems within the domain of fluid mechanics, which involves different

---

P. Paranthoën (✉) · J.-C. Lecordier
Laboratoire de Thermodynamique CNRS UMR 6614 – CORIA, Université de Rouen Site Universitaire du Madrillet, 675, Avenue de L'Université, BP 12, 76801 Cedex Saint Etienne du Rouvray, France
e-mail: pierre.paranthoen@laposte.net

J.-C. Lecordier
e-mail: jclecordier@orange.fr

N. Abcha et al. (eds.), *Nonlinear Waves and Pattern Dynamics*,
https://doi.org/10.1007/978-3-319-78193-8_12

phenomena such as wake characteristics, vortex shedding, drag, and lift coefficients. A large number of theoretical investigations have been developed in terms of the concepts of absolute and convective instabilities. The inception of wake instability has been described in the framework of the Stuart-Landau model [3, 4]. This problem has also been significantly studied as the circular cylinder is the most widely used shape in various engineering applications making appearances in aeronautical, chemical, civil, electrical, nuclear, offshore, and wind engineering [5]. A very large number of results concerning vortex shedding have already been discussed in the literature and several reviews for the wake of a cylinder are available, [6–8].

Most of the authors agree that over the laminar state of flow, there is a transition from a 2D steady to a 2D periodic wake at $Re_c = 45$ and a 3D transition at a Reynolds number Re_c between 150 and 210. Over the 2D laminar vortex regime, a universal $St - Re$ number relationship is found when parallel and oblique shedding is considered, Hammache and Gharib [9]. Here, $St = fd/U_\infty$ is the Strouhal number, where f is the frequency of eddy shedding.

The majority of researches concerning this flow has been mainly devoted to the case, where the cylinder and the oncoming flow are at the same temperature. In comparison, the case of heat input on the cylinder wake has received little attention. This situation is also of great importance as it is also related to a large class of engineering applications like hot-wire anemometry, cooling of electronic equipment, combustion devices, heat exchangers and chemical reactors, etc.

The wake behavior downstream a heated cylinder is generally more complicated. Depending on the value of the ratio between buoyancy and inertial forces, characterized by the Richardson number $Ri = Gr/Re^2$, the heat transfer can be controlled by forced convection, mixed convection or free convection. Here, $Gr = g\beta(T_w - T_\infty)d^3/\nu^2$ is the Grashof number, g is the acceleration of gravity, β is the coefficient of thermal expansion, T_w and T_∞ are the temperatures of the heated cylinder and the free stream, respectively. When mixed or free convection is present, the influence of heating also depends on orientation of the flow direction with respect to the direction of gravity. The case of a horizontal heated cylinder embedded in an incoming flow directed either horizontally or vertically—upward or downward—involves various phenomena [10–17].

To limit the scope of the material, the primary focus of this chapter is restrained to the study of the heated cylinder in the forced convection regime, i.e., when the Richardson number $Ri \ll 1$.

For a horizontal heated cylinder with a horizontal oncoming flow, even in absence of buoyancy effects, the wake is already complicated. Due to the presence of heat transfer, the fluid temperature varies, which causes variations of its physical properties as density ϱ, kinematic viscosity, ν, and thermal diffusivity a. The choice of a reference temperature for the kinematic viscosity of fluid ν in order to calculate the reference Reynolds number for describing the flow regime is a crucial issue for studying the flow around a heated cylinder. It is important to point out that, 30 years ago, it did not exist any consistent analysis to select this reference temperature. Therefore, it was not possible to determine the value of the Reynolds number of a heated cylinder over the laminar regime and to anticipate on the steady or periodic nature of the flow regime around and downstream the cylinder.

Most of the previous studies concerning the horizontal heated cylinder exposed to a horizontal air cross-flow rather were focused on the determination of semiempirical correlations to characterize the forced convective heat transfer. From these approaches, a large number of $Nu - Re$ relationships have been proposed in the literature, Mc Adams (1954) [18–24].

The Nusselt number Nu is defined as $Nu = hd/\lambda$, where h is the mean heat transfer coefficient over the whole cylinder surface and λ is the thermal conductivity of the fluid. Some of these relations are also function of the Prandtl number $Pr = \nu/a$ and can be used for fluids other than air. In these relations, the Reynolds number is dependent on the temperature through the temperature dependence of the kinematic viscosity $\nu = \mu/\rho$. Depending on the authors, various reference temperatures were selected. Fluid properties were calculated either at the film temperature, defined as $T_{film} = (T_w + T_\infty)/2$ [20–24], or the dynamic viscosity μ at the film temperature and the density ρ at the free stream temperature, Mc Adams [19].

In addition to the value of the mean heat transfer coefficient, local heat transfer coefficient around the circumference of the cylinder was measured by Eckert and Soehngen [25]. On the other hand, information concerning the velocity and temperature fields in the forced regime over this low Reynolds numbers range was scarce. One of the main reason for this situation was linked to the experimental difficulties of performing accurate velocity and temperature measurements at low velocities in a wake of small dimensions.

In this context, extensive experiments on the laminar wake of a heated cylinder have been carried out since 1988 at Rouen and Nizhny Novgorod in order to improve the knowledge of this flow. Initially, these researches were conducted in an independent way until some cooperation has been developed between the two laboratories via the support of CNRS. These experiments have used a wide variety of specific measurements techniques including visualization, hot-wire, cold wire, LDA, PIV, acoustic scattering. The first researches on this subject have shown that the structure of the wake downstream a heated cylinder was very sensitive to the heat input. It was found that even in absence of buoyancy effects, heat was never a passive contaminant [26, 27].

In order to get a better knowledge of the phenomenon, further researches have been led to identify and quantify the conditions controlling the flow regime in the wake of a heated cylinder, namely:

- How the heat input modifies the transition from a 2D periodic to a 2D steady wake or vice versa?
- How the vortex shedding frequency varies with the heat input?
- Is it possible to find out an effective Reynolds number and an effective temperature for characterizing the flow regime?
- These are some of the questions discussed in the chapter.

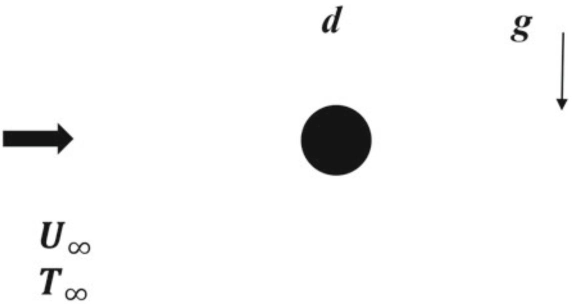

Fig. 1 Schematic of horizontal flow arrangement around a heated cylinder with wall temperature T_w higher than the free stream temperature T_∞

This chapter is organized as follows. After a brief description of the onset of vortex street in isothermal conditions, the history of the effective Reynolds number and effective temperature concepts is presented in Sect. 2. The experimental determination of the effective temperature is discussed in Sect. 3. The physical reality of the effective temperature is examined in Sect. 4 in relation to similarities of the flow dynamic and heat transfer at the same effective Reynolds numbers. Some limitations of this approach are discussed in Sect. 5.

2 The Isothermal Bénard–Kárman Vortex Street

In the case of a horizontal unheated cylinder exposed to a horizontal cross-flow, as presented in Fig. 1, the description of the flow is commonly characterized by the Reynolds number *Re*:

$$Re = U_\infty d/\nu_0 \tag{1}$$

For unheated cylinders, the onset of the vortex shedding appears at a Reynolds number Re_{c0} defined by:

$$Re_{c0} = U_c d/\nu_0 \tag{2}$$

where U_c is the critical velocity.

As shown in Table 1, the critical Reynolds number Re_{c0} of a cylinder determined in isothermal conditions ranges from 40 to 49. For Reynolds numbers $Re > Re_{c0}$, the wake becomes unstable which generates the vortex shedding phenomenon in which vortices are shed alternately at each side of the cylinder at a given frequency f. A cross-sectional view of the vortex shedding illustrates in Fig. 2 the development of the Bénard–Kárman street.

For a ribbon, the critical Reynolds number was found to be $Re_{c0} = 32$, LeMasson [32]. The Strouhal number $St = fd/U_\infty$ is commonly used to characterize the vortex shedding. For the isothermal case, the $St - Re$ relations given by Roshko [34]

Table 1 Values of the critical Reynolds number for unheated cylinder

Authors	Re_{c0}
Collis and Williams [24]	44
Fey et al. [28]	47
Godard et al. [29]	45
Hamma [27]	45.5
Kovasznay [30]	40
Lange et al. [31]	45.9
Le Masson [32]	43.3
Wang et al. [33]	46.1
Williamson [8]	49

Fig. 2 Flow visualization of the vortex street behind a ribbon located in a water flow

$$St = A - B/Re \quad \text{with}\, A = 0.212 \,\text{and}\, B = 4.452 \tag{3}$$

or Williamson and Brown [35]:

$$St = A' - B'/\sqrt{Re} \quad \text{with}\, A' = 0.2665 \,\text{and}\, B' = 1.0175 \tag{4}$$

are often used.

3 The Heated Bénard–Kárman Vortex Street

In the case of a horizontal heated cylinder exposed to a horizontal cross-flow, the description of the flow is commonly characterized by the Reynolds number *Re* and the overheat ratio η defined from the cylinder temperature T_w and the free stream temperature T_∞ by:

$$\eta = \Delta T_w / T_\infty, \tag{5}$$

where:

$$\Delta T_w = (T_w - T_\infty) \tag{6}$$

When the cylinder is heated, temperature differences generated within the fluid lead to variations of its physical properties: viscosity ν, density ρ, thermal diffusivity a. The temperature variations also modify the value of the Prandtl number $Pr = \nu/a$, which controls the relative thickness of the *momentum* and thermal layers.

3.1 Background and History of the Effective Reynolds Number Concept

An extensive review of the literature revealed that previous experimentalists had already mentioned that cylinder heating stabilizes the wake flow. It would appear that this result was first mentioned by Freymuth, Berger (private communication). The same result was also briefly cited in the report of the IUTAM symposium on concentrated vortex motions in fluids [36]. In this symposium, Uberoi presented some experimental results on the formation and properties of the vortex wake behind a heated circular cylinder. He found that with increasing cylinder temperature, the critical Reynolds number for the cylinder itself increases and the Strouhal number of the periodic vortex shedding decreases.

The same interest concerning the periodic or steady character of the near-heated wake was found in experiments of dispersion of heat in turbulent flows [37–41]. In these experiments, heat was injected in turbulent flow by means of a fine wire heated by direct current. The initial instantaneous wake was supposed to be a steady laminar wake in relation to the increase of the kinematic viscosity. However, for the authors, the precise value of the effective temperature to be used for the physical properties of fluid was no clear. It is worth to note, as for the $Nu - Re$ relationships, the authors rather used the wire temperature T_w [26], Crum and Hanratty (1970), or the film temperature T_{film} [32, 34, 28] to identify an effective kinematic viscosity in order to calculate an effective Reynolds number.

The previous examples show that while, in air, the phenomenon of stabilization of the wake owing to a heat input was already well-known, there was no clear answer to the question of how to determine the effective Reynolds number of a heated cylinder. In order to clarify this issue, detailed and controlled experimental studies of the thermal wake of a horizontal heated cylinder have been carried out at Rouen [27, 42, 43].

By using fine cold wire, authors measured the wake temperature downstream a horizontal heated wire (d = 0.254 mm). In air, with a constant free stream velocity, the experiments showed that the heat input P/l could significantly alter characteristics of vortex shedding. Total suppression could be achieved by increasing the power per unit length P/l sufficiently. An example of suppression of vortex shedding is presented in Fig. 3. Measurements of temperature fluctuations in the near heated wake showed that $I_\theta = \left(\overline{\theta'^2}\right)^{1/2} / \overline{\Delta\theta}$ the intensity of temperature fluctuations, canceled when P/l reaches a critical value. The minimum heat input needed to suppress the vortex shedding increases when $(Re - Re_{c0})$ increased. The influence of heating on the

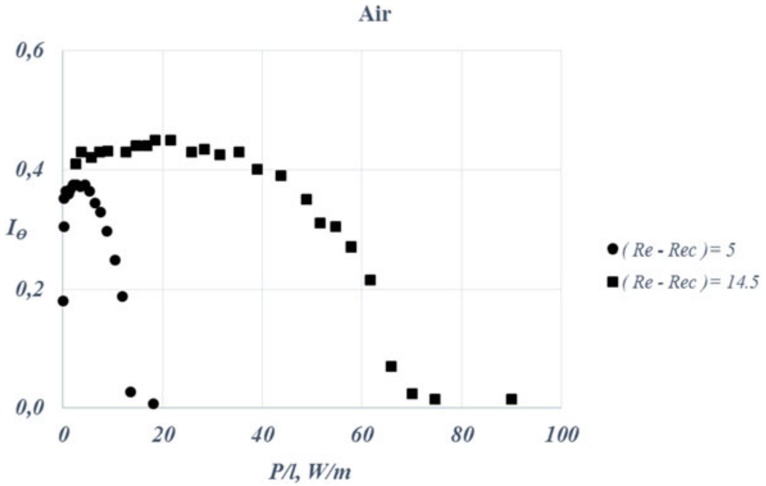

Fig. 3 The effect of heating on the intensity of temperature fluctuations measured in the heated wake of the cylinder showing the suppression of vortex shedding in air [27]

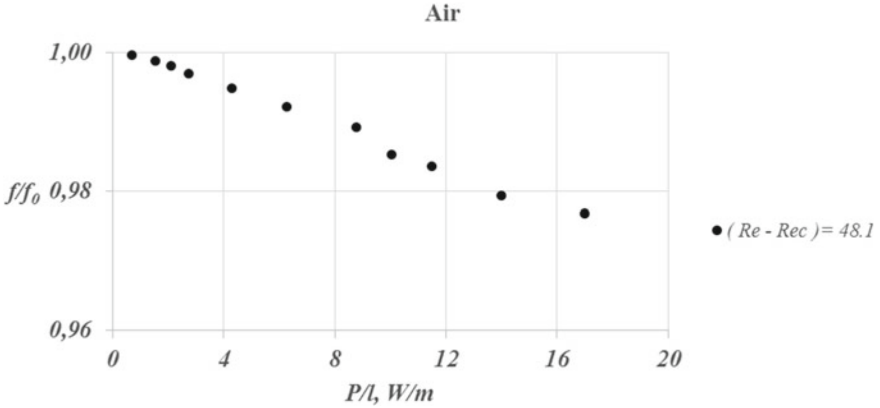

Fig. 4 The effect of heating on the vortex shedding frequency f for the cylinder in air, f_0 is the frequency measured in isothermal conditions [27]

frequency f of vortex shedding in air appears in Fig. 4, where f/f_0 has been plotted as a function of P/l. Here, f_0 is the frequency of vortex shedding in the absence of heating. Cylinder heating caused a decrease in frequency similar to that observed when the free velocity decreased in an unheated flow.

At the same time, similar experiments performed at Nizhny Novgorod by Ezersky [26] led to the same results. By using vertical heated wires (d = 0.1–0.8 mm), hot-wire measurements indicated that an increase in the temperature of a streamlined cylinder provided a decrease in shedding frequency and eventually led to suppression of periodic shedding of vortices. The characteristics of temperature fluctuations observed for increasing cylinder temperature and the characteristics of velocity fluctuations observed in the wake of a decreasing flow velocity were similar for moderate heating.

For both experiments, this stabilizing effect was attributed to the increase in kinematic air viscosity ν and the apparent decrease of the Reynolds number. Further analysis of this phenomenon showed a broad similarity of the near-wake flows in isothermal and non-isothermal conditions. This led the authors to the definition of an effective Reynolds number Re_{eff} associated with an effective temperature T_{eff} [27, 42]. The effective Reynolds number was proposed on the basis of a similarity hypothesis that the onset of vortex shedding occurs at the same value of the critical effective Reynolds number for all heated and unheated cylinders. At the transition, the critical Reynolds numbers Re_{c0} and $Re_{c,eff}$ were the same for both unheated and heated cases:

$$Re_{c0} = Re_{c,eff} \tag{7}$$

$$U_c d/\nu_0 = U d/\nu_{eff}, \tag{8}$$

where $\nu_{eff} = \nu\left(T_{eff}\right)$ is the effective viscosity. By knowing the temperature dependence of the air kinematic viscosity ν, it was then possible to deduce the effective temperature T_{eff}. The determination of this effective temperature T_{eff} is presented in Sect. 3.2 for various experiments.

Another possible explanation for this thermal effect was also proposed by Lecordier et al. [42], suggesting that the control could result of a slight change of the location of the separation point due to the increase of the dynamic viscosity of the fluid. However, additional experiments realized with a heated ribbon showed the same result, in a situation, where the separation point of the bluff body is fixed, [44].

At the same time, a different interpretation of this phenomenon was given by Yu and Monkewitz [45]. These authors linked the suppression of vortex shedding, through heat addition to the near wake, to the reduction of absolute instability due to the decrease of the density in the near wake. In their stability analysis, using similar profiles for velocity and temperature, calculations for constant or temperature-dependent viscosity did not lead to significant differences. These authors concluded that "the change in the stability characteristics brought about by heating the cylinder was the result of a subtly modified interaction between the two mixing layers via the inertial terms and not a viscous effect". For a heated circular cylinder [4] showed suppression of vortex shedding up to twice the critical Reynolds number based on free stream temperature. Following the analysis of Yu and Monkewitz [45], they related this control to ratio of average density in the recirculation region to free stream density. These authors had to point out that in their experiment, buoyancy effects could be considerable.

In the presence of these two plausible interpretations related to the predominant role either of kinematic viscosity or density, new experiments were carried out at Rouen in water with heated cylinder and ribbon. This choice was related to the

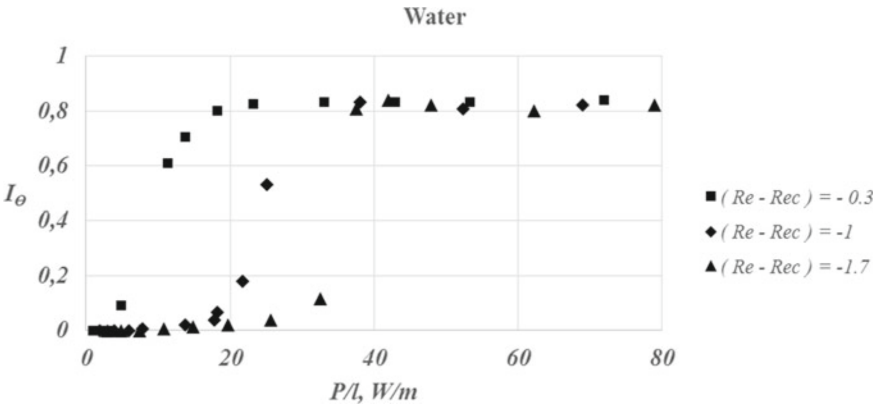

Fig. 5 The effect of heating on the intensity of temperature fluctuations measured in the heated wake of the ribbon, showing the onset of vortex shedding in water [32]

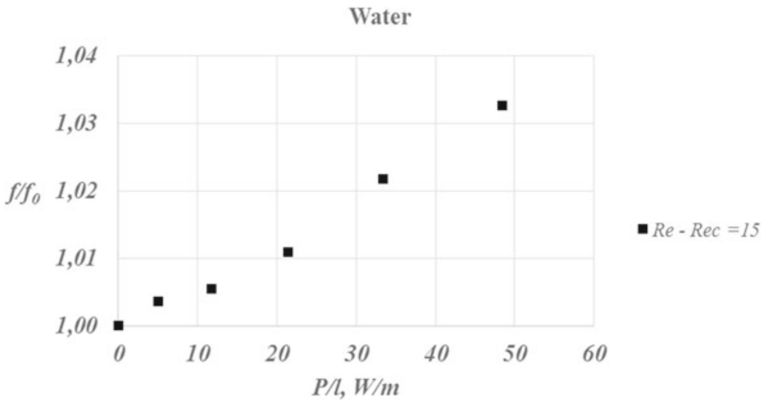

Fig. 6 The effect of heating on the vortex shedding frequency f for the cylinder in water. f0 is the frequency measured in isothermal conditions, [32]

opposite dependence of kinematic viscosity with temperature for water and air. As shown in Fig. 5, in water the reverse tendency was observed indicating that the heating of the cylinder destabilizes the flow. The minimum heat input needed to generate the vortex shedding increased when $(Re_c - Re)$ increases. In parallel, as shown in Fig. 6, the cylinder heating increased the frequency of vortex shedding, [32, 34, 28, 29–31, 33, 35]. This dominant viscous effect supported by the opposite behavior observed for air and water was confirmed numerically by Socolescu et al. [46].

Since then, a large amount of experimental and numerical investigations has closely confirmed the influence of these thermal effects on the wake flow behind a heated circular cylinder operating in the forced convection regime. For the case of air, Yahagi [47] studied experimentally the heated wake behind a cylinder at a very high overheat ratio $\eta = 3.66$. He observed a decrease of the vortex shedding frequency when cylinder temperature increased, indicating that the local kinematic viscosity plays a key role in the vortex structure. As a result, the vortex frequency of the heated cylinder could be expressed as a function of the Strouhal and Reynolds numbers, when the local kinematic viscosity was reasonably estimated by taking into account the effect of the cylinder heating.

Wang and his collaborators have brought a large body of information concerning the determination of the effective temperature in air [33, 48, 49, 50] (see Sect. 3.2). Their results were concerned also with the validity of the $St - Re_{eff}$ relationship [33]. Other studies focused on the heat transfer and showed that a representative temperature could also be used to describe the heat transfer correlation as well [51]. More recently, consistently with the known effect of flow stabilization by cylinder heating, they showed that cylinder cooling destabilizes the wake flow in air [52]. Sabanca and Durst [53], were the first to obtain numerically the decrease of the wake frequency with heating in absence of free convection effects. Shi et al. [54] investigated numerically the influence of the overheat ratio on characteristic quantities of the 2D horizontal flow past a heated cylinder. They showed the strong stabilizing effect on the flow due to the increase in the kinetic viscosity of air. The Strouhal number St at various overheat ratios could be satisfactorily correlated by the effective Reynolds number based on the effective temperature given by Wang et al. [33]. Baranyi et al. [55] investigated experimentally and numerically the effect of heat transfer on the flow around a heated cylinder. Results for heated and unheated cylinders in terms of $St - Re$ relationships agreed reasonably well with Williamson [8] results providing the use of an effective temperature depending on the overheat ratio. For the case of water, Vit et al. [56] confirmed experimentally that cylinder heating in water increases the frequency. They showed that the concept of effective temperature, originally suggested for heated cylinders in air, can be also used for heated cylinders in water. Pech [57] studied numerically the impacts of heating for flow of water and air. Computations showed that the Strouhal number decreases with temperature increase in the case of air and increases in case of water. The separation angle also showed some dependence on temperature ratios.

3.2 *Experimental Determination of the Effective Temperature*

As mentioned above, the concepts of effective Reynolds number and effective temperature were introduced on the assumption that onset of vortex shedding is the same for both heated and unheated cases, i.e., $Re_{c0} = Re_{c,eff} = Ud/\nu_{eff}$.

Here, the effective viscosity $\nu_{eff} = \nu(T_{eff})$ is used to account for the thermal effect. The effective temperature T_{eff} is related to the cylinder temperature T_w by the following relation:

$$T_{eff} = T_\infty + c\,(T_w - T_\infty)\,, \tag{9}$$

where $0 \le c \le 1$ is a constant. The ratio of viscosities is then given by:

$$\nu_{eff}/\nu_0 = \left(T_{eff}/T_\infty\right)^{1,777} = (1 + c\,\eta)^{1,777}\,, \tag{10}$$

where the power-law exponent of the dynamic viscosity of air is given by [58]. However, various methods have been used to determine experimentally the effective temperature.

Determination of the effective temperature at the transition

The more simple method consists of deducing T_{eff} at the transition from the definition of $Re_{c,eff}$:

$$U_c d/\nu_0 = U d/\nu_{eff} \tag{11}$$

where U_c is the critical velocity determined without heating and U is the critical velocity with the heated cylinder. From (11) the ratio ν_{eff}/ν_0 is calculated and the relative effective temperature T_{eff}/T_∞ can be deduced from (12):

$$T_{eff}/T_\infty = (U/U_c)^{0.563} \tag{12}$$

and the value c from the relation (9). Using this method, the experiments carried out by Hamma [27] and Lecordier et al. [42] with a 0.254 mm diameter heated wire led to c-values: 0.275 and 0.3. Dumouchel et al. [59, 60] with a 1 mm diameter tube found c-values: 0.27 and 0.24. Wang et al. [33] showed that their experimental results with $c = 0.28$ satisfies the concept of constant critical Reynolds number for the temperature ratio T_w/T_∞ up to 2.

The value of the effective temperature T_{eff} can be also determined at the transition in an instationnary situation. When the heating is sufficient to stabilize the wake, it is possible to observe, on the temperature signal $T_s(t)$ measured in the wake, the apparition of vortices after the electric power is put off at $t = 0$, as shown in Fig. 7. The decrease in the cylinder temperature $T_w(t)$ is controlled with the thermal inertia of the heated cylinder and involves the decrease in the wake temperature $T_s(t)$. When the vortices appear at $t = t_{app}$ the effective temperature can be deduced from the measurement of $T_s(t_{app.})$. With this method, Hamma [27] found a value $c = 0.275$.

Determination of the effective temperature from a universal $St - Re_{eff}$ relationship

When the heat input is not sufficient to suppress the vortex shedding, it is then possible to determine the effective temperature from frequency measurements. Assuming that the effective Reynolds concept is also valid for the $St - Re_{eff}$, the effective temperature can be deduced from the best fit found between the $St - Re_{eff}$ curve and the St–Re relation of the isothermal case. This method of determination of T_{eff} was used by Vit et al. [56] due to experimental difficulties to detect the critical Reynolds in their experiment in water. Using the St–Re relation given by Williamson and Brown [35], the best fitting of all $St - Re$ data onto one $St - Re_{eff}$ curve was obtained for $c = 0.97$.

Other authors have also deduced the effective temperature assuming the validity of the $St - Re_{eff}$ relationship at some particular values. By measuring the same frequency f both downstream an unheated cylinder and a heated cylinder, Lecordier et al. [42]

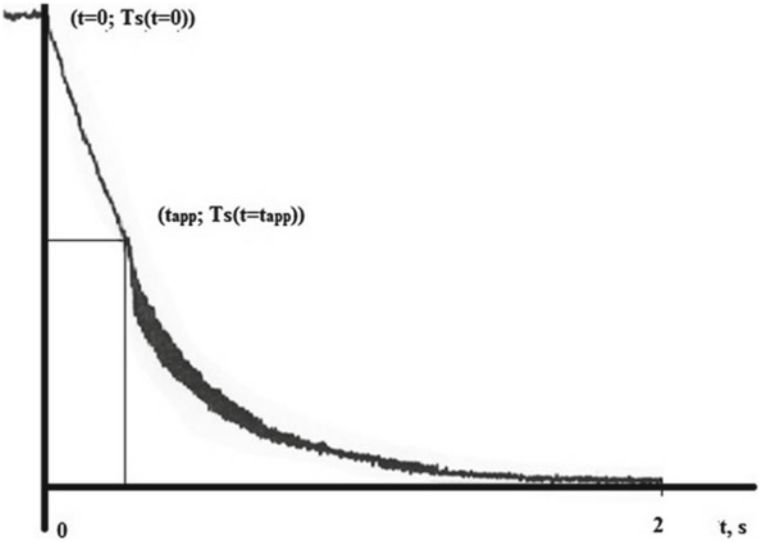

Fig. 7 Temperature signal measured in the heated wake. After suppression of the heating at t = 0, the onset of vortex shedding occurs at t = t_{app} [27]

determined two values of Strouhal numbers $St_0 = fd/U_0$ and $St_{eff} = fd/U$. Using the relation of Roshko [24] with A = 0.212, they deduced the ratio ν_{eff}/ν_0:

$$\nu_{eff}/\nu_0 = (U/U_0)((1 - St_{eff}/A)/(1 - St_0/A)) \tag{13}$$

The relative effective temperature T_{eff}/T_∞ deduced from this relation gave $c = 0.30$. Ezersky [26] used a similar approach by considering at constant velocity U, the variation of the Strouhal number St with the overheat ratio η. By using the relation of Roshko [34],

$$St = fd/U = A - B/Re_{eff} \tag{14}$$

$$St = A - B\nu_g(T_{eff})/Ud \tag{15}$$

$$\partial St/\partial\eta = -(B/Ud)\partial\nu_g(1 + c\eta)/\partial\eta \tag{16}$$

$$\partial St/\partial\eta = -1.777(Bc/Re_0)(1 + c\eta)^{0.777} \tag{17}$$

With B=4.494, experiments carried out with 0.1 mm and 0.8 mm diameter heated wires led to c-values: 0.23 and 0.255.

The values of c are listed in Table 2. If we exclude the value given by Baranyi et al. [55], it appears that the mean value of c is about 0.275, very close to the c-value 0.28 determined by Wang et al. [33] and commonly accepted for the effective temperature in air. The higher value proposed by Baranyi et al. [56] could be due to the fact that

Table 2 Experimental values of *c* for the heated cylinder in air and water

Authors	Fluid	Cylinder	l/d	η	c
Hamma [27]	Air	d = 0.254 mm wire	590	$0 < \eta < 1.17$	0.3 0.275
Ezersky [26]	Air	d = 0.1 mm d = 0.3 mm d = 0.8 mm wires	3000 1000 375	$0 < \eta < 0.75$	0.255 0.255 0.23
Lecordier et al. [42]	Air	d = 0.254 mm wire	590	$0 < \eta < 1.17$	0.3
Dumouchel et al. [59, 60]	Air	d = 1 mm tube	150	$0 < \eta < 1.2$ $0 < \eta < 0.5$	0.275 0.24
Wang et al. [33]	Air	d = 1.07 mm tube	93.5	$0 < \eta < 1$	0.28
Vit et al. [56]	Water	d = 4.5 mm tube	45.3	$0 < \eta < 0.0096$	0.97
Baranyi et al. [55]	Air	d = 10 mm tube	60	$0 < \eta < 1.3$	0.5–0.55

their experiments were related to the transitional regimes in modes A and B, instead of to the laminar regime as mentioned by Trávníček and Wang [61]. In water, the *c*-value is 0.97 in relation with the higher value of the Prandtl number in water.

Fedorchenko et al. [49] have shown that assuming small $c\Delta T_w^*$ values, the *c*-value for any dilute gas is related to an exponent *n* of the kinematic viscosity–temperature power law by a simple formula $c = 1/2n$. They deduced a linear increase of the critical Reynolds number in the heated case given by the relation:

$$Re_c = Re_{c0} T_{film}^* \tag{18}$$

and arrived at the important conclusion that the effective Reynolds number can be determined for any dilute gas without knowing the particular *c*-value. Here, $\Delta T_w^* = \Delta T_w / T_\infty$ and $T_{film}^* = T_{film} / T_\infty$.

However, when higher values of $c\Delta T_w^*$ are considered, the effective Reynolds number is given by the nonlinear expression:

$$Re_c = Re_{c0}(1 + 2c\Delta T_{film}^*)^{1.777} \tag{19}$$

Figure 8 shows Re_c/Re_{c0}—T_{film}^* dependence for air according to relations (18) and (19). The solid line is the linear prediction given by relation (18) [48]. Dashed lines are the prediction given by using relation (19) for the *c*-values 0.24 and 0.3. The points are experimental data of Wang et al. [33], Hamma [27], Dumouchel et al. [59]. For air, whatever the selected c-value, the linear assumption seems sufficient for overheat ratio lower than 0.4. For higher overheat ratio, the nonlinear character appears and depends on the selected *c*-value.

It is worth to note that in water the linear assumption would be only valid for overheat ratio lower than 0.03. This could complete the issue raised by Fedorchenko et al. [49].

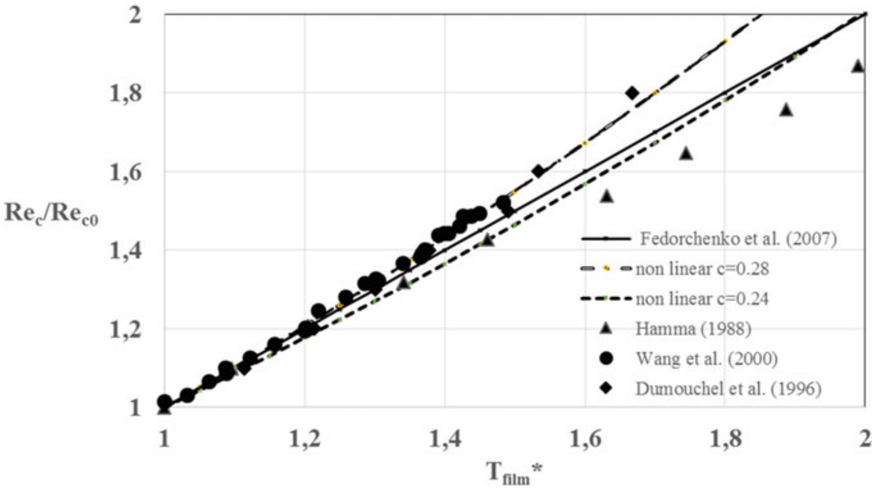

Fig. 8 Variation of Re_c/Re_{c0} with T^*_{film}

3.3 *Interpretation of the Effective Temperature*

It is worth to note that the effective temperature T_{eff} is much lower than the film temperature T_{film} generally used to take into account the influence of temperature on fluid properties on $Nu - Re$ relationships. As mentioned by Dumouchel et al. [60], in air the effective temperature T_{eff} is close to the temperature of the recirculation zone and is not just an artificial value. Temperature measurements obtained at Rouen, in air and water, in the near wake for both heated cylinder and ribbon are shown in Fig. 9, [27, 60, 62]. The values of $\Delta T_{max}/\Delta T_w$ have been plotted as a function of x/d. In air, the relative maximum temperature in the near wake is between 0.2 and 0.3, the range of values found in c. Temperatures measured at $x/d = 1.25$ by Yahagi [47] are also presented. They are very close to the $\Delta T_{eff}/\Delta T_w$ values calculated by Wang et al. [33] for this experiment. In water, the values of $\Delta T_{max}/\Delta T_w$ in the near wake are higher than in air. They reach 0.5–0.6 at $x/d = 1$ and are consistent with the rather high value of $c = 0.97$ measured by Vit et al. (2006). A comparison of the results obtained for heat transfer, in air and water, require to account for the values of Prandtl number Pr. The Prandtl number of air and water, at the free stream temperature, are about 0.7 and 7. Experimental and numerical studies have shown that just behind the heated cylinder the velocity fields, in air, oil, and water, at the same effective Reynolds number are similar [44, 63]. Conversely, the corresponding thermal fields are very different. In air, a relatively thick thermal layer near the cylinder transforms into a thinnest layer in oil. In the near wake of a heated cylinder in oil, the isotherms show a small temperature protuberance in the vicinity of the separation point [63]. This situation can also explain the strong double-peaked character of the temperature profiles observed in the near wake in water, Lecordier et al. [62].

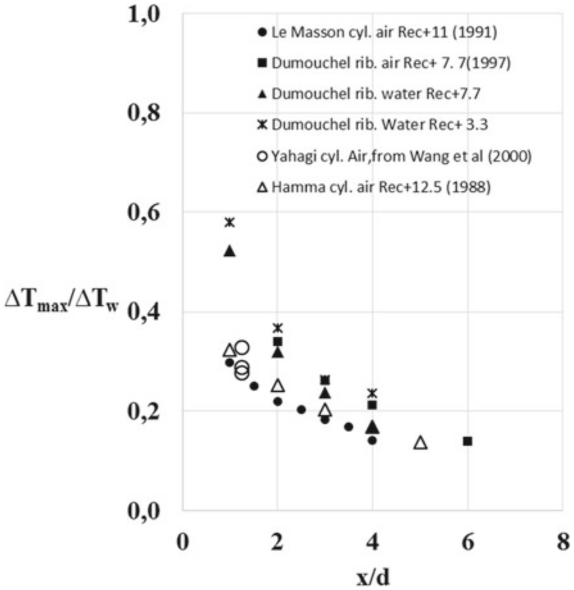

Fig. 9 Variation of $\Delta T_{max}/\Delta T_w$ in the near wake of heated cylinder and ribbon

In air, recent numerical simulation of Xin et al. [64] showed that heating different places of cylinder surface results in different control effects. The stabilization effect was found stronger for heating on the leeward side. This can be related to the results of Strykowski and Sreenivasan [65], Paranthoën and Lecordier [66], where the use of a heated secondary cylinder located just at the end of the recirculation zone allows to suppress the vortex shedding phenomenon. In this case, for the same value of $(Re - Re_{c0})$, the power per unit length needed to suppress the vortices was about one hundred times lower in this second situation.

3.4 Similarities of the Heated Wake in Relation to Re_{eff}

Concerning the dynamics of the flow, some similarities were found with the effective Reynolds number concept for the global quantities such as Strouhal number St.

Wang et al. [33] found experimentally that their experimental data of the parallel vortex shedding (PVS) mode fell on a "universal" $St - Re_{eff}$ curve over a wide range of overheat ratio. This result was confirmed numerically by Shi et al. [54]. Wu et al. [67] showed that similar trend also can be found for the vortex shedding frequency of Oblique Vortex Shedding (OVS) mode. Moreover, the onsets of OVS that results in discontinuities in the $St{-}Re_{eff}$ relationships were found at about the same effective Reynolds number for both isothermal and non-isothermal cases.

In accordance with the similarity of this global quantity St with Re_{eff}, Shi et al. [54] indicated the existence of a local similarity in the dimensionless viscous force over the cylinder surface for flows with the same effective Reynolds number. This local similarity was also observed in the rear portion of the cylinder for the dimensionless pressure force. Moreover, the results indicated that the same effective Reynolds number also characterizes the velocity field in the proximity of the cylinder and in the near-wake region with good accuracy.

Extensive measurements of velocity carried out downstream of a heated circular cylinder or ribbon have shown the influence of heat input on the velocity field in the near wake [44]. In presence of the heating in air, the heated mean longitudinal velocity profiles were slightly wider than the isothermal profiles. This behavior was also characterized in each section by a decrease of the centerline mean longitudinal velocity and of the RMS values of the transverse velocities in comparison with the isothermal case. By considering the effective Reynolds number Re_{eff}, some characteristics of the heated or unheated wake were found in close agreement. For example, for the same values of Re_{eff}, the length of the wake bubble $s*$, the evolutions of the normalized RMS transverse velocity σ_v^* were found similar in both isothermal and non-isothermal cases. Furthermore, detailed comparison of experimental results showed that, in similar effective Reynolds numbers conditions, the interaction between the two shear layers at the end of the recirculation zone was roughly the same. Following the analysis of Abernathy and Kronauer, Gerrard [68, 69], this interaction could be calculated, at the end of the recirculation zone, as the ratio I between the rate of circulation in the shear layer and the shear layer spacing Δ [44, 70].

$$I = \left| \frac{d\Gamma}{dt} \right| / \Delta = \frac{(\partial U / \partial y)_{max}}{\Delta} \delta \mathrm{U}(\Delta/2)$$

In this term, δ is the shear layer thickness.

For better comparison between experiments with the cylinder and the ribbon in air and in water I was normalized by using the frequency of vortex shedding f_{Re_c} and the velocity $\mathrm{U}(\Delta/2)_{Re_c}$ determined at the critical Reynolds number:

$$I^* = \frac{(\partial U / \partial y)_{max} \delta \mathrm{U}(\Delta/2)}{\Delta} \frac{1}{f_{Re_c} \mathrm{U}(\Delta/2) \mathrm{U}(\Delta/2)_{Re_c}}$$

In Fig. 10, this normalized interaction term $I*$ has been plotted as a function of $(Re_{eff} - Re_c)$. As shown in this figure, the results obtained from cylinder and ribbon experiments in air and water agree reasonably well. Vortex shedding is present when the normalized interaction term $I*$ is larger than a threshold value of about 5.5–6. In air, in presence of heating, the value of $I*$ decreases with increasing heating and suppression of vortices could occur when this threshold value is reached. In water, the opposite trend was observed.

The same unanimity for the choice of T_{eff} was not observed for the global heat transfer aspect characterized by the Nusselt number Nu. Shi et al. [54] found that the calculated values of Nu were well correlated with the relation of Collis and Williams (1956) when the fluid properties were evaluated at the film temperature T_{film}. The tem-

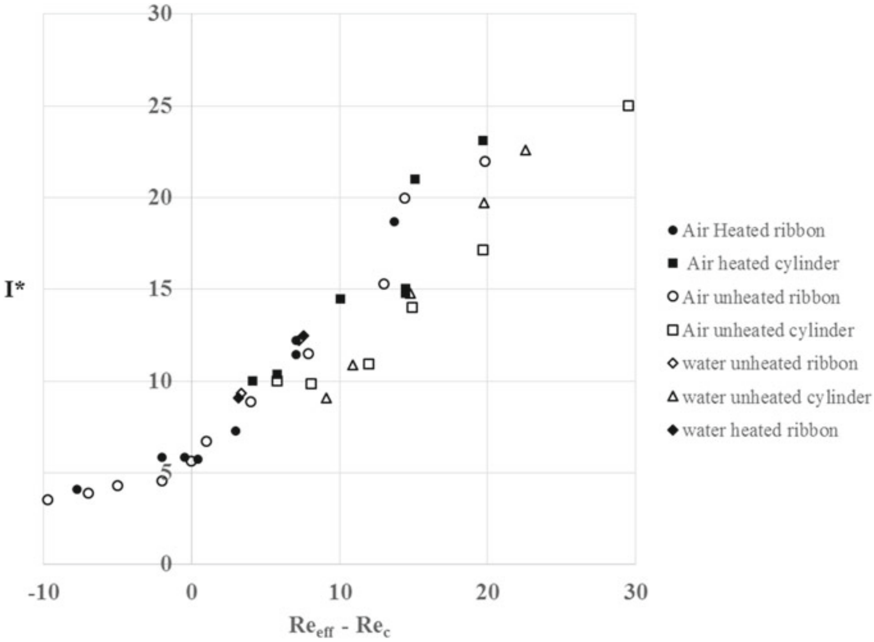

Fig. 10 Variation of the normalized interaction term for heated and unheated cylinders and ribbons versus $(Re_{eff} - Re_c)$, [32, 71]

perature loading factor $(T_{film}/T_\infty)^{-0.17}$ was needed to take into account the variation of the overheat ratio. Dumouchel et al. [60] showed that it was possible to plot Nu as a continuous function of either $(Re_{film})^{0,45}$ or $(Re_{eff})^{0,45}$ under the condition to use a temperature loading factor $(T_{film}/T_\infty)^{-0.25}$, close to the value of Collis and Williams [24], or $(T_{eff}/T_\infty)^{0.28}$, respectively. They noted that the change of slope of the heat transfer curve appeared more clearly in the $Nu\ (T_{eff}/T_\infty)^{0.28}$—$Re_{eff}$ formulation as Re_{eff} characterize the regime of the wake. Wang and Trávníček [51] proposed a different correlation method based on the "representative" Reynolds number deduced from "representative temperature" defined as $T_{rep} = T_\infty + 0.36(T_w - T_\infty)$. By introducing this "representative" Reynolds number Re_{rep} linear correlation equations were successfully derived.

Shi et al. [54] compared these different approaches by examining the local similarity of the Nusselt number. For steady conditions, they observed a better local similarity on the correlation concept of Collis and Williams [24]. For the unsteady regime, a local similarity was observed except for the rear part of the cylinder. These results suggested that the front part of the cylinder from the stagnation point up to the separation point could be only dependent on the thermal boundary layer around the cylinder characterized by Re_{film}. Conversely, the downstream part of the cylinder, from the separation point up to the rear stagnation point would depend on the wake by the influence of the recirculation zone and would be characterized by Re_{eff}. A similar analysis has been made by various authors [20, 23, 72] who proposed a correlation in the following form: $Nu = aRe_{film}^{0.5} + bRe_{film}^{0.67}$, where the first term represents the heat transfer through the laminar boundary layer on the front part of the cylinder and the second term, the heat transfer of the rear portion. This second term could depend on Re_{eff}.

4 Limits of the Effective Reynolds Number Approach

As shown in the previous examples, the effective Reynolds number concept allows to take into account the influence of the thermal effect on the heated wake. However, there seems to be some evidence that some phenomena appearing when the cylinder is strongly heated cannot be only reduced to renormalization of the Reynolds number, even in the absence of buoyancy forces. When the effective Reynolds number approach works, the spectral characteristics of temperature fluctuations observed for increasing cylinder temperature and the characteristics of velocity fluctuations observed in the wake of a decreasing flow velocity have to be similar. However, some experiments [73–76] showed that such similarity only exists for a range of heating power. Over a definite range of P/l values, spectra of temperature fluctuations or acoustic wave scattering became essentially nonsymmetrical relative to the maximal values, whereas at higher and lower heating, power spectra had the same symmetrical shape for all Reynolds numbers. Signal amplitude $A(t)$ and phase $\phi(t)$, extracted from the time series of temperature fluctuations using Hilbert transformation, showed that for the regime of nonsymmetrical power spectrum, a sequence of defects occurred in the time series of temperature fluctuations. For a such defect, the amplitude dropped down to zero and the phase decreased by about 2π and one period was lost in such an impulse, which explains the nonsymmetrical spectra [74]. The visualizations of the heated wake for $Re = 89$, showed that these defects existed over the range $2.02 \leq T_w^* \leq 2.6$ [76]. Outside this range, no defects were formed either at small or at large heating power. For large heating, the wake was stabilized as $Re_{eff} < Re_c$. It is worth to note that, in isothermal conditions, similar defects have already been observed for the Reynolds numbers range $160 < Re < 230$ [77]. This kind of defects may also be excited artificially, at smaller Reynolds numbers ($Re = 140$) by creating on the cylinder a zone of larger diameter, Williamson [8]. These defects caused by heating arising at lower Reynolds numbers might result from the instability described by [78]. They showed that for a single vortex, flexible modes are excited when a large enough difference existed between the core and periphery densities. For a strongly heated cylinder, the motion of temperature stratified and, hence, density stratified vortices could become important and differ from the motion of a homogeneous fluid, even in the absence of buoyancy forces. The generation of these modes connected with the motion of a density stratified fluid under the action of centrifugal forces may change the wake dynamics fundamentally. It seems that there are no studies mentioning the existence of the defects arising in the street at certain heating intensities.

5 Conclusion

This chapter is concerned with a review of the heated Bénard–Kármán street in relation to the effective Reynolds number concept. From the literature, it is clear that this laminar flow regime is strongly dependent on the level of heating and, even in absence of buoyancy effects, heat is never a passive contaminant. The results obtained in the pioneer works of [26, 42] have been fully confirmed. In air, the frequency of vortex shedding is found to decrease with heating while the opposite trend is observed in water. This is due to the increase in the kinematic viscosity of air and the decrease in the kinematic viscosity of water with increasing overheat ratio. This phenomenon has led to the definition of an effective Reynolds number Re_{eff} that is associated to an effective temperature $T_{eff} = T_\infty + c(T_w - T_\infty)$. This concept assumes that the critical Reynolds numbers in isothermal and no isothermal situations is the same. In relation to the respective values of Prandtl number Pr, c-values of 0.28 for air and 0.97 for water have been found. The values of the corresponding effective temperature were found close to the near-wake temperature.

The underlying physics of the concept of effective temperature was revealed with the similarities of global (Strouhal number, drag coefficient, etc.) or local (dimensionless viscous force on the cylinder surface, dimensionless pressure force in the rear portion of the cylinder surface, etc.) flow characteristics found with the same Re_{eff}. Concerning the Nusselt number, in air, there is no consensus on the choice of the temperature selected for use in the $Nu - Re$ relationships. The film temperature T_{film} or the representative temperature T_{rep} are both used by authors to characterize fluid properties for the steady and the periodic wake regimes. It is worth noting that at least for the rear part of the heated cylinder, the correlation ought to take into account the effective temperature linked to the flow regime.

However, when the cylinder is strongly heated, there exists some range of heating power within which defects are able to grow in a vortex street against the background of a periodic structure. In this case, the phenomena cannot be only reduced to renormalization of the Reynolds number.

Over the past three decades, many advances have been made in the understanding of the wake downstream a heated cylinder in the periodic laminar regime. Nevertheless, the complexity of this flow should continue to motivate the development of further numerical simulations and experimental works. These studies could help resolve some of the problems associated with small scales in the heated turbulent flows. Up to now, these researches have especially concerned the case of air flows and, to a lesser extent, the case of water flows. They could be extended to fluid flows at various Prandtl numbers.

Acknowledgements The authors would like to thank past collaborators on the subject of this chapter including Laurence Hamma, Stéphane LeMasson, Fabien Dumouchel, Franck Weiss and Gilles Godard. The authors gratefully acknowledge the assistance of the technical staff of CNRS UMR 6614. During these researches, owing to the support of CNRS, we have also had the privilege to work with Alexander Ezersky. We remember Alexander as a brilliant scientist both renowned theorist, skilled experimenter and a great man.

References

1. Bénard, H.: Formation de centres de giration à l'arrière d'un obstacle en mouvement. C. R. Acad. Sci. Paris, 147, 839–842 (1908)
2. Kármán, Th. von: Uber den Mechanismus der Widerstander den ein bewegter Korper in einer Flüsseigkeit afahrt. Gott. Nadir, 509–517 (1911)
3. Provansal, M., Mathis, C., Boyer, L.: Bénard-von Karman Instability: Transient and forced regimes. J. Fluid Mech., 182, 1–22 (1987)
4. Schumm, M., Berger, E., Monkewitz, P.A.: Self-excited oscillations in the wake of two-dimensional bluff bodies and their control. J. Fluid Mech., 271, 17–53 (1994)
5. Zdravkovich, M.M.: Flow around Circular Cylinders, Volume 2: Applications. Oxford University Press (2003)
6. Zdravkovich, M.M.: Flow around Circular Cylinders, Volume 1: Fundamentals. Oxford Science Publications, New York, USA (1997)
7. Berger, E., Wille, R.: Periodic Flow Phenomena. Annual Review of Fluid Mechanics, 4, 313–340 (1972)
8. Williamson, C.H.K.: Vortex dynamics in the cylinder wake. Ann. Rev. Fluid. Mech. 28, 477 (1996)
9. Hammache, M., Gharib, M.: An experimental study of the parallel and oblique vortex shedding from circular cylinders, J. Fluid Mech., 232, 567–590 (1991)
10. Badr, H.M.: Laminar combined convection from a horizontal cylinder-parallel and contra flow regimes. Int. J. Heat Mass Transfer, 27, 15–27 (1984)
11. Michaux-Leblond, N., Belorgey, M.: Near wake behaviour of a heated circular cylinder: viscosity–buoyancy duality. Exp. Therm. Fluid Sci. 15, 91–100 (1997)
12. Hu, H., Koochesfahani, M.: Thermal effects on the wake of a heated circular cylinder operating in mixed convection regime. J. Fluid Mech., 685, 235–270 (2011)
13. Singh, S.K., Panigrahi, P.K., Muralidhar, K.: Effect of buoyancy on the wakes of circular and square cylinders: a schlieren-interferometric study. Exp. Fluids, 43, 101–123 (2007)
14. Kieft, R.N., Rindt, C.C.M., Steenhoven, A.A. van: The wake behaviour behind a heated horizontal cylinder. Exp. Thermal Fluid Sci., 19, 183–193 (1999)
15. Kieft, R.N., Rindt, C.C.M., Steenhoven, A.A. van: Heat induced transition of a stable vortex street. Int. J. Heat Mass Transfer, 45, 2739–2753 (2002)
16. Kieft, R.N., Rindt, C.C.M., Steenhoven, A.A. van: Near-wake effects of a heat input on the vortex-shedding mechanism. Int. J. Heat Fluid Flow, 28, 938–947 (2007)
17. Steenhoven, A.A. van, Rindt, C.C.M.: Flow transition behind a heated cylinder. Int. J. Heat Fluid Flow, 24, 322–33 (2003)
18. King, L.V.: On the Convection of Heat from Small Cylinders in a Stream of Fluid: Determination of the Convection Constants of Small Platinum Wires with Applications to Hot-Wire Anemometry. Proc. Roy. Soc. London, 90, 563–570 (1914)
19. Mc Adams, W. : Heat transmission, Mc-Graw-Hill, NewYork (1954)
20. Hilpert, R.: Wärmeabgage von geheitzen Drähten und Rohren im Lufstrom. Forsch. Gebiete Ingenieurw, 4, 305–314 (1933
21. Churchill, S.W., Brier, J.C.: Convective heat transfer from a gas stream at high temperature to a circular cylinder normal to the flow. Chem. Eng. Progr. Symp. Series, 51, 57 (1955)
22. Kramers, H.: Heat transfer from spheres to flowing media. Physica, 12, 61–80 (1946)
23. Van Der Hegge Zijnen, B.G.: Heat transfer from horizontal cylinders to a turbulent air flow. Applied Scientific Research, Section A, 7, 2, 205–223 (1958)
24. Collis, D.C., Williams, M.J.: Two-dimensional convection from heated wires at low Reynolds numbers. J. Fluid Mech., 6, 3, 357–384 (1959)
25. Eckert, E.R.G., Soenghen, E.: Distribution of heat transfer coefficients around circular cylinder in cross flow at Reynolds numbers from 20 to 500. Trans. ASME J. Heat Transfer, 74, 343–347 (1952)
26. Ezersky, A.B.: Detached flow around a heated cylinder at small Mach number. Prikladnaya Mekhanika i Tekhn. Fizika, 5, 56 (1990)

27. Hamma, L.: Etude de la diffusion de la chaleur en aval d'un cylindre chauffé à faible nombre de Reynolds (40< Re< 160). Thèse Sc.Phys. Université de Rouen (1988)
28. Fey, U., König, M., Eckelmann, H.: A new Strouhal-Reynolds number relationship for the circular cylinder in the range 47< Re <2. 10^5. Phys. Fluids, 10, 1547–1549 (1998)
29. Godard, G., Weiss, F., Gonzalez, M., Paranthoën, P.: Heat transfer from a line source in the periodic laminar near wake of a circular cylinder. Experimental Thermal and Fluid Science, 29, 547–558 (2005)
30. Kovasznay, L.S.G.: Hot -wire investigation of the wake behind cylinders at low Reynolds numbers. Proc. Roy. Soc. A, 198, 174–190 (1949)
31. Lange, C.F., Durst, F., Breuer, M.: Momentum and heat transfer from cylinders in laminar crossflow at 10^{-4} < Re < 200. Int. J. Heat Mass Transfer, 41, 22, 3409–3430 (1998)
32. Le Masson, S.: Contrôle de l'instabilité de Bénard-Kármán en aval d'un obstacle chauffé à faible nombre de Reynolds. Thèse Sc. Phys., Université de Rouen (19Mc Adams, W.: Heat transmission, Mc-Graw-Hill, NewYork (1954)
33. Wang, A.B., Trávníček, Z., Chia, K.C.: On the relationship of effective Reynolds number and Strouhal number for the laminar vortex shedding of a heated circular cylinder. Phys. Fluids 12, 6, 1401–1410 (2000)
34. Roshko, A.: On the drag and shedding frequency of two-dimensional bluff bodies. NACA Technical Note 3169 (1954)
35. Williamson, C.H.K., Brown, G.L.: A series in $1/\sqrt{\mathrm{Re}}$ to represent the Strouhal–Reynolds number relationship of the cylinder wake. J. Fluids Struct. 12, 1073–1085 (1998)
36. Kücheman, D.: Report on the I.U.T.A.M. symposium on concentrated vortex motions. J. Fluid Mech. 21, 1, 1–20 (1965)
37. Crum, G.F., Hanratty, T.J.: Dissipation of a Sheet of Heated Air in a Turbulent Flow. Applied Scientific Research, A15, 177–195 (1966)
38. Uberoi, M., Corrsin, S.: Diffusion of heat in isotropic turbulence. NACA Report 1142 (1953)
39. Shlien, D.J., Corrsin, S.: Dispersion measurements in a turbulent boundary layer. Int. J. Heat Mass Transfer, 19, 285–295 (1976)
40. Stapountzis, H., Sawford, B.L., Hunt, J.C.R., Britter, R.E.: Structure of the temperature field downwind of a line source in grid turbulence. J. Fluid Mech., 165, 401–424 (1986)
41. Paranthoën, P., Fouari, A., Dupont, A., Lecordier, J-C.: Dispersion measurements in turbulent flows (boundary layer and plane jet). Int. J. Heat Mass Transfer 31, 1, 153–165 (1988)
42. Lecordier, J-C., Hamma, L., Paranthoën, P.: The control of vortex shedding behind heated cylinder at low Reynolds numbers. Exp. Fluids, 10, 224–229 (1991)
43. Lecordier, J-C., Hamma, L., Paranthoën, P.: The control of vortex shedding behind heated cylinder at low Reynolds numbers. Internal Report UA CNRS 230, Thermodynamics Laboratory, University of Rouen (1988)
44. Lecordier, J-C., Browne, L.W.B., Le Masson, S., Dumouchel, F., Paranthoën, P.: Control of vortex shedding by thermal effect at low Reynolds numbers. Experimental Thermal and Fluid Science, 21, 4, 227–237 (2000)
45. Yu, M.H., Monkewitz, P.A.: The Effect of Nonuniform Density on the Absolute Instability of Two-dimensional Intertial Jets and Wakes. Phys. Fluids A, 2, 1175–1181 (1990)
46. Socolescu, L., Mutabazi, I., Daube, O., Huberson, S.: Etude de l'instabilité du sillage bidimensionnel derrière un cylindre faiblement chauffé. C. R. Acad. Sci., Série IIb, 322, 203–208 (1996)
47. Yahagi, Y.: Structure of two dimensional vortex behind a highly heated cylinder. Trans. Japan Society of Mech. Engineers, Part B, 64, 622, 1825–1831 (1998)
48. Fedorchenko, A.I., Travníček, Z., Wang, A.B.: On the effective concept in the problem of laminar vortex shedding behind a heated cylinder. Phys. Fluids, 19, 5, 051701-1-051701-3 (2007)
49. Fedorchenko, A.I., Marsik, F., Travníček, Z.: On the effective temperature concept for liquid: Paradox of the similarity? Int. Comm. Heat Mass Transfer, 38, 852–854 (2011)
50. Wu, M.H., Wang, A.B.: On the transitional wake behind a heated circular cylinder. Phys. Fluids 19, 084102 (2007)

51. Wang, A.B., Trávníček, Z.: On the linear heat transfer correlation of a heated circular cylinder in laminar crossflow using a new representative temperature concept. Int. J. Heat Mass Transfer, 44, 4635–4647 (2001)
52. Travníček, Z., Wang, A.-B., Tu, W.Y.: Laminar vortex shedding behind a cooled circular cylinder. Exp. Fluids, 55, 1679 (2014)
53. Sabanca, M., Durst, F.: Flows past a tiny circular cylinder at high temperature ratios and slight compressible effects on vortex shedding. Phys. Fluids 15, 7, 1821–1829 (2003)
54. Shi, J.-M., Gerlach, D., Breuer, M., Biswas, G., Durst, F.: Heating effect on steady and unsteady horizontal laminar flow of air past a circular cylinder. Phys. Fluids, 16, 4331 (2004)
55. Baranyi, L., Szabó, S., Bolló, B.: Analysis of low Reynolds number flow around a heated circular cylinder. J. Mech. Sci. Technol., 23, 1829 (2009)
56. Vit, T., Ren, M., Trávníček, Z., Marsik, F., Rindt, C.C.M.: The influence of temperature gradient on the Strouhal-Reynolds number relationship for water and air. Exp. Thermal Fluid Sci., 31, 751–760 (2007)
57. Pech, J.: On computations of temperature dependent incompressible flows by high order methods. EPJ Web of Conferences 114, 02089 (2016)
58. Gebhart, B.: Heat conduction and mass diffusion. Mc Graw-Hill Inc., New York (1993)
59. Dumouchel, F., Paranthoën, P., Lecordier, J-C.: The effective Reynolds number of a heated cylinder. 2nd European Thermal Sciences Symposium, Rome, Italy (1996)
60. Dumouchel, F., Lecordier, J-C., Paranthoën, P.: The effective Reynolds number of a heated cylinder. Int. J. Heat Mass Transfer, 41, 12, 1787–1794 (1998)
61. Trávníček, Z., Wang, A.B.: On the effective temperature and Reynolds number concept for a heated circular cylinder: commentary of the article by Baranyi et al. (2009). Journal of Mechanical Science and Technology, 25, 8, 1881–1884 (2011)
62. Lecordier, J-C., Dumouchel, F., Paranthoën, P.: Heat transfer in a Bénard-Karman vortex street in air and in water. Int. J. Heat Mass Transfer, 42, 16, 3131–3136 (1999)
63. Isaev, S.A., Baranov, P.A., Zhukova, Y.V., Sudakov, A.G.: Enhancement of heat transfer in unsteady laminar oil flow past a heated cylinder at Re = 150. Thermophysics and Aerodynamics, 21, 5, 531–543 (2014)
64. Xin, X.F., Chen, C., Wang, B.F., Ma, D.J., Sun, D.J.: Local Heating Effect of Flow Past a Circular Cylinder. Chin. Phys. Lett. 27, 4, 044701–1- 044701-4 (2010)
65. Strykowski, P.J., Sreenivasan, K.R.: On the suppression of vortex shedding at low Reynolds numbers. J. Fluid Mech., 218, 71–107 (1990)
66. Paranthoën, P., Lecordier, J-C.: Control of the wake instability at low Reynolds numbers by thermal effect. Bluff-Body Wakes, Dynamics and Instabilities IUTAM Symposium, Göttingen, Germany, September 7–11 (1992)
67. Wu, M.H., Trávníček, Z., Wang, A.B.: The onset of oblique vortex shedding behind a heated circular cylinder in laminar wake regime,. Phys. Fluids, 24, 011701 (2012)
68. Abernathy, F.H., Kronauer, R.E.: The formation of vortex street. J. Fluid Mech., 13, 1–20 (1962)
69. Gerrard, J.H.: The mechanism of the formation region of vortices behind bluff bodies. J. Fluid Mech., 25, 401–413 (1966)
70. Paranthoën, P., Browne, L.W.B., Masson, S. L., Dumouchel, F., Lecordier, J-C.: Characteristics of the near wake of a cylinder at low Reynolds numbers, European J. Mech. B, 18, 4, 659–674 (1999)
71. Dumouchel, F. : Etude expérimentale des champs dynamiques et thermiques de l’écoulement de Bénard-Karman en aval d’un obstacle chauffé dans l’air et dans l’eau. Thèse Sc.Phys. Université de Rouen (1997)
72. Douglas, W.J.M., Churchill, S.W.: Recorrelation of Data for Convective Heat Transfer between Gases and single Cylinders with Large Temperature Differences. Chem. Engng. Prog. Symp. Series 52, 23–28 (1956)
73. Ezersky, A.B., Gharib, M., Hammache, M.: Spatio temporal structures of wake behind a heated cylinder. Prikladnaya Mekhanika i Tekhn. Fizika, 5, 74 (1994)

74. Ezersky, A.B., Paranthoën, P.: The Transition in a Wake Caused by Heating of a Streamlined Cylinder. Int. J. Trans. Phenomena, 7, 45–53 (2005)
75. Dumouchel, F., Paranthoën, P.: Etude expérimentale de la transition 2D-3D dans le sillage laminaire périodique d'un cylindre chauffé. Congrès Français de Thermique, SFT 2007, Ile des Embiez (2007)
76. Ezersky, A.B., Cherov, V., Gromov, P., Nazarovsky, A., Soustov, P., Paranthoën, P.:, Remote acoustic diagnostics of defects arising in a Kármán vortex street behind a heated cylinder. Fluid Dyn. Res., 43, 1 (2010)
77. Zhang, H.Q., Fey, U., Noack, B.R., König, M., Eckelmann, H.: On the transition of the cylinder wake. Phys. Fluids, 7, 4, 779–794 (1995)
78. Ezersky, A.B., Ermoshin, D.A.: The instability of density stratified vortices. Eur. J. Mech. B/Fluids, 14, 617 (1995)

Laboratory Modelling and Acoustic Diagnostics of Hydrodynamical Processes

Vladimir Chernov and Alexander Ezersky

Abstract In the present chapter, results of modelling of wind interaction with a water layer surface and research of the vortical structures arising downstream of the flow around bodies are described. Results using the method of acoustic diagnostics of spatially periodic vortical flows are presented. At physical modelling in laboratory conditions wind was created with a low-velocity wind tunnel. The structure of an air stream and convective cells on water surface was investigated with the help of visualization. Some pictures of structures on the shallow sea surface are also demonstrated and discussed.

1 Introduction

Study of interaction of wind with ocean surface is important for the understanding of heat exchange between the ocean and the atmosphere and for interpretation of radar and visual pictures of the ocean surface. The important role for this is played by the thin subsurface water layer.

A large amount of experimental observations of a near-surface layer in different water basins (including the ocean, seas and lakes) showed that in many cases the water surface is colder compared to the bulk [1]. The cooling of water surface due to evaporation gives rise to the formation of a thermal boundary layer having the scale of about one millimeter, which is frequently termed ‘a cold liquid film’ [1]. The inverse temperature distribution can give rise to the convective instability, which usually develops in the presence of a wind-driven flow. The convective instability

---

V. Chernov (✉)
Institute of Applied Physics, Russian Academy of Sciences
of the Nizhny Novgorod, Nizhny Novgorod, Russia
e-mail: vcher@appl.sci-nnov.ru

A. Ezersky
CNRS, M2C, Normandie Université, UNICAEN, UNIROUEN, 14000 Caen, France

N. Abcha et al. (eds.), *Nonlinear Waves and Pattern Dynamics*,
https://doi.org/10.1007/978-3-319-78193-8_13

is one of the possible causes of the Langmuir circulations in natural water basins, which are associated with roll-like vortex, structures elongated in the direction of the wind [2]. Besides, interaction of wind with sea surface produces vortices in the water and in the air. However, it is extremely difficult to study such processes in the ocean.

Numerical simulation of the roll convection caused by evaporation was performed mainly for the sea conditions (e.g., [2, 3]). In this work, the convective (Rayleigh–Bénard) instability in the liquid layer affected by evaporation and tangential wind stresses is studied from the viewpoint of the non-linear dynamics, i.e. attention is focused on the peculiarities of structure development. The laboratory experiment is performed with heated silicon oil and a well-evaporating liquid (alcohol) and a two-dimensional theoretical model corresponding to the experimental conditions is constructed.

Currently, laboratory remote acoustic diagnostics of vortical and temperature pulsations in air flows have been carried out for a number of well-studied flows: the Karman vortex street behind a round cylinder [4–6], vortex rings [7], vortices behind a heated body [8], buoyant thermic [9] and heated jet [10]. These experiments have established the parameters of hydrodynamic flows, which can be determined by the characteristics of scattered sound. The experimental concept was that data obtained for flows with controlled parameters were to be compared to a calculation carried out within the models described by a small number of parameters: vortex circulation, vortex motion velocity and quantity of heat transferred by vortices. The flows studied were actually laminar.

Laboratory acoustic diagnostics, making it possible to control all the parameters of flows, can be efficient in the simulation of acoustic sounding of the atmosphere and water reservoirs. However, to compare laboratory and field experimental data on acoustic diagnostics of the atmosphere [11], scattering at more complex flows is to be studied.

The laminar flow was accompanied by systematic vortex separations, as well as Karman streets behind cylinder. In the turbulent mode, the flow consists of a large number of randomly arranged vortices. Thus, for full research of a vortical Karman street behind the heated up cylinder, we have executed experiments on visualization and remote acoustic diagnostics of vortical current. Earlier, it was found that topological defects may arise in a wake behind a heated cylinder [12] as vortex merging that results in the loss of one spatial period. To control two-dimensional flows, a method of acoustic diagnostics was developed that allows one to detect topological defects in a periodic street by spectra of the scattered sound [13].

2 Modelling of Convective Processes

A rectangular, cavity filled with alcohol is allocated in the plate of organic glass. The plate is placed in the operating part of the low-turbulence wind tunnel. For the flow visualization, the light-reflecting powder is used. After impeller of the wind tunnel is switched on, the wind velocity V_0 reaches quickly (in the time less than 1 min) a steady value within 1.5–2.5 m/s range and a turbulent boundary layer is formed over the cavity. The measured thickness of the boundary layer is equal approximately to 2 cm.

The velocity of the wind-driven flow increased progressively to its steady value (which is about 2.5 cm/s). Top view of the flow structure in the cavity is presented in Fig. 1a. A sequence of visualization pictures arising with growing wind velocity is displayed in Fig. 1b–d. Figure 1b shows hexagon-like structures, which were observed without wind blowing. Figure 1c demonstrates the effects of enlargement of the hexagons and their elongation in the direction of the wind at fairly small wind velocity. When the wind velocity approaches its steady value, the system of black and white strips corresponding to the roll convection in the liquid layer appears on the surface (Fig. 1d).

Similar experiments were carried out with 0.4 cm silicon oil layer heated from below. In absence of wind above liquid surface (2$V = 0$) at excess of critical value of temperature difference convection arises. A picture of convective cells obtained for bottom temperature 50 °C is shown in Fig. . After turning on wind tunnel wind stress on silicon oil surface produces shear current in liquid that results in increase of the convective cell size and their drift in the direction of air stream ($V = 12$ cm/c). Thus, characteristic spatial period of cells increases in wind direction. Above the critical value of stream velocity, cellular convection is replaced by convective roll patterns whose axes are directed along the wind ($V = 160$ cm/c). At higher wind velocities, convective rolls contain numerous defects.

The similar phenomenon occurrence of roll structure was observed by Woodcock on water surface in narrow straits, bays and on a surface of long waves at the high-sea states [14]. We also observed similar structures on surface of the “Nizhny Novgorod sea” (a reservoir at Volga river). Corresponding picture is presented in Fig. 3. It was obtained in solar weather at 25 °C and at weak wind. Visualization of roll structure, in this case, became possible due to phytoplankton. Rolls are extended along wind direction, the spatial period of rolls is few centimeters. More detailed description of experiment and the theoretical analysis are given in [15, 16].

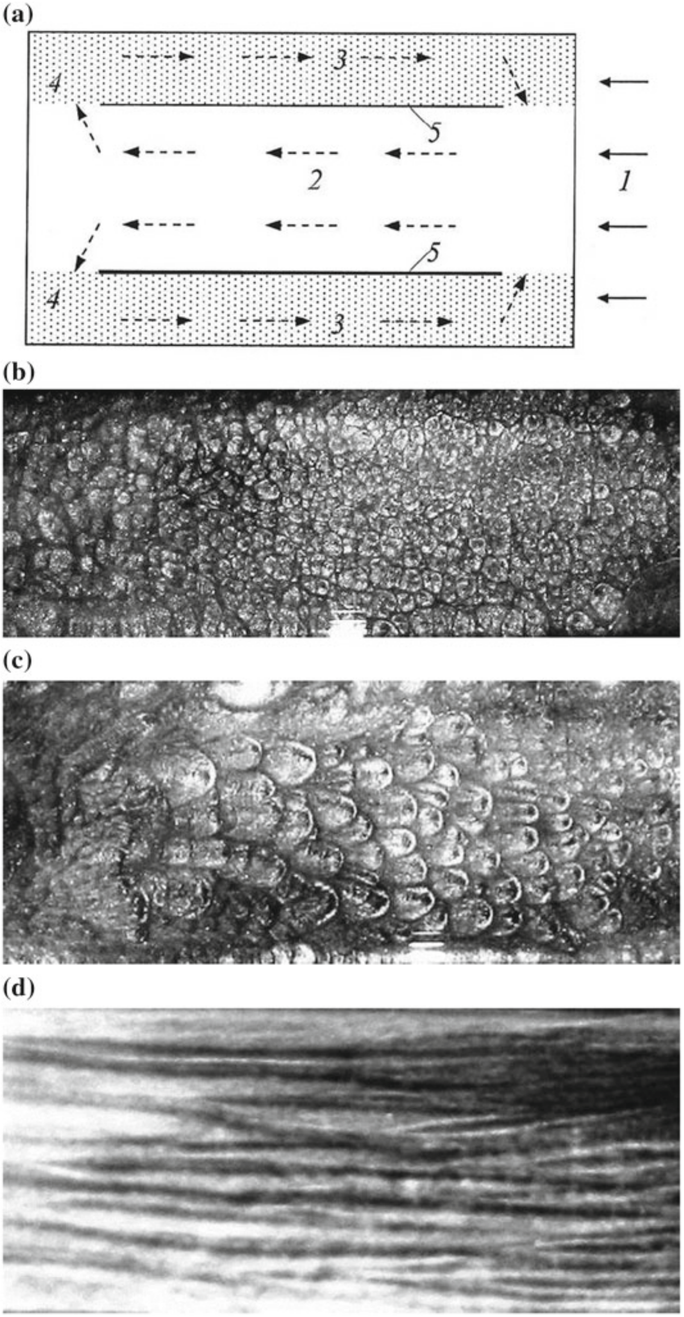
(a)
3
4
5
2
1
5
4
3
(b)
(c)
(d)

◂**Fig. 1** Sketch of the experimental setup **a** and images of the fluid surface for immovable air (**b**) immediately after starting of the wind blowing (**c**) and at the steady wind velocity V_o = 1.5 m/s (**d**). Designations in (**a**) are *1*-forward air flow, *2* (dashed arrows)—wind-driven fluid flow, *3* (dashed arrows)—counter fluid flow, *4* (shaded fields)—horizontal screens above the counter flow, *5*—vertical screens delimiting the accompanying and counterflows

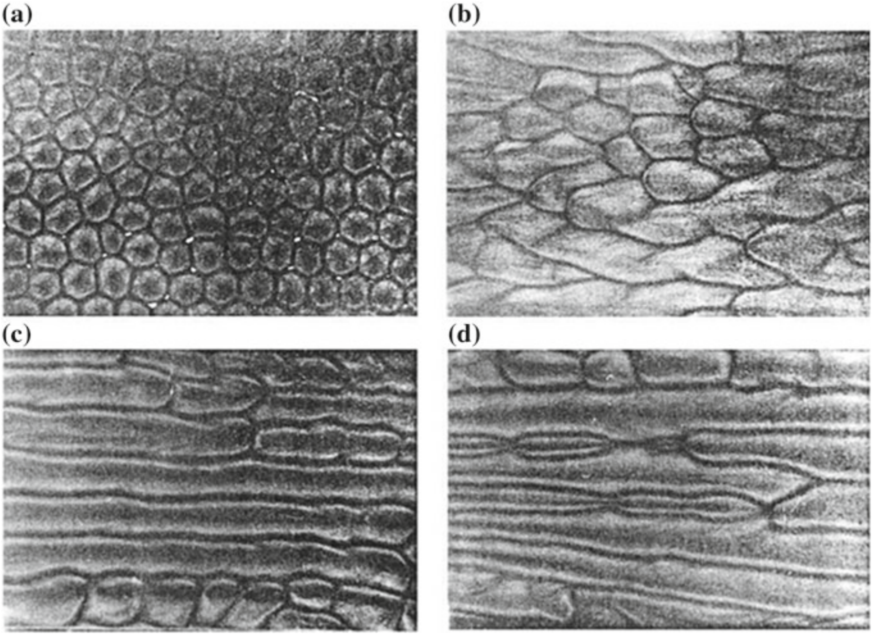

Fig. 2 Photo images of the silicon oil heated from below for immovable air (**a**), immediately after starting of the wind blowing (**b**, V = 12 cm/c) and at the steady wind velocity V_o = 160 cm/s (**c**), and 180 cm/c (**d**)

3 Acoustic Diagnostics of Vertical Structures

This part of the work is devoted to the study of vortical flows in air by means of the acoustic diagnostic method. The main attention is paid to investigation of vortical flows behind a heated cylinder—influence of heating on characteristics of vortical structure. The experimental setup is similar to that in [17]. The used cylinder is made of a nickel-chrome alloy wire of 0.6 mm diameter. It was heated from a source of the direct current. The temperature of the cylinder can be estimated from the known heat transfer expression established empirically for the round cylinders [18]: $Nu = 0.36\sqrt{\mathrm{Re}} + 0.057\sqrt[3]{\mathrm{Re}^2}$ and was equal $T_C - T_\infty = \Delta T = \frac{Q}{\pi.L.\lambda_0.Nu(Re)}$, where Q—quantity of heat in Joules generated in the cylinder by the direct electrical current, L—length of the cylinder, λ_0—heat conductivity of gas at temperature of the air stream. Reynolds number of an accumulating stream was $\mathrm{Re} = 81$, and Reynolds effective number changed in a range $35 < \mathrm{Re}_{eff} < 81$.

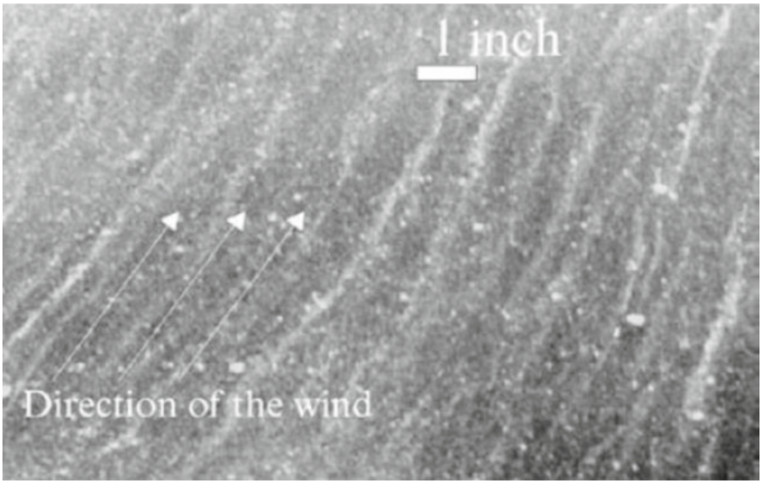

Fig. 3 The roll structure on the surface of the "Nizhny Novgorod sea"

A piezoceramic sound source was placed behind a screen with a square hole (2×2 cm). The source was placed 65 cm apart from the Karman's street center for the Fraunhofer approximation to be satisfied $D_F \approx \Lambda^2/\lambda = 30$ cm, where Λ is the source size. The radiator settled down under angle 40° to the normal to air flow.

The periodic vortical street was observed downstream behind the cylinder. To measure parameters of the received ultrasound we used a high-frequency 4135 B&K microphone. Signal was transferred into the frequency range 0–20 kHz by the heterodyning technique. The microphone was placed 1.6 m apart from the vortex street. Its position varied in the angular range from 45° to −45° with respect to the direction of the ultrasound source. The spectral characteristics of the scattered signal were measured using a computer.

Angular dependence of sound scattered by the vortex street (that is the moving periodic grid) represents a few number of angular maxima and minima, which correspond to spatial harmonics of scattered sound field. During experiments, we measured time spectra of the first spatial harmonic of scattered sound for several temperatures of the cylinder. Measurements were carried out as follows: for each temperature of the cylinder, first of all, it was found the angle of the first spatial harmonics (maximum of amplitude), and then the time spectrum of signal was registered and analyzed. Increase of the cylinder temperature resulted in the downshift of vortex frequency that was also observed in [19]. The obtained data are shown in Fig. 4. It is seen from the figure that in the definite range of temperatures of the cylinder, some asymmetry in the spectrum arises. Below and above this temperature range, spectra are symmetric. This asymmetry is similar to that was observed in [19] in a spectrum of pulsations of a field of temperature.

In experiments, we also used visualization of a vortical street at various temperatures of the cylinder. Visualization was carried out by means of a thin wire of 0.2 mm,

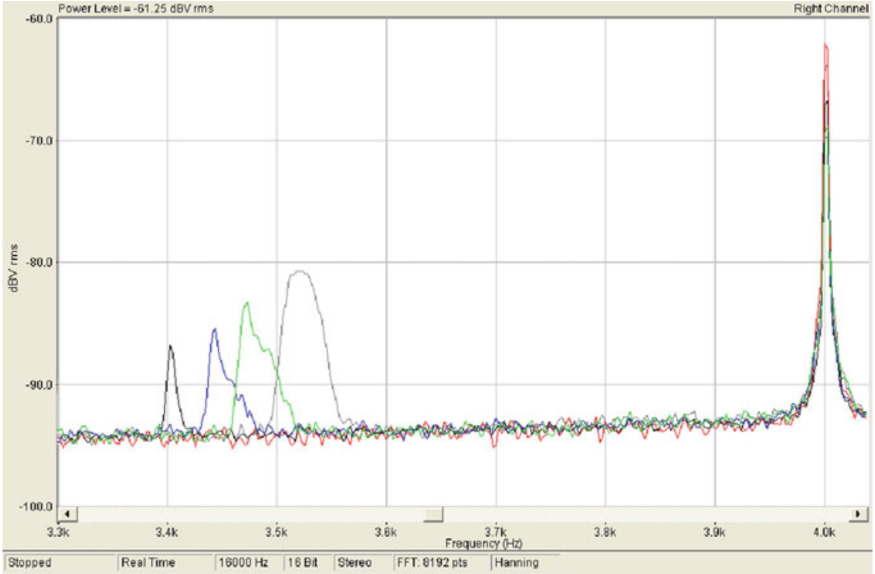

Stopped | Real Time | 16000 Hz | 16 Bit | Stereo | FFT: 8192 pts | Hanning

Fig. 4 Spectra of the scattered sound

which was stretched parallel to the basic cylinder at distance of ~ $9d$ downstream. The wire was covered by oil and electrical current through it was turned on. Smoke from the wire made it possible to visualize the vortical trace. Pictures were taken by means of a digital camera (Fig. 5). From Fig. 5 one can see defects in vortical street. In the photo, the basic cylinder and a visualizing wire are located on the right side, the air flow is directed from right to left and the distance from the cylinder to the left side of picture is $\sim 200d$. It is necessary to note that without heating axes of vortices have some vertical angle relatively the basic cylinder, while during heating axes of vortices are parallel to the axis of the basic cylinder. Thus, even small heating ($\Delta T = 155$ °C) resulted in 'ordering' a vortical street. For temperatures above $\Delta T = 308$ °C, large-scale defects can be observed. At $\Delta T = 434$ °C a number of defects such as « pulses of blackout » are observed up to the temperature $\Delta T = 480$ °C. Further increase in heating, results in ordered vortical street again with axes parallel to the cylinder. At the maximal heating, $\Delta T = 665$ °C a vortical street is not observed anymore, since $\mathrm{Re}_{eff} < \mathrm{Re}_c$ (where Re_c—Reynolds critical number at which there is a periodic vortex street). In this case, there are only low-frequency pulsations caused, apparently, by the convective instability of the heated air. Defects in vortical street are responsible for asymmetry of spectra in Fig. 4.

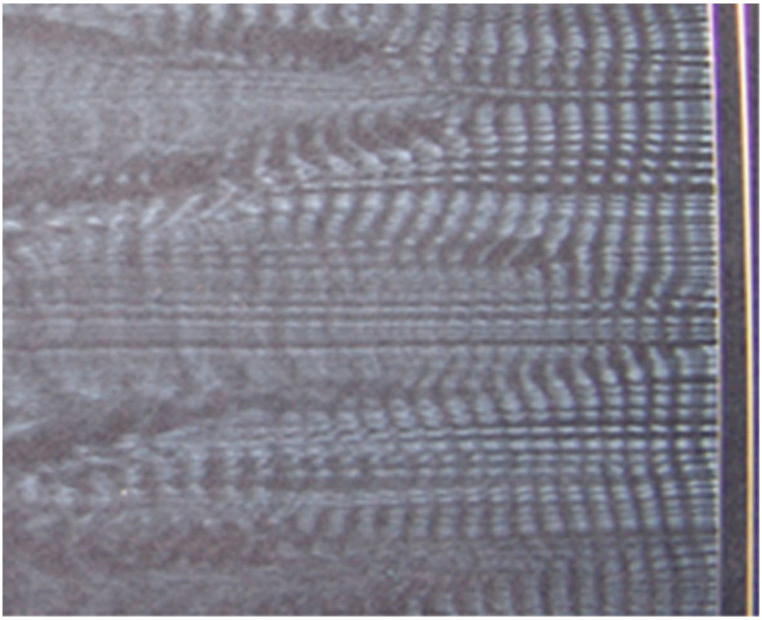

Fig. 5 Visualization of a vortical trace

4 Conclusion

The method of physical modelling was used in the given work for research of features of thermoconvection in the upper sea layer. Thermoconvection is caused by cooling of a thin water film under action of wind. Wind stress, in turn, results in formation of roll structure convective flows against well-known cellular structure of the convection in absence of wind.

The method of acoustic diagnostics of hydrodynamic vortex flow was demonstrated for the vortical structure generated in an air flow behind heated cylinder. Experiments have for the first time shown that in a vortical street behind the heated cylinder at not too big supercriticality ($\mathrm{Re}_{\mathit{eff}} \sim 45 \div 55$) and temperatures of heating of the cylinder (300°–480 °C) there are defects such as ≪ pulses of blackout ≫. The visualization of vortex flow at the specified parameters has allowed to confirm the existence of these defects, which are related to the density stratification of the vortex flow. Detailed theoretical description of this phenomenon is to be done.

Thus, the method of acoustic diagnostics can be effectively used for investigation of flow structures in gas and liquids.

References

1. G.N. Panin. The heat-mass transfer between the basin and atmosphere under natural conditions. Nauka-press, Moskow, (1985) (in Russian).
2. O.V. Emel'anova, A.E. Ordanovich. Vestnik Moskovskogo Universiteta, Ser. 1, Matematika. Mekhanika., N. 3, 36 (2002) (in Russian).
3. V.A. Shlychkov. Vichislitelnye Tehnoiogii., 3, N.6, 97 (1998) (in Russian).
4. P. Gromov, A. Ezersky, A. Fabrikant. Sound Scattering on the vortex street from cylinder, Akust. Zh., Vol. 28(6), 763–765, (1982).
5. C. Baudet, S. Giliberto, J. Pinton. Phys. Rev. Lett., Vol. 67(2), 193–195, (1991).
6. A. Ezersky, P. Soustov, V. Chernov. Sound Scattering by Karman street, Acoust. Phys., Vol. 46(6), 764–769, (2000).
7. P. Gromov, A. Ezersky, S. Kiyashko, A. Fabrikant. Preprint No. 59, Inst. Appl. Phys., Gorky, (1982).
8. A. Ezersky, A. Zobnin, P. Soustov. Radiophys. & Quantum Electronics, Vol. 38(8), 832–839, (1995).
9. J. Pinton, C. Laroche, S. Fauve, C. Baudet. Ultrasound scattering by, buoyancy driven flows, J. Phys. II (Paris), Vol. 7, 767–773, (1993).
10. A. Petrossian, J. Pinton. J. Phys. II (Paris), Vol. 7, 801–812, (1997).
11. V. Rapoport, N. Mityakov, V. Zinichev. Radiophys. & Quantum Electronics, Vol. 41(7), 241–245, (1998).
12. A.B. Ezersky, P. Paranthoen. Int. J. Transport Phenomena, v. 7, p. 45, (2005).
13. P.L. Soustov, P.R. Gromov, A.B. Ezersky, V.V. Chernov, "Proceedings of the XIX session of the Russian Acoustical Society, Nizhny Novgorod, September 24–28, v. 1, p. 115, (2007).
14. A.H. Woodcock. J. Mar. Res. V. 4, p. 153, (1941).
15. A.B. Ezersky, V.V. Chernov. Izv. RAN. Fizika Atmosfery i Okeana. 35, 656, (1999) (in Russian).
16. A.B. Ezersky, V.P. Reutov, G.V. Rybushkina, V.V. Chernov. Simulation of the convective structures in a thin liquid layer in the presence of a wind driven flow. In: Frontiers of Nonlinear Physics, Nizhny Novgorod, pp. 243–247, (2005).
17. A. Ezersky, P. Gromov, P. Soustov, V. Chernov, « Acoustic sensing of hydrodynamic vortex flow » , Hydroacoustics, V. 8, pp. 47–52, (2005).
18. P. Tchjen. Tearing off currents. M., Mir, (1973) (in Russian).
19. An-bang Wang at all., "On the relationship of effective Reynolds number and Strouhal number for laminar vortex shedding of a heated circular cylinder," Physics of Fluids, Vol. 12, No. 6, (2006).